UNIVERSITÄT DUISBURG ESSEN

Martin Ingo Busch

Catalysts for low temperature conversion of nitrogen oxides

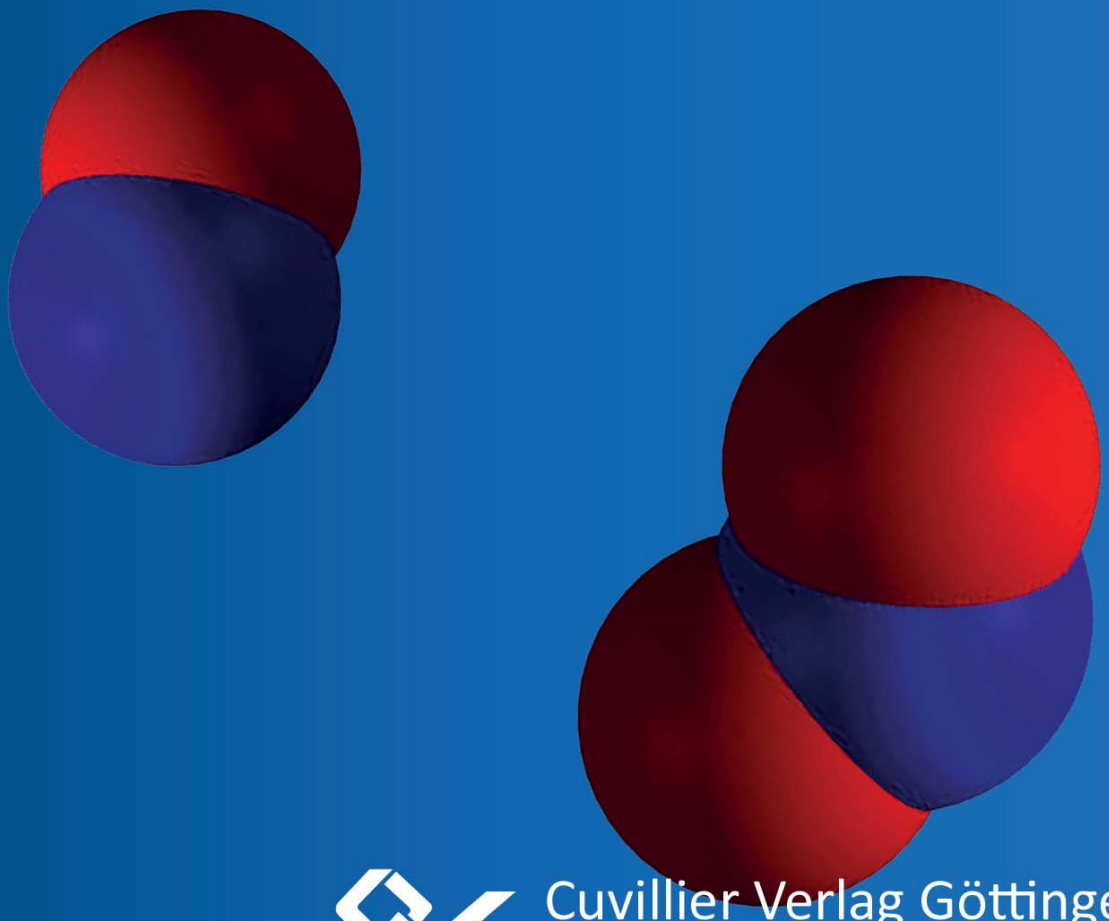

Cuvillier Verlag Göttingen
Internationaler wissenschaftlicher Fachverlag

Catalysts for low temperature conversion of nitrogen oxides

Catalysts for low temperature conversion of nitrogen oxides

Der Fakultät für Ingenieurwissenschaften, Abteilung Maschinenbau

der

Universität Duisburg-Essen

zur Erlangung des akademischen Grades

DOKTOR-INGENIEUR

vorgelegte Dissertation

von

Martin Ingo Busch
aus
Moskau

Tag der Einreichung: 23.09.2014

Bibliografische Information der Deutschen Nationalbibliothek
Die Deutsche Nationalbibliothek verzeichnet diese Publikation in der
Deutschen Nationalbibliografie; detaillierte bibliografische Daten sind im Internet
über http://dnb.d-nb.de abrufbar.
1. Aufl. - Göttingen : Cuvillier, 2015
Zugl.: Duisburg-Essen, Univ., Diss., 2014

Nonnenstieg 8, 37075 Göttingen
Telefon: 0551-54724-0
Telefax: 0551-54724-21
www.cuvillier.de

1. Auflage, 2015
Gedruckt auf umweltfreundlichem, säurefreiem Papier aus nachhaltiger Forstwirtschaft.

ISBN 978-3-95404-990-5
eISBN 978-3-7369-4990-4

Acknowledgements/Danksagung

Nach einer aufrichtig wundervollen Zeit der Dissertation, möchte ich einigen Personen danken, die mich in besonderer Weise unterstützt haben.

Zunächst möchte ich mich ganz herzlich bedanken bei Professor Winterer und Professor Atakan für Ihr großes Vertrauen in meine Fähigkeiten, für die Möglichkeit in Ihren Gruppen zu arbeiten und für die Betreuung meiner Dissertation.

Professor Winterer bin ich tief dankbar für seine äußerst motivierende Art, mich für neue Herausforderungen zu begeistern und das Beste erreichen zu wollen. Die vielen guten Diskussionen haben mir viel wissenschaftlich-chemisches Wissen vermittelt und entscheidend zum Erfolg meiner Arbeit beigetragen. Die Atmosphäre in seiner Arbeitsgruppe ist etwas Besonderes, motivierend und inspirierend.

Professor Atakan danke ich besonders für die vielen wissenschaftlichen Gespräche, die meiner Arbeit Systematik und Tiefe verliehen haben. Sein Rat und seine Hilfe haben meinen Blick immer wieder auf das Wesentliche gelenkt und so manche Herausforderung lösbar gemacht.

Zu großem Dank verpflichtet bin ich Ulf Bergmann und Christian Notthoff. Beide haben mich in der Arbeit oft zeitaufwändig unterstützt und viel zu meinem wissenschaftlichen Verständnis beigetragen.

Ebenfalls zu großem Dank bin ich Wolfgang Schmidt vom Max-Planck-Institut in Mülheim an der Ruhr verpflichtet. Die Diskussionen mit ihm, sein Rat und seine Erfahrung haben mir oft geholfen.

Ich danke meinem Bürokollegen und Freund Fikri Sen für die Zeit die er auf Arbeit mit mir verbringen musste und für seine Hilfe bei meinen Messungen. Großer Dank geht an Ruzica Djenadic für Ihre Hilfe bei meinen ersten CVI-Versuchen und BET-Messungen. Andreas Görnt und Ulf Spengler danke ich für ihre Unterstützung und Hilfe bei meinen Versuchsaufbauten.

Ich danke zudem meinen Kollegen Benjamin Curdts, Christian Pflitsch, Susanne Staude, Abdelkader Nebatti, Erdal Akyildiz, Manfred Richter, Victoria Khlopyanova, Stefan Steinbrink, Herrn Siddiqi, Frau Marten, Valerius Venzik, Daniel Stenders und Donya Alan für die schöne Zeit und ihre Hilfe am Lehrstuhl Thermodynamik.

Ebenfalls bedanken möchte ich mich bei meinen Kollegen Alice Sandmann, Carolin Schilling, Frau Lünsmann, Udo Dörfler, Moazzam Ali, Devedraprakash Gautam, Yong San Cho, Frank Schmidt, Uta Sager, Gerhard Rapp, Suhartininghsi, Heike Feiten, Julia Gebauer, Achim Breidenbach, Sasa Lukic und Stevan Ognjanovic für die schöne Zeit und für ihre Hilfe am Lehrstuhl Nanopartikel-Prozesstechnik.

Ich bedanke mich bei Ulrich Visser und den Kollegen in der Werkstatt Maschinenbau für ihre Hilfe bei der Erstellung meines Versuchsaufbaus. Ich danke außerdem Vadim Migunov und Andreas Beckel für ihre Unterstützung bei wissenschaftlichen Fragestellungen.

Danken möchte ich auch den Studenten Alexander Hein, Claudia Gorinsky, Samer Suleiman, Lukas Helmbrecht, Andreas Klein, Florian Birkmann, Severin Lorenz, Emmanuel Flores und

Viktor Mackert für ihre vielfältige Unterstützung bei meiner Arbeit und für die schöne Zeit nach der Arbeit.

Besonderer Dank gilt Christopher Eckert und Alexander Kompch. Beide habe ich als Kollegen kennengelernt und mit beiden verbindet mich nun eine lange Freundschaft. Durch Alexander habe ich Düsseldorf kennen und schätzen gelernt, durch Christopher habe ich das Ruhrgebiet mit all seinen liebevollen Eigenheiten entdeckt.

Großer Dank gilt Michael Becker und Thomas Schüth vom Center for Coatings and Laser Applications, Fraunhofer USA, für ihre entscheidende Motivation und Anregung zur meiner wissenschaftlichen Arbeit.

Ganz besonders danken möchte ich meiner Freundin Katharina für ihre Liebe, ihre Geduld, für ihre Unterstützung meiner Arbeit und ihren Fokus auf deren Abschluss.

Meinen Eltern, Achim sowie meinen Großeltern möchte ich danken für Ihre lange und liebevolle Unterstützung meines Studiums und meiner Promotion. Besonders meinem Opa bin ich tief dankbar für die „Keimbildung“ meines Interesses an chemischen Fragestellungen, für all die guten und hilfreichen Diskussionen und für seine aufopferungsvolle Akribie beim Redigieren dieser Arbeit.

Martin Busch

Duisburg, September 2014

Table of contents

I. Zusammenfassung

Titel: Katalysatoren für die Niedertemperatur-Umsetzung von Stickoxiden

Stickoxide (NO_x) zählen zu den industriellen Luftschadstoffen und sind eine der Hauptursachen für den sogenannten sauren Regen. Das Ziel der vorliegenden Arbeit ist die Herstellung und Charakterisierung eines geeigneten Katalysatorsystems zur Filterung und zum Abbau von Stickoxiden in der Umgebungsluft.

Handelsübliche aktivierte Kugelkohlen und Zeolithe werden im Rahmen dieser Arbeit als vielversprechende Ausgangsstoffe für eine hohe Beladung mit katalytisch aktiven Materialien ausgewählt. Durch die Katalysatorpräparation mithilfe chemischer Gasphaseninfiltration kann das Matrixmaterial stärker beladen werden als mit der etablierten nasschemischen Infiltration. Die Trägermaterialien sind mit Eisen, Kupfer, Mangan, bzw. deren Oxiden infiltriert.

Die so hergestellten Katalysatoren werden zunächst strukturell und chemisch charakterisiert, anschließend wird die Stickoxidadsorption und Stickoxidumsetzung untersucht. Die Strukturanalyse erfolgt mit Hilfe von Rasterelektronen- und Transmissionselektronenmikroskopie, Röntgendiffraktometrie sowie Stickstoffadsorptionsmessungen. Die chemische Zusammensetzung wird durch energiedispersive Röntgenspektroskopie bestimmt. Die Adsorption von Stickoxiden wird mithilfe von Thermogravimetrie und Differenzthermoanalyse untersucht. In einem Kreislaufreaktor mit angeschlossenem Massenspektrometer wird schließlich die katalytische Umsetzung von Stickstoffdioxid analysiert.

In den Untersuchungen zeigt sich, dass die Kugelkohlekatalysatoren über den gesamten Primärpartikelquerschnitt homogen infiltriert werden. Größere Partikel (20-50 nm) finden sich nur in größeren Poren und entlang von Rissen im Matrixmaterial. Die Adsorption von NO_2 beginnt zunächst überwiegend in den Mikroporen und diese scheinen die katalytische Aktivität insgesamt stark zu beeinflussen. Alle untersuchten Katalysatormaterialien setzen NO_2 nahezu vollständig um. Die Hauptreaktionsprodukte sind NO und N_2O. Aktivkohlen, die mit Übergangsmetallen infiltriert sind, katalysieren die Umsetzung von NO zu CO und N_2O. Der zusätzliche Eintrag von Siliziumdioxid in die Aktivkohlen fördert die Freisetzung von CO und N_2O und stabilisiert das Porensystem während des Katalyseprozesses.

Die Zeolithkatalysatoren weisen einige Metall- oder Metalloxidpartikel außerhalb der Porenstruktur auf. Während der chemischen Gasphaseninfiltration werden die Primärpartikelzwischenräume teilweise durch abgeschiedenes Material gefüllt. Die Umsetzung von NO_2 wird vor allem von Mordenit-Zeolithen katalysiert. Die Infiltrationsmethode hat keinen unabhängigen Einfluss auf die katalytische Aktivität der Proben. Unter allen hergestellten Zeolithkatalysatoren zeigt der Eisen-infiltierte Mordenit die höchste Aktivität in der Umsetzung von Stickoxiden bei 425 K und die größte Freisetzung der Reaktionsprodukte Sauerstoff und Stickstoff. Dieser Katalysator ist unter den genannten Niedertemperaturbedingungen aktiver als die hergestellten Kugelkohlekatalysatoren und sogar aktiver als der ausgiebig charakterisierte Cu-ZSM-5-Katalysator.

II. Abstract

Nitrogen oxides are one of the industrial pollutants in the environment and a major cause of acid rain. The objective of the present work is to prepare and characterize an appropriate catalyst system for low temperature removal and conversion of nitrogen oxides.

The work is focused on commercially available activated carbon and zeolite catalyst supports as promising candidates with a high load of catalytically active species. The chosen catalyst preparation via chemical vapor infiltration is expected to introduce a higher infiltration load into these catalysts than common wet chemistry techniques. The support materials are infiltrated with iron, copper, manganese and their oxides.

The synthesized catalysts are characterized regarding their structure, chemical composition as well as nitrogen oxide adsorption and conversion. Structural characterization is performed with scanning electron microscopy, transmission electron microscopy, X-ray diffraction and low temperature nitrogen adsorption. The chemical composition is derived by means of energy-dispersive X-ray spectroscopy. Nitrogen oxide adsorption and decomposition properties are investigated using thermal gravimetric analysis, differential thermal analysis and mass spectrometric monitoring of the catalytic decomposition of nitrogen dioxide in recycle flow.

The ball-shaped activated carbon catalysts are homogeneously infiltrated over the entire cross section. Some metal species formation (20-50 nm) in larger cavities and cracks is observed. The adsorption of nitrogen dioxide starts predominantly in micropores and the micropores seem to have a significant effect on the catalytic activity in general. All investigated catalysts convert nitrogen dioxide almost completely and the major conversion products are nitric oxide and nitrous oxide. Metal infiltration of the activated carbons can increase the conversion of nitric oxide into nitrous oxide while forming carbon monoxide. The additional co-deposition of silica enhances the desorption of carbon monoxide and nitrous oxide and stabilizes the pore system during the catalysis process.

The zeolite-based catalysts exhibit some metal/metal oxide species deposited on the surface of the framework. During the chemical vapor infiltration the inter-crystallite pores seem to be partially filled with deposited metal species. The decomposition of nitrogen dioxide is highly preferred in the mordenite zeolites. No influence is observed from the infiltration method on the catalytic activity of the zeolite catalysts. Of all zeolite samples, iron-infiltrated mordenite shows the largest nitrogen oxide conversion at 425 K and the largest release of oxygen and nitrogen as decomposition products. At low temperature, this catalyst is outperforming the synthesized carbon-based catalysts and even the well-characterized Cu-ZSM-5 catalyst.

III.Index of tables

IV. Index of figures

V. List of abbreviations, acronyms and symbols

A	Area covered by one adsorbed molecule	p. 41
a.u.	Arbitrary units	p. 24
AC	Activated carbon	p. 19
AES	Auger electron spectroscopy	p. 10
AFM	Atomic force microscopy	p. 10
bcc	Body-centered cubic	p. 32
BEA	Zeolite Beta	p. 20
BET	Brunauer-Emmett-Teller-method	p. 18
BJH	Barrett-Joyner-Halenda-method	p. 41
c_{calib}^{g}	Concentration of the gas species *g* for mass spectrometer calibration	p. 131
$\vec{c}_{t}^{g}$	Concentration of gas species *g* at time *t*	p. 131
C_{BET}	BET-constant	p. 40
C_g	Concentration of chemical reactant in the gas phase	p. 16
C-SEM	Continuous secondary electron multiplier	p. 47
CSTR	Continuously stirred tank reactor	p. 10
CVD	Chemical vapor deposition	p. 15
CVI	Chemical vapor infiltration	p. 15
D_{eff}	Effective diffusivity	p. 53
D_{Kn}	Knudsen diffusivity	p. 54
d_m	Molecular diameter	p. 16
d_{pore}	Pore width	p. 54
DRIFT	Diffuse reflectance infrared Fourier transform	p. 10
DTA	Differential thermal analysis	p. 10
E_{diss}	Energy of dissociation	p. 9
EDX	Energy-dispersive X-ray spectroscopy	p. 10
ELO	Extra-lattice oxygen	p. 15
EXAFS	Extended X-ray absorption fine structure	p. 15

FFKM	Perfluoro-elastomer	p. 45
FFT	Fast-Fourier transform	p. 10
FIB	Focused ion beam	p. 37
FIR filter	Finite impulse response filter	p. 48
FTIR	Fourier transform infrared spectroscopy	p. 99
g	Gas species	p. 129
GRG	Generalized Reduced Gradient approximation algorithm	p. 130
h_g	Gas phase mass transfer coefficient of reactants to the substrate	p. 16
HRTEM	High-resolution transmission electron microscopy	p. 10
I	Ion current signal of the mass spectrometer	p. 129
$\tilde{I}$	Normalized ion current signal of the mass spectrometer	p. 129
$\bar{I}$	Average of subsequently measured normalized ion current signals	p. 130
ICP-MS	Inductively-coupled plasma mass spectrometry	p. 10
IWM	Incipient wetness method	p. 32
K	Shape factor	p. 39
k_B	Boltzmann constant	p. 16
k_S	Rate constant for heterogeneous decomposition of gaseous reactants	p. 16
l	Distance from the surface of the spherical particle	p. 53
L	Characteristic length	p. 53
$\bar{L}$	Average distance from the surface of the spherical particle	p. 53
$\langle L \rangle$	Particle diameter	p. 39
LIE	Liquid ion exchange	p. 33
LNB	Low NO_x burners	p. 2
M	Metal species	p. 27
M	Molar mass	p. 41
$M_{m/e}$	Matrix of gas species calibration vectors	p. 129
m_c	Sample mass	p. 45
m_S	Mass of the substrate	p. 41
m/e-ratio	Mass-charge-ratio	p. 46

MFI	Mordenite framework-inverted zeolite	p. 20
MOR	Mordenite zeolite	p. 20
M_{FC}	Molar mass of Ferrocene	p. 54
M_{ms}	Matrix of acquired ion current signals over the measurement time	p. 130
M_{ms}^{*}	Approximation of matrix M_{ms}	p. 130
n	Number of active sites	p. 11
n.m.	Value not measured	p. 52
n.r.	Gas species not significantly detected	p. 93
N_A	Avogadro number	p. 41
N_o	Number of atoms incorporated into a film per unit volume	p. 16
NLDFT	Non-local density functional theory	p. 41
NMR	Nuclear magnetic resonance	p. 10
NO_x	Nitrogen oxides	p. 2
NSR	NO_x-storage-reduction	p. 4
p	Pressure	p. 16
p_0	Vapor pressure	p. 40
P/B-ZAF	Peak-to-background model and subsequent correction of atomic number, absorption and fluorescence	p. 38
QMS	Quadrupole mass spectrometer	p. 46
r	Radius of the meniscus of the liquid in a capillary	p. 41
R	Radius of the primary particle	p. 53
r_{dep}	Film deposition rate	p. 16
r_{exp}	Experimental reaction rate	p. 9
S	Number of active sites	p. 11
S_s	Specific surface area	p. 41
SCR	Selective catalytic reaction	p. 2
SEM	Scanning electron microscopy	p. 10
STM	Scanning tunneling microscopy	p. 10
SV	Space velocity	p. 45

t	Estimated statistical thickness of the adsorbed layer	p. 42
T	Temperature	p. 16
T_{decomp}	Decomposition temperature	p. 29
TEM	Transmission electron microscopy	p. 10
T_{evap}	Evaporation temperature	p. 29
TGA	Thermal gravimetric analysis	p. 10
TOF	Turnover frequency	p. 10
TPD	Temperature programmed desorption spectroscopy	p. 10
TWC	Three-way catalysis	p. 2
U	DC-voltage	p. 46
U_f	Deflection voltage	p. 46
$\vec{v}$	Vector of calibration coefficients of a gas species	p. 130
$\dot{V}_R$	Volumetric flow rate	p. 45
V_m	Molar volume	p. 41
V_p	Pore volume	p. 42
V_x	Adsorbed nitrogen volume at a relative pressure x	p. 42
$V \cdot cos\,\omega t$	AC-voltage	p. 46
W	Mass of the adsorbent	p. 40
W_m	Mass of one adsorbed monolayer	p. 40
x	Oxidation state	p. 27
XANES	X-ray Absorption Near Edge Structure	p. 15
XPS	X-ray photoelectron spectroscopy	p. 10
XRD	X-ray diffraction	p. 10
y	m/e-ratio	p. 129
ZSM	Zeolite Socony Mobil	p. 2
ΔH_{ads}	Heat of adsorption	p. 40
ΔH_c	Enthalpy of combustion	p. 27
ΔH_{cond}	Latent heat of condensation	p. 40

ΔH_f^0	Standard enthalpy of formation	p. 27
ΔH_r^0	Standard enthalpy of reaction	p. 12
β	Peak width of a reflection	p. 39
γ	Surface tension	p. 41
φ	Thiele modulus	p. 53
δ	Contact angle of adsorbent and adsorbate	p. 41
ε	Void fraction of a porous sample	p. 54
λ	Mean free path length	p. 16
λ	Wavelength	p. 39
ρ	Density	p. 42
ϑ	Angle of the incident beam to the normal of the reflecting lattice plane	p. 39

1. Introduction

Nitrogen oxides (NO_x) comprise species like N_2O, NO, NO_2, N_2O_3, N_2O_4, NO_3, and N_2O_5. Among these most abundant are nitrous oxide (N_2O) as a relevant greenhouse gas and the important air pollutants nitric oxide (NO) and nitrogen dioxide (NO_2) (Skalska et al. 2010). The latter two are commonly summed in the term NO_x.

Although NO_x are also emitted in biological and geological processes, the vast majority (83%) of NO_x in the atmosphere are anthropogenic (Delmas et al. 1997). In 2010 the worldwide NO_x emissions were 67 million tons, whereas emissions of the second important air pollutant SO_2 sum up to 56 million tons (UNSD 2009). Together with sulfur oxides, NO_x are the main air pollutant and responsible for phenomena like the so called “acid rain” (Hameed & Dignon 1992).

The largest part of NO_x emissions (about 38%) stem from road transport, especially from Diesel engines (see Fig. 1) (Bradley & Jones 2002; European Environment Agency 2011). While more than 90% of the NO_x emissions from these fossil fuel power units are NO, it is quickly oxidized at the atmosphere to NO_2 (Neathery et al. 1997). NO_2, however, is even more harmful to human than NO (Pietrzak & Bandosz 2007).

In the European Union, Iceland, Liechtenstein, Norway, Switzerland and Turkey the NO_x emissions have been decreased by 41% between 1990 and 2009, primarily due to the broad introduction of three-way catalysts and NO_x-abatement technologies (European Environment Agency 2011). So far, the control of NO_x emissions from light-duty engines has been successful in many ways and the perspective in the future is a focus on reducing emissions from heavy-duty engines (McDonald et al. 2012).

In addition to NO_x emission reductions, direct NO_x removal in human workspace would be a great progress. In automobiles, incumbent cabin air filters usually remove dust particles, pollen grains and also some pollutant gases, but modification of these filters to add catalytic NO_x conversion would be favorable. For such application the operational temperature would be preferentially at room temperature or – by use of waste heat from the car engine – at about 373 K. A broad introduction in human workspace would require inexpensive and nontoxic materials. Hence, modification and adaption of commercial catalysts for low temperature application seems to be a preferential path.

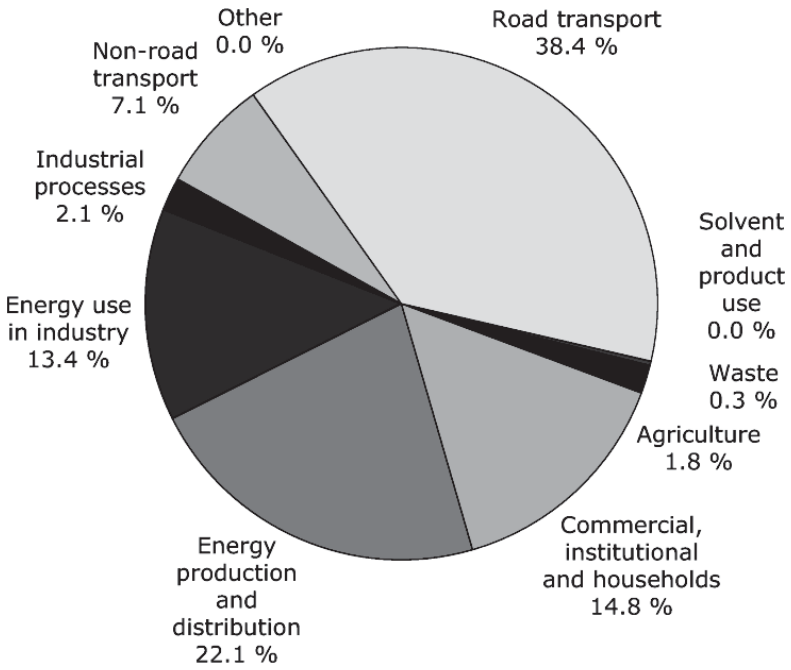

Fig. 1. Sector share of NO_x emissions in European Union and Iceland, Liechtenstein, Norway, Switzerland, Turkey; adapted from (European Environment Agency 2011)

The objective of this work is to prepare and characterize an appropriate catalyst system for low temperature removal and conversion of nitrogen oxides in human workspace. On the route, two separate questions need to be answered: Which catalyst system is most efficient in NO_x removal at low temperature? And which catalyst is most efficient in NO_x decomposition at low temperature?

This work is focused on carbon- and zeolite-based catalysts as promising candidates with a high load of catalytically active species. The chosen catalyst preparation via chemical vapor infiltration is expected to confer these catalysts with a higher infiltration load and different species than common wet chemistry techniques (Pieterse et al. 2004). Samples from either preparation method are likely to differ structurally and chemically, which is often associated with a difference in their catalytic performance (Aksoylu et al. 2003; Capek et al. 2005; Pérez-Ramírez & Gallardo-Llamas 2005).

Subsequent to an overview of the state of the art in NO_x conversion, important theoretical aspects are introduced. Experimental methodologies and procedures are explained and reference catalyst systems are defined. The results and discussion part is subdivided into a section for activated carbon-based catalysts and another for zeolite-based catalysts. Each catalyst is characterized in structure, chemical composition, NO_x adsorption and NO_x conversion. Finally, the work is summarized and conclusions from the discussion are drawn. The work finishes with a prospect and further research recommendations.

1.1. State of the art of NO_x conversion

1.1.1. History of NO_x removal and conversion

The investigation of the catalytic decomposition of NO_x has a long history going back to the beginning of the 20th century when the earliest attempts were carried out with pure platinum

catalysts (Jellinek 1906; Green & Hinshelwood 1926). A first report on reduction and conversion of N_2O and NO with activated carbon has been published by Shah (Shah 1929a; 1929b). In the following decades an abundant number of catalyst systems have been screened, mainly comprising supported and unsupported noble metals, transition metals and their oxides (Elving & McElroy 1941; Shelef et al. 1969; Bosch & Janssen 1988). Several catalytic and non-catalytic NO_x removal technologies have been developed with a special focus on combustion processes (Gohlke et al. 2010).

Today, catalytic and non-catalytic NO_x abatement technologies are well established and broadly deployed. They mainly comprise three-way catalysis (TWC) (Farrauto & Heck 1999; Roy et al. 2009), the selective catalytic reaction (SCR) by addition of ammonia or hydrocarbons (Burch & Millington 1995; Shelef 1995; Heck 1999; Burch et al. 2002) and technologies which aim at minimizing the synthesis of NO_x already during combustion like low NO_x burners (LNB) (Ballester et al. 1997). However, most of these technologies require either high temperature, or they apply harmful additives.

1.1.2. Overview of NO_x removal catalysts

The common catalyst materials for NO_x decomposition include a large number of noble metals, transition metals, their oxides, combinations and alloys (Bosch & Janssen 1988). Typical catalysts for the SCR reaction are Fe_2O_3, Fe_2O_3-Cr_2O_3, Fe_2O_3-WO_3 and Fe_2O_3 or V_2O_5 supported on $A1_2O_3$ (Nakajima & Hamada 1996). The mechanisms for their adsorption behavior, catalytic decomposition reaction and reaction kinetics have been elaborately investigated (Parvulescu et al. 1998; Garin 2001; Al-Abadleh & Grassian 2003).

The additive-free direct removal of NO_x still suffers from slow reaction kinetics. Substantial conversion rates require high temperature (Jobson 2004). A number of transition metal oxides have been investigated at elevated temperatures (573-1073 K), the most promising being an unsupported Co_3O_4 catalyst, even outperforming a platinum catalyst (Shelef et al. 1969).

Starting from the late 1980s, zeolite-based catalysts have been considered for NO_x decomposition. Transition metal ion-exchanged zeolites proved to be good catalysts for selective and direct catalytic NO_x removal (Iwamoto et al. 1986; Centi & Perathoner 1995; Konduru & Chuang 1999; Garin 2001; Tang et al. 2002; Kumar et al. 2004). In their function as molecular sieves they selectively adsorb NO_x from waste gas (Sundaresan et al. 1967).

The first reports on ZSM-5, highly exchanged with copper, revealed very promising results in direct NO decomposition (Iwamoto et al. 1986). In Cu-ZSM-5 direct decomposition of NO is notable above 493 K (Teraoka et al. 2000). The adsorption of NO is increasing with higher exchange level. Among various transition metals for ion exchange in zeolites, copper and iron have been identified to be among the most promising candidates (Bosch & Janssen 1988; Centi & Perathoner 1995).

While zeolite catalysts in the SCR reaction are well investigated (Bosch & Janssen 1988; Heinrich et al. 2002; Schwidder et al. 2005), studies on direct NO_x decomposition with zeolites other than ZSM-5 remain scarce. Recent studies try to elucidate for example the low temperature direct removal of N_2O by iron-exchanged zeolites (Pieterse et al. 2004; Bulushev et al. 2005).

Drawbacks in the application of the SCR technology include the considerably high reaction temperatures (> 573 K) and the possible slip of unreacted reactants (Neathery et al. 1997; Illán-Gómez et al. 1999; Shirahama et al. 2002). Harmless reactants like carbon may be preferential in human workspace applications and the working temperature of activated carbon based catalysts can be considerably lower than required in the efficient selective catalytic reaction (SCR) with ammonia (Busca et al. 1998; Skalska et al. 2010).

A good activity of an activated carbon catalyst is often correlated with a good activity in carbon decomposition with oxygen, producing a loss of carbon material in a NO_x-polluted air flow (Illán-Gómez et al. 1999). The addition of oxygen has a positive effect on NO decomposition with copper-infiltrated activated carbon (Yamashita et al. 1993), but the effect of copper could rather be attributed to the catalytic conversion of carbon with oxygen than to the catalytic NO decomposition itself (Aarna & Suuberg 1997).

1.1.3. Availability, application, problems and limitations of the described processes

On the other hand, oxidation of the carbon catalyst surface during NO_x decomposition is often responsible for catalyst deactivation (Illán-Gómez et al. 1996). Catalyst deactivation is also observed at low temperatures for zeolite catalysts due to the accumulation of oxygen at the catalyst surface (Iwamoto et al. 1981; Modén et al. 2002; Cejka et al. 2012). At temperatures above 873 K zeolites like ZSM-5 tend to lose alumina which can destabilize their framework structure (Grinsted et al. 1993).

Several authors have studied the effects caused by co-adsorption of other reactants – e.g. H_2O (Sager & Schmidt 2009), CO (Aarna & Suuberg 1999) or SO_2 (Rubel & Stencel 1997) – which may be present in common flue gases. For example, the co-adsorption of water vapor with NO_2 or NO can easily lead to formation of nitric acid, which may decompose the zeolite support (Richter et al. 1990; Kong & Cha 1996):

$$4\,NO_2^{ads} + 2\,H_2O + O_2 \leftrightarrow 4\,HNO_3^{ads} \qquad \textbf{(1)}$$

Larger quantities of water vapor seem to bear an inhibiting effect on the catalytic conversion of NO on activated carbon catalysts (Stegenga et al. 1993). Excess oxygen in the gas phase can limit NO conversion in copper-exchanged zeolites, since it prohibits the reduction of Cu^{2+} species to the more active Cu^{+} (Li & Hall 1991).

In the last years, the NO_x-storage-reduction (NSR) has been developed as a new concept (Takahashi et al. 1996; Gómez-García et al. 2005; Liu & Gao 2011). In this two-step-process NO_x from flue gas is first stored in the catalyst system under lean burn conditions and it is subsequently decomposed under fuel rich combustion. Promising further attempts of direct NO_x conversion include investigation of perowskites, like $Ba_{0.8}La_{0.2}Mn_{0.8}Mg_{0.2}O_3$, and rare earth oxides like Ba/CeO_2-MnO (Imanaka & Masui 2012). However, all investigation is performed at temperatures well above 973 K. In general, recent studies on direct NO_x conversion became scarce.

1.2. Motivation of this work

The review of the literature shows that elaborate research has been performed in order to limit NO_x emissions or to decompose these harmful flue gases. Progress in the catalytic decomposition with additives, or at high temperature and the modification of fuel combustion processes leads to a lower rise of NO_x emissions, than without these actions.

However, air pollution by nitrogen oxides remains a major issue of industrial environments and road traffic, which cannot be eliminated in short term. Hence, the removal of emitted nitrogen oxides at least from ambient air at human workspace is a topic of high priority, thus leading to the motivation of the present work.

Complementary to the state of the art, this work is focused on the removal and decomposition of nitrogen oxides close to ambient temperature and avoiding the use of any harmful additives. The expectable chemical reactions at such conditions are likely to be kinetically much slower than at their maximum efficiency temperature. Hence, the applied measurement methods need to be adapted to slow chemical conversion processes and to the investigation of possibly different reactions than at higher temperature.

The proposed solution in this thesis includes the stabilization of nano particles of catalytically active transition metals and their oxides, well dispersed in microporous matrix materials, in order to achieve a large number density of active sites per unit volume of catalyst material. Therefore, activated carbons and zeolites are infiltrated with different metal organic precursors via chemical vapor infiltration and liquid ion exchange processes. The resulting catalyst materials are investigated in a recycle flow reactor regarding their decomposition behavior of nitrogen oxides at low temperature.

2. Theoretical background

2.1. Heterogeneous catalysis

2.1.1. Definition and history of heterogeneous catalysis

The concept of catalysis dates back to works of Berzelius in the beginning of the 19th century (Boreskov 2003, p. 1ff; Deutschmann et al. 2009, p. 5ff). According to Boreskov, catalysis is the "change of the rate of chemical reactions under the action of certain substances – catalysts, which repeatedly enter intermediate chemical interactions with the reactants and restore their chemical composition after each cycle of intermediate interactions" (Boreskov 2003, p. 1). Hence, for a given temperature and pressure, not the equilibrium of a reaction is shifted, but the kinetics to achieve equilibrium are accelerated.

Depending on the phase of the reactants a catalytic process may be homogeneous or heterogeneous. In homogeneous catalysis the reactants and the catalyst have the same phase, i.e. both are gaseous or liquid. In heterogeneous catalysis – like in this work – the reactants and the catalyst have different phases, e.g. gaseous reactants and a solid catalyst (Boreskov 2003, p. 38).

2.1.2. Principles of heterogeneous catalysis

Catalytic conversion of gaseous reactants in a porous catalyst can be described as a process in five steps (Ponec & Bond 1995, p. 247):

1) The reactants diffuse from the gas atmosphere to the catalyst surface or into catalyst pores.
2) The reactants adsorb at the active centers.
3) The chemical reaction proceeds.
4) The adsorbed products desorb from the catalyst surface.
5) The products diffuse from the catalyst surface or out of the pores into the gas atmosphere.

Steps 1 and 5 are interparticle or intraparticle transportation processes, depending of the location of the reaction site inside the pores or on the external surface of the catalyst. Steps 2, 3 and 4 are usually comprised in one step and one rate equation, although each of the steps can be rate limiting for the overall catalytic throughput.

The Langmuir-Hinshelwood reaction mechanism of adsorbed species is the most common mechanism in heterogeneous catalysis. It is based on the Langmuir equation, describing the surface coverage of the catalyst by an adsorbent as an equilibrium between adsorbing and desorbing species at a certain temperature and partial pressure (Langmuir 1918). Hinshelwood suggested an interaction of the reactant species in the adsorbed state (Hinshelwood 1940, p. 187ff; Ponec & Bond 1995, p. 268ff). The overall reaction rate can be limited by the adsorption kinetics of reactants, the chemical reaction itself or by the desorption rate of products.

In contrast to the Langmuir-Hinshelwood mechanism, the mechanism described by Eley and Rideal assumes the participation of at least one reactant directly from the gas phase without adsorption on the catalyst (Schwab 1928; Rideal 1939; Eley & Rideal 1940).

2.1.3. Role of the catalytically active species

Taylor introduced the concept after which not the entire catalyst surface, but only certain surface sites participate in the reaction (Taylor 1925). These active centers can be high energy sites like defects, step sites, vacancies, locally unsaturated or oversaturated sites. At these sites foreign molecules can adsorb, dissociate, change their oxidation state or change their polarity. The surface number density of active centers is typically larger in small particles due to their high surface to volume ratio and due to the defects induced by surface lattice tensions or interaction of surface molecules with the support material.

Adsorption of specific reactants and subsequent chemical reactions can be highly sensitive to the geometric or electronic nature of the active site (Norskov et al. 2008), the local composition of the material and to the catalyst particle size (Bell 2003). The particle size effect plays a large role for nano particles as for example the electron binding energy quickly decreases with decreasing cluster size (Ponec & Bond 1995, p. 227ff).

2.1.4. Role of the support

Catalytically active materials are often supported by a foreign material. The role of this support includes the stabilization of the catalytically active material in a well dispersed form even under chemically harsh conditions, facilitating the adsorption of reactants or the desorption of reaction products, facilitating diffusion kinetics, i.e. exchange of reactants and reaction products, and to prevent attrition upon mechanical stress (Ponec & Bond 1995, p. 320ff).

Many catalysts have a monolithic macro-form with many smaller, possibly interconnected passages inside the material (Cybulski & Moulijn 1994). Inside these passages the actual catalytically active material is incorporated or deposited on the surface. Support materials with very narrow passages are porous and according to IUPAC nomenclature the pore sizes can range from microporous (< 2 nm) to mesoporous (2 – 50 nm) and macroporous (> 50 nm) (Smith et al. 1994).

Additionally, charged sites of the support - e.g. unsaturated surface atoms in activated carbons or Brønsted acidic sites in zeolites – may impose changes in polarity to neighboring small catalyst particles, thus changing the catalytical properties (Ponec & Bond 1995, p. 234ff).

2.1.5. Adsorption of reactants at the catalyst surface and desorption of products

The adsorption of reactants at the catalyst surface is classified as physisorption and chemisorption, according to the binding energy of the adsorptive. Physisorbed species are weakly bonded to the surface, mainly as the result of van der Waals forces and Pauli repulsion, whereas chemisorbed species form a rather strong bond (typically more than 40 kJ mol^{-1} binding energy) (Chorkendorff & Niemantsverdriet 2007, p. 217ff). Chemisorption of molecular reactants is often associated with dissociation, if the molecule in its dissociated state has a lower potential energy compared to the adsorbed molecule (Ertl 2010, p. 7ff).

The desorption of reaction products from the catalyst surface to the atmosphere usually requires activation and is essential in catalytic steady-state processes (Thomas et al. 1997, p. 94ff). The catalytic activity will decrease if the active centers become inaccessible for reactants due to coverage by accumulating reaction products.

The rate of the catalytic reaction strongly depends on the interaction of reactants with the catalyst surface. Interactions between catalyst and reactants, which are too weak, prevent adsorption or reactant dissociation of the species (Chorkendorff & Niemantsverdriet 2007, p. 264). Interactions, which are too strong, may prevent desorption of reaction products and consequently inhibit the overall reaction after some time. Hence, there is an optimum heat of adsorption for a specific catalyst material, known as Sabatier's principle. It is typically depicted in a volcano plot, the ordinate showing some measure of the reaction rate and the abscissa showing some measure of the interaction energy, e.g. the heat of adsorption. For NO decomposition over metal catalysts the corresponding volcano plot is displayed in Fig. 2 (Falsig et al. 2007).

In addition to the accumulation of surface species, catalysts can be deactivated due to thermal or chemical degradation, fouling, poisoning or mechanical wear (Forzatti & Lietti 1999; Bartholomew 2001). Many of these causes are reversible and the catalytic activity may be restored after chemical or thermal recovering.

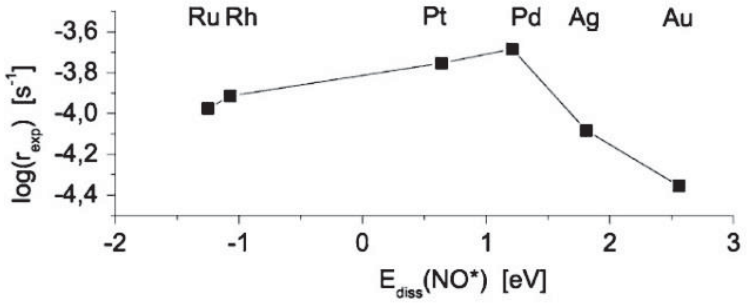

Fig. 2. Experimental activities (log r_{exp})/s of metal catalysts on $MgAl_2O_4$ support versus the dissociation energy E_{diss}(NO*) of adsorbed nitric oxide, T = 873-923 K, taken from (Falsig et al. 2007)

2.2. Characterization of catalysts

Table 1. Common methods of catalyst characterization for physical and chemical properties (Chorkendorff & Niemantsverdriet 2007, p. 129ff; Deutschmann et al. 2009, p. 52ff)

Catalyst property	Measurement technique	Comments
Physical properties		
Accessible surface area	Low temperature nitrogen adsorption*	
Surface topology	Atomic force microscopy (AFM)	
	Scanning tunneling microscopy (STM)	Limited to conducting materials
Sample porosity	Low temperature nitrogen adsorption*	
Particle size	Scanning electron microscopy (SEM)*	Limited to a small part of the sample
	Transmission electron microscopy (TEM)*	Limited to a small part of the sample
	X-ray diffraction (XRD)*	Limited to crystalline species and provides average particle size
Crystal structure and phase	XRD*	
	High-resolution electron transmission microscopy (HRTEM) followed by fast-fourier transform (FFT)*	Provides only information of a small part of the sample
Catalyst dispersion in matrix material	SEM*	Typically inspection of the surface or cross section of the particle
	TEM*	Typically inspection of a cross section or thin lamella of the particle
	STM*	Typically inspection of the surface of the primary particle; only for conducting materials, but allows spatial resolution even of atoms
Local coordination of atoms	Extended X-ray absorption fine structure (EXAFS)	Requires synchrotron radiation
Chemical properties		
Elemental analysis and	Energy-dispersive X-ray spectroscopy (EDX)*	Elemental composition in spatial resolution
	Inductively-coupled plasma mass spectrometry (ICP-MS)	High accuracy of elemental quantification
	X-ray photoelectron spectroscopy (XPS)	Surface-sensitive
	Auger electron spectroscopy (AES)	Surface-sensitive
Oxidation state of elements	XPS	Surface-sensitive
	AES	Surface-sensitive
	Mössbauer spectroscopy	Limited to investigation of some elements (e.g. iron, cobalt)
	X-ray Absorption Near Edge Structure (XANES)	Allows analysis of elemental composition and oxidation states
Surface groups	Diffuse reflectance infrared fourier transform spectroscopy (DRIFT)	Not exclusively sensitive to surface groups
	X-ray photoelectron spectroscopy (XPS)	
Chemical and structural environment	Nuclear magnetic resonance (NMR) spectroscopy	Applicable for example for investigation of ion accomodation in zeolites
Acid/base properties	Adsorption of probe molecules combined with microcalorimetry	Interesting for example for zeolites
Thermal analysis	Thermal gravimetric analysis (TGA)*	Information on mass change of catalyst upon thermal treatment
	Differential thermal analysis (DTA)*	Information on enthalpy changes upon thermal treatment
	Temperature programmed desorption spectroscopy (TPD)	Information on desorbing species upon thermal treatment by means of mass spectrometric analysis, can be combined with isotope-labelling

*) measurement technique applied in the present work

Many catalyst systems react very sensitive to small variations of the experimental conditions and the actual mechanisms are not yet thoroughly understood. An overview of the most common scientific characterization methods of catalysts is provided in Table 1 (Chorkendorff &

Niemantsverdriet 2007, p. 129ff; Deutschmann et al. 2009, p. 52ff). The methods applied in this work are presented in more detail in sections 3.2 and 3.3.

Investigation of the catalytic activity

The catalytic activity of solid catalysts with gaseous reactants is mostly investigated in plug flow reactors on the laboratory scale where the catalyst material is fixed in a heatable reactor tube and a defined gas mixture with reactants is passed over or through the catalyst (Thomas et al. 1997, p. 472ff). At the exhaust of the reactor the gas mixture is monitored using a mass spectrometer, gas chromatography or similar analytical technique. Batch reactors with closed inlet and outlet during the reaction are also applied, especially in the fluidized-bed form or as continuously stirred tank reactor (CSTR).

In a recycle reactor a defined volume of gaseous (or liquid) reactants is pumped continuously through the plugged catalyst material in a cycle. For a large number of pumping cycles the gas mixture composition in the recycle reactor is close to that in the CSTR at similar conditions, but it combines the advantages of easy handling and adjustable flow rate of the plug flow reactor. Such recycle flow reactors are also used for the investigation of NO decomposition via carbon catalysts (Mochida et al. 1985).

The activity of a catalyst is usually specified by calculation of a reaction rate. For many catalysts this is not straightforward as not the entire catalytically active material is accessible to the reactants, but a large amount remains inaccessible in closed pores or buried in the bulk. An alternative measure is the turnover frequency (TOF), defined as the conversion rate of reactants per number of active surface atoms of the catalyst (Thomas et al. 1997, p. 27):

$$TOF = \frac{1}{S}\frac{\mathrm{d}n}{\mathrm{d}t} \qquad \textbf{(2)}$$

Where S is the number of active sites, n is the number of molecules of a given reaction product and t is the time. However, problems arise from this definition, too: In many reactions the active centers are unknown and if they are known, they may be difficult to count. Furthermore, not all the active centers may be available during the catalysis process.

Another viable alternative is to state the mass specific reaction rate in mol s^{-1} g^{-1} describing the molar quantity of converted reactants per unit time and unit mass of catalyst (Ponec & Bond 1995, p. 266ff). A common measure for the overall efficiency of a porous catalyst system is provided by the Thiele modulus, indicating whether the reaction yield is controlled by the reaction kinetics or by the reactant diffusion (Deutschmann et al. 2009, p. 68).

Since the catalytic reactions often proceed in multiple steps, complex mechanisms are not easy to analyze. Fast secondary reactions of reaction products can occur in any type of reactor. However, secondary reactions of reaction products are much more likely to influence the observed gas mixture in the batch and recycle reactors, since the residence time of reactants and products is generally larger than in plug-flow reactors. Therefore, mechanisms and kinetics should be derived and interpreted with care.

2.3. Decomposition mechanisms of nitrogen oxides

2.3.1. NO_x adsorption mechanisms

Even at ambient conditions activated carbons are able to adsorb a substantial amount of NO_x, especially NO_2 (Xia et al. 1999). The critical temperatures of N_2 (126 K), O_2 (155 K), CO_2 (304 K) and NO (180 K) are considerably lower than the one of NO_2 (431 K). Hence, the former gases have a smaller tendency to adsorb in micropores at ambient conditions (Neathery et al. 1997). Secondly, NO_2 adsorption is sensitive to the pore size distribution of micropores in the activated carbon. Best adsorption results are observed for carbons which contain mostly very small micropores (Rubel et al. 1995b).

Two main mechanisms of NO adsorption are suggested for low temperatures (< 500 K). The dissociative NO adsorption on carbon is accompanied with an enthalpy of 92 kJ/mol (Aarna & Suuberg 1997). Upon further heating NO or carbon oxides and nitrogen are released (Teng et al. 1992). The other proposed mechanism describes the adsorption of NO on activated carbons to be followed by dimerization to $(NO)_2$ and subsequent formation of two C-NO complexes (Teng & Suuberg 1993a). The reactive $(NO)_2$ dimer is also likely to oxidize the activated carbon surface with associated release of nitrogen (Bashkova & Bandosz 2009b). In presence of oxygen NO_2 is formed on the carbon surface and the net NO adsorption is vastly increased (Richter et al. 1990; Rubel et al. 1995a; Aarna & Suuberg 1997).

Since the formation of surface nitrogen species with carbon (C-N) is usually very small (Teng & Suuberg 1993b), the second of these two NO adsorption mechanisms is probably dominant. In iron oxide-infiltrated activated carbon Fe_2O_3 or Fe_3O_4 species can participate in the retention of NO by forming Fe_2O_3-NO complexes (Bashkova & Bandosz 2009a; 2011). This mechanism can also succeed an NO_2 reduction step at the surface.

In copper-exchanged zeolite ZSM-5 NO adsorbs dissociatively and forms adsorbed N_2O_3 (NO_2 + NO) at 300 K (Spoto et al. 1992; Adelman et al. 1994). NO_2 adsorbs by formation of nitrate species and release of NO (Despres et al. 2003):

$$3\,NO_2 + [CuO] \rightarrow NO + Cu(NO_3)_2 \qquad \textbf{(3)}$$

where [CuO] denotes half of the $[Cu\text{-}O\text{-}Cu]^{2+}$ species present in a highly exchanged zeolite.

2.3.2. Non-catalytic NO_x decomposition

The non-catalytic decomposition of nitrogen oxides is given by equations (Holleman & Wiberg 2007, p. 704ff):

$$2\,NO_2 \rightarrow 2\,NO + O_2\,,\ \ \Delta H_r^0 = +114.2\,\frac{kJ}{mol} \qquad \textbf{(4)}$$

$$NO \rightarrow N_2 + O_2,\ \ \Delta H_r^0 = -180.6\,\frac{kJ}{mol} \qquad \textbf{(5)}$$

$$N_2O \rightarrow N_2 + \frac{1}{2}O_2,\ \ \Delta H_r^0 = -82.1\,\frac{kJ}{mol} \qquad \textbf{(6)}$$

At room temperature all nitrogen oxides (NO_2, NO and N_2O) are metastable. At 298 K about 80% of NO_2 is dimerized in N_2O_4. At an elevated temperature of 413 K almost no dimerization

is observed any more. The decomposition of NO_2, NO and N_2O starts to be notable above 423 K, 1373 K and 873 K, respectively.

2.3.3. Catalytic NO_x decomposition

Transition metals on carbon support

The NO_x reduction reaction can be catalyzed by several metals and metal oxides. Activated carbon catalysts infiltrated by transition or alkali metals (e.g. Cr, K, Co, Ni, Cu, Ca) exhibit good activity in the reduction of NO (Illán-Gómez et al. 1995; Illán-Gómez et al. 1996; Illán-Gómez et al. 1999). The presence of metals with unpaired electrons (paramagnetic or ferromagnetic like Fe, Co, Ni) seems to affect the NO-metal-interaction at low temperature, since NO has an unpaired electron itself. On copper reportedly no dissociative chemisorption occurs.

Mechanisms of NO_x conversion with carbon catalysts

The reactive sites in activated carbons are probably unsaturated carbon surface atoms or highly Lewis basic edge sites (Xia et al. 1999). Several mechanisms for the NO_x conversion reaction in non-infiltrated carbons are proposed (Richter et al. 1990; Teng et al. 1992; Shirahama et al. 2002; Jeguirim et al. 2004; Azambre et al. 2006; Zhang et al. 2008a; Gao et al. 2011) and the essentials of these mechanisms are summarized in the following. Details of the mechanisms are provided in appendix 9.1.

It is commonly accepted that CO and CO_2 can be released during the reduction of NO_x in activated carbon (Teng et al. 1992). NO_2 can chemisorb and form C-NO_3 (Shirahama et al. 2002) or C-(ONO_2) complexes on the carbon surface (Jeguirim et al. 2004). Additionally, the formation of C_2-(ONO_2) complexes is suggested (Gao et al. 2011) and upon carbon oxidation at room temperature NO_2 may form NO-O_2 surface complexes on the surface (Zhang et al. 2008a).

The release of N_2O is mainly neglected in these mechanisms, but it is observed during NO decomposition at low temperature (Illán-Gómez et al. 1996). Okuhara and Tanaka conclude from isotope labeling studies on potassium-infiltrated activated carbon a Langmuir-Hinshelwood mechanism for N_2O release from adsorbed NO species at temperatures below 423 K (Okuhara & Tanaka 1986).

The desorption of CO_2 after NO decomposition on char is typically observed at low temperature (about 373 K), whereas CO formation mostly starts at higher temperature (Teng & Suuberg 1993b). Since reaction products like CO or N_2O join the feed gas, their participation should be considered in the overall reaction mechanism (Chan et al. 1983; Furusawa et al. 1985; Stegenga et al. 1993) (see appendix 9.1).

The introduction of a metal catalyst into activated carbon leads to the chemisorption of NO at the catalyst surface and additional evolution of N_2O (Illán-Gómez et al. 1996). The metal species undergo redox reactions like Fe/FeO or Fe_xO_y/Fe_xO_{y+1}. At low temperature (well below 398 K) NO_2 adsorbs on Fe_2O_3 by formation of surface nitrites and nitrates, especially in presence of oxygen (Underwood et al. 1999; Bashkova & Bandosz 2011). A full coverage of the active centers of Fe_2O_3 by NO may even lead to gradual deactivation of the catalyst, if further reaction with carbon is hindered and the active sites are not available any more for further dissociative NO_x adsorption (Bashkova & Bandosz 2009a).

Transition metal exchanged zeolites

Cu-ZSM-5 has been intensively studied in direct NO decomposition (Iwamoto et al. 1986; Iwamoto 1990; Centi & Perathoner 1995). Prior to the catalytic decomposition reaction NO may be oxidized and stored (Yokoyama & Misono 1994).The maximum NO conversion activity is observed between 773 and 873 K, enhanced by a high copper-exchange level and a high Si/Al-ratio of the zeolite (Shelef 1995, p. 212). It has to be noted that for example in copper-exchanged mordenite not all copper sites are accessible for gaseous reactants (Centi & Perathoner 1995, p. 222).

Mechanisms for catalyst systems with zeolites

The direct catalytic decomposition of NO in copper-exchanged ZSM-5 follows a four-step-scheme (Giamello et al. 1992; Spoto et al. 1992; Centi & Perathoner 1995, p. 212):

1) The sample is activated, for example in inert gas flow a fraction of Cu^{2+} ions accommodated in the zeolite framework are reduced to Cu^{+},
2) NO adsorbs on Cu^{+} forming a dinitrosyl complex ($Cu^{+}(NO)_2$) which is further decomposed to N_2 or N_2O, depending on the temperature, while oxygen adatoms remain at the copper ions,
3) NO reacts with oxygen adatoms and forms adsorbed NO_2^{-} followed by conversion with further NO into NO-Cu^{+}-NO_2^{-} nitrato complexes,
4) As the nitrate species are relative inactive, their rate of decomposition limits the overall catalytic activity.

Usually both, Brønsted acid sites and different copper species can be present in highly exchanged Cu-ZSM-5 catalysts and contribute to the catalytic activity. There is a dynamic change of the species during the reaction as investigated in XANES and EXAFS experiments by Robota (Kharas et al. 1995). Therefore, the catalytic activity is likely to change during the catalysis process. The reduction of Cu^{2+} to Cu^{+} can be enhanced by addition of reductants like hydrocarbons to the feed gas and as a consequence the number of dinitrosyl species increases upon NO adsorption (Burch & Millington 1993).

Although it seems generally accepted that a high level of copper exchange in a zeolite enhances the catalytic activity, Centi and Perathoner point out contradicting NO decomposition results originating from different levels of copper species aggregation on the ZSM-5 external framework (Centi & Perathoner 1995, p. 200). While Cu^{+} is reactive in the conversion of NO into N_2, residual oxygen remains adsorbed at the surface as extra-lattice oxygen (ELO) and reacts faster with another NO molecule to form Cu-NO_2 than recombining with another ELO and desorbing as O_2 (Centi & Perathoner 1995, p. 232). Moreover, not only ELO, but also lattice oxygen may take part in this reaction (Centi & Perathoner 1995, p. 203; Chang & McCarty 1997).

An alternative reaction mechanism of NO decomposition in Cu-ZSM-5 is suggested by Shelef on Cu^{2+} ions (Shelef 1992):

1) Two neighboring Cu^{2+} ions are activated to Cu^{+} ions by losing O^{2-} during heating,
2) Adsorption of 2 NO molecules at the 2 Cu^{+} leads to formation of a $2Cu^{2+}$-NO^{-} intermediate complex,
3) The pair of adsorbed NO anions desorbs as N_2 and O_2, thus restoring the two neighboring Cu^{+} adsorption sites, which are stabilized in the zeolite framework, thus preventing their oxidation.

In NO decomposition experiments (0.39% NO, 0.11% Ar, He balance) at ambient conditions, N_2O and N_2 are detected in the gas phase during the first four minutes, but vanish from the gas phase after some time (Li & Armor 1991). The transient observation of N_2O is interpreted by the authors as disproportionation of adsorbed NO into N_2O and NO_2, accompanied by desorption of some N_2O. The residual adsorbed N_2O is further decomposed to N_2 and surface-adsorbed oxygen. The oxygen either reacts with NO to form NO_2 or oxidizes the catalyst. Hence the reaction stops when the active sites are blocked by NO_2 or oxygen.

2.4. Chemical vapor infiltration

2.4.1. Introduction to CVI

Chemical vapor deposition (CVD) is the “deposition of a solid on a heated surface from a chemical reaction in the vapor phase” (Pierson 1999, p. 26). As a specific kind of CVD, chemical vapor infiltration (CVI) describes deposition processes inside (porous) substrates (Hüttinger 2003, p. 75). Typically the precursor diffusion kinetics inside the porous substrate require adjusted process parameters and lower deposition rates compared to similar CVD processes (Pierson 1999, p. 129ff). During CVD the mass contribution of the thin coating to the substrate is usually very small (about 1 wt.-%), whereas in CVI processes the deposited mass is often much larger (Golecki 2003).

The basic steps in a CVI process comprise (Golecki 2003):

1) Transport of the precursor vapor from the center of the gas stream to the boundary layer,
2) Diffusion of the precursor across the boundary layer onto the surface of the substrate,
3) Diffusion of the precursor into the pores of the substrate,
4) Decomposition of the precursor inside the pores and formation of deposited species or coating.

Due to pore diffusion (3), deposition on the outer surface of the substrate can be controlled by the surface reaction, whereas the simultaneous deposition inside the pores is often mass transfer controlled, thus leading to non-uniform deposition rates on and inside the substrate. Often, metal organic precursors (e.g. carbonyls, alkyls or acetylacetonates) are applied for the infiltration (Pierson 1999, p. 147ff).

CVI processes are broadly applied for example in densification of carbon fibers or ceramic matrix composites (Delhaès 2003; Naslain et al. 2007). An isothermal-isobaric hot-wall reactor

is most widely applied. Its advantages include rather straightforward application and good control of process parameters, whereas the process can suffer from long deposition time and low precursor efficiency due to parasitic reactions on the hot reactor walls (Delhaès 2003).

A special challenge is the infiltration of zeolites with very narrow defined pore channels, due to the steric hindrance which may hamper the introduction of larger foreign molecules (Sircar & Myers 2003). The introduction of ions with a high formal oxidation state can facilitate the infiltration and encourage the accommodation of the ions at the charged sites inside of the pore structure.

2.4.2. Kinetics of CVI

The deposition rate r_{dep} during CVD processes can be adapted to the deposition in pores in CVI processes and can be calculated as (Ohring 1992, p. 172):

$$r_{dep} = \frac{C_g}{N_o} \cdot \frac{k_S h_g}{k_S + h_g} \tag{7}$$

where C_g is the concentration of the chemical reactant in the gas phase, k_S is the rate constant for heterogeneous decomposition of the gaseous reactants as a film on the substrate, h_g is the gas phase mass transfer coefficient of the reactants to the substrate, both rate constants share the same unit m/s. N_o is the number of atoms incorporated into the film per unit volume. If $k_S \ll h_g$, the process is surface-reaction controlled, shown in Fig. 3 as the right part of the curve (Golecki 2003). If $k_S \gg h_g$, the process is controlled by the supply of precursor in the gas phase. If the temperature is even further increased, homogeneous nucleation will compete with heterogeneous film deposition. In this case, the deposition rate decreases as displayed in the left part of the plot in Fig. 3.

The diffusion kinetics during CVI of microporous matrix materials are usually in the transition to the Knudsen regime. For such diffusion processes molecular flow of the gas species can be assumed, and hence collisions with the walls play the main role. The mean free path length λ of molecules is given by:

$$\lambda = \frac{k_B T}{\sqrt{2}\pi {d_m}^2 p} \tag{8}$$

where k_B is the Boltzmann constant, T is the temperature, d_m is the diameter of the molecule and p is the working pressure.

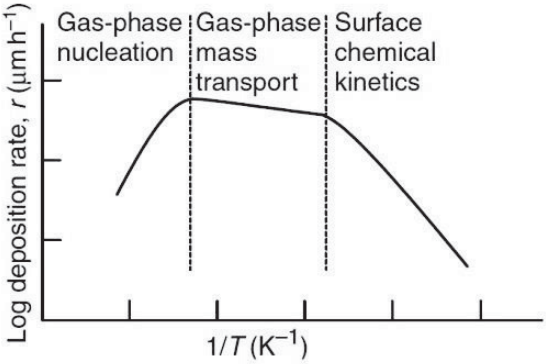

Fig. 3. Three temperature regimes in chemical vapor deposition, adapted from (Golecki 2003)

2.4.3. Mechanisms of process control

Activated carbons typically have a large volume fraction of slit-like micropores (Kaneko 1987). The deposition rate along a pore is not uniform, but is highly sensitive to the process parameters and the nature of the precursor. A decreasing deposition rate along a pore of uniform width will close the pore mouth early (Dupel et al. 1994). More homogeneous deposition from a continuous precursor flow can possibly be achieved, if the precursor residence time is increased or if the reaction complexity increases (Sohda & Diefendorf 1985; Hu & Hüttinger 2001; Zhang & Hüttinger 2001). In these cases homogeneous gas phase reactions become more likely than heterogeneous reactions inside the pore system.

The ratio of pore surface area to pore volume has another strong impact on the deposition profile along the pores. Surface reactions are favored with increased ratio due to a larger concentration of active sites per unit volume (Hüttinger 2003).

Mathematical models are developed for CVI processes (Sotirchos 1991), but also the Thiele modulus is considered to be a good measure for the process efficiency, since the reactions during CVI are sufficiently comparable to those occurring during heterogeneous catalysis (Delhaès 2003).

2.5. Catalyst support materials

The conversion rate in heterogeneous catalysis is often related to the accessible catalyst surface area and to the supply of new reactants. Hence, a good catalyst system preferentially provides a high surface area which is easily accessible. Small particles, especially particles in nanoscale, are more likely to bear a high density of potentially active defect sites on their surface. Many catalytic processes are particle size sensitive as described before (Bell 2003). However, the agglomeration of catalyst particles and sintering of adjacent nanoparticles can significantly limit the conservation and accessibility of the actual catalyst surface for new reactants. A particle support material is preferentially applied for spatial separation of catalyst particles to avoid particle growth or agglomeration (Ponec & Bond 1995, p. 320ff).

Silica and alumina are the most common support materials since they combine thermal stability and relative chemical inertness at the working temperature for many prominent catalytic processes. Their powders can provide surfaces of up to 300 m^2/g (Chorkendorff & Niemantsverdriet 2007, p. 192). For applications which require even greater mass specific surface areas or isolated ions as active centers, framework structures like zeolites or amorphous activated carbons can be a good choice. Dispersed nanoparticles or even single ions immobilized in their microporous channels provide a large catalytically active surface.

2.5.1. Activated carbons

Activated carbons are an intensively studied and broadly applied support in heterogeneous catalysis (Rodríguez-Reinoso 1998; Marsh & Rodríguez-Reinoso 2006). For many catalytic processes in liquid media as well as in gas phase they provide an ideal catalyst support and intrinsic active centers (Reimerink 1999; Calvino-Casilda et al. 2010). The material usually consists to a large extent of mainly slit-like micropores and few macro- and mesopores with a large specific surface area from 700 to more than 2000 m^2/g (Kaneko 1987; Marsh & Rodríguez-Reinoso 2006; Chorkendorff & Niemantsverdriet 2007, p. 195).

The preparation of activated carbon can be performed by pyrolysis of natural or synthetic, typically long-chained hydrocarbons in an oxygen-free atmosphere (e.g. water vapor or carbon dioxide) while avoiding significant gasification of too much carbon (Chorkendorff & Niemantsverdriet 2007, p. 195). Subsequent thermal and pressure treatment in oxygen, water vapor, carbon dioxide or acids "activates" the carbon surface leaving various functional surface groups, high energy sites, e.g. on edge sites, and unsaturated carbon atoms, so called "dangling bonds".

Natural source materials for the preparation of activated carbons include coconut shell, wood or charcoal. These sources are usually well available and inexpensive, but the received product typically contains catalytically active impurities like sulfur, iron or potassium, depending on the impurity load of the parent material. Activated carbons made from processed sources like petroleum or resin pitch can be better designed in chemical composition, porosity and shape. The oxygen content can reach up to 10 wt.-% (Schüth 2010).

Besides the effect of incorporated impurities, the surface chemistry of functional groups and high energy sites can generate a catalytic effect (Xia et al. 1999). Moreover, the structure of narrow micropores often plays an important role as overlapping Lennard-Jones-potentials from opposite pore walls of narrow micropores can influence the adsorption of reactants and the catalytic activity.

Depending on the reaction and temperature, functional surface groups and unsaturated carbon atoms can change its chemistry and pores can collapse or can be blocked during the catalytic process. Especially in oxidizing environment at elevated temperatures the carbon support may be less chemically inert and suffer from carbon gasification. However, in several cases the surface change is even desired and a slight consumption of the material is accepted, since the replacement is inexpensive. In fact, no loss of activated carbon is measured after heating to 623 K in NO/SO_2 atmosphere (Rubel & Stencel 1997) and less than 2% of activated carbon are gasified in 0.73% NO/He at 1173 K for 30 min (Chan et al. 1983).

2.5.2. Applied activated carbon support

A commercially available activated carbon (R1407, Rütgers/CarboTech, Fig. 4) is applied as substrate material for the carbon-based catalysts. The particles have a spherical shape with a diameter of about 0.5 mm (Fig. 5). For this particle size mass transfer limitations during the catalysis process are unlikely (Stegenga et al. 1993; Aarna & Suuberg 1997). Fig. 6 shows the cross section of the activated carbon with pore entries of macropores. The smaller micropores could not be resolved by SEM. Elemental analysis by EDX revealed less than 0.01% impurities of sulfur.

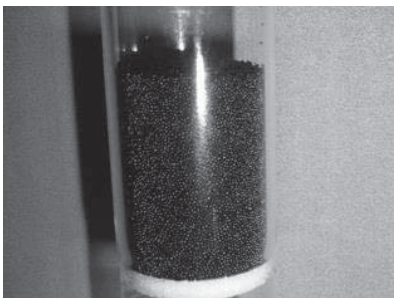

Fig. 4. Photograph of ball-shaped activated carbon Rütgers/Carbotech R1407 in the CVI-reactor glass tube

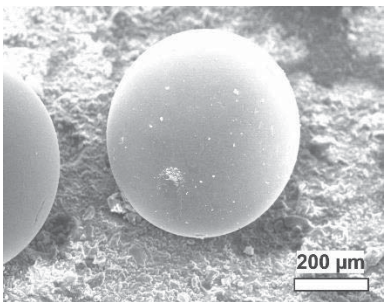

Fig. 5. SEM micrograph of ball-shaped activated carbon Rütgers/Carbotech R1407

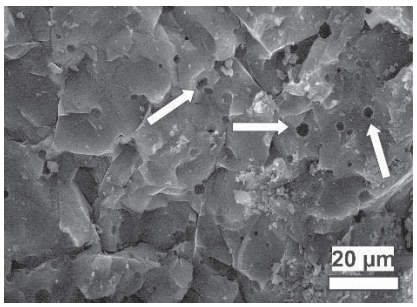

Fig. 6. SEM micrograph of the cross section of activated carbon Rütgers/Carbotech R1407, white arrows point at pore entries of macropores

The specific surface area according to the Brunauer-Emmett-Teller (BET)-method of the activated carbon is 1604 m²/g and the micropore volume derived from the α_s-method is 0.19 cm³/g. The nitrogen adsorption isotherm (Fig. 7) shows the form of a type I isotherm. The type I isotherm is characterized by a large amount of adsorbing nitrogen at very low relative pressures, which is typically caused by the capillary condensation of nitrogen in micropores (Sing et al. 1985). Details on the measurement method will be provided in section 3.2.5.

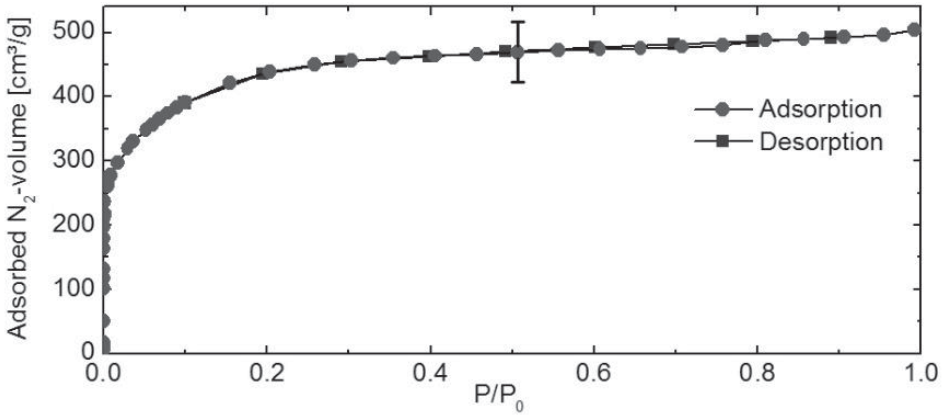

Fig. 7. Nitrogen sorption isotherm at 77 K for non-infiltrated Rütgers/Carbotech R1407 activated carbon

2.5.3. Zeolites

Zeolites are a group of crystalline microporous alumosilicates. They are usually synthesized by hydrothermal treatment of a sol-gel and are widely applied in adsorption, catalysis and detergents (Flanigen et al. 2001; Maesen et al. 2001; Payra & Dutta 2003; Cejka et al. 2012). The zeolite crystal structure consists of SiO_4 and AlO_4 tetrahedra sharing neighboring O-atoms and forming characteristic micropore channels (McCusker et al. 2001). Although each zeolite has a unique framework structure, differences can occur in the ratio of silicon to aluminum atoms in a zeolite without major effect on the pore channels.

At some framework sites coordinated Si^{4+} is replaced by Al^{3+}, creating locally a negative charge. In order to prevent framework destabilization, these sites are usually charge neutralized during preparation by Na^+ or H^+. In the latter case, the zeolite can serve as a Brønsted acid and is often called a “solid acid”. In thermal or wet chemical treatment the accommodated cations can be exchanged for other cations like Ca^+, Cu^+, Fe^+, Mn^+ or Mg^+. Even cations with a higher

oxidation state can be incorporated without destabilization of the framework, for example by bridging the respective number of neighboring charged sites.

The specific pore channel geometry, charge distribution and channel size of a certain zeolite can be selective for the adsorption of larger and/or charged molecules leading to the well-established application as a "molecular sieve". Hence the industrial use for ion exchange, separation and catalytic applications.

The thermal and chemical stability and the non-hierarchical pore system make many zeolites an interesting catalyst support. Incorporated catalytically active cations can be well dispersed in the framework, stabilized and prevented from agglomeration while being still accessible for reactants. The accommodation of a large number of metal cations inside the framework increases the number of potentially active sites for catalytic applications. Even the introduction of an excess amount of cations compared to the number of accessible basic sites is often intended in order to increase the number of truly accommodated cations. Such zeolites are called highly exchanged or "over-exchanged" and they are generally considered to exhibit superior catalytic properties in the decomposition of nitrogen oxides (Centi & Perathoner 1995; Yahiro & Iwamoto 2001; Brandenberger et al. 2011). The acidic nature of the protonated sites in the zeolite can promote the catalytic activity.

The introduction of metal ions into zeolite frameworks via chemical vapor infiltration has been of great interest, although the most often applied liquid ion exchange-preparation of zeolites is relatively straightforward and the results are usually well reproducible (Konduru & Chuang 1999; Teraoka et al. 2000; Bulushev et al. 2005; Pieterse et al. 2007; Brandenberger et al. 2011). However, for an excessive infiltration of the zeolite the liquid ion exchange procedure needs to be repeated for several times (Shpiro et al. 1994). As an alternative, allowing even larger metal loads, the sample can be infiltrated via gas phase (Brandenberger et al. 2008). Especially for oxide-free precursors with a high vapor pressure like $FeCl_3$ the CVI methods seems to be most commonly used, since the catalytic activity is expected to work best for non-oxidic iron (Pieterse et al. 2004).

2.5.4. Applied zeolite support

The zeolites mordenite, ZSM-5 and Zeolite Beta exhibit well-accessible pore channels and a high chemical and thermal stability. They are reported to be active in the decomposition of nitrogen oxides with ammonia (Brandenberger et al. 2008) or hydrocarbons (Chen et al. 2000) and in the direct decomposition of nitrous oxide (Pieterse et al. 2004). Hence they are chosen as matrix materials. In this work they are denoted with the three-letter-code MOR, MFI and BEA (mordenite, ZSM-5 with the mordenite framework inverted-type structure and Zeolite Beta, respectively), according to IUPAC classification.

MFI (= Mordenite Framework Inverted), commonly known as ZSM-5 (ZSM = Zeolite Socony Mobil), is one of the most intensively studied zeolites. Bearing a relatively high Si/Al-ratio, dealumination and hence destabilization of the framework in harsh conditions is less likely (Pieterse et al. 2007). The herein investigated substrates (NH_4^+-MFI-27) are delivered by Südchemie exchanged with ammonium cations. Some particles of the as-delivered powder have a spherical shape and are about 50 nm in diameter (Fig. 9 A). Another fraction of the same material exhibits agglomerations in larger macrostructures (Fig. 9 B) with an irregular shape (in greater enlargement Fig. 9 C).

The gas phase infiltrated samples are prepared from zeolite substrates with a larger fraction of the agglomerated structure (Fig. 9 B, C). The liquid ion exchanged reference catalysts are synthesized from as-delivered material with predominantly spherical particles (Fig. 9 A). The corresponding Si/Al-ratios vary between 10 and 31 among the as-synthesized substrates and are stated according to our own EDX-quantifications further below in Table 4 and Table 11.

A scheme of the 3-dimensional channel system of MFI is shown in Fig. 8. Both of two different 10-ring channels, one straight and the other sinusoidal, have an inner diameter of ca. 5.5 Å (Baerlocher et al. 2007). Due to intersections of the sinusoidal channels with both neighboring planes of straight channels, foreign molecules can diffuse in all three dimensions of the crystal. The pore channel volume is 0.15 cm^3/g (Chorkendorff & Niemantsverdriet 2007, p. 202). The micropore volume of the MFI is not affected by the described differences in the macrostructure of the particles.

Mordenite (MOR) is a common zeolite which can be found also in nature. The herein applied material (NH_4^+-MOR-14) is delivered by Südchemie exchanged with ammonium cations. The structure, shown in Fig. 10, forms 1-dimensional 12-ring channels with an inner diameter of ca. 6.5 x 7.0 Å and smaller 8-ring channels of 5.7 x 2.6 Å (Baerlocher et al. 2007). In practice, only the large channels participate in foreign molecule transport (Lobo 2003). The pore channel volume is about 0.20 cm^3/g (Chorkendorff & Niemantsverdriet 2007, p. 202).

Zeolite Beta (BEA) is always a disordered intergrowth of two different polymorphs A and B which differ in the stacking sequence of crystal layers (Newsam et al. 1988). The applied substrate (H^+-BEA-35) is delivered by Südchemie in the protonated form.

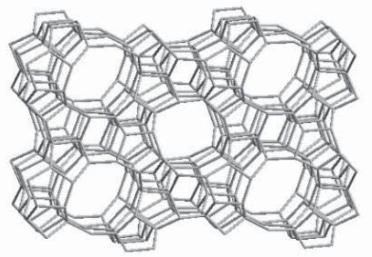

Fig. 8. MFI structure, adapted from (Baerlocher & McCusker 2012)

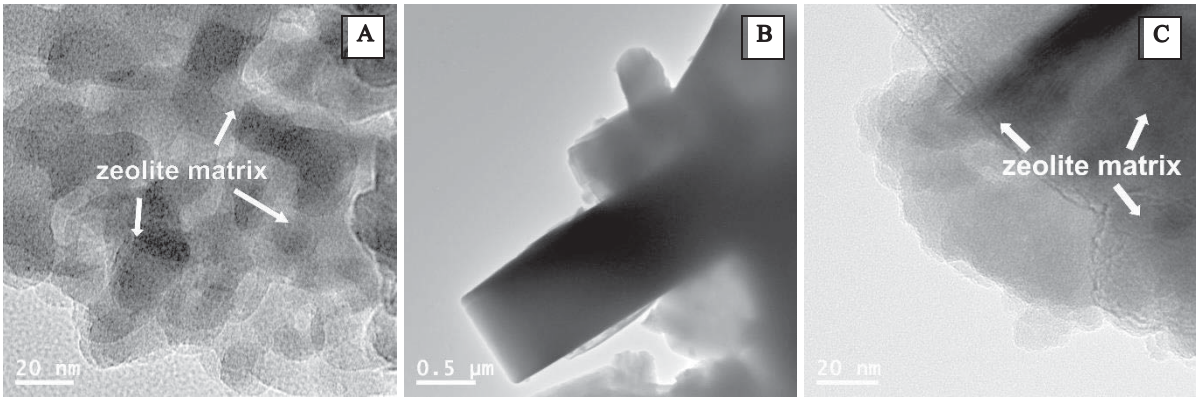

Fig. 9. TEM micrographs showing non-infiltrated NH_4^+-MFI-27 with spherical zeolite particles (A) and an agglomerated macrostructure (B) with irregular forms (C)

The 3-dimensional structure (Fig. 11) contains two sorts of 12-ring channels: straight channels of ca. 7.1 x 7.6 Å in two dimensions and, perpendicular to the straight channels, sinusoidal channels of ca. 5.6 Å inner diameter (Baerlocher et al. 2007). The pore channel volume of about

0.25 cm³/g is not notably affected by the stacking faults (Chorkendorff & Niemantsverdriet 2007, p. 202). All investigated zeolites are microporous as indicated by type I isotherms in low temperature nitrogen adsorption shown in Fig. 12.

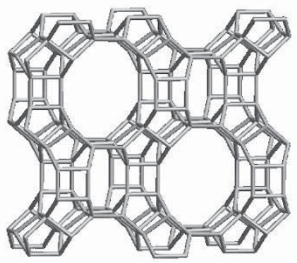

Fig. 10. Mordenite structure, adapted from (Baerlocher & McCusker 2012)

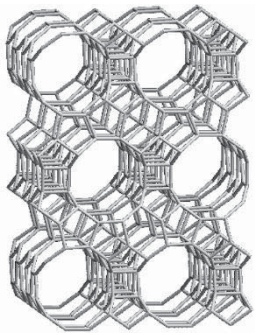

Fig. 11. Zeolite Beta structure (polymorph A), adapted from (Baerlocher & McCusker 2012)

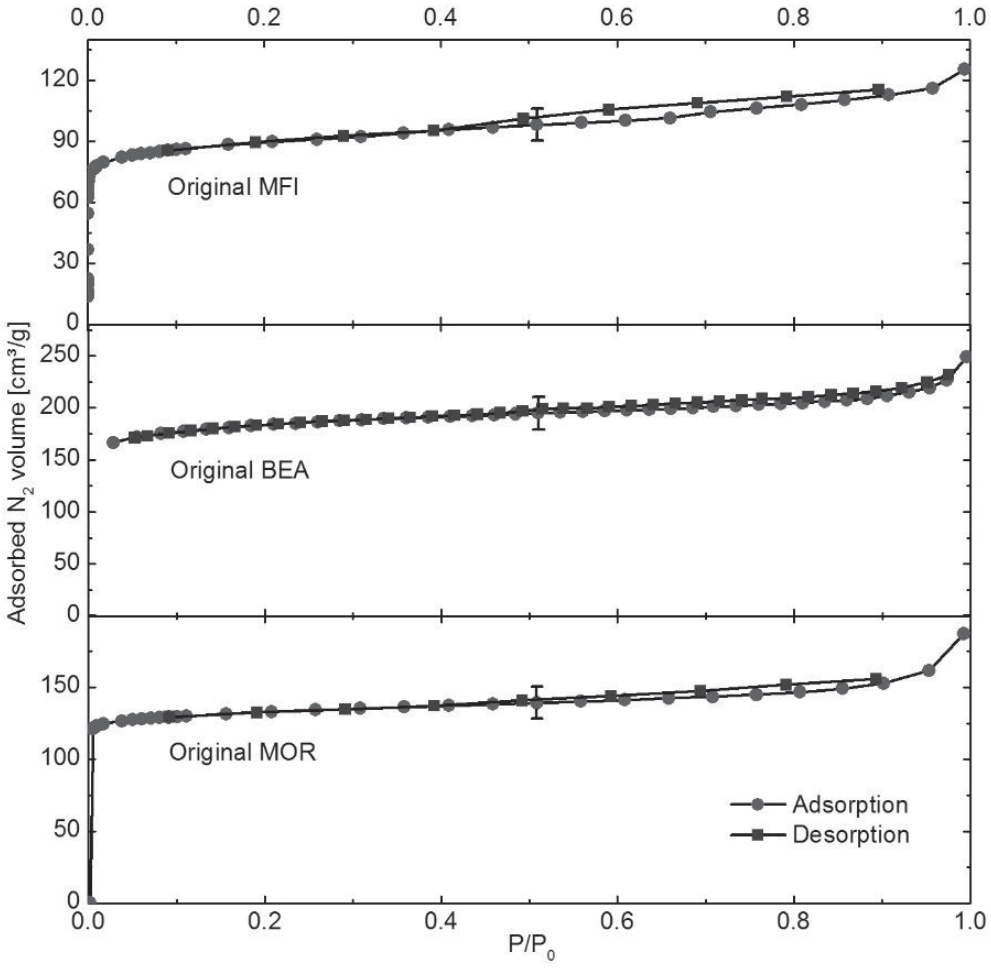

Fig. 12. Nitrogen sorption isotherms at 77 K of non-infiltrated zeolite samples

Due to the narrow and defined pore channels of zeolites, they are often referred to as "molecular sieves" for foreign gases (Sircar & Myers 2003). In the activated carbons the pore channel widths are less defined. Hence, the molecules of the applied precursor gases Ferrocene, $Fe(acac)_3$, $Cu(acac)_2$ and $Mn(acac)_2$ (see section 3.1.2) may diffuse comfortably into most of the micropores of the applied activated carbon samples, as derived from the comparison of their kinetic molecular diameter and the pore size distribution of activated carbon (see Fig. 13).

From this steric perspective, only the large pore channels of zeolites BEA and MOR may take part in the adsorption of Ferrocene molecules. For the applied MFI zeolite the precursor diffusion may be accompanied by some steric hindrance due to the narrow pore width. The large molecule diameter of the non-decomposed acetylacetonates may also hamper their diffusion into the zeolite pore channels. Only zeolites BEA and MOR seem to be good candidates for the introduction of Ferrocene. The targeted reactant gas molecules (NO, NO_2) and the main possible products (N_2O, CO, CO_2, O_2, N_2) are small enough to easily diffuse through the pore channel system of the applied activated carbon and zeolites.

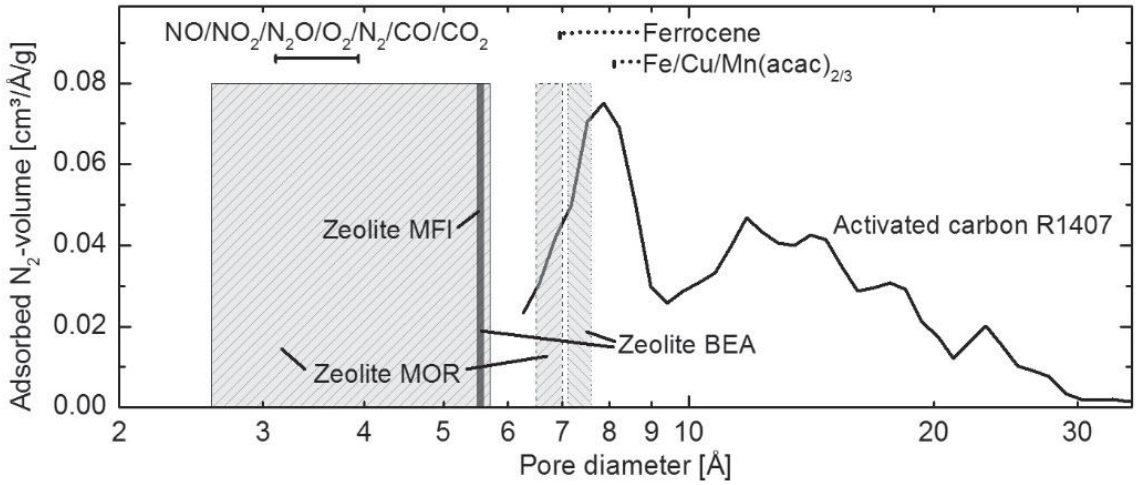

Fig. 13. Pore size distribution of the applied non-infiltrated catalyst support materials (activated carbon R1407, schematic pore width range for zeolites MFI, BEA and MOR) and schematic depiction of the kinetic diameter of applied precursor molecules (Ferrocene, $Fe(acac)_3$, $Mn(acac)_2$, $Cu(acac)_2$) and of gaseous reactants and products (NO, NO_2, N_2O, O_2, N_2, CO, CO_2); kinetic diameters of molecules are taken from (Yamamoto 1984; Maeda et al. 1987; Rubel & Stencel 1996; Sircar & Myers 2003)

The X-ray diffractograms of the non-infiltrated zeolites are shown in Fig. 14. At ambient conditions water molecules from air humidity can additionally adsorb close to accessible framework-oxygen atoms or around extra-framework ions in the pore channels. Upon dehydration the charge distribution in the framework alternates and the extra-framework ions are likely to shift their position into the new electrostatic minima (Lobo 2003, p. 21ff). Furthermore, stacking faults apart from the ideal crystal structure shown above are common in most industrially produced zeolites. Hence, the respective X-ray reflections are likely to shift, broaden or alternate the intensity depending on the surrounding conditions.

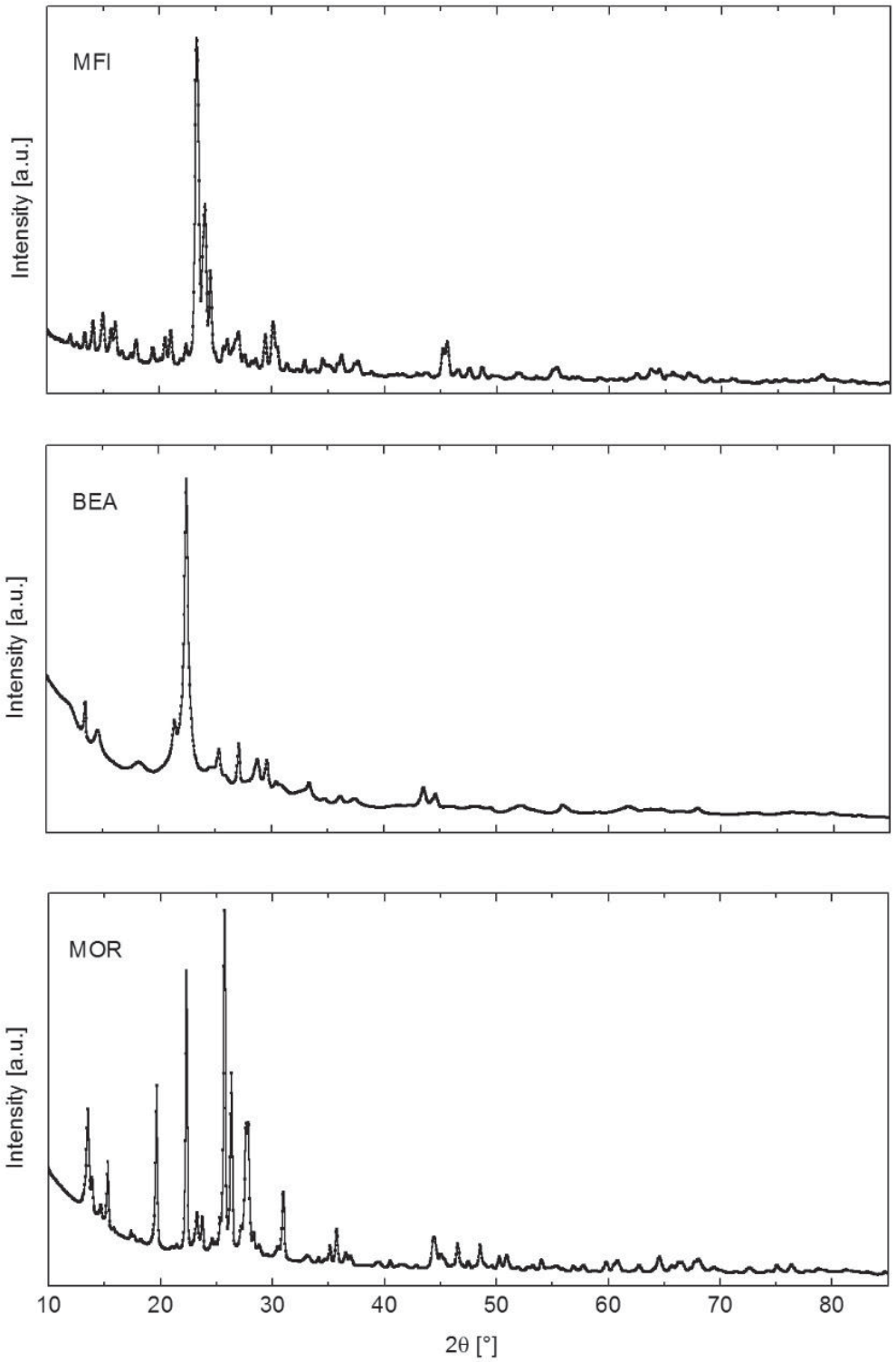

Fig. 14. X-ray diffractograms of non-infiltrated MFI, BEA and MOR zeolite samples

3. Experimental methods

In the present work the described commercial activated carbons and zeolites are applied as support materials for the infiltration with iron, copper and manganese species. In this section an overview is provided on the set of applied experimental techniques.

3.1. Preparation of catalysts

For catalytic applications, a deep and homogenous infiltration of the substrate is usually desired in order to yield a large active surface of deposited material. The chosen chemical vapor infiltration process comprises two main steps: (1) homogeneous infiltration of the porous sample matrix and (2) subsequent precursor decomposition. As a common alternative, the sample infiltration is often performed in a continuous precursor flow (Sohda & Diefendorf 1985; Hu & Hüttinger 2001; Zhang & Hüttinger 2001). However, such a process is more difficult to control in complex pore systems like activated carbons or zeolites and it utilizes precious precursors less efficiently (Delhaès 2003).

3.1.1. Reactor setup

The infiltration of the substrates is performed in a setup schematically shown in Fig. 15 and previously applied in (Busch et al. 2011). Photographs of the setup are provided in appendix 9.8.

The substrate is placed in a vertical quartz glass tube (1.1 m long, 17 mm inner diameter) on a glass frit in the center of the tube (see Fig. 4). The glass tube is placed inside a tube furnace (Gero F70-500/13-3, 3 heating zones). At the lower end of the glass tube a cooling trap and the vacuum pump system are connected (turbo molecular pump Pfeiffer Vacuum HiPace80 and membrane pump Pfeiffer Vacuum MVP 015-4). The reactor pressure is monitored in a range of $1 \cdot 10^{-9}$ to 1100 mbar by a combination of two pressure transducers (Pfeiffer Vacuum PKR 251 and Pfeiffer Vacuum CMR 361). The actual reactor volume is about $300 \cdot 10^{-6}$ m³.

The precursor supply unit at the upper end of the glass tube consists of a lockable steel tube which is connected via a gate valve to the reactor glass tube (see Fig. 16). The precursor powder is kept in a small lockable glass container with a porous glass frit as bottom plate. Before precursor evaporation, the precursor container is placed into a precursor supply unit, standing upright on the gate valve. A slightly opened gate valve allows the simultaneous evacuation of the precursor supply unit and the reactor tube prior to sample preconditioning.

During the actual preconditioning process the precursor supply unit is kept closed in an evacuated state. Upon complete opening of the gate valve, the whole precursor glass falls down into the reactor glass tube right onto the preconditioned substrate. Gas lines for argon and air supply are connected to the tube fitting between precursor gate and reactor glass tube.

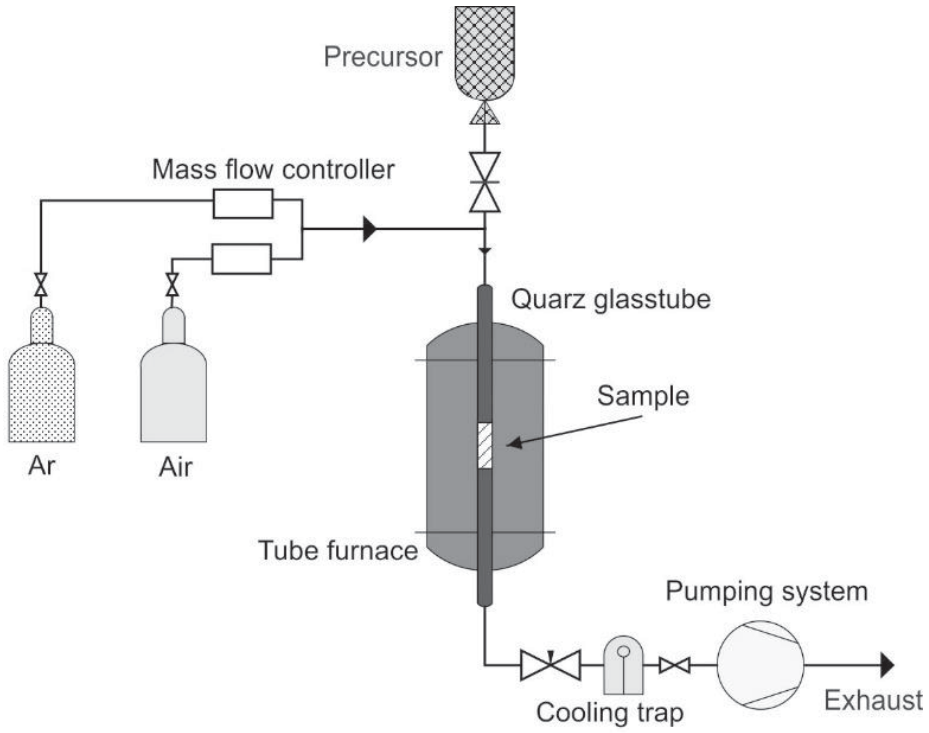

Fig. 15. Chemical vapor infiltration setup

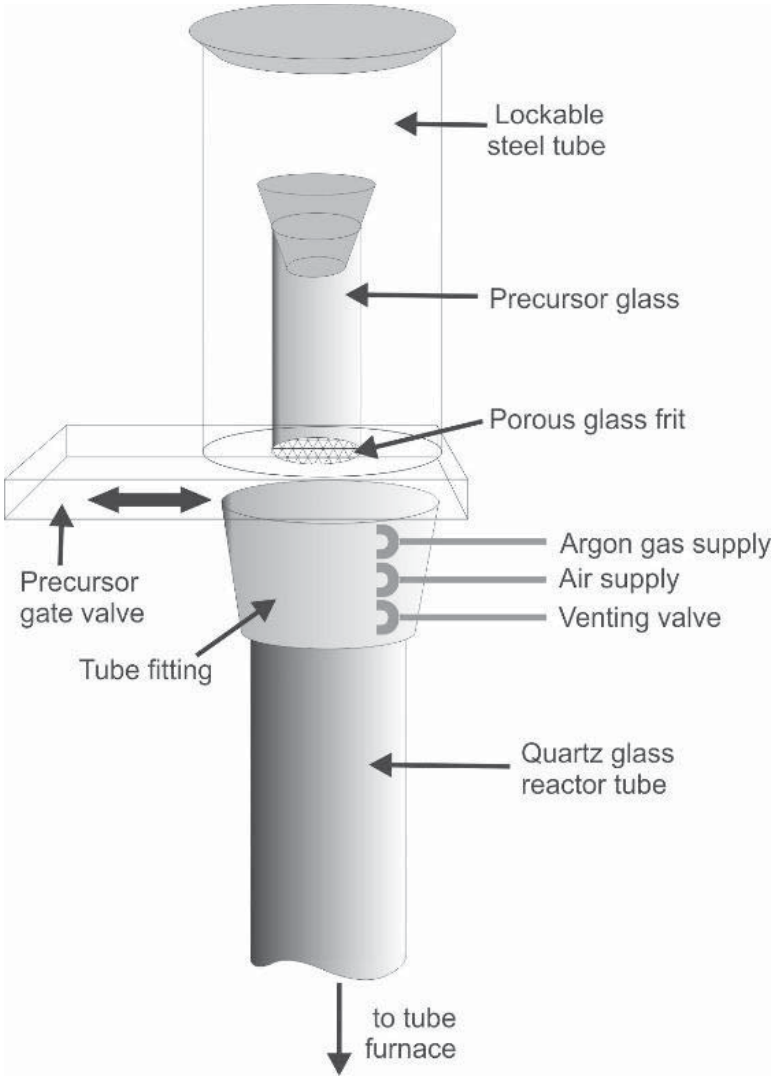

Fig. 16. Precursor supply unit of chemical vapor infiltration setup

3.1.2. Precursors

The metal organic precursors used for the infiltration of substrates are needed to fulfill five basic requirements:

1) Low vapor pressure at ambient conditions,
2) Facile evaporation in vacuum at a temperature low enough to prevent precursor decomposition,
3) Decomposition at a temperature low enough not to damage the substrate structure or chemistry,
4) Small molecular diameter of precursor molecules for unhampered diffusion into the micropores of the substrate,
5) Low polarity of the molecule in order to prevent unwanted sticking at charged sites.

Commonly, in chemical vapor infiltration applied precursors with a high vapor pressure ore often toxic and contain chlorine (e.g. $FeCl_3$) which needs to be removed after the infiltration (Chen & Sachtler 1998; Heinrich et al. 2002; Bitter et al. 2003; Hensen et al. 2004). Metal acetylacetonates and metallocenes seem feasible to resolve such issues and meet the above stated requirements.

In metal acetylacetonates the metal cation is surrounded by a number of acetylacetonate anions corresponding to the metal ion oxidation state (see Fig. 17). Metallocenes are sandwich complexes of a metal cation wrapped between two carbocyclic rings (see Fig. 18). In these complexes the metal ion charge is well shielded by the surrounding ligands which are relatively easy to remove by thermal treatment. As the metallocenes do not contain oxygen atoms, generation of metallic species is straightforward and their oxidation can be controlled by adjusting the exposure to oxygen.

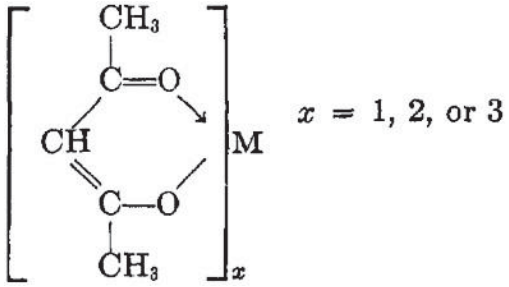

Fig. 17. Scheme of metal acetylacetonate, adapted from (Hoene et al. 1958); x = oxidation state of metal M

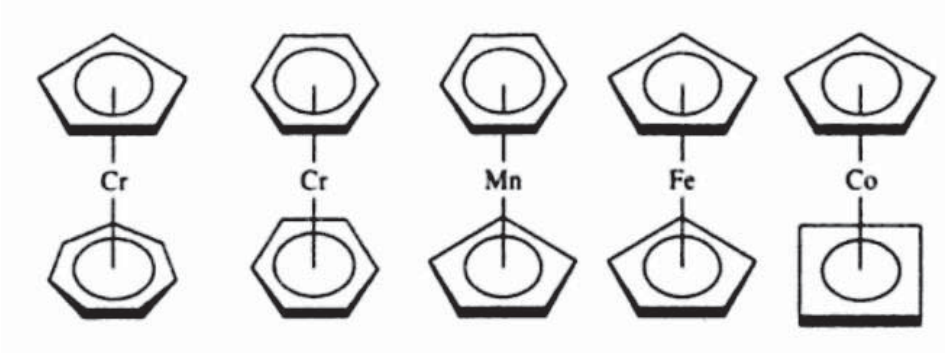

Fig. 18. Examples of metallocenes, adapted from (Huheey et al. 2003, p. 787)

For iron deposition Iron-II-acetylacetonate (99.95%, Sigma-Aldrich Inc., CAS: 14024-17-0, denoted as "$Fe(acac)_2$"), Iron-III-acetylacetonate (99%, ABCR GmbH&Co.KG, CAS: 14024-18-1, denoted as "$Fe(acac)_3$") and Ferrocene (98%, Sigma-Aldrich Inc., CAS: 102-54-5) – one of the most stable metallocenes – are used. Copper is deposited by using Copper-II-acetylacetonate (99.99%, Sigma-Aldrich Inc., CAS: 13395-16-9, denoted as "$Cu(acac)_2$") and for manganese deposition Manganese-III-acetylacetonate (techn., Sigma-Aldrich Inc., CAS: 14284-89-0, denoted as "$Mn(acac)_3$") is applied.

The differential-thermal and thermogravimetric analysis during heating of precursor samples from room temperature to 830 K (Fig. 19) reveals the evaporation and decomposition temperatures which are used during the infiltration and metal oxide formation (Table 2). Some evaporation temperatures are chosen lower than derived from Fig. 19, since the acetylacetonates tend to decompose during evaporation. The application of $Fe(acac)_2$ was waived after preliminary experiments due to its significant decomposition during the evaporation.

Decomposition of the metal organic precursors requires activation for dissociation of the ligands (Premkumar et al. 2007) which decompose for example into acetone and carbon dioxide (Hoene et al. 1958). The enthalpies of combustion ΔH_c of Ferrocene (Cotton & Wilkinson 1952), $Fe(acac)_3$ (Farrar & Jones 1964), $Mn(acac)_3$ (Wood & Jones 1964) and $Cu(acac)_2$ (own estimation with ΔH_f^0 of $Cu(acac)_2$ from (Irving & da Silva 1981)) are determined as:

$$Ferrocene\colon\ \Delta H_c = -5878\ kJ/mol$$
$$Fe(acac)_3\colon\ \Delta H_c = -7867\ kJ/mol$$
$$Mn(acac)_3\colon\ \Delta H_c = -8005\ kJ/mol$$
$$Cu(acac)_2\colon\ \Delta H_c = -5031\ kJ/mol$$

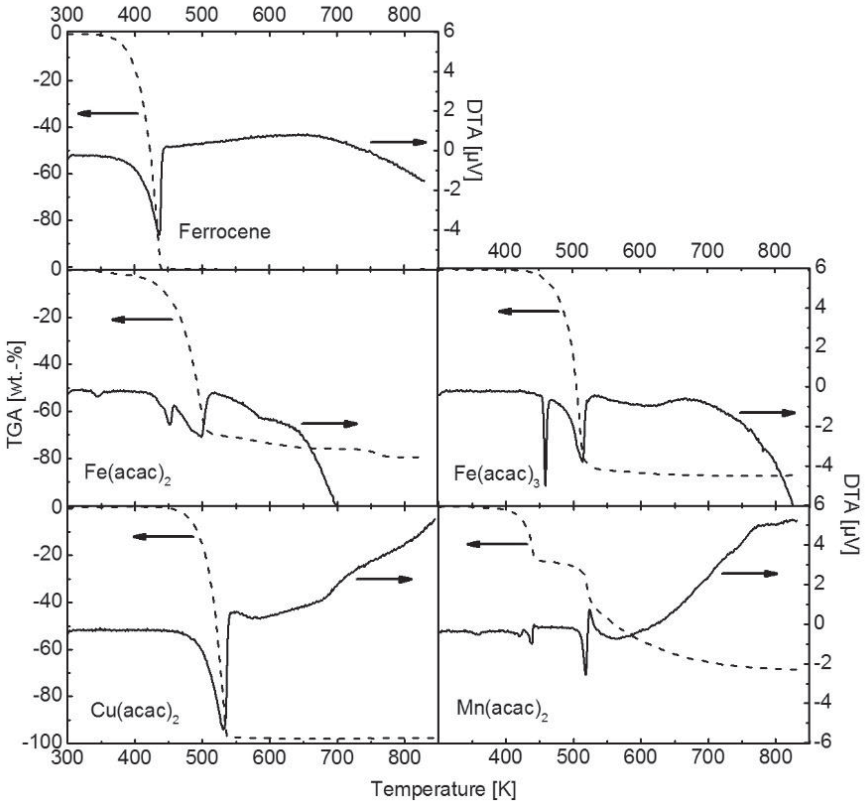

Fig. 19. TGA (dashed line) and DTA (solid line) investigations of applied precursors in helium gas flow

Table 2. Evaporation and decomposition temperatures of applied precursors

Precursor	T_{evap1} (K)	T_{evap2} (K)	$T_{decomp1}$ (K)	$T_{decomp2}$ (K)	Notes
Ferrocene	420	403	n.a.	AC: 653 Zeolites: 773	In vacuum precursor completely evaporated at 403 K.
$Fe(acac)_3$	450	443	455	AC: 653 Zeolites: 673	Chosen T_{evap2} was 443 K due to possible precursor decomposition at T_{evap1}.
$Cu(acac)_2$	510	433	n.a.	AC: 653 Zeolites: 773	In vacuum precursor completely evaporated at 433 K.
$Mn(acac)_2$	420	413	525	AC: 653 Zeolites: 773	Chosen T_{evap2} was 413 K due to possible precursor decomposition at T_{evap1}.

T_{evap1} = evaporation temperature derived from Fig. 19, T_{evap2} = evaporation temperature applied in experiments, $T_{decomp1}$ = decomposition temperature derived from Fig. 19, $T_{decomp2}$ = decomposition temperature applied in experiments

3.1.3. Infiltration procedure

The infiltration procedure for activated carbon-based catalysts comprises the following steps:

1) Mounting of the activated carbon matrix in the quartz glass reactor tube and precursor in the precursor supply unit;
2) Preconditioning of the activated carbon matrix in vacuum (< 0.1 mbar, usually 10^{-4} mbar) at 573 K for 240 min, heating rate: 3K/min;
3) Cooling of the sample to T_{evap2} (see Table 2) in the evacuated state;
4) Addition of the precursor close to the sample;
5) Evaporation of the precursor at T_{evap2} and infiltration of the sample for 180 min;
6) Cooling of the sample to 303 K;
7) Isothermal pressure increase to 1000 mbar with air;
8) Isobaric heating of the sample to $T_{decomp2}$ (see Table 2) in air, heating rate: 10 K/min;
9) Precursor decomposition at $T_{decomp2}$ for 30 min;
10) Evacuation of the setup and cooling to 303 K;
11) Venting with air and release of the sample.

Precursor decomposition in the carbon matrix (step 9) is an exothermal reaction due to combustion processes with carbon in air. Hence, the temperature of the sample increases to ca. 723 K as investigated in preliminary in-situ-measurements. A schematic depiction of the time-pressure- and time-temperature-profile during the infiltration process is provided in Fig. 20.

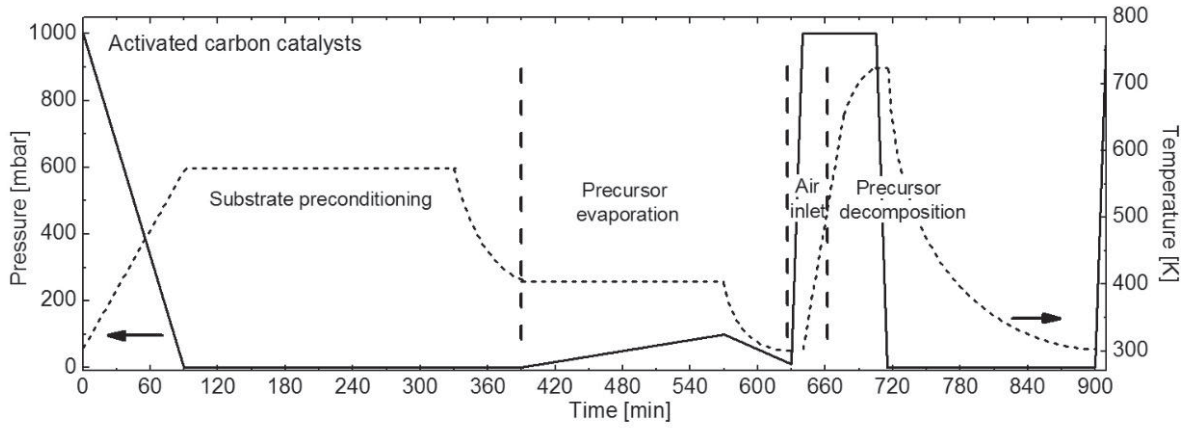

Fig. 20. Schematic depiction of pressure (solid line) and temperature (dashed line) during the preparation process of activated carbon-based catalysts infiltrated by Ferrocene

Zeolite-based catalysts require a more careful evacuation and heating procedure in order to prevent framework damage and delocalization of substrate material in the reactor due to the kinetics of water desorption. The zeolite sample preconditioning is similar to the procedure applied by the group of Grünert (Heinrich et al. 2002). The scheme of pressure and temperature during the infiltration process is provided in Fig. 21:

1) Mounting of the zeolite matrix in the quartz glass reactor tube and precursor in the precursor supply unit;
2) Preconditioning of the zeolite matrix in vacuum according to the following scheme:
   Evacuation at room temperature to < 0.1 mbar (usually 10^{-4} mbar)
   T_1 = 353 K for 60 min, heating rate: 1 K/min
   T_2 = 393 K for 30 min, heating rate: 1 K/min
   T_3 = 523 K for 60 min, heating rate: 3 K/min
   T_4 = 973 K for 120 min, heating rate: 3 K/min
3) Cooling of the sample to T_{evap2} (see Table 2) in the evacuated state;
4) Addition of the precursor close to the sample;
5) Evaporation of the precursor at T_{evap2} and deposition on the sample for 180 min;
6) Cooling of the sample to 303 K;
7) Isothermal pressure increase to 1000 mbar with air, pressure increase rate: 60 mbar/min;
8) Isobaric heating of the sample to $T_{decomp2}$ (see Table 2) in air, heating rate: 4 K/min;
9) Precursor decomposition at $T_{decomp2}$ for 60 min;
10) Evacuation of the setup and cooling to 303 K, pressure decrease rate: 60 mbar/min;
11) Venting with air and release of the sample.

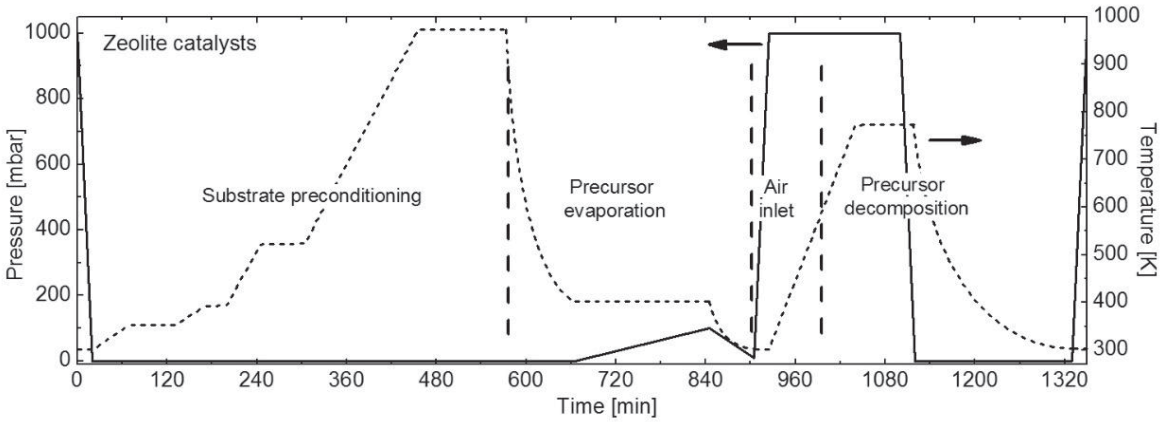

Fig. 21. Schematic depiction of pressure (solid line) and temperature (dashed line) during the preparation process of zeolite-based catalysts infiltrated by Ferrocene

3.1.4. Reference catalysts

Reference catalysts are applied in this work in order to compare the synthesized catalysts to known and well characterized catalyst systems. Hence, certain catalytic behavior of the new samples can be more easily attributed to specific properties of the material. The chemical vapor infiltrated activated carbons catalysts are compared to activated carbons which are prepared by the well-established incipient wetness method and to commercial carbon-containing microporous silica sorbent. The chemical vapor infiltrated zeolite catalysts are compared to zeolites which are prepared by the commonly applied liquid ion exchange technique. Additionally, the catalytic activity is compared to a common platinum catalyst and to magnetite. Details on the applied reference catalysts are presented in the following.

IWM-infiltrated activated carbon samples

Reference catalysts for activated carbons samples are prepared and provided by the Max-Planck-Institute for Carbon Research in Mülheim/Ruhr. A commercial ball-shaped activated carbon (Rütgers/CarboTech R1407, see section 2.5.2) is infiltrated with metal organic precursors using the incipient wetness method (IWM). For the infiltration a 1-molar metal nitrate solution of iron or copper is applied and subsequent thermal decomposition of the precursors is performed at 523 K. The resulting Fe-AC-IWM exhibits crystalline metallic iron species (Fig. 22). The estimated average crystallite size is about 24 nm (Scherrer equation, see section 3.2.4). The reflections of iron oxide particles are largely broadened, suggesting an average particle size below 2 nm.

In order to prevent sintering of adjacent iron oxide particles and stabilize the carbon matrix, silicon oxide is co-deposited in some of the substrates (Curdts et al. 2013). The impregnation is performed with tetraethoxysilane prior to impregnation with the metal nitrate solution. The pore size distribution of the samples is provided in Fig. 23. During impregnation and co-doping of silicon dioxide the pore structure is well preserved.

An overview of the investigated activated carbon based reference catalysts is provided in Table 3.

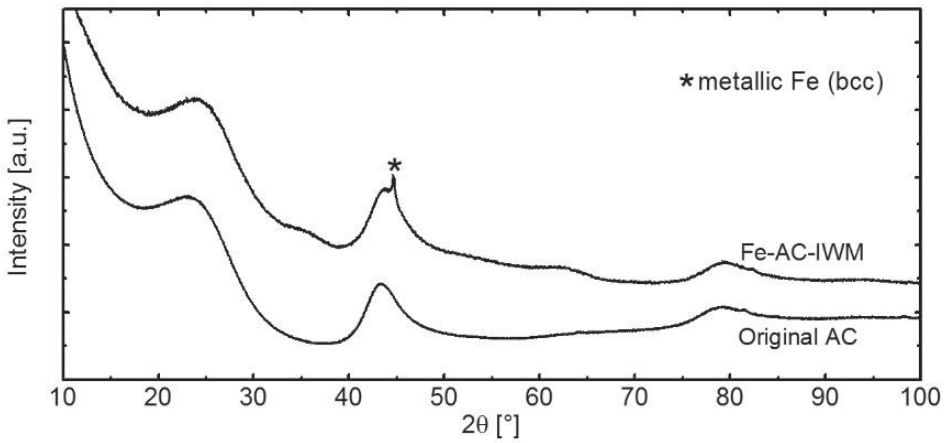

Fig. 22. X-ray diffractogram of Fe-AC-IWM in comparison to the non-infiltrated activated carbon

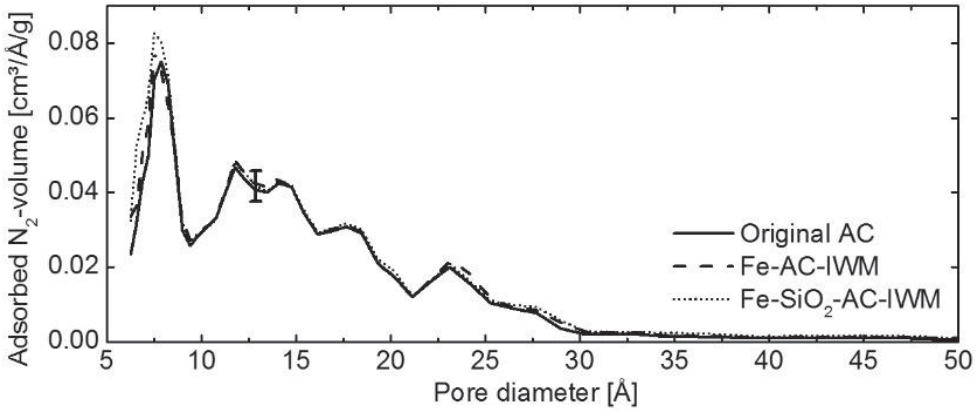

Fig. 23. Pore size distribution of IWM infiltrated activated carbon samples (iron and iron with co-doping of silica)

Table 3. Overview of IWM-infiltrated activated carbon catalysts, infiltrated load is approximately 5 wt.-%

Sample name	Precursor	Specific surface area (m^2/g)	Total pore volume (cm^3/g)	Micropore volume (cm^3/g)
R1407-substrates				
Original AC	-	1604	0.69	0.190
Cu-AC-IWM	$Cu(NO_3)_2$	1385	0.63	0.159
Fe-AC-IWM	$Fe(NO_3)_3$	1800	0.78	0.222
R1407-substrates with silica				
Cu-SiO2-AC-IWM	$Cu(NO_3)_2/Si(OC_2H_5)_4$	1594	0.63	0.190
Fe-SiO2-AC-IWM	$Fe(NO_3)_3/Si(OC_2H_5)_4$	1824	0.80	0.227

LIE-infiltrated zeolite samples

The zeolite reference catalysts are prepared at the Max-Planck-Institute for Carbon Research in Mülheim/Ruhr by liquid ion exchange (LIE). MFI, MOR and BEA substrates (delivered by Südchemie, details see section 2.5.4) are applied. For LIE the samples are stirred in a 1-molar aqueous solution of iron or copper nitrate for 30 minutes. The procedure is repeated three times in a fresh solution, followed by calcination at 923 K. The resulting ion load is about 5 wt.-% of the sample mass.

A TEM micrograph of the copper-infiltrated MFI (Cu-MFI-LIE) is provided in Fig. 24. The zeolite crystallites are about 30-50 nm in diameter, copper species are not visible. The TEM

micrograph in Fig. 25 shows the iron-infiltrated MFI (Fe-MFI-LIE). Iron particles are not visible either, but an EDX spectrum (Fig. 26) of the spot in the white circle in Fig. 25 proves successful iron infiltration of the sample.

The EDX elemental quantification also reveals the Si/Al-ratio of the investigated samples to an accuracy of about ±1 (Table 4). Among reference catalysts of the same zeolite structure the Si/Al-ratio varies, most probably due variations in the material delivered by the supplier.

Fig. 27 provides a comparison of the pore size distribution of the LIE-infiltrated MFI and BEA samples with the original non-infiltrated material. No differences are observed in the micropore region, i.e. in the pore channel structure (left graphs). Significant changes occur in the mesopore region (right graphs). Larger pores are observed after infiltration, possibly indicating a disintegration of zeolite particles during the infiltration procedure from the larger crystallite-agglomeration and the formation of more inter-crystallite pores. Hence, the total pore volume is increased for most zeolite catalysts after the infiltration (see Table 4).

The XRD diffractograms of iron- and copper-infiltrated MFI and BEA samples are shown in Fig. 28. No significant differences in the crystal structure or phase transformations are observed in comparison to the preconditioned non-infiltrated substrate. An overview of all applied zeolite reference catalysts is provided in Table 4.

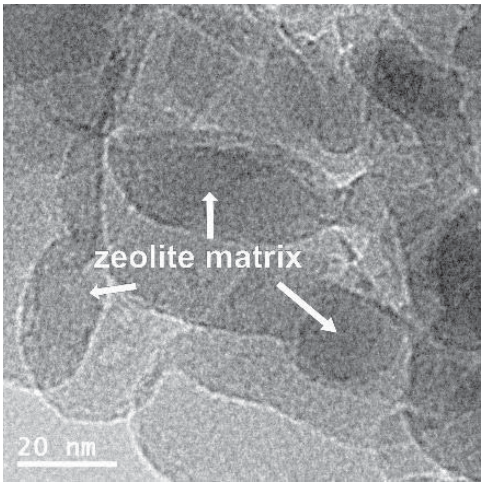

Fig. 24. TEM micrograph of Cu-MFI-LIE

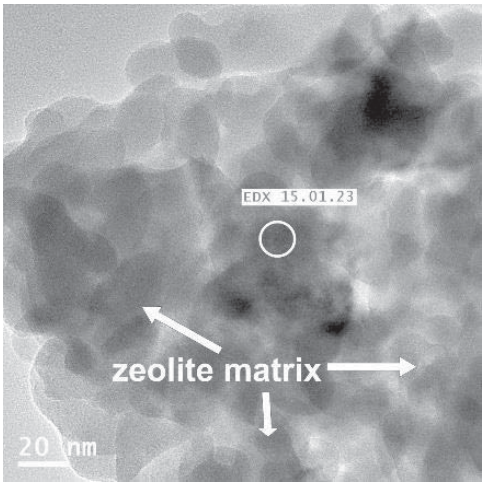

Fig. 25. TEM micrograph of Fe-MFI-LIE, EDX spectrum taken from the spot in the white circle is shown in Fig. 26

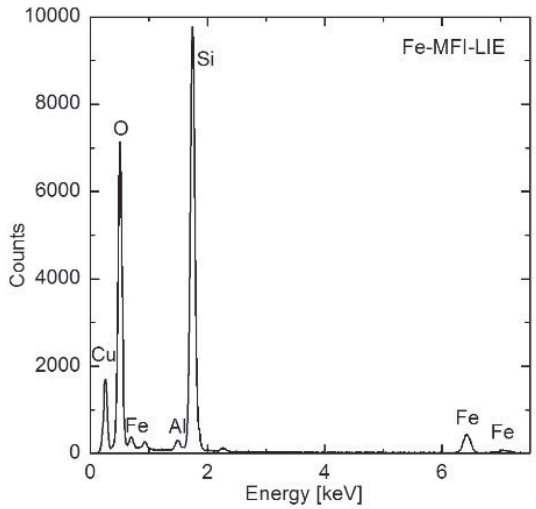

Fig. 26. EDX spectrum of spot marked in Fig. 25, the copper signal stems from the TEM grid

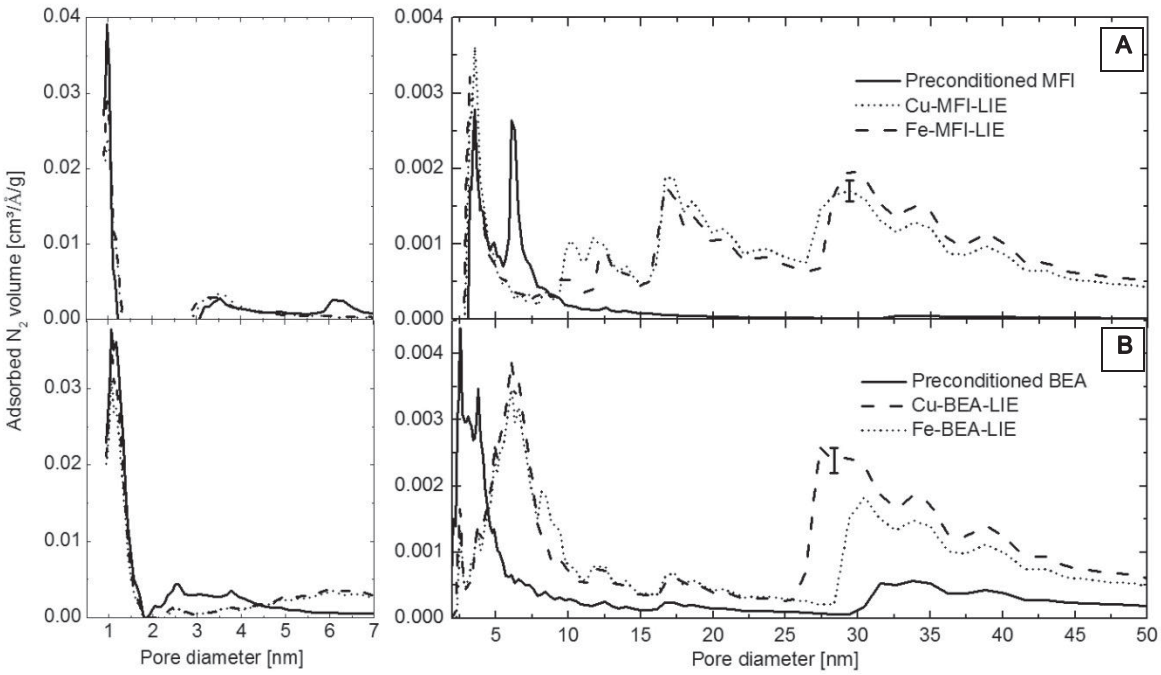

Fig. 27. Pore size distribution of LIE-infiltrated MFI (A) and BEA (B) samples in the micropore/small mesopore region (left) and in the mesopore region (right)

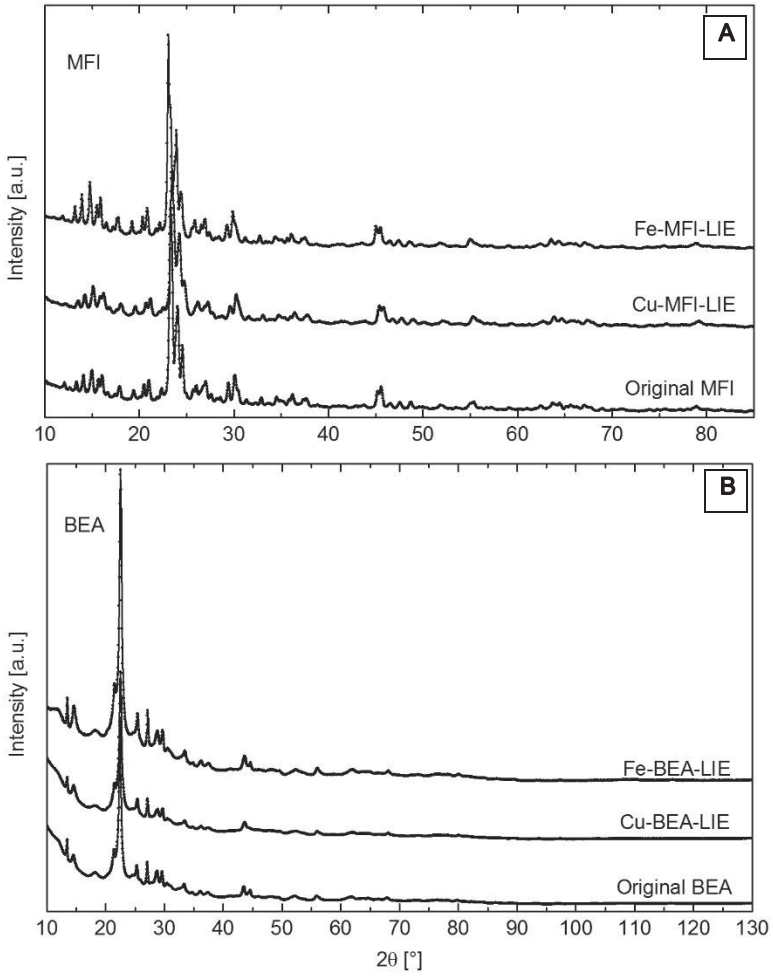

Fig. 28. X-ray diffractograms of LIE-infiltrated MFI samples (A) and BEA samples (B)

Table 4. Overview of zeolite reference catalysts

Sample name	Precursor	Infiltrated ion	Ion load (wt.-%)[1)]	Si/Al-ratio[1)]	M/Al-ratio[1),2)]	Specific surface area (m^2/g)	Micropore volume (cm^3/g)	Total pore volume (cm^3/g)
ZSM-5 (MFI) matrix								
Preconditioned MFI	-	-	-	16	-	400	0.087	0.23
Fe-MFI-LIE	$Fe(NO_3)_3$	Fe	0.6	32	0.3	433	0.048	0.66
Cu-MFI-LIE	$Cu(NO_3)_2$	Cu	0.9	31	0.3[3)]	412	0.041	0.64
Zeolite Beta matrix								
Preconditioned BEA	-	-	-	16	-	695	0.108	0.45
Fe-BEA-LIE	$Fe(NO_3)_3$	Fe	0.8	52	0.6	601	0.060	0.69
Cu-BEA-LIE	$Cu(NO_3)_2$	Cu	1.3	48	0.6[3)]	663	0.062	0.84
Mordenite matrix								
Preconditioned MOR	-	-	-	5	-	536	0.125	0.28
Fe-MOR-LIE	$Fe(NO_3)_3$	Fe	2.1	13	0.4	545	0.102	0.33
Cu-MOR-LIE	$Cu(NO_3)_2$	Cu	2.6	11	0.4[3)]	540	0.101	0.31

[1)] quantified by EDX, standard error: +/-30%; [2)]M/Al-ratio = ratio of foreign metal atoms per Al-atoms; [3)]corrected impact of brass sample holder

Envisorb

An infiltrated silica-based commercial drying agent (BASF Envisorb B+, herein denoted as Envisorb) is used as a reference catalyst for activated carbons. Envisorb is a porous silica with integrated dispersed activated carbon (about 10 wt.-%). The as-delivered substrate is infiltrated with iron, copper and manganese by the same CVI-procedure as applied in this work for activated carbon catalysts (see section 3.1.3).

The pore size distribution of infiltrated Envisorb reveals some structural changes in the small mesopore region after infiltration (Fig. 29). Infiltration with copper opens up the access to mesopores, whereas infiltration with manganese widens small mesopores.

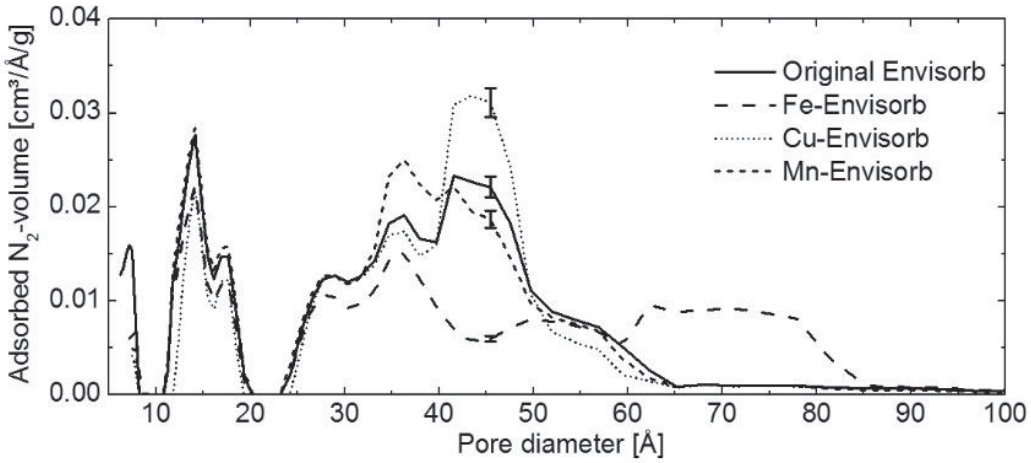

Fig. 29. Pore size distribution of Envisorb samples

Magnetite and Pt/Al_2O_3

The reference catalyst for iron oxide is pure magnetite powder (iron-II,III-oxide, black (magnetite), min. 95%, STREM Chemicals, CAS: 1317-61-9) with a BET specific surface area of 8.4 m²/g.

The commercial platinum reference catalyst contains 5 wt.-% platinum stabilized on alumina (5 wt.-% platinum on alumina powder, reduced, Alfa Aesar, LOT: F02R004) and exhibits a specific surface area of 144 m²/g. Table 5 provides an overview of the investigated Envisorb, Pt/Al_2O_3 and magnetite reference catalysts.

Table 5. Overview of reference catalysts Envisorb, Pt/Al_2O_3 and magnetite

Sample name	Precursor	Infiltrated load (wt.-%)	Specific surface area (m^2/g)	Micropore volume (cm^3/g)	Total pore volume (cm^3/g)
Envisorb substrates					
Original Envisorb	-	-	776	0.17	0.70
Fe-Envisorb-CVI	Ferrocene	5	577	0.12	0.62
Cu-Envisorb-CVI	$Cu(acac)_2$	5	583	0.10	0.64
Mn-Envisorb-CVI	$Mn(acac)_3$	5	722	0.15	0.67
Reference catalysts					
Pt/Al_2O_3	-	4.0	144	-	-
Magnetite	-	-	8	-	-

3.2. Structural and chemical investigation

The structural properties of the synthesized catalysts are investigated with scanning electron microscopy (SEM), transmission electron microscopy (TEM), X-ray diffraction (XRD), low temperature nitrogen adsorption, thermal gravimetric analysis (TGA) and differential thermal analysis (DTA). The elemental composition is determined using energy-dispersive X-ray spectroscopy (EDX).

3.2.1. Scanning electron microscopy

Scanning electron microscopy allows a straightforward inspection of the deposited particle sizes and a rough estimation about the distribution on the surface or in the cross section of infiltrated samples. An electron beam is directed on the sample and either the backscattered electrons or secondary electrons expelled from the sample are detected. The beam is focused by an electromagnetic lens system. Excessive focusing on one spot can cause sample charging and smearing of the contrast or even damage the sample.

Secondary electrons usually have low energy and stem rather from the surface region of the sample. The number of detected secondary electrons is a function of the surface angle of the sample. Hence, good information on the topography of the sample can be derived. Backscattered electrons stem from deeper beam penetration and typically exhibit higher energy. Elements with larger atomic mass cause more electron scattering and information on the sample composition can be derived.

Catalyst characterization by SEM is applied in this work for investigation of the distribution of particles on the surface of the catalyst. Metal particles with a large atomic mass cause a good

contrast relative to the carbon matrix. Oxygen cannot be detected due to low contrast compared to carbon and the oxidized carbon surface.

The applied JEOL JSM 7500F microscope can be operated in secondary electron mode and for energy-dispersive X-ray spectroscopy (see below). The acceleration voltage is 15-20 kV at a working distance of 8 mm. The ball-shaped activated carbon samples are fixed on a carbon tape and split with a scalpel resulting in hemispheres of carbon. Mainly the cross sections are investigated. Zeolite samples are dispersed on a brass sample holder. The SEM investigations are performed in cooperation with Christian Notthoff from the group of Markus Winterer (Nanoparticle Process Technology, University of Duisburg Essen).

3.2.2. Transmission electron microscopy

Transmission electron microscopy provides information on particle size, location and crystal structure of synthesized catalysts. Similar to SEM, a focused electron beam (typically 100-200 keV beam energy) is directed to the sample, but only electrons transmitting the sample are detected. The electrons can be backscattered, diffracted, scattered or even pass without energy loss. The beam can be significantly attenuated depending on the sample thickness and density, but high energy impact can also damage the sample structure and cause artifacts. Since particles can only be investigated in vacuum, the sample surface groups or morphology may be different than in ambient conditions.

On a fluorescent screen a 2D-image of transmitted electrons shows a projection of the mass of atoms of the sample. This is called the bright-field image. Limitations in the contrast can arise if different elements of similar contrast, i.e. atomic mass, are present on the substrate. The dark-field image visualizes the electron diffraction and reveals information on the crystal structure of the sample.

The applied HRTEM instrument is a FEI Tecnai F20 Supertwin microscope with 200 kV field emission gun and a maximum point resolution of 0.23 nm. The electron flux during the experiment does not exceed $3 \cdot 10^5$ electrons/nm^2, which is small enough to avoid any sample damage by the electron beam irradiation. The high-resolution micrographs are analyzed by fast-Fourier transform (FFT). The crystal structure is derived by measuring the separations and angles between the reflections in the FFT patterns. All TEM investigations are performed in cooperation with Vadim Migunov from the group of Michael Farle (Experimental Physics, University of Duisburg Essen).

The investigated zeolites are dispersed in n-hexane and deposited on a copper TEM grid covered with a thin film of amorphous carbon. Prior to the HRTEM investigation of an activated carbon sample, the spherical particle is cut into two hemispheres by a focused gallium ion beam. Then, thin lamellae (10×10×3 µm) are extracted by a focused gallium ion beam (FIB, FEI Helios Nanolab) (Fig. 30) (Langford & Petford-Long 2001). A micro manipulator is attached to the carbon lamella by deposition of platinum via a precursor gas and the short side of the lamella is thinned to 100 nm while decreasing the FIB current to reduce gallium implantation. The remaining lamella is attached to a copper lift-out grid using platinum deposition. The sample preparation with FIB is performed in cooperation with Andreas Beckel from the group of Axel Lorke (Experimental Physics, University of Duisburg Essen).

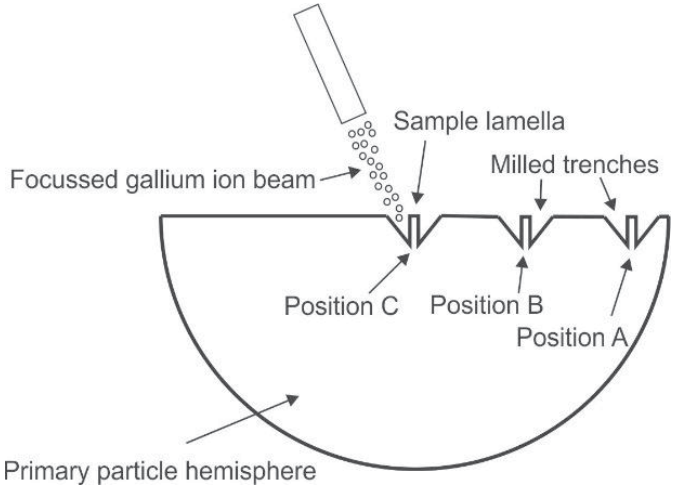

Fig. 30. Sample preparation by focussed ion beam for investigation with TEM; positions A, B and C denote sample lamellae close to the border, at half radius and in the center of the particle, respectively; drawing not to scale

3.2.3. Energy-dispersive X-ray spectroscopy

Energy-dispersive X-ray spectroscopy (EDX) can provide information on the elemental composition of the substrate and on the spatial dispersion of deposited material in the substrate. Especially the ion load of zeolites is quantified by EDX, providing an indication of the ion exchange level.

EDX is applied in combination with SEM and TEM investigations. The elemental composition is derived from the X-ray spectra emitted by inelastic electron scattering of the sample upon irradiation by an incident electron beam. The local resolution of elemental quantification is limited as the irradiated area can comprise several nanometers in depth and secondary irradiation of neighboring atoms can deteriorate the signal. Further error sources contribute, e.g. the sample holder or the applied carbon tape.

The spatial distribution of the infiltrated metal inside the infiltrated activated carbons is investigated by analyzing cross section hemispheres of the sample. Along a defined path a line scan and on a larger area a map of elemental composition is acquired.

EDX measurements for quantification of the zeolite exchange level are acquired in a JEOL JSM 7500F microscope with Quantax 200 EDX system. The quantification of elements is performed using the P/B-ZAF method by Esprit software (Bruker AXS).

The elemental analysis of deposited species in zeolites and activated carbons is performed in a FEI Tecnai F20 Supertwin microscope with attached EDX detector. The quantification of elements is performed using FEI TIA software. EDX investigations in the JEOL instrument are carried out in cooperation with Dr. Christian Notthoff from the group of Markus Winterer (Nanoparticle Process Technology, University of Duisburg Essen). The EDX investigations in the FEI instrument are performed in cooperation with Dr. Vadim Migunov from the group of Michael Farle (Experimental Physics, University of Duisburg Essen).

3.2.4. X-ray diffraction

X-ray diffraction (XRD) measurements allow the investigation of crystalline species deposited in the catalyst samples. Changes in crystallinity during catalyst preparation and catalytic investigation can be monitored.

The principle of XRD relies on detecting the intensity of Bragg reflections of a monochromatic X-ray beam that is diffracted by the planes of a crystal substrate. Depending on the angle of the incident beam, the beam wavelength and the distance between crystal planes, the diffracted beam intensity can increase or decrease upon constructive or destructive interference, respectively.

During diffraction measurements of catalyst powders only a fraction of the crystallites is oriented in a way yielding reflections. In order to minimize preferred orientation effects and record reflections from as many crystals as possible, the sample is mounted on a spinning stage.

Nanocrystallites bear a high density of defects, lattice straining and lattice tension effects. Thus, the reflections are broadened as compared to the bulk material. Furthermore, there can be a coexistence of crystalline species, amorphous clusters and partially crystalline species causing an increased background intensity. Artifacts may be caused by high secondary radiation of iron containing species when a conventional copper X-ray source is used. In this case a monochromator has to be applied.

For zeolites the XRD reflections can be broadened or shifted by the nature of accommodated extra-lattice cations and by the amount of adsorbed water. In case of zeolite Beta, the fraction of different polytypes present in the investigated sample causes additional peaks in the diffractogram.

A rough estimation of the volume weighted average crystallite size can be derived from the Scherrer equation:

$$\langle L \rangle = \frac{K\lambda}{\beta \cos\vartheta} \qquad \textbf{(9)}$$

where $\langle L \rangle$ is the column length of the diffracting crystal planes of the particle in the direction perpendicular to the reflecting planes, K is a shape factor (0.94 for cubic particles), λ is the wavelength of the incident X-ray beam, β is the peak width and ϑ is the angle of the incident beam to the normal of the reflecting lattice plane. Prior to particle size estimations in this work, a baseline and superposed reflections are subtracted by fitting the respective reflections with a pseudo-Voigt function by the software Origin 8.6.

In the present experiments a Panalytical X'Pert Pro MPD instrument, using Cu-K_α radiation, with X'Celerator detector is applied. The parameters are listed in Table 6. For iron containing samples a monochromator is used.

Table 6. Typical parameter settings for XRD-measurements in this work

Parameter	Settings
Radiation wavelength	1.54 Å (Cu-K_α)
Acceleration voltage	40 kV
Emission current	40 mA
Mask	15 mm
Soller slit	0.04 rad
Antiscatter slit	1°
Step size	0.05°
Time per step	100 s

3.2.5. Low temperature nitrogen adsorption (BET)

Low temperature nitrogen adsorption measurements allow the investigation of the catalyst surface area, porosity and the pore volume. Structural changes, changes in the surface area or pore blocking can be monitored during the catalyst preparation and during the catalysis processes.

Surface area calculation

The measurement principle is based on the assumption that the surface of a substrate can be derived from the amount of gas that it can adsorb in a monomolecular layer completely covering the substrate. Langmuir first described a relation between the coverage of a substrate with a monomolecular layer of adsorbing gas on a solid and the gas pressure below saturation pressure (Langmuir 1918). Since the model of Langmuir does not take into account multilayer adsorption, it has been further advanced by Brunauer, Emmett and Teller (BET) (Brunauer et al. 1938). The following five assumptions are made:

1) The substrate has a homogeneous surface, i.e. all adsorption sites have similar nature,
2) Only one molecule can adsorb per adsorption site,
3) There is no lateral interaction of adsorbed molecules,
4) Every adsorbed molecule can serve as a new adsorption site (vertical to the substrate surface),
5) Only molecules of the first layer interact with the substrate surface while in all subsequent layers the heat of adsorption is equal to the heat of condensation of the adsorbent.

The BET-equation shows the relation between adsorbed gas volume and the experimental pressure:

$$\frac{p}{W(p-p_0)} = \frac{1}{W_m C_{BET}} + \frac{C_{BET}-1}{W_m C_{BET}} \cdot \frac{p}{p_0} \qquad \textbf{(10)}$$

where p is the equilibrium experimental pressure, p_0 is the vapor pressure of the adsorbate gas (e.g. nitrogen) at the applied temperature (77 K for N_2 adsorption), W is the adsorbed mass, W_m is the the mass of one adsorbed monolayer, C_{BET} is the BET-constant defined as:

$$C_{BET} = \exp\left(\frac{\Delta H_{ads} - \Delta H_{cond}}{RT}\right) \qquad \textbf{(11)}$$

where ΔH_{ads} is the heat of adsorption in the first physisorbed layer and ΔH_{cond} is the latent heat of condensation of additional layers. C_{BET} provides a rough indication on the enthalpy of adsorption. Large values of C_{BET} (> 100) indicate the formation of a sharp knee in the adsorption isotherm (Sing et al. 1985). Negative values of C_{BET} are physically impossible (Rouquerol et al. 2007).

The BET equation can be plotted as an adsorption isotherm and has usually a linear region in the range of $0.05 < p/p_0 < 0.35$. For microporous samples this linear region can be shifted to significantly lower values, e.g. $0.01 < p/p_0 < 0.20$. From adsorption data in this region the mass of the first adsorbed monolayer W_m, the BET-constant C and finally the specific surface area S_s can be calculated as:

$$S_s = \frac{A_M N_A W_m}{M m_S} \tag{12}$$

where A_M is the area covered by one adsorbed molecule (for nitrogen: 16.2 Å²), N_A is the Avogadro number, M is the molar mass of the adsorbate and m_S is the mass of the substrate.

For application of the BET equation to microporous materials the surface area is often overestimated. Capillary condensation of the adsorbate in micropores increases the adsorbate volume which is accounted in the BET calculation for monolayer adsorption. Hence, respective data should be interpreted with care.

Pore size calculation

In a porous substrate the approximate pore size can be derived from the amount of adsorbed gas if the pressure of the adsorbate is stepwise varied at constant temperature according to the Kelvin equation. The Kelvin equation relates the meniscus radius of a liquid in a cylindrical pore to the experiment pressure. For a cylindrical pore filled with a liquid with hemispheral meniscus the Kelvin equation is:

$$ln\frac{p}{p_0} = \frac{2\gamma V_m}{rRT}\cos\delta \tag{13}$$

where p is the actual vapor pressure, p_0 is the saturated vapor pressure, γ is the surface tension and V_m is the molar volume of the liquid at temperature T, R is the ideal gas constant, r is the radius of the meniscus of the liquid and δ is the contact angle of adsorbent and adsorbate and is usually assumed to be 0°.

Barrett, Joyner and Halenda developed a famous pore size calculation model (BJH-method) based on the Kelvin equation (Barrett et al. 1951). Pore size calculations based on the Kelvin equation are, however, valid for diameters larger than 4 to 10 nm and the equation is not suitable for slit-shaped pores (Storck et al. 1998; Casanova et al. 2008). To overcome these limitations, refined concepts like non-local density functional theory (NLDFT) models provide better results as they are based on the weighted summation of pre-calculated adsorption isotherms describing adsorption of a certain adsorbate on a certain adsorbent for each pore width. Hence, each NLDFT model is only applicable for a predefined adsorbent-adsorbate-system and a defined pore geometry (Groen et al. 2003).

Hysteresis effects during gas adsorption and desorption on a substrate can give an indication on the pore geometry in the material. However, for pores widths smaller than 4 nm usually no hysteresis is observed due to the limited stability of the adsorbed film (Neimark et al. 2000).

Pore volume calculation

The micropore volume is often determined according to the α_s-method. This method is a modification of the t-plot model. It derives the thickness of an adsorbed nitrogen layer by division of the adsorbed volume by the BET surface area (Gregg & Sing 1967; Mikhail et al. 1968). The t-plot concept adapts, however, the BET overestimation of the monolayer capacity (Kaneko & Ishii 1992). Hence, t is replaced by α_s with

$$\alpha_s = \frac{V_x}{V_{0.4}} \tag{14}$$

where V_x is the adsorbed nitrogen volume at a relative pressure $p/p_0 = x$, and $V_{0.4}$ is the adsorbed volume at $p/p_0 = 0.4$ (Bhambhani et al. 1972; Lowell et al. 2006, p. 139). At $p/p_0 = 0.4$ the micropore filling is usually completed. The actual micropore volume is then calculated by comparing the adsorption isotherm of the (microporous) substrate to a similar non-microporous standard material.

The total pore volume is derived from the adsorbed nitrogen volume at p/p_0 close to unity (Lowell et al. 2006, p. 111):

$$V_p = \frac{W}{\rho} \tag{15}$$

where V_p is the pore volume, W is the adsorbed mass and ρ is the density of the adsorbate at p/p_0.

Applied instrumentation

The low temperature nitrogen adsorption measurements in this work are all performed using a Quantachrome Autosorb 1C instrument and the original equipment software. The pore size distribution is calculated by means of an integrated NLDFT adsorption branch module for zeolite samples assuming cylindrical pore geometry.

All investigated activated carbons and zeolites are microporous. However, nitrogen adsorption at 77 K in pores below 0.5 nm pore width can be kinetically hindered (Jagiello & Thommes 2004; Klank & Lohmeier 2012) leading to very long equilibration times (Groen et al. 2003). The large quadrupole moment of nitrogen can limit the resolution of pore size distribution measurements in the micropore region of zeolites (Storck et al. 1998). In order to estimate these effects, pre-investigation measurements are performed.

Fig. 31 shows three nitrogen adsorption and desorption isotherms of a non-infiltrated activated carbon (R1407). For each isotherm the equilibration time and the samples mass is varied. The adsorption of N_2 increases with longer measurement time and is limited by increased sample mass. A small sample (10.2 mg) in a measurement of 47 hours can adsorb nearly four times more nitrogen than a larger sample (25.2 mg) during fast measurement (6 hours). The corresponding calculated BET surface areas vary respectively.

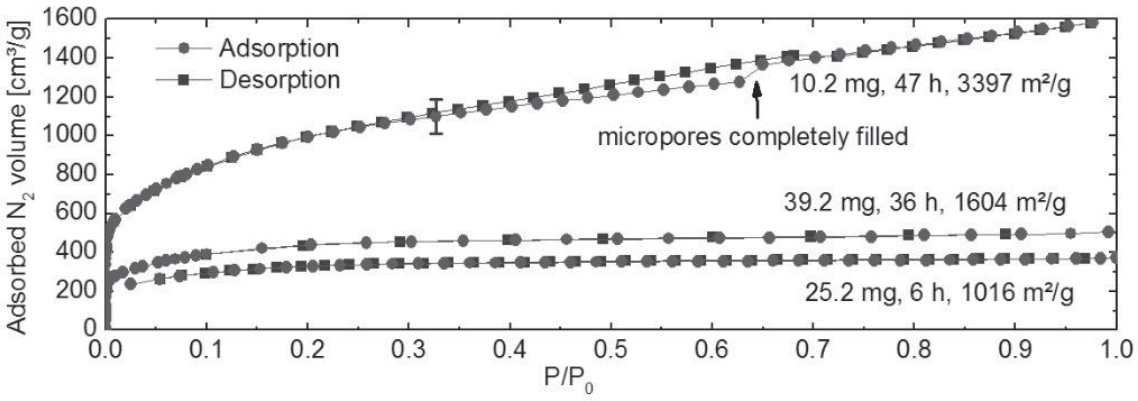

Fig. 31. N_2 sorption isotherms of non-infiltrated activated carbon at three different measurement times; stated figures indicate the investigated sample mass, the total measurement time and the resulted BET surface area

The full realization of the adsorption equilibrium at each p/p_0 measurement point requires an unreasonably long measurement time. Reduction of the sample mass can reduce the measurement time, but considering an accuracy of +/-1 mg of the applied mass balance system, the resulting measurement error vastly increases.

Application of CO_2 adsorption at 273 K could possibly resolve the diffusion issue and provides deep insight into the small micropore region, but information from measurements at lower than atmospheric pressure remain limited to pore widths smaller than 1 nm (Ravikovitch et al. 2000). Deep analysis of small pore sizes can be derived by the adsorption of probe molecules with different diameters like N_2, Ar, CO_2 or H_2 (Jagiello & Thommes 2004), but the measurement of each sample would require a very large effort.

As a compromise, all measurements in the current work are carried out at similar parameters, i.e. in the same setup, at same equilibration time and applying a similar sample mass of about 20 mg for activated carbons and 40 mg for zeolites, representing an equivalent of roughly 32 m² and 20 m², respectively. In this case, there proves to be a linear correlation between the micropore volume and the BET surface area (Fig. 32), as investigated exemplary for iron-infiltrated activated carbon samples in this work.

Even if the surface area may be overestimated, the induced error seems to be systematic. Hence, comparisons among equally measured samples based on the BET equation should be valid. The stated values of specific surface area, micropore volume, etc. in this work are all generally based on the mass of an equivalent non-infiltrated sample.

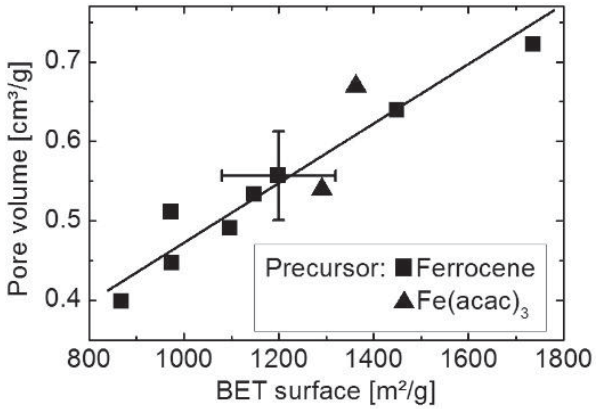

Fig. 32. Pore volume in relation to specific surface area (BET surface) of Fe-infiltrated activated carbons

3.2.6. Thermal gravimetric analysis and differential thermal analysis

Thermal gravimetric analysis (TGA) is carried out for the investigation of mass changes of the catalyst in relation to temperature and time, for example evaporation of components or gasification in an inert or reactive atmosphere. Differential thermal analysis (DTA) allows investigation of temperature dependent phase changes of the synthesized catalyst in inert or reactive atmosphere.

Both methods are applied in order to monitor the behavior of the catalysts at a certain temperature and atmosphere. For the measurement, the sample is placed into an alumina crucible inside a thermal balance system. The DTA-signal is acquired by means of a thermocouple fixed at the bottom of the crucible and it is compared with the signal of a neighboring empty crucible as reference.

For the measurements an instrument of Bähr Thermoanalyse GmbH (STA 503) with 55 cm^3 sample room is operated at 298 K up to 1773 K with a heating rate up to 100 K/min. The DTA signal is acquired using a Pt-100 temperature sensor. The noise level of the thermal balance is 1 µg. A possible buoyancy effect – caused by the density change of the working gas flow upon heating – and the estimated difference in heating capacity between sample and reference crucible are both corrected in the displayed measurements in this work.

3.3. Catalytic investigation

3.3.1. NO_2 adsorption measurements

The adsorption and desorption properties of catalysts can change with changing temperature and with increasing process time, for example due to saturation effects, changing surface chemistry or structural changes of the surface. In this work the maximum NO_2 adsorption capacity and the desorption behavior of the synthesized catalysts are compared. The measurements are performed in the same instrument and setup as applied for TGA/DTA measurements (Bähr Thermoanalyse GmbH, STA 503).

3.3.2. Recycle flow reactor

Investigations on the catalytic activity are performed in a recycle flow reactor. Such an equipment allows the time and temperature resolved monitoring of the catalytic activity for kinetically very slow reactions. It simulates more realistically the application of catalysts in a circulating gas volume like cabin air or in human workspace. However, the reactions of primary educts are difficult to be analyzed separately in recycle flow as described in section 2.2.

Despite the combined advantages of stirred tank and plug flow reactors, recycle reactors are less often applied. Due to the long residence time of the monitored gas mixture inside the reactor, the setup needs to be highly inert and vacuum tight. Own preliminary measurements with a reactor applying stainless steel lines showed a substantial decomposition of nitrogen oxide in the recycle flow.

The comparability of measurements with different catalysts is usually granted by normalization to the catalyst mass or catalyst surface area. In fact, the catalyst surface area would be optimal for standardization, but it is often difficult to measure (Aarna & Suuberg 1997). In this work, the activity is normalized to catalyst mass. 0.2 g of the sample are fixed in a borosilicate glass

cell by glass wool plugs, similar to the setup applied by other authors (Gruenert et al. 1994; Voskoboinikov et al. 1998). The contribution of the empty reactor and glass wool to the gas conversion activity is evaluated prior to the catalytic investigation measurement and is discussed in section 3.3.3.

A scheme of the recycle flow reactor setup is presented in Fig. 33, photographs of the setup are provided in appendix 9.8. The sample cell is embedded in a heating mantle and can be heated up to 723 K at a maximum heating rate of 10 K/min. The heat flux from the heating mantle to the sample cell is mediated by 10 mm thick bulk copper brackets in order to provide homogenous heat distribution along the entire relevant part of the sample cell. The temperature of the sample is measured right at the glass wall of the sample cell by a type K thermocouple. The typical test gas mixture consists of 0.9% NO_2, 10% argon and 89.1% helium, premixed in a 10 l glass bulb by dosing the respective partial pressure of each gas using a Leybold Ceravac CTR91 capacitive pressure transducer. The applied NO_2 concentration is larger than in typical workspace environments in order to allow the investigation of catalytic conversion with the applied instrumentation. An overview of the applied parts and respective materials with contact to the test gas mixture in the recycle reactor is provided in Table 7.

Table 7. Relevant reactor parts with exposure to test gas mixture and applied materials

Recycle reactor part	Material	Notes
Sample cell	Borosilicate glass	
Reactor tubing	Borosilicate glass	
Reactor tube fittings	Borosilicate glass and FFKM	Double sealings applied
Gas supply lines	Stainless steel, type 1404	Only short exposure to NO_2
Premixer	Borosilicate glass	10 l volume
Connection lines to premixer	FFKM (perfluoro elastomer)	
Pressure transducer	Stainless steel	Only short exposure to NO_2
Piston in recycle pump	FFKM (perfluoro elastomer)	
Needle valve of mass spectrometer	Stainless steel	Constantly heated to 323 K preventing condensation of any gas species or water vapor

For gas flow control the power of the piston pump (Bühler Analysenpumpe P2.3 SP) is controlled by a power controller. At the standard setting the gas flow in the reactor with mounted sample is 400 sccm, calibrated with a gilibrator (Gillibrator 2, Sensidyne Gillian) in standard conditions. Thus, the gas mixture circulates in the reactor constantly about once every minute and the space velocity SV in the recycle reactor is defined as

$$SV = \frac{\dot{V}_R}{m_c} = \frac{400\ cm^3\ min^{-1}}{0.2\ g} = 0.12\ m^3\ g^{-1}\ h^{-1} \qquad \textbf{(16)}$$

where $\dot{V}_R$ is the volumetric flow rate of feed gas in the recycle reactor and m_c is the sample mass of the catalyst (Choi et al. 2003).

Before each measurement, the reactor system and supply lines are evacuated to a residual gas pressure of 1 mbar. Hence, the residual gas fraction at 1000 mbar working pressure is 0.1%. The working pressure is slightly decreasing during a catalysis experiment by 1-2% over two

hours due to helium escape. For pressure monitoring a combined Pirani and capacitance gauge (Pfeiffer Vacuum PCR 260) for a range from $5 \cdot 10^{-4}$ to 1500 mbar is applied.

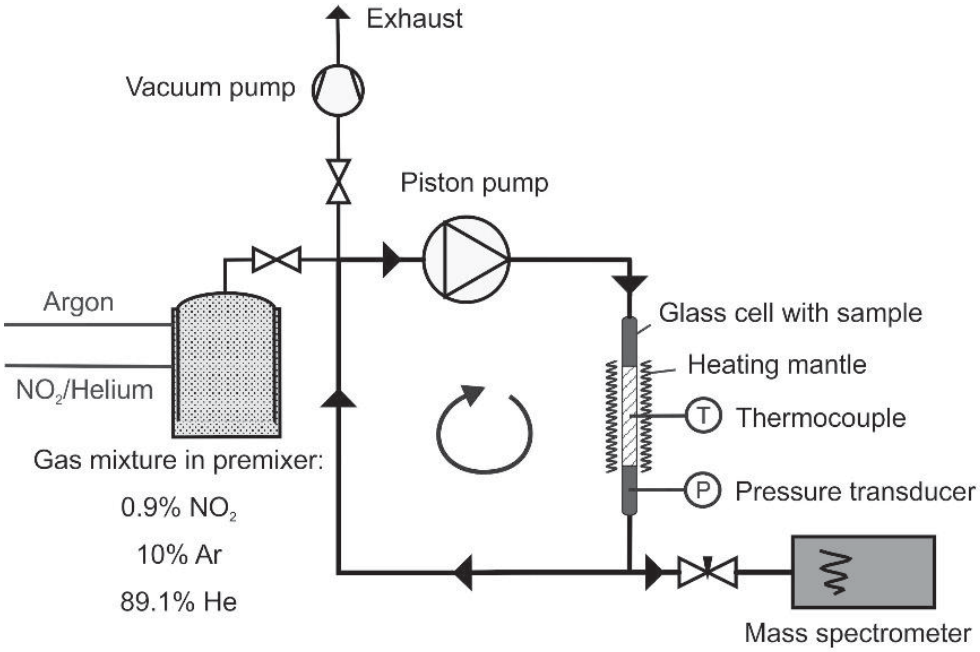

Fig. 33. Recycle flow reactor for catalytic investigation

3.3.3. Kinetic studies

Mass spectrometric investigation

The time resolved changes in the test gas mixture during catalysis experiments are investigated by means of a quadrupole mass spectrometer (QMS). This equipment allows monitoring of all relevant gas species simultaneously. The principle of a QMS is based on ionization and acceleration of atoms, molecules or even small particles in an electromagnetic field. During their travel in the field ions are separated according to their mass/charge (m/e)-ratio and counted separately. The result is a spectrum of m/e-ratios in close relation to the abundance of parent molecules in the investigated sample gas.

The applied QMS (Pfeiffer Vacuum QMS 200 with Quadstar software) is an industrially well established, reliable, easy to handle and moderately priced instrument. The m/e-separation is performed by guiding ions of similar energy and velocity along a trajectory between four parallel cylindrical rods (Fig. 34). The rods induce a radio frequency quadrupole field and only ions of a certain m/e-ratio can travel along a stable helical trajectory to the detector (Pfeiffer Vacuum GmbH 2007).

Each pair of opposing rods have the same deflection voltage U_f:

$$U_f{}^{+} = U + V \cdot \cos \omega t \text{ or } U_f{}^{-} = -U - V \cdot \cos \omega t \qquad \textbf{(17)}$$

where U is a DC-voltage and $V \cdot \cos \omega t$ is an AC-voltage. By varying U and V the trajectory is adjusted to be stable for a resonant ion and all non-resonant ions are trapped by the rods.

The detector unit is a continuous secondary electron multiplier (C-SEM or Channeltron) allowing high sensitivity for low ion signals. The C-SEM detector consists of a glass tube coated

with a conductive layer with high resistance. Upon excitation by an incident ion, a multiplying cascade of secondary electrons is ejected and eventually detected. Either positively or negatively charged ions can be analyzed according to the polarization of the analyzer system. In this work only positively charged ions are analyzed.

The applied ion source is a tungsten filament emitting electrons which are accelerated in an electromagnetic field and occasionally colliding with neutral molecules extracted from the sample gas mixture. The molecules are ionized, accelerated and extracted through an electromagnetic lens system to the quadrupole field.

Prior to a set of measurements, the QMS needs to be calibrated and tuned to the gas-specific ionization and fragmentation. After this procedure any mixture of pre-calibrated gas species can be interpreted more reliably. Fig. 35 shows the typical spectrum of the applied standard test gas mixture (0.9% NO_2, 10% Ar, 89% He).

A common error source is the ionization process. The applied ionization energy can be too weak to ionize a significant quantity of some of the relevant species and the resulted spectrum would not be representative. On the other hand, the ionization can be too harsh and as a result larger molecules of the sample gas are completely fragmented into smaller parts or multiply charged.

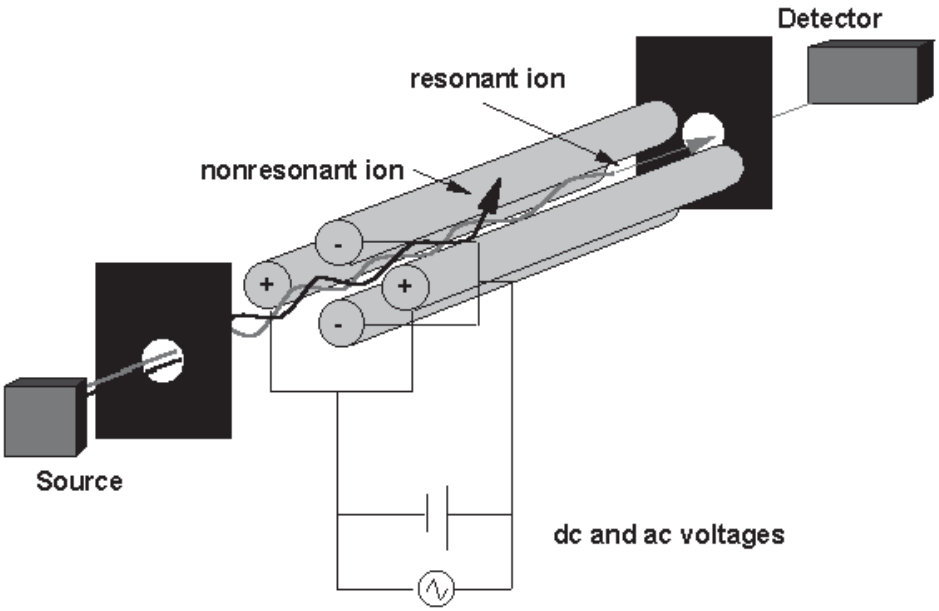

Fig. 34. Principle scheme of the quadrupole mass filter unit, adapted from (Tissue 2000)

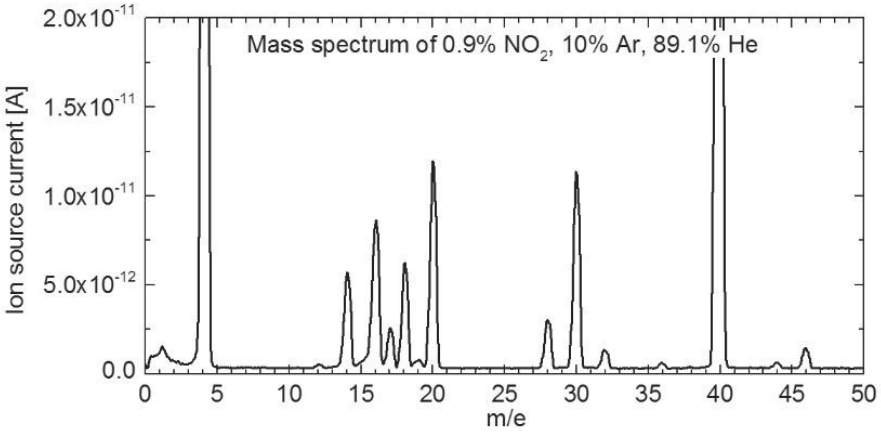

Fig. 35. Mass spectrum of the applied standard test gas mixture (0.9% NO_2, 10% Ar, 89.1% He)

For example, NO_2 is known to decompose at the hot filament ion source and an accurate calibration is needed for quantitative interpretation (Shirahama et al. 2002). Hence, in the current settings the base peak of NO_2, i.e. the peak of the highest measured signal intensity (m/e = 30), is different from the actual single ionized NO_2 molecule peak (m/e = 46).

Erroneous settings in the electronic lens system or of the software filtering can additionally cause artifacts. The accuracy of the mass filter is related to the accuracy of the quadrupole field radius. Hence, mechanical tolerances can be compensated by larger dimension of the quadrupole mass filter unit (Pfeiffer Vacuum GmbH 2002). Plausibility checks with defined reference gas mixtures are performed in order to resolve these issues.

The recorded spectra are normalized to the signal of argon (m/e = 40), in order to compensate any signal effects caused by pressure variations, and fitted with spectra of calibrated gases by means of Microsoft Excel Solver 2010. The applied parameter settings are summarized in Table 8 and details of the calibration routine are provided in appendix 9.2.

Possible effects of the reactor walls without any sample on the conversion of the standard test gas mixture are investigated in preliminary measurements. The pre-investigation is performed under typical conditions, i.e. the sample holder including glass wool plugs is heated from 298 K to 425 K and the experimental pressure is about 1000 mbar. Fig. 36 shows the time resolved gas mixture composition for the test gas (0.9% NO_2, 10% Ar, 89.1% He) during 120 minutes experimental time at 298 K. Fig. 37 shows the same experiment while heating the sample holder and glass wool plugs to 425 K.

At room temperature, no gas conversion apart from some NO_2 adsorption probably on reactor walls and glass wool plugs is observed. At 425 K a fraction of NO_2 is adsorbed on the reactor and some NO_2 is reduced to NO as expectable at 423 K (Holleman & Wiberg 2007, p. 714). The other gas species concentrations are not affected by the reactor.

Table 8. Parameter settings of the applied quadrupole mass spectrometer

Parameter	**Data**
Mass spectrometer model	Pfeiffer Vacuum Prisma QMS200
Filament	Tungsten
Electron emission current	1.00 mA
Ion reference potential	150 V
Cathode voltage (= nominal ionisation energy)	100 eV
Focus	10 V
Field Axis	8 V
Extraction	35 V
Detector type	Continuous secondary electron multiplier (C-SEM)
Scan mode	SCAN-F (with FIR filter)
SEM voltage	2 kV
Resolution	50
Mass scan speed	1s $(m/e)^{-1}$
Vacuum chamber residual pressure	ca. $4 \cdot 10^{-8}$ mbar
Vacuum chamber working pressure	ca. $1 \cdot 10^{-6}$ mbar

Data evaluation of mass spectra

The recorded mass spectra are fitted by scaled spectra of pre-calibrated gas mixtures of nitrogen dioxide, nitric oxide, nitrous oxide, carbon monoxide, carbon dioxide, oxygen, nitrogen and helium. The calculation procedure and fitting routine is explained in detail in appendix 9.3. Test measurements with predefined reference gas mixtures (Table 16 in appendix 9.3) ensure the validity of measurements to a good certainty reflected in the stated exemplary error bars.

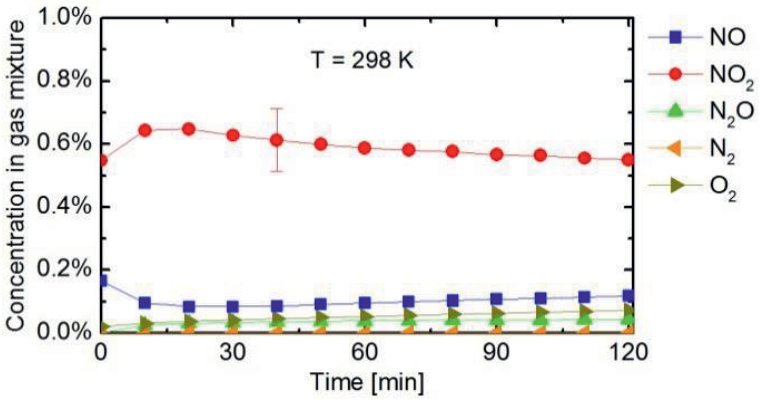

Fig. 36. Gas species concentration in the recycle reactor without catalyst sample with 0.9% NO_2, 10% Ar, 89.1% He at 298 K during 120 minutes experimental time

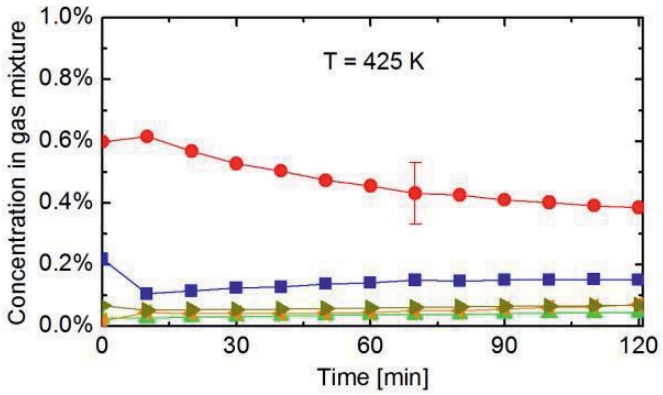

Fig. 37. Gas species concentration in the recycle reactor without catalyst sample with 0.9%NO_2, 10%Ar, 89.1% He at 425 K during 120 minutes experimental time

4. Results and discussion of activated carbon-based catalysts

The application of activated carbons in the decomposition of nitrogen oxides has a very long history (Shah 1929a; 1929b). The material is well characterized, easily applicable, non-toxic and last, not least – inexpensive. In the high temperature conversion of nitrogen oxides the application of carbon is not straightforward, since it may suffer from carbon gasification in the oxidative environment. However, for the here intended low temperature application it seems to be most appropriate.

Iron-, copper- and manganese infiltrated activated carbons are prepared by chemical vapor infiltration (CVI). After providing an overview of the catalysts, the sample structures are characterized and the performance in the direct catalytic decomposition of nitrogen dioxides is compared to similar samples, which are prepared by the incipient wetness method (IWM).

4.1. Sample overview

Table 9 provides an overview of the synthesized chemical vapor infiltrated activated carbon samples. The samples marked with the black circle are used in the discussion as typical examples for the iron-, copper- and manganese-infiltrated samples.

A large span of infiltrated metal load is observed, reaching from 0 to more than 20 wt.-% of the sample mass. The pore volumes and specific surface areas vary accordingly and the relations will be analyzed in section 4.4. The quantification of the infiltrated metal species load is usually estimated from the mass gain of the sample during the infiltration procedure. For some iron-infiltrated samples it is derived from the residual mass of the iron oxide after combustion of the carbon sample at 830 K in air. At this temperature any mass loss contribution of evaporized iron oxide is considered to be negligible (Shchedrin et al. 1978).

The large number of iron-infiltrated activated carbon catalysts presented in Table 9 are prepared in order to investigate the preparation effects, variations of the load, the infiltration of different precursors, implications on the pore volume and on the catalytic properties that will be discussed in the following. The parameters of preparation procedure of each sample are provided in Table 26 in appendix 9.7.

Table 9. Overview of CVI- infiltrated activated carbons; samples marked with a black circle are used in this work as typical examples due to their similar infiltration load

Sample name	Precursor	Infiltrated load (wt.-%)	Specific surface area (m^2/g)	Total pore volume (cm^3/g)	Micropore volume (cm^3/g)
Fe-infiltrated activated carbons					
Fe-AC-CVI (MB46)	Ferrocene	8.9	973	0.51	n.m.
Fe-AC-CVI (MB63)	Ferrocene	0.7	1148	0.53	n.m.
Fe-AC-CVI (MB67)	Ferrocene	12.5	1098	0.49	0.119
Fe-AC-CVI (MB67) after catalysis	Ferrocene	12.5	846	0.38	0.091
Fe-AC-CVI (MB84)	Ferrocene	12.1	1200	0.56	0.128
Fe-AC-CVI (MB88)	Ferrocene	20.6	868	0.40	0.094
Fe-AC-CVI (MB96)	Ferrocene	13.2	974	0.45	0.103
Fe-AC-CVI (MB100)	Ferrocene	0.0	1541	0.66	0.180
Fe-AC-CVI (MB101)	Ferrocene	5.7	1449	0.64	0.162
Fe-AC-CVI (MB105)	Ferrocene	4.0	2067	1.03	n.m.
• Fe-AC-CVI (MB112)	Ferrocene	3.2	1737	0.72	0.215
Fe-AC-CVI (MB112) after catalysis	Ferrocene	3.2	1585	0.79	0.173
Fe-AC-CVI (MB122)	$Fe(acac)_3$	1.0	1363	0.67	n.m.
Fe-AC-CVI (MB131)	$Fe(acac)_3$	2.8	1291	0.54	n.m.
Cu-infiltrated activated carbons					
Cu-AC-CVI (MB163)	$Cu(acac)_2$	0.7	1636	0.80	0.185
Cu-AC-CVI (MB164)	$Cu(acac)_2$	1.1	1834	0.80	0.219
• Cu-AC-CVI (MB336)	$Cu(acac)_2$	3.4	1759	0.72	0.220
Cu-AC-CVI (MB336) after catalysis	$Cu(acac)_2$	3.4	1560	0.63	0.198
Mn-infiltrated activated carbons					
• Mn-AC-CVI (MB165)	$Mn(acac)_3$	1.9	1651	0.68	0.215
Mn-AC-CVI (MB165) after catalysis	$Mn(acac)_3$	1.9	1789	0.78	0.209
Mn-AC-CVI (MB168)	$Mn(acac)_3$	0.8	1736	0.73	n.m.

Specific surface area: BET-method applied with $0.01 \leq p/p_0 \leq 0.10$; Total pore volume: derived from NLDFT-calculation; Micropore volume: α_s-method applied; n.m. = not measured

4.2. Preparation parameter studies

Homogeneous infiltration and a good control of the infiltration load are two main challenges of the preparation procedure of porous catalysts by chemical vapor infiltration. The porous substrates are often infiltrated from a continuous precursor flow. Factors like high precursor partial pressure and a high residence time of the precursor molecules inside of the pores favor gas phase reactions and promote a homogenous deposition inside of the pore network (Hu & Hüttinger 2001; Zhang & Hüttinger 2001). However, the application of metal organic precursors in a continuous precursor flow appears to be difficult to control due to its different chemistry in comparison for example with rather easily diffusing hydrocarbons. Furthermore, parasitic reactions on the reactor walls may decrease the efficiency of the infiltration process.

As an alternative, in this work the infiltration processes are performed in two separate steps: At first the precursor is sublimed, diffuses deeply into the activated carbon matrix and is homogeneously deposited, presumably in a non-decomposed state inside the carbon matrix. In the second step, the infiltrated sample is heated and the precursor decomposes thermally inside the pores.

Preliminary experiments showed that approximately 75% of the sublimed precursor, e.g. Ferrocene, can be trapped this way inside the activated carbon sample. The residual 25% of the precursor are condensed on the cold parts of the reactor wall. An intentionally long precursor evaporation time – two hours at 403 K for Ferrocene – at low experimental pressure promote the diffusion and smooth dispersion of the precursor inside the matrix material.

The subsequent decomposition of the precursor is performed at normal pressure with air and at an elevated temperature. The temperature needs to be large enough to efficiently decompose the precursor and low enough to avoid excessive gasification of the activated carbon with oxygen. At too low temperatures, however, the once deposited precursor may diffuse out of the pore channels prior to its decomposition. As an unwanted result, at least some surface-near regions of the spherical activated carbon particles would be depleted.

Hence, an estimation of the precursor decomposition reaction and precursor diffusion during the decomposition process is favorable. A good measure for such a purpose is a modification of the Thiele modulus (Thiele 1939; Deutschmann et al. 2009, 68f.). The modulus is typically applied for the efficiency characterization of heterogeneous catalysts and provides an estimation whether a given catalytic reaction with a given catalyst macrostructure occurs in the reaction or diffusion controlled regime.

The Thiele modulus φ for spherical catalyst particles and first order reactions is given as:

$$\varphi = L\sqrt{\frac{k_s}{D_{eff}}} \tag{18}$$

where k_s is the reaction rate constant, L is a characteristic length for the reactant inside of a spherical particle, for example the particle radius, and D_{eff} is the effective diffusivity of the reactant. In the present decomposition process in the activated carbons, the interest is directed on the behavior of a representative Ferrocene molecule at the average distance $\bar{L}$ of all homogenously dispersed Ferrocene molecules in the spherical activated carbon particle from the surface:

$$\bar{L} = \int_0^R \frac{3}{R^3} l^2 (R - l) dl = \frac{1}{4} R \tag{19}$$

where R is the radius of the activated carbon particle and l is the distance of any deposited Ferrocene molecule from the particle surface. In the narrow pore system of activated carbon (1-3 nm pore diameter, see section 4.4, Fig. 50) and with the molecular diameter of Ferrocene of 0.7 nm (Maeda et al. 1987), the effective diffusivity of Ferrocene molecules is determined by the Knudsen diffusivity D_{Kn}, the void fraction of the activated carbon ε and a measure for the tortuosity τ (Deutschmann et al. 2009):

$$D_{eff} = D_{Kn}\frac{\varepsilon}{\tau} \quad \textbf{(20)}$$

Typical values for the tortuosity in the activated carbon ($\tau = 7$) and for the void fraction of the sample ($\varepsilon = 0.4$) are adopted from other authors (Mayfield & Do 1991; Gray 1993; Bertrand et al. 2000; Schieferstein et al. 2013). The respective Knudsen diffusivity is defined by (Thomas et al. 1997):

$$D_{Kn} = \frac{4}{3} d_{pore}\sqrt{\frac{RT}{2\pi M_{FC}}} \quad \textbf{(21)}$$

with the gas constant $R = 8.314\, J \cdot K^{-1} \cdot mol^{-1}$, the applied decomposition temperature $T = 653\, K$ (see Table 2 in section 3.1.2), the molar mass of Ferrocene $M_{FC} = 186.04\, g/mol$ and a measured pore width mode d_{pore} of approximately 1 nm.

The decomposition rate k_s mainly depends on the considered Ferrocene decomposition reaction. Lewis and Smith suggest for the low pressure gas phase pyrolysis of Ferrocene a decomposition rate with a quite large activation energy of 382.4 kJ (Lewis & Smith 1984). In more reactive environments a reduced activation energy of 209 kJ or 218 kJ is suggested (Linteris et al. 2000; Kuwana & Saito 2005). Additionally, already deposited iron or iron-carbon coatings are believed to exhibit catalyzing effects and the activation energy may be further reduced (Dyagileva et al. 1979; Kuwana & Saito 2007). The decomposition with hydrogen or with oxygen radicals reportedly requires even lower activation energies of 51.5 kJ and 8.4 kJ, respectively (Hirasawa et al. 2004). Table 10 provides an overview of the respective decomposition rates and the derived Thiele modulus at 653 K with the characteristic length L of 0.0625 mm, representing the average distance $\bar{L}$ of a deposited Ferrocene molecule from the activated carbon particle surface.

The (modified) Thiele modulus largely differs between $6.4 \cdot 10^{-8}$ and $1.8 \cdot 10^{6}$, depending on the reaction. At 653 K, the upper four reactions Table 10 would be considered to describe a reaction kinetics controlled regime ($\varphi \ll 0.1$) inside of the pores, since the derived Thiele modulus is very low. The lower two reactions describe a diffusion controlled reaction regime ($\varphi \gg 10$). For the infiltration of copper into activated carbons, the rate constant of the decomposition of copper-II-acetylacetonate with oxygen is reported to be $k_s = 3.02 \cdot 10^{7} exp(-115.4\, kJ/RT)$ (Tsyganova & Dyagileva 1996) and the resulting Thiele modulus is 0.06, hence the decomposition is probably both diffusion and reaction controlled.

The actual infiltration of the activated carbons, probably comprises a mixture of several reactions: The precursor may react with oxygen, catalyzed by the carbon walls, by already deposited metal and oxide species and by high-energy carbon sites, which are typical for activated carbons (Xia et al. 1999). Furthermore, the true decomposition temperature inside the pore system may be somewhat larger than the applied 653 K due to the exothermic reaction of the precursor with oxygen. Hence, the overall reaction rate of the decomposition process may be considerably larger than expected for the stated temperature.

Table 10. First order decomposition reactions of Ferrocene with respective decomposition rate expression and Thiele modulus at 653 K

Ferrocene decomposition reaction	**Decomposition rate expression**		**Reference**	**Calculated Thiele-modulus**
	k_0	E_A		
Low pressure pyrolysis of Ferrocene	$2.19 \cdot 10^{16}$	382.4 kJ	(Lewis & Smith 1984)	$6.4 \cdot 10^{-8}$
Ferrocene + iron coating	$1.00 \cdot 10^{7}$	171 kJ	(Kuwana & Saito 2007)	$4.0 \cdot 10^{-4}$
Ferrocene + iron-carbon-coating	$2.15 \cdot 10^{9}$	171.1 kJ	(Dyagileva et al. 1979)	$5.8 \cdot 10^{-3}$
Pyrolysis of Ferrocene	$1.00 \cdot 10^{14}$	209 kJ	(Kuwana & Saito 2005)	$3.8 \cdot 10^{-2}$
Ferrocene + H	$1.00 \cdot 10^{13}$	51.5 kJ	(Hirasawa et al. 2004)	$3.4 \cdot 10^{4}$
Ferrocene + O	$2.00 \cdot 10^{13}$	8.4 kJ	(Hirasawa et al. 2004)	$1.8 \cdot 10^{6}$

The dashed line marks the transition from the reaction kinetics to the diffusion controlled reaction regime

A first indication for the efficient decomposition of the precursor inside the pore system, can be derived from the linear correlation of the applied precursor/sample mass-ratio with the deposited metal (oxide) load. The relation is shown in Fig. 38 for the iron-infiltrated activated carbon samples. At a precursor/sample mass-ratio below 0.2 the infiltration load is less than 7 wt.-%. With higher ratios the mass gain increases proportionally. Hence, the quantity of introduced metal species can be well controlled by the quantity of evaporated precursor, without achieving saturation up to 20 wt.-% mass gain.

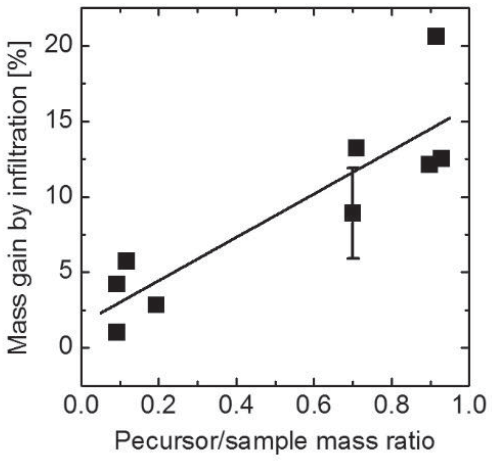

Fig. 38. Mass gain of activated carbon samples during iron-infiltration in relation to the ratio of precursor mass per initial sample mass; mass of the activated carbon was measured in the as-delivered state and after precursor decomposition

4.3. Microscopic investigation of selected samples

Further insight into the infiltration results can be gained from the microscopic inspection of the cross sections of the samples. The dispersion of infiltrated metallic elements inside the synthesized catalyst samples is investigated by SEM, TEM and EDX. EDX of a cross section of Fe-AC-CVI (Fig. 39) shows the homogeneous dispersion of iron across the entire sample. SEM investigation (Fig. 40) reveals some larger particles in the carbon matrix. These particles are probably iron or iron oxide species as they appear brighter than the surrounding matrix due to their higher atomic mass.

For a more detailed analysis, three 100 nm thin lamellae are extracted from the cross section of a spherical particle of Fe-AC-CVI using a focused ion beam (see section 3.2.2). The lamellae are extracted as depicted in Fig. 41: One from the border region (position A), one from half radius (position B) and one from the center of the sample (position C). This procedure allows the investigation of differences in the deposition in relation to the distance from the pore mouths.

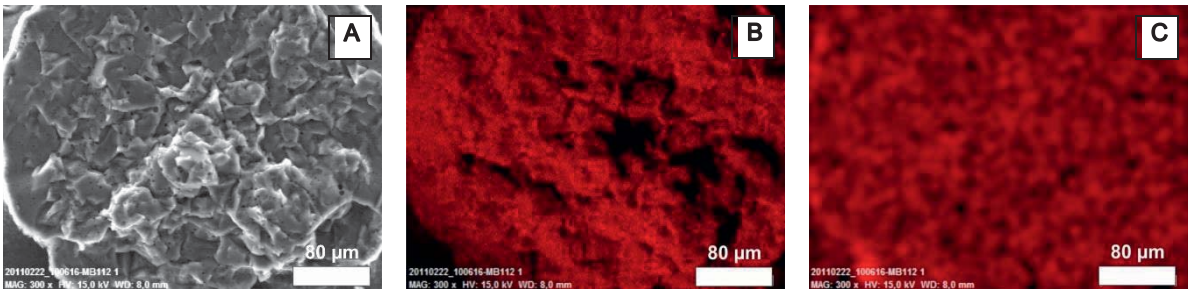

Fig. 39. SEM micrograph of the cross section of Fe-AC-CVI (A) and EDX maps of the same spot show carbon (B) and iron (C); 15 kV acceleration voltage, 8 mm working distance

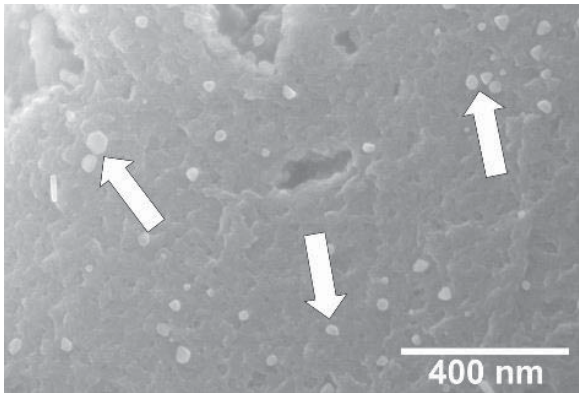

Fig. 40. SEM micrograph of Fe-AC-CVI in cross section with large iron/iron oxide species (arrows) embedded in carbon matrix

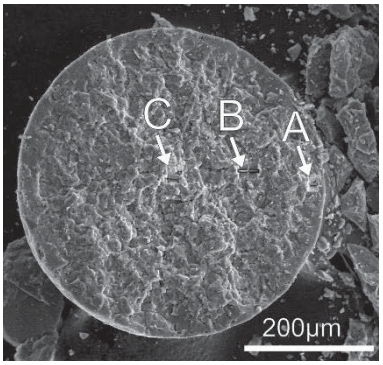

Fig. 41. SEM micrograph showing the cross section of ball-shaped Fe-AC-CVI sample; A (close to the surface), B (intermediate depth) and C (center) denote FIB extraction sites of carbon lamellae

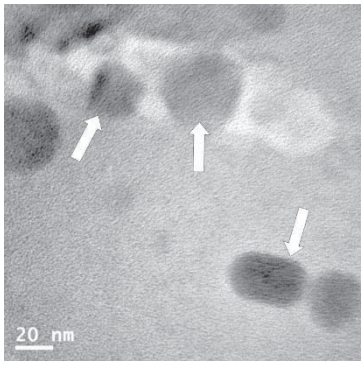

Fig. 42. TEM micrograph showing iron/iron oxide species (arrows) at position A (close to the surface) of Fe-AC-CVI

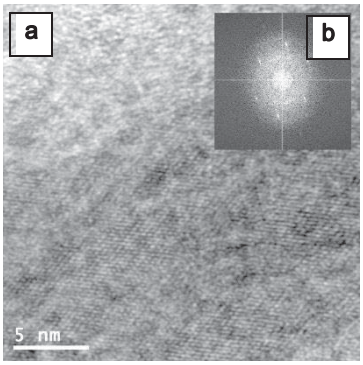

Fig. 43. HRTEM micrograph (a) of one of the larger iron/iron oxide particles in Fig. 42 at the border (position A) of Fe-AC-CVI and FFT of the HRTEM micrograph (b) showing maghemite or magnetite

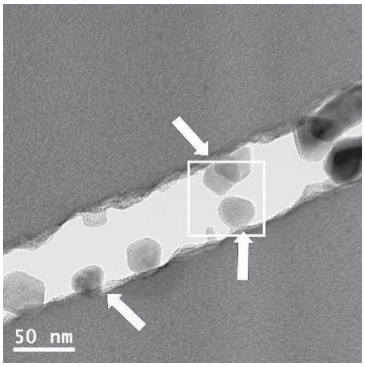

Fig. 44. TEM micrograph showing large iron/iron oxide particles (arrows) inside a macropore at half radius (position B) of Fe-AC-CVI; Fig. 45 displays an enlargement of the white frame

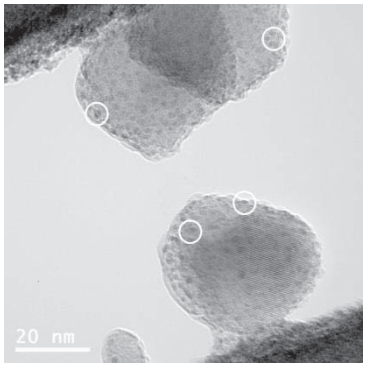

Fig. 45. TEM micrograph showing small particles (white circles) on the surface of large iron/iron oxide particles at half radius (position B) of Fe-AC-CVI; enlarged excerpt of Fig. 44

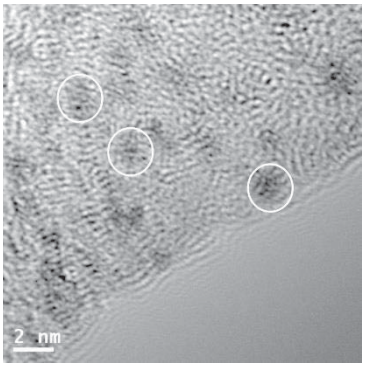

Fig. 46. HRTEM micrograph showing particles of about 2 nm diameter (examples in white circles) in the carbon matrix at half radius (position B) of Fe-AC-CVI

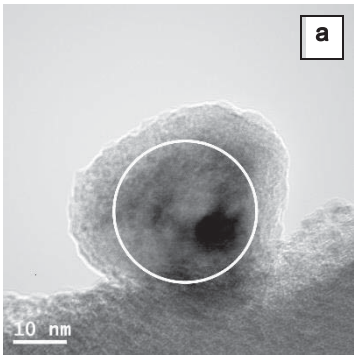

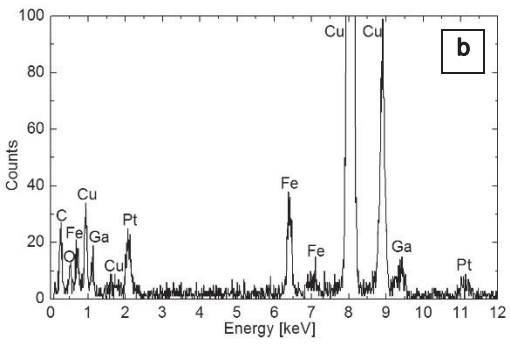

Fig. 47. a: TEM micrograph showing one particle at half radius distance from the macro particle surface (position B) of Fe-AC-CVI; b: EDX spectrum of the spot (white circle) of the displayed particle

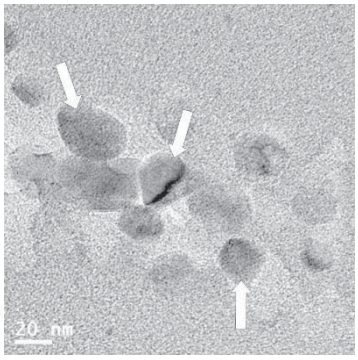

Fig. 48. TEM micrograph showing iron/iron oxide species (arrows) in carbon matrix in the center (position C) of Fe-AC-CVI

At all three positions A, B and C (Fig. 42, Fig. 44 and Fig. 48), particles of 30 to 50 nm in diameter and smaller particles of around 2 nm are found. The particles are mainly formed in macropores or along larger cracks, whereas the small particles seem to be embedded in the matrix. In the center of the sample the concentration of particles seems slightly smaller than at half radius or in the border region.

The large particles at half radius of the sample (Fig. 44) are decorated by small particles on their surface (Fig. 45). A closer look with HRTEM on the small particles (Fig. 46) reveals an estimated particle size of about 2 nm or below. Elemental analysis by EDX of one of the particles (Fig. 47) reveals a large quantity of iron and a low quantity of oxygen, but also copper from the applied copper grid as well as platinum and gallium from the preparation routine. The HRTEM investigation of a larger particle at the border of the sample and subsequent FFT reveal the face-centered cubic lattice of maghemite or magnetite (Fig. 43b). The observed contrast of the particles suggests that at least the larger particles obtain a metallic core and an oxidized shell.

In summary, the infiltration procedure seems suitable for a deep and homogeneous infiltration of iron into the activated carbon samples. In comparison to samples received by IWM (see section 3.1.4), CVI samples exhibit the additional formation of larger particles in macropores, independent of the distance from the pore mouths.

4.4. Structural characterization

Despite of the homogenous infiltration, the preparation procedure can have a detrimental effect on the pores in the activated carbons. With the infiltration of larger metal loads, the pore volume of the samples decreases (Fig. 49), The relation seems to be linear.

At small infiltration levels the pore volume is reduced more by the $Fe(acac)_3$ precursor than by Ferrocene. One reason may be the larger stability of Ferrocene at the chosen evaporation temperature of 403 K compared with the evaporation temperature of 443 K for $Fe(acac)_3$ (see section 3.1.2). The decomposition of $Fe(acac)_3$ starts right at 455 K. Hence, $Fe(acac)_3$ is more likely to decompose at the pore mouths and may close some of them before diffusing deeply into the pore system.

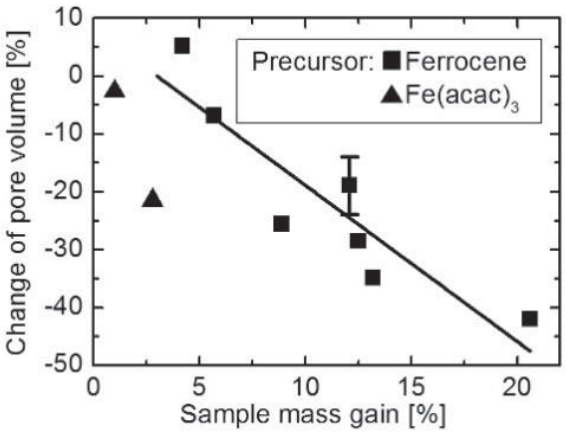

Fig. 49. Change of the specific pore volume of activated carbons in relation to sample mass gain during iron-infiltration; the linear fit curve includes only samples with precursor Ferrocene

Another reason might be a better diffusion and deposition of $Fe(acac)_3$ or of its fragment $Fe(acac)_2$ into the micropores and subsequent micropore filling. The relatively large Ferrocene molecule may be rather shielded from the intrusion into very small micropores due to steric hindrance as will be discussed in more detail in section 5.4 for the infiltration of zeolites. In any of the two cases the micropore volume is more reduced by $Fe(acac)_3$ than by Ferrocene.

The pore size distribution in the micro- and mesopore region is well preserved during the infiltration of copper or manganese (Fig. 50 A). Infiltration of a small iron load results in a clogging of some small micropores (Fig. 50 B). At higher infiltration levels (13 wt.-% sample mass increase) pores in the large micropore region (1-3 nm pore diameter) seem to be substantially clogged. Such a pore clogging effect during the infiltration is also observed by other authors (Illán-Gómez et al. 1999; Seredych et al. 2010).

The thermal treatment of carbons can remove edge atoms and surface imperfections, thus decreasing the surface area and the number of reactive sites (Aarna & Suuberg 1997). On the other hand, the thermal and chemical treatment of the infiltration procedure can enlarge ultramicropores and makes them accessible for the low temperature nitrogen adsorption (Kakei et al. 1990). The actually observed pore volume change is probably a net result of these opposing effects.

Considering the reduced pore volume in the micropore region of Fe-AC-CVI in Fig. 50 B, Ferrocene obviously adsorbs in micropores and forms larger particles there (see Fig. 48), thus blocking the pores or at least hampering the nitrogen intrusion at low temperature. The preference for such a particle formation seems to be less for $Mn(acac)_3$ and $Cu(acac)_2$. At higher infiltration loads (Fe-AC-CVI-13%) Ferrocene additionally blocks the large micropores. Other authors report this effect also for silver-infiltrated activated carbon samples (Seredych et al. 2010): a large infiltrated silver-load results in the clogging especially of small mesopores. Hence, a moderate infiltration seems to be preferential if the pore system should be kept well accessible.

XRD diffraction reveals that at least some of the particles in the iron-infiltrated samples are crystalline. Fig. 51 shows the diffractogram of samples with two different infiltration loads. The highly iron-loaded Fe-AC-CVI-13% exhibits metallic iron crystallites derived from the 44.8° 2ϑ single Bragg reflection, which is superposed by a broad reflection from the carbon, and magnetite/maghemite crystallites derived from the reflection peaks at 30.2°, 35.5°, 57.2° and 62.9° 2ϑ. The moderately infiltrated Fe-AC-CVI accommodates some metallic iron as well as magnetite/maghemite crystallites, but with larger infiltration load these crystallites become more pronounced.

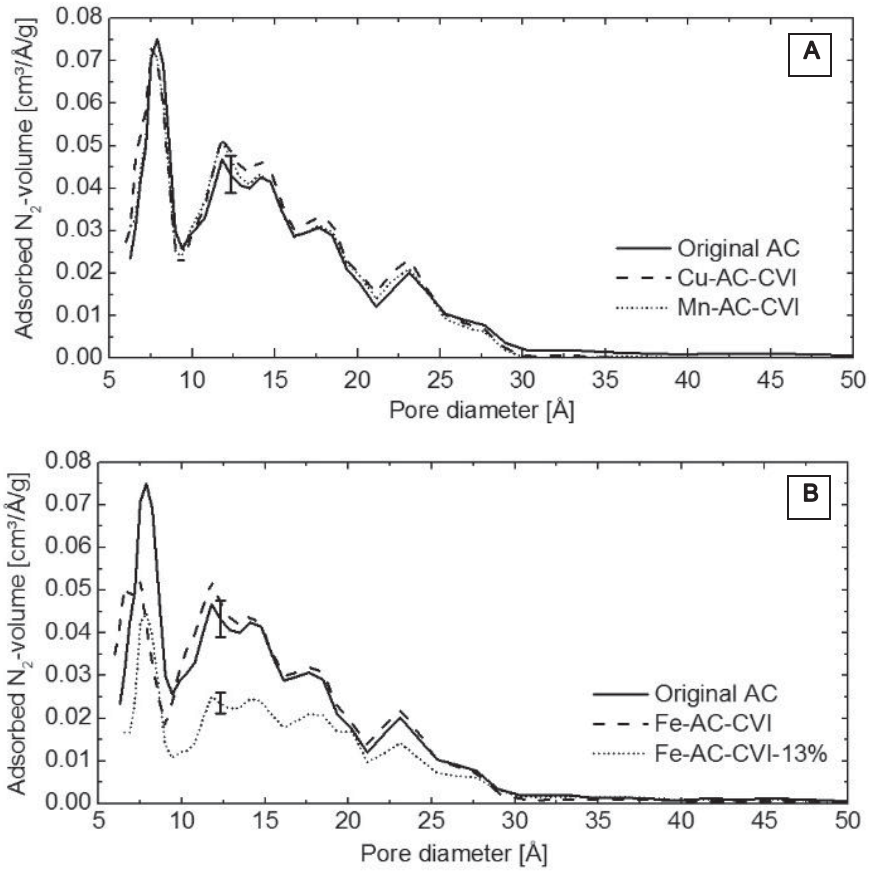

Fig. 50. Pore size distribution of copper- and manganese-infiltrated activated carbon (A) and iron-infiltrated activated carbon samples (B)

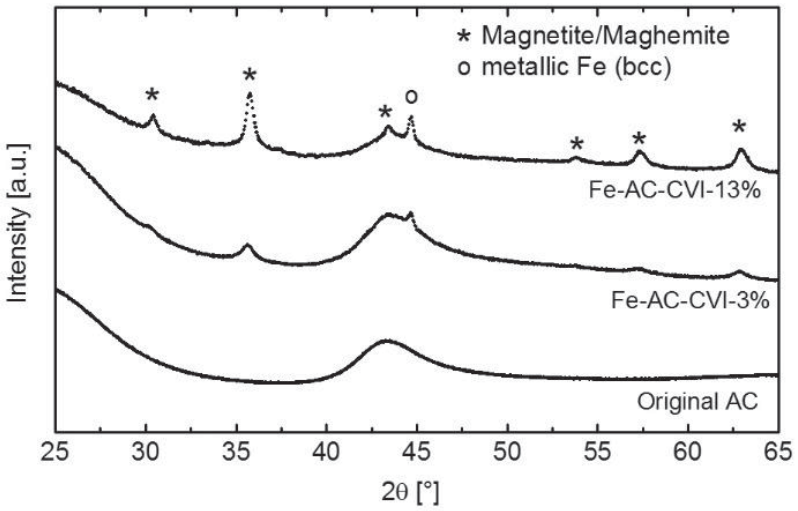

Fig. 51. X-ray diffractograms of iron-infiltrated activated carbon samples

The average size of the metallic iron crystallites in Fe-AC-CVI – estimated by means of the Scherrer equation – is about 20 nm. In the highly loaded Fe-AC-CVI-13% sample these crystallites are larger with about 26 nm. The average magnetite/maghemite crystallite size – derived from the 35.5° 2ϑ reflections – is about 11 nm in Fe-AC-CVI, whereas in Fe-AC-CVI-13% these crystallites are larger with 17-19 nm. The estimated crystallite sizes are hence in good accordance with the observations in the HRTEM investigation (see section 4.3). Obviously, the iron crystallites grow with higher infiltration load, and perhaps they exhibit a larger crystalline iron oxide shell.

Further information about the deposited iron phases can be gained from the investigation of temperature-dependent phase changes. Fig. 52 shows the sample mass change and the differential thermal analysis of Fe-AC-CVI (B) in comparison to the original activated carbon (A) during heating in air to 830 K.

Carbon gasification starts at 650 K for the non-infiltrated sample, whereas for Fe-AC-CVI the gasification is catalyzed by the deposited iron and starts already at about 500 K. In the DTA signal of Fe-AC-CVI two exothermic reactions at 550 K and 650 K are detected. The first signal may originate from a change of the deposited iron oxide phase. Although the actual phases of iron oxides are not determined directly, it may be speculated that the formed metal iron particles are oxidized in the presence of water vapor (Holleman & Wiberg 2007, p. 1652), stemming from the precursor decomposition, and form magnetite particles. The further oxidation may reveal metastable γ-Fe_2O_3 (maghemite) and at about 573 K this phase changes into the stable α-Fe_2O_3 (Holleman & Wiberg 2007, p. 1653):

$$\gamma\text{-}Fe_2O_3 \xrightarrow{573\ K} \alpha\text{-}Fe_2O_3 \qquad \textbf{(22)}$$

The DTA signal at about 550 K can probably be related to this phase change. The second signal at about 650 K may be attributed to the exothermic, catalyzed carbon gasification.

Summarizing the results of the structural characterization, the infiltration of larger metal loads increasingly blocks the pores of the activated carbon. During the moderate infiltration of copper and manganese the pore size distribution is well preserved, whereas the infiltration of iron blocks especially the small micropores. As revealed from the XRD and DTA measurements, the deposited species in the iron-infiltrated activated carbon could be a mixture of crystalline metallic iron, magnetite and maghemite. Preliminary investigations with TEM suggest that at least some of the larger iron particles bear an iron oxide shell.

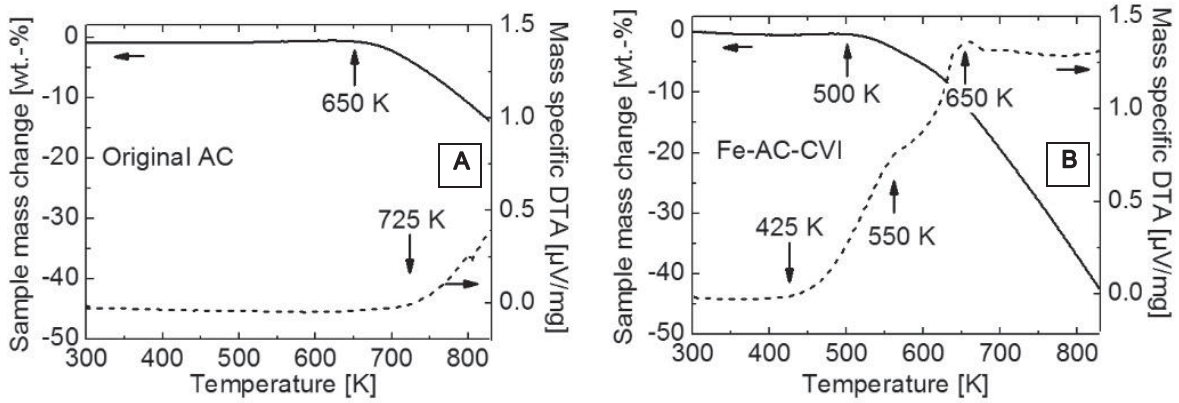

Fig. 52. Mass loss and DTA signal of original AC (A) and Fe-AC-CVI (B) with 3 wt.-% Fe_xO_y after precursor decomposition during heating from 300 to 830 K in air; heating rate: 10 K/min

4.5. NO_x adsorption properties

The observed modifications of the pore volume of the infiltrated activated carbons are likely to affect its adsorption properties of the material. Fig. 53 compares the time dependent NO_x-adsorption behavior of samples prepared by chemical vapor infiltration and by the incipient wetness method. The graphs show a mass change of the samples due to the adsorption of NO_2 (10 sccm gas flow of 0.3% NO_2 diluted in helium) at 303 K. In Fig. 54 the average hourly NO_2 adsorption rates of these samples are displayed for two time intervals: the first (triangles) averages the adsorption rate during the first ten hours of the experiment and the second (squares) averages the adsorption rate during the last four hours.

At the beginning of the experiment the non-infiltrated original AC, Fe-AC-CVI (with 3.2 wt.-% iron oxide load) and Fe-AC-IWM (about 5 wt.-% iron oxide load) exhibit identical adsorption rates of 1.6 wt.-% per hour. Only the heavily loaded Fe-AC-CVI-13% shows right from the beginning a significantly lower adsorption rate of 0.6 wt.-% per hour. After about 12 hours experimental time the adsorption rates decrease for all samples. When the original AC is almost saturated, the adsorption rate of Fe-AC-IWM decreases to 0.3 wt.-% per hour. For Fe-AC-CVI the adsorption rate is decreased, but at this stage it is the largest of all samples with 0.6 wt.-% per hour.

In Fig. 55 the NO_2 adsorption of the samples after the full experimental time of 24 hours is related to their micropore volume. The reduced micropore volume of Fe-AC-CVI-13% is probably responsible for the limited NO_2 uptake in comparison with the other samples (Illán-Gómez et al. 1998; Bashkova & Bandosz 2009a).

For the samples with moderate infiltration levels, i.e. all samples except Fe-AC-CVI-13%, the NO_2 uptake within 24 hours seems not to be exclusively related to the micropore volume. Rather the effective pore width mode plays the major role for the NO_2 uptake (Rubel et al. 1995a; 1995b) as well as for the NO conversion (Zhang et al. 2008b; Gao et al. 2011).

The CVI-infiltrated Fe-AC-CVI with a moderate load exhibits the largest adsorption rates and the maximum sample mass increase of 25 wt.-% at the end of the experiment. This is an astonishing result, since in investigations of other authors similar activated carbons are quickly saturated and the adsorption capacity for NO_2 is stated to be 10-15 wt.-% at maximum (Rubel et al. 1995b).

The rate change during the adsorption points to a probable change in the adsorption mechanism. At the beginning, micropores are the dominant adsorption sites and are filled with NO_2 (Rubel et al. 1995a; 1995b; Neathery et al. 1997). As soon as most of the preferred adsorption sites in the micropores are saturated, an adsorption mechanism involving the iron or iron oxide species might become rate controlling and Fe_2O_3-NO_x complexes are formed (Bashkova & Bandosz 2011). Due to the absence of such iron oxides in the non-infiltrated sample, this sample exhibits no change in the adsorption rate.

Subsequent to the NO_2 adsorption experiment, the moderately infiltrated samples are heated (3 K/min) in the same gas flow (0.3% NO_2 diluted in helium, to keep the gas composition constant) from originally 303 K to 660 K. Fig. 56 A, shows the mass change of the samples and Fig. 56 B, provides the corresponding DTA signals.

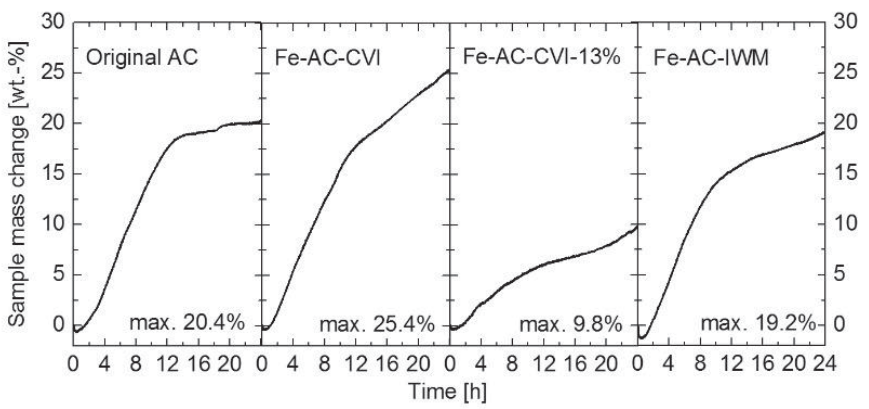

Fig. 53. Mass increase of activated carbon samples due to NO_2 adsorption at 303 K for 24 hours; gas mixture: 0.3% NO_2 in helium

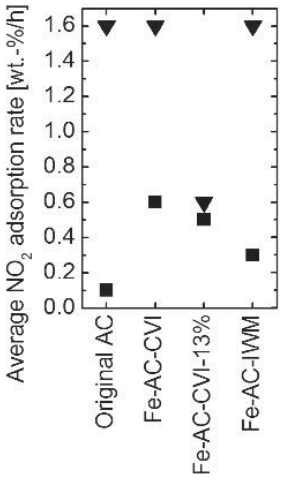

Fig. 54. Average adsorption rates of NO_2 in the first 10 hours (triangles) and in the last 4 hours (squares) of 24 hours

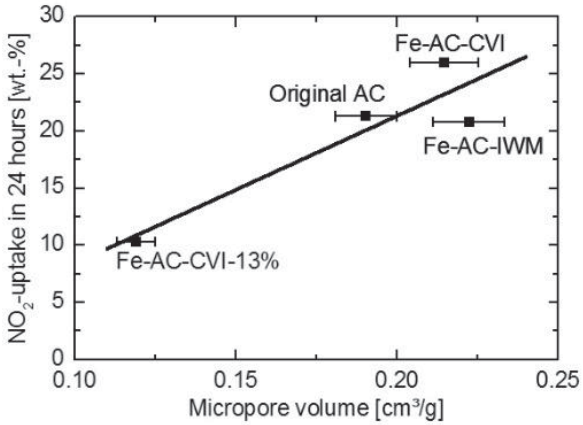

Fig. 55. Relation of micropore volume and NO_2 uptake of activated carbon samples; The linear curve marks not a correlation, but visualizes the best linear fit

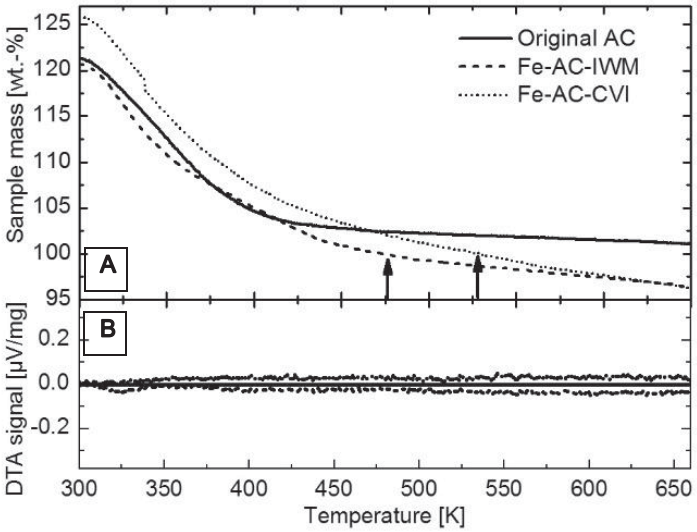

Fig. 56. A: Mass change of NO_2-preloaded activated carbon samples during heating from 303 to 660 K in 0.3% NO_2/He atmosphere; arrows mark the original mass level (100 wt.-%) before NO_2 uptake (Fe-AC-IWM: 473 K, Fe-AC-CVI: 528 K); B: Corresponding mass specific DTA signals

All of the investigated samples loose even more mass than they had loaded during the NO_2 adsorption. For Fe-AC-CVI the original mass is retrieved at 520 K and for Fe-AC-IMW at even 440 K. For the original AC the original mass is retrieved at 640 K, but already above 450 K there is hardly any further mass loss. No phase change or reaction is observed in the DTA signal.

The mass loss is also split in two phases. At the beginning of the heating the mass loss rate is large and similar for all three samples. At higher temperature (400 K) the mass loss rate decreases for all samples. The slope is steepest for the gas phase infiltrated Fe-AC-CVI.

The first part of the mass loss curve is probably dominated by the desorption of loosely bound nitrogen oxides up to 400 K (Gao et al. 2011). The second stage of the mass loss at temperatures above 400 K is rather associated with the gasification of oxidized carbon material. Since the NO_2 adsorption is accompanied by an oxidation of the carbon surface (Zhang et al. 2008a), the better availability of oxidized carbon leads to a larger gasification rate. Hence, Fe-AC-CVI, as the sample with the largest NO_2 adsorption, exhibits the largest mass loss due to carbon gasification. Additionally, the gasification reaction is probably catalyzed by the deposited iron species.

As a rough estimation, the number density of carbon atoms ($3.84 \cdot 10^{19}$ m^{-2}) in a perfect basal plane of graphite (Thonstad et al. 1973) is assumed to account for the number of NO_2 adsorption sites in the activated carbon (1700 m^2/g BET surface area). In this case the full coverage of the carbon surface with a monolayer of nitrogen dioxide (M = 46 $g \cdot mol^{-1}$) would equal a mass increase of almost 500 wt.-%. The observed mass loss of 5 wt.-% of carbon (M = 12 $g \cdot mol^{-1}$) would equal the gasification of about 1.5% of a carbon monolayer in the activated carbon. Hence, the observed values of mass increase and mass loss are very reasonable for the suggested mechanisms.

In summary, the NO_2 adsorption capacity is increased for the moderately iron-infiltrated substrates. A large iron infiltration load reduces the available pore volume and hence decreases the adsorption capacity. The adsorption occurs in a two stage process: At first, probably the micropores are pore size-selectively filled and subsequently iron oxide sites might be involved in the formation of nitrite or nitrate complexes. The desorption of NO_x species upon heating is probably followed by the gasification of oxidized carbon at higher temperature. The Fe-AC-CVI sample with moderate iron load exhibits both the largest NO_x adsorption and desorption rates.

4.6. Effect of the temperature on NO_x conversion

The intended application of the catalysts prepared in this work is the removal and conversion of nitrogen oxides close to ambient pressure and temperature. However, catalytic reactions typically exhibit an optimum temperature range for a maximum conversion rate (Thomas et al. 1997, p. 99ff and p. 120ff; Ertl 2010, p. 51ff), while considerable amounts of the carbon may be consumed in the oxidizing conditions of NO_x decomposition. Taking these parameters into account, the optimum temperature for the catalytic conversion experiments in this work needs to be derived experimentally.

All the performed catalytic conversion experiments follow the same procedure: 0.2 g of an activated carbon catalysts are fixed between two glass wool plugs inside of a glass tube (see

section 3.3.2). Since the reaction kinetics is expected to be slow at low temperature, a standardized test gas mixture of 0.9% NO_2, 10% argon and 89.1% helium circulates through the sample for 120 minutes experimental time. The sample can be heated up to 573 K and the composition of the circulating test gas mixture is continuously monitored by a connected mass spectrometer.

Iron-infiltrated activated carbon (Fe-AC-CVI) is investigated at temperatures between 373 and 573 K. For each of the five experiments at different temperatures a fresh sample is used, respectively. Fig. 57 shows for each of the isothermal experiments the gas species concentrations of NO, NO_2, N_2O, CO, CO_2 and N_2 after 120 minutes experimental time. Molecular oxygen is also monitored, but it is not detected in the gas mixture.

At low temperatures NO_2 is completely adsorbed. Above 523 K a small amount of less than 0.1% NO_2 is detected. The NO concentration is relatively large at low temperatures with a maximum between 423 and 473 K. Above 473 K the concentration is decreasing and at 573 K NO is completely decomposed, which is in good accordance with other studies (Illán-Gómez et al. 1995; Illán-Gómez et al. 1996).

CO and N_2O are released simultaneously with increasing temperature. At 573 K the release of CO and N_2O stops completely. Instead, CO_2 starts to be notable at 523 K and becomes the dominant species at 573 K together with desorbing N_2.

The elemental mass balances at the end of the experiments (Fig. 58) show the increasing carbon gasification at temperatures larger than 473 K. Interestingly enough, adsorbed nitrogen species are retained at high temperature (573 K), probably due to the reduction of iron oxides with NO_x into iron nitrites or nitrates by carbon oxidation (Busca & Lorenzelli 1981; Bashkova & Bandosz 2009a) as will be discussed in the next section.

At low temperature nitrogen oxides chemisorb dissociatively and probably oxidize the metal catalyst (Illán-Gómez et al. 1995). The oxygen needs to be transferred from the metal catalyst sites to the activated carbon support and desorb from the surface. Otherwise the catalyst deactivates when the metal and the carbon surfaces become completely oxidized. Hence, the temperature-controlled desorption of CO is probably rate limiting for the overall process at low temperature.

The slight spread between the concentrations of CO and N_2O at 573 K may be caused – if it is assumed to be significant – by the direct formation of CO_2 (Jeguirim et al. 2004) or by the oxidation of some of the released CO with surface oxygen to CO_2 (Chan et al. 1983; Furusawa et al. 1985). The possible mechanisms for the formation of CO_2 are provided in detail in appendix 9.1. At elevated temperatures, N_2O may be formed as an intermediate and it is decomposed in the oxidation of CO to CO_2 with parallel release of N_2 (Stegenga et al. 1993; Moulijn & Kapteijn 1995).

Concluding the results, an almost complete NO_x conversion is only observed at 573 K, but it is accompanied by severe carbon gasification and probably the formation of surface nitrites/nitrates. The complete NO_2 removal and its considerably efficient conversion into N_2O and CO are observed at 423 K. At this temperature only a small fraction of carbon is gasified. Hence, a temperature of about 423 K – in particular 425 K, as measured at the wall of the sample holding tube – is chosen in all standard catalytic conversion experiments in this work. This temperature

is commonly achievable in human environment, for example in automobiles from the engine waste heat.

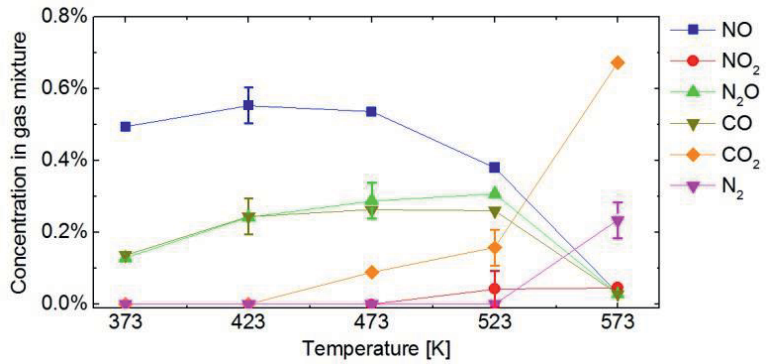

Fig. 57. Composition of the gas mixture for F-AC-CVI after 120 minutes NO_2 conversion in recycle flow at different temperatures; initial gas mixture: 0.9% NO_2, 10% Ar, 89.1% He

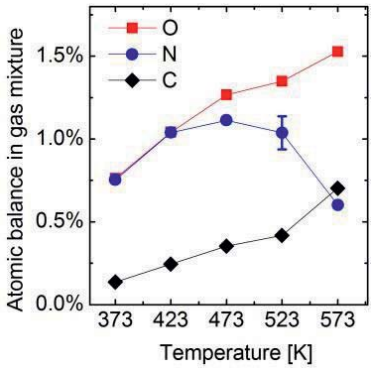

Fig. 58. Elemental composition in the gas mixture derived from experiments in Fig. 57 of Fe-AC-CVI

4.7. NO_x conversion properties

The actual catalytic performance of the synthesized samples is investigated in a recycling flow of the test gas mixture (0.9% NO_2, 10% argon, 89.1% helium) at normal pressure (1000 mbar) and at 425 K, as derived from the experiments in the previous section. This experimental setup is referred to as the standard catalysis experiment in the following.

The applied nitrogen dioxide concentration of 0.9% is considerably larger than what would be expected in human environments. However, a large fraction of the gas is adsorbing on the catalysts and an investigation of lower concentrations in preliminary experiments proved to be less informative. Fig. 59 provides an overview of the final gas mixture composition at the end of the 120 minutes experimental time for all investigated carbon samples and for the reference catalysts.

All carbon catalysts convert NO_2 almost completely. The major conversion products are NO and N_2O and a substantial amount of CO. A minor fraction of catalysts release a notable quantity of CO_2. Only the magnetite reference catalyst and – surprisingly – the empty setup with an idle sample holder including glass wool plugs, convert a small quantity of NO_x completely into O_2 and N_2. However, magnetite and the empty setup leave a large fraction of the supplied NO_2 unconverted and the final concentration of NO_2 is even significantly larger from the magnetite than in the empty setup. Apparently, some NO_2 is adsorbed or even decomposed at the reactor parts, while iron oxides catalyze the oxidation of some of the released NO back to NO_2 (Busca & Lorenzelli 1981).

Among all catalysts, the alumina-supported platinum catalyst adsorbs the largest amount of NO_x, although without releasing any reaction products, except of some NO. The copper-infiltrated activated carbon, prepared by the incipient wetness method (Cu-AC-IWM), removes the largest fraction of nitrogen oxides from the test gas atmosphere, but it rather seems to only adsorb these species, instead of decomposing them completely. In order to identify promising catalysts, a more detailed investigation of the decomposition of the intermediately formed and still toxic nitric oxide is performed.

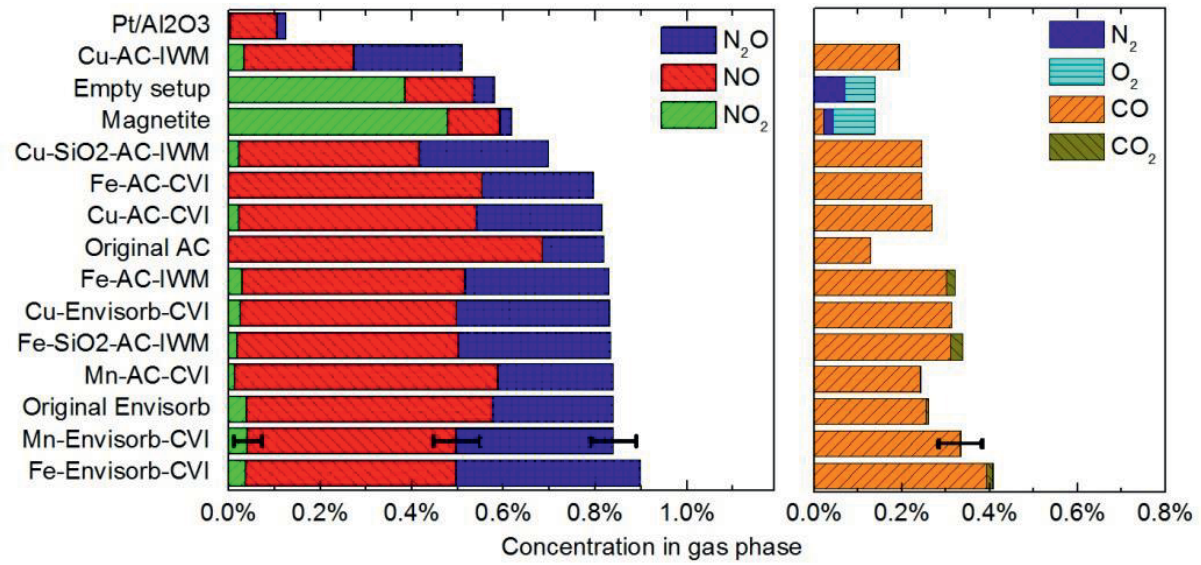

Fig. 59. Gas species concentrations using activated carbon catalysts and reference catalysts after 120 minutes NO_2 conversion in recycle flow at 425 K; initially 0.9% NO_2

4.7.1. Nitric oxide conversion

As derived from Fig. 59, all of the prepared catalysts remove the supplied NO_2 completely and convert a large fraction of it into NO. The maximum concentration of NO is typically achieved after 10 minutes experimental time. However, the catalysts perform very differently in the further decomposition of NO. Fig. 60 shows the absolute change of the NO concentration for each sample between the 10^{th} minute and the 120^{th} minute of the standard catalysis experiment.

The manganese- and copper-infiltrated activated carbons clearly exhibit the largest decomposition of NO. Iron-infiltrated samples show still a good conversion of NO, but all other samples do not outperform the non-infiltrated activated carbon. The platinum and magnetite reference catalysts initially release only small amounts of NO. Hence, their performance in the NO decomposition cannot be measured reliably. The Envisorb samples exhibit a considerable conversion of NO_2 and even some decomposition of NO, but their reaction kinetics is very slow.

In order to obtain a better understanding for the catalytic processes, four main parameters of the synthesized catalysts are studied in detail: The infiltrated metal, the preparation method, the pore volume and the effect of the co-deposition of silica inside the activated carbon. Subsequent to the comparison of each of these parameters by their impact on the catalytic activity, the performance of five interesting catalysts is studied time resolved and the possible mechanisms are discussed.

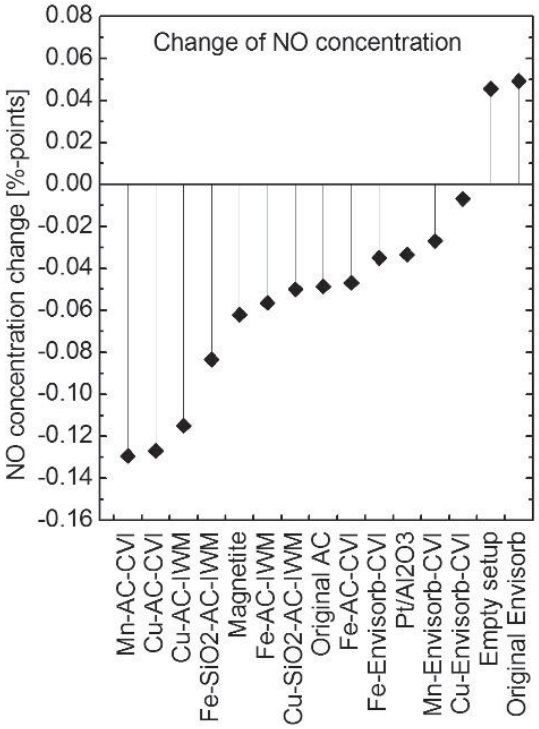

Fig. 60. Absolute change of the NO concentration between the first ten minutes and the end of the standard NO_2 catalysis experiment for 120 minutes at 425 K

4.7.2. Effect of the infiltrated metal

Iron, copper and manganese are infiltrated into the activated carbons and their effect on the catalytic activity is likely to vary (Illán-Gómez et al. 1995; Illán-Gómez et al. 1999). Fig. 61 provides an overview of the change of the NO, N_2O and CO concentrations during the 10th and the 120th minute of the catalysis experiment, sorted by the infiltrated metal of the catalysts.

All metal-infiltrated catalysts outperform the non-infiltrated activated carbon. The copper- and manganese-infiltrated carbons exhibit a superior performance in the decomposition of NO. The formation of N_2O and CO seems to be rather promoted by the infiltration of iron.

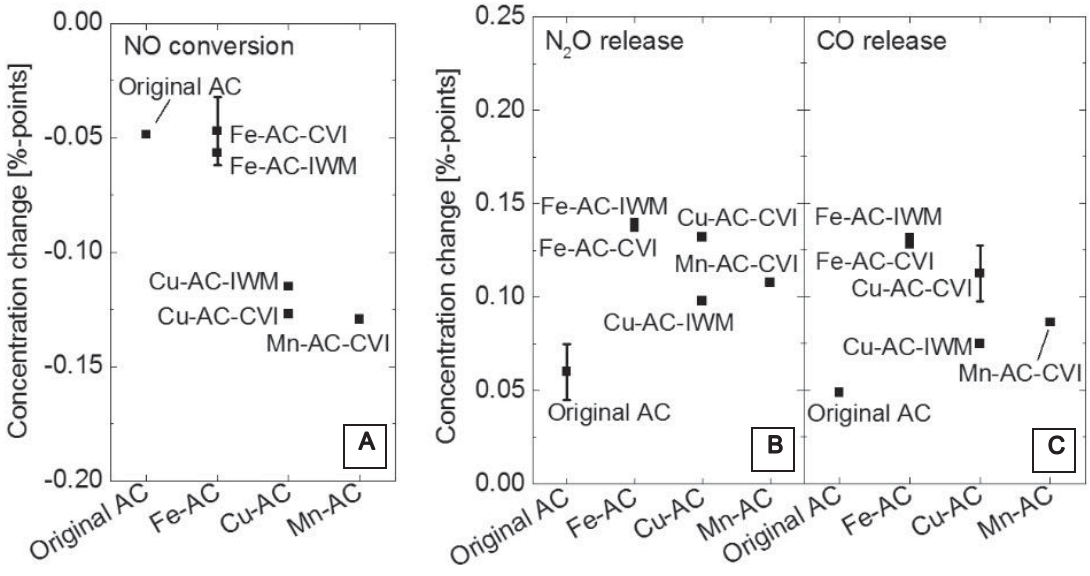

Fig. 61. Comparison of concentration change of NO (A), N_2O (B) and CO (C) in gas mixture between the 10th and 120th minute of catalysis experiment for Cu-, Fe- and Mn-infiltrated activated carbon catalysts

4.7.3. Effect of the preparation method

In Fig. 62 the samples are sorted by their infiltration method. The figure compares the change of concentration of the gas species NO, N_2O and CO during the catalysis experiment between the 10th minute and the 120th minute.

There is no obvious relation between the conversion reactions and the method of infiltration. The CVI-infiltrated copper-AC seems to be slightly more active in the release of CO and N_2O, whereas for iron-infiltrated samples the IWM-infiltrated catalyst releases more of these species than the CVI-infiltrated catalyst.

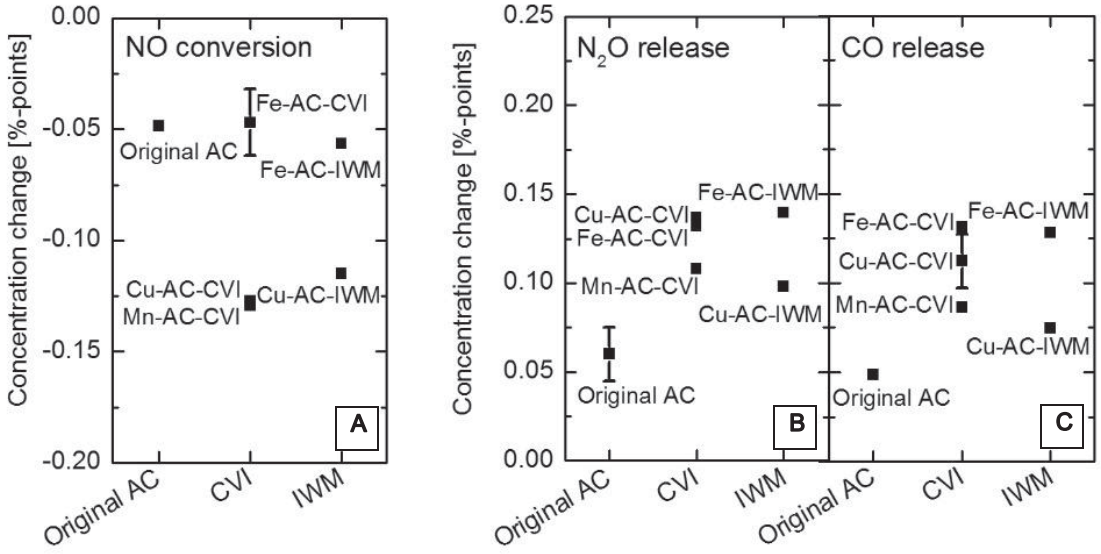

Fig. 62. Comparison of concentration change of NO (A), N_2O (B) and CO (C) in gas mixture between the 10th and 120th minute of catalysis experiment for activated carbon catalysts prepared CVI and IWM

4.7.4. Effect of co-doping with silica

Silica is known to be a good catalyst support due to its chemical and thermal stability. Many transition metal catalyst systems use silica support (Chorkendorff & Niemantsverdriet 2007, p. 191ff) and its deposition in activated carbons may mechanically and chemically stabilize the carbon particles (Curdts et al. 2013).

In Fig. 63 the concentration change of NO, N_2O and CO during the catalysis experiment between the 10th minute and the 120th minute is compared for silica-doped and un-doped IWM-infiltrated samples.

In comparison to the respective silica-free sample, the removal of NO is faster for the catalyst containing iron/silica, and slower for the catalyst containing copper/silica. A weakly positive effect of silica is observed for the release of N_2O and CO. Although any strong direct relation between the catalytic activity and the co-deposition of silica cannot be derived, the silica-doped Fe-SiO_2-AC-IWM releases the largest amount of N_2O and CO, while converting a large quantity of NO. Hence, this sample could be an interesting catalyst for the efficient conversion of NO into less harmful gases.

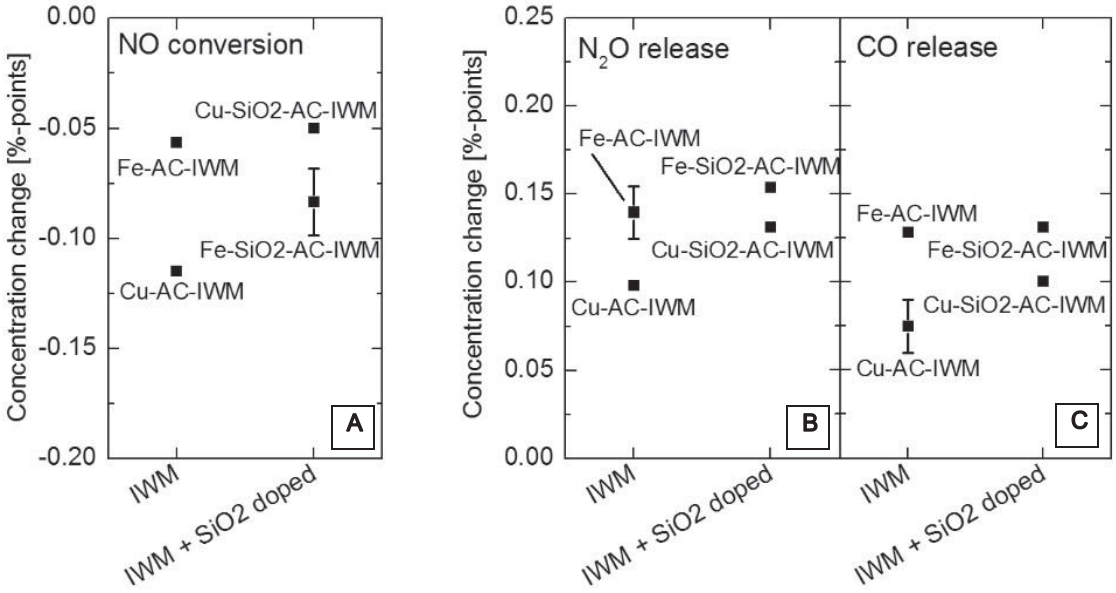

Fig. 63. Comparison of concentration change of NO (A), N_2O (B) and CO (C) in gas mixture between 10th and 120th minute of catalysis experiment for IWM-infiltrated activated carbons and SiO_2-doped catalysts

4.7.5. Effect of the pore volume

As stated before in section 2.3.1, the micropore diameter (or pore size distribution) can influence the NO_2 adsorption as well as the NO_x decomposition. The effect of micropores is probably related to the interactions of overlapping potentials inside of the pores (Kaneko 1987). The pore size distributions of the activated carbon catalysts applied in this work are very similar, since the original matrix materials are identical. However, the pore system could become partially blocked or damaged during the infiltration procedure.

Fig. 64 relates the α_s-micropore volume of the applied catalysts to the concentration of the monitored gas species at the end of the catalysis experimental time. The micropore volumes are between 0.21 and 0.23 cm³/g and hence the span is very small among the compared samples.

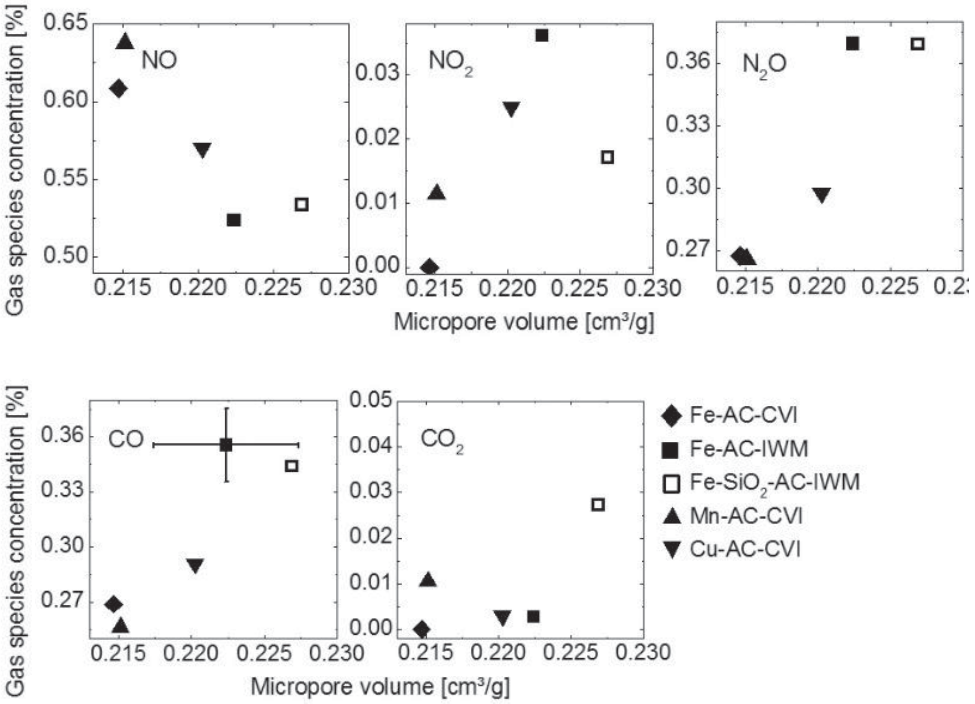

Fig. 64. Concentration of NO, NO_2, N_2O, CO and CO_2 in the test gas mixture after 120 minutes NO_2 conversion in recycle flow at 425 K, in relation to the pore volume of the samples

NO conversion, CO and N_2O desorption are correlated to the micropore volume with Pearson correlation coefficients of -0.9, 0.9 and 0.9, respectively. The NO_2 concentration at the end of the experiment is very low for all samples and actually below the accuracy limit of the measurement. The observed CO_2 concentrations are very low, too.

4.7.6. Time-resolved NO_x catalysis experiments

So far, the catalytic activity seems to be mainly influenced by the kind of the infiltrated metal and by the effective micropore volume. In the following, the CVI-prepared catalysts with different metal infiltration and the catalyst with the largest micropore volume (Fe-SiO_2-AC-IWM) are compared to each other with detailed time-resolution.

Fig. 65 A-D presents the development of the gas mixture composition during the standard catalysis experiments with iron-, copper- and manganese-CVI-infiltrated activated carbons. The left part of the graphs provides a closer insight into the first 90 seconds of the catalysis experiment and the right part of the graphs shows the development over the entire 120 minutes.

All samples quickly adsorb NO_2 and release NO during the first seconds. The release of NO is completely mirrored by the NO_2 concentration decrease, best observable for Fe-AC-CVI, where the kinetics is slower than for the other samples. The greatest NO concentration maximum (0.75%) is observed for the non-infiltrated original AC, whereas the lowest concentration maximum (0.6%) is observed for the iron-infiltrated carbons.

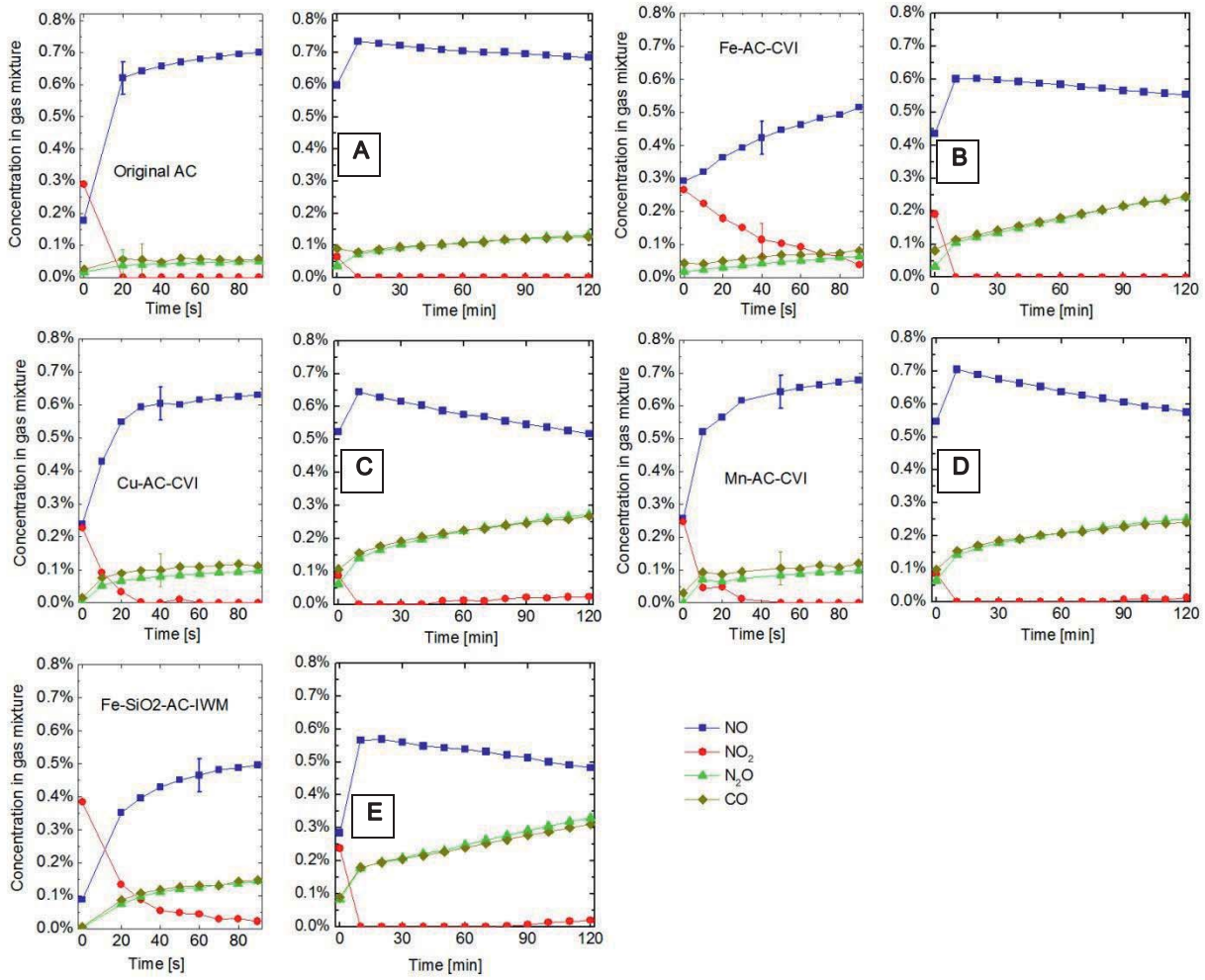

Fig. 65. Gas mixture composition of original AC (A), Fe-AC-CVI (B), Cu-AC-CVI (C), Mn-AC-CVI (D) and Fe-SiO2-AC-IWM (E) during 120 minutes NO_2 conversion in recycle flow at 425 K; initially: 0.9% NO_2

After the first ten minutes the decomposition rate of NO is nearly constant and increasing in the following order: original AC ≈ Fe-AC-CVI < Fe-SiO_2-AC-IWM < Cu-AC-CVI ≈ Mn-AC-CVI. Right from the beginning nearly equimolar amounts of N_2O and CO are released. While the NO concentration slowly decreases with progressing experimental time, N_2O and CO are released. The release of N_2O rises in the order: original AC < Mn-AC-CVI < Cu-AC-CVI ≈ Fe-AC-CVI < Fe-SiO_2-AC-IWM and the release of CO is observed to increase in the order: original AC < Mn-AC-CVI < Cu-AC-CVI < Fe-AC-CVI ≈ Fe-SiO_2-AC-IWM.

The amount of released CO_2 of Fe-SiO_2-AC-IWM is below the detection limit for the other CVI-infiltrated samples and within the expected measurement error (see Fig. 59). Hence, it is not displayed in the graphs.

Generally, the metal infiltrated samples are more active than the non-infiltrated activated carbon, as derived from the decomposition of NO and the release of N_2O and CO. While the non-infiltrated activated carbon and Mn-AC-CVI release the largest amount of NO, the further NO decomposition rate is greatest for Cu-AC-CVI and Mn-AC-CVI. The iron-infiltrated samples release the largest quantities of CO and N_2O.

4.7.7. Elemental balances

Fig. 66 shows the respective quantitative balance of elements for the experiments in Fig. 65. The onset of the graphs starts after the adsorption of NO_2 from the feed gas. The balances count all the released nitrogen from NO_2, NO, N_2O, N_2, oxygen from NO_2, NO, N_2O, O_2, CO, CO_2 and carbon from the release of CO and CO_2.

During the first seconds of the experiment NO_2 is adsorbed on the catalyst. The reaction products from the subsequent decomposition of NO_2 are released over the experimental time and hence the displayed elemental fractions are continuously increasing. About 50% of the initially adsorbed oxygen atoms remain adsorbed on the catalyst surface, while almost the entire nitrogen is released to the gas atmosphere. Without any adsorption the elemental balance would reflect the stoichiometric ratio of nitrogen and oxygen in the initial gas mixture of 1:2 and the initially supplied 1% NO_2 in the gas mixture would reveal an elemental composition of 1% N and 2% O in Fig. 66.

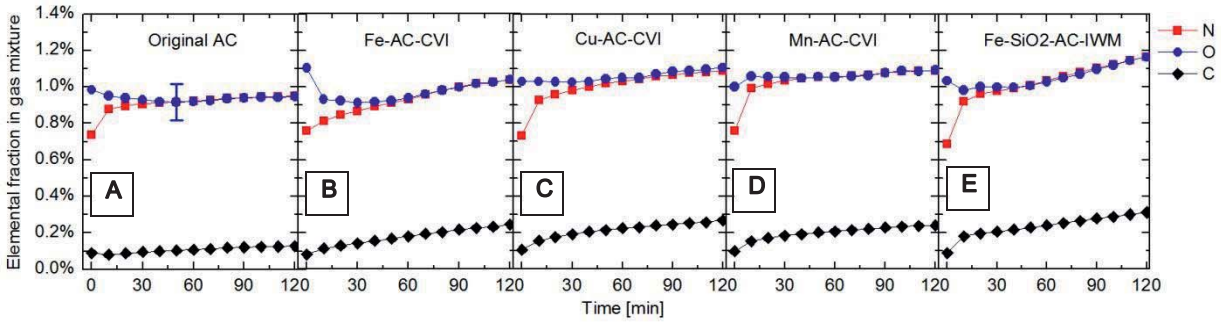

Fig. 66. Elemental composition in gas mixture derived from experiments in Fig. 65 of original AC (A), Fe-AC-CVI (B), Cu-AC-CVI (C), Mn-AC-CVI (D) and Fe-SiO2-AC-IWM (E)

4.7.8. Discussion

The initial concentration of NO_2 is quickly decreasing probably due to the previously discussed selective adsorption of NO_2 in micropores (Richter et al. 1990; Neathery et al. 1997; Bashkova & Bandosz 2009b) (see section 4.5). Upon reduction of NO_2 on the catalyst surface, the largest part of the resulting NO is released to the gas phase, while the carbon or metal catalyst surface is oxidized and residual NO_x species form surface complexes (Shirahama et al. 2002; Jeguirim et al. 2004; Zhang et al. 2008a). Equilibrium concentrations of physisorbed NO and NO_2 may co-exist on the surface of the activated carbons, but NO is more easily released to the gas atmosphere, since the NO_2 is more strongly adsorbed than NO (Richter et al. 1990).

Once the quickly formed NO is released to the gas phase, the produced NO concentration is slowly decreasing again in the course of the experiment, although metal-infiltrated activated carbon has been reported to be inactive in the NO reduction below 723 K (Illán-Gómez et al. 1996). NO is probably chemisorbed back to the carbon surface in form of C-NO complexes (Teng & Suuberg 1993a) and/or it is dissociated on the carbon or metal catalyst (Illán-Gómez et al. 1995). Additionally, some (adsorbed) NO_2 can be formed by the reaction of gaseous NO with carbon surface oxides (Richter et al. 1990).

The above described results (Fig. 59 and Fig. 65) indicate the preferred adsorption of nitrogen oxides in form of C-(NO_x) or C-$(NO)_x$ complexes rather than C-N, which would be a direct precursor for the formation of N_2 (Aarna & Suuberg 1997). The formation of stable nitrogen surface groups on activated carbons is generally very scarce and probably occurs only on very

high energy sites that are quickly saturated (Aarna & Suuberg 1997). Other surface-adsorbed nitrogen will at least partially desorb from the carbon surface (Okuhara & Tanaka 1986), but the release of molecular nitrogen to the gas phase is not observed in the conducted experiments.

The decomposition of NO and the simultaneous and equimolar release of N_2O and CO suggest a connected mechanism. The reduction of NO into N_2O is reported for example for metal oxides like iron oxide (Otto & Shelef 1970) or copper oxide (London & Bell 1973) catalysts, thus further oxidizing the catalyst surface (e.g. from Fe_3O_4 to Fe_2O_3). This reaction is obvious for the magnetite reference catalyst, whose color turns from deep black to red during the catalysis experiment.

In the activated carbon catalysts the oxidized surfaces of metal particles are reduced by the carbon matrix and release CO to the gas atmosphere (Holstein & Boudart 1983). This observation is more pronounced for the metal-infiltrated samples, but it is also observed for pure activated carbon, releasing N_2O for example from two neighboring C-NO complexes (Okuhara & Tanaka 1986).

The metal oxide reduction and carbon monoxide desorption reportedly follow the same order as the desorption of the most loosely bound oxygen from the metal oxide: $CuO \leq MnO_2 < Fe_2O_3$ (Holstein & Boudart 1983). This order is different from the order of CO or N_2O desorption observed in the current experiments: Mn-AC-CVI < Cu-AC-CVI ≤ Fe-AC-CVI. However, the nature of the introduced metal species, the amount of introduced metal and the actual micropore volume may additionally influence the catalytic activity.

The N_2O and CO release is fast at an early stage of the experiment, probably due to the abundant presence of C-(NO) and/or M-(NO) (M = any metal species) after the dissociative adsorption of NO_2. The desorption rate of N_2O and CO is slightly decreasing as soon as some of the reactive centers become inactive. Alternatively, some of the released species may re-adsorb and occupy the active sites at iron/iron oxide (Ponec & Bond 1995, p. 42).

The decomposition of NO would also be expected to slow down as soon as the amount of N_2O in the gas phase increases. N_2O may compete with the NO_2 and NO adsorption and block some of the reaction sites (Moulijn & Kapteijn 1995; Carabineiro et al. 2008), but this effect is not observed, probably due to the low gas concentrations of N_2O in the current experiments.

Chemisorbed oxygen atoms from the NO_x reduction reactions are probably more loosely adsorbed on silica or on metal oxides and they are more strongly chemisorbed on activated carbon (Marsh & Rodríguez-Reinoso 2006, p. 265f). Hence, the surface mobility and recombination of oxygen atoms to form carbon dioxide is facilitated on silica surfaces as observed in Fig. 59 for the Envisorb samples and for the silica-co-deposited activated carbon samples. In the absence of carbon, some of the abundant oxygen atoms on the catalyst surface can recombine and form molecular oxygen as observed for the magnetite reference catalyst and for zeolite catalysts as will be described in section 5.

The observed dependence of the catalytic activity of the micropore volume can be attributed to the large available surface area of the catalysts with a large micropore volume and possibly to catalytic effects, which may be explained by the interactions of overlapping potentials of opposing pore walls (Wang & Kaneko 1998). However, these effects might be sensitive to the

actual pore size distribution of the activated carbon, since other authors do not find any correlation between the micropore volume and the decomposition of NO (Illán-Gómez et al. 1993).

Summarizing the results, the infiltrated metal as well as the micropores influence the catalytic activity of the investigated activated carbon catalysts. NO_2 is probably adsorbed in the micropores and immediately reduced to NO. The infiltration of activated carbon with transition metals/metal oxides notably increases the subsequent conversion of NO into CO and N_2O. The copper- and manganese-infiltrated activated carbon catalysts show the highest activity in the removal of NO, whereas the iron-infiltrated samples release the largest amount of CO and N_2O. The micropores seem to have a significant effect on the conversion activity, possibly due the larger available surface area and their overlapping potentials. The effect is even observed for only 6 % change in the micropore volume. Doping of the carbon matrix with silica probably enhances the mobility and recombination of adsorbed oxygen atoms.

4.8. Structural changes during the catalysis process

During the investigated catalytic reactions the catalysts may undergo surface changes (aging), which can sustainably influence the catalytic processes (Boehm 1994; Thomas et al. 1997, p. 449f; Gurrath et al. 2000; Menendez & Fuertes 2001). XRD measurements show the change of the crystalline phases and low temperature nitrogen adsorption is applied in order to discover changes in the pore structure of the support.

Fig. 67 shows the X-ray diffractograms of moderately and highly iron-CVI-infiltrated activated carbons after the preparation (which is discussed for Fig. 51 in section 4.4) and after the catalysis experiment. The samples exhibit magnetite/maghemite and metallic iron crystallites. The magnetite/maghemite particles in the as-synthesized Fe-AC-CVI have an average size of 11 nm and the average size of the iron particles is about 20 nm. In the highly iron-loaded Fe-AC-CVI-13% the average magnetite/maghemite particle size is 17-19 nm and the metallic iron particle size is even about 26 nm. All species approximately preserve their average size during the catalysis experiment and hence the crystalline species seem not to be notably influenced by the conditions of the catalysis experiment.

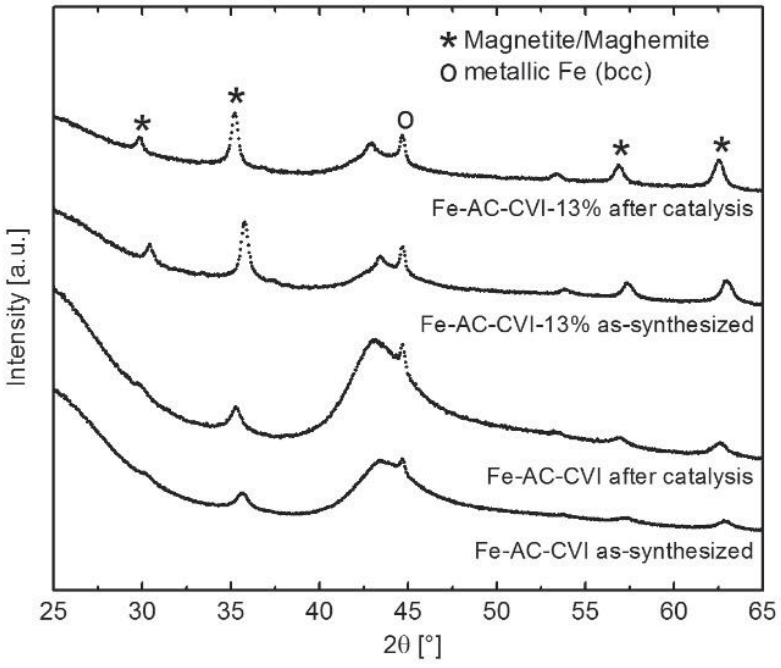

Fig. 67. X-ray diffractograms of iron infiltrated activated carbon samples before and after catalysis

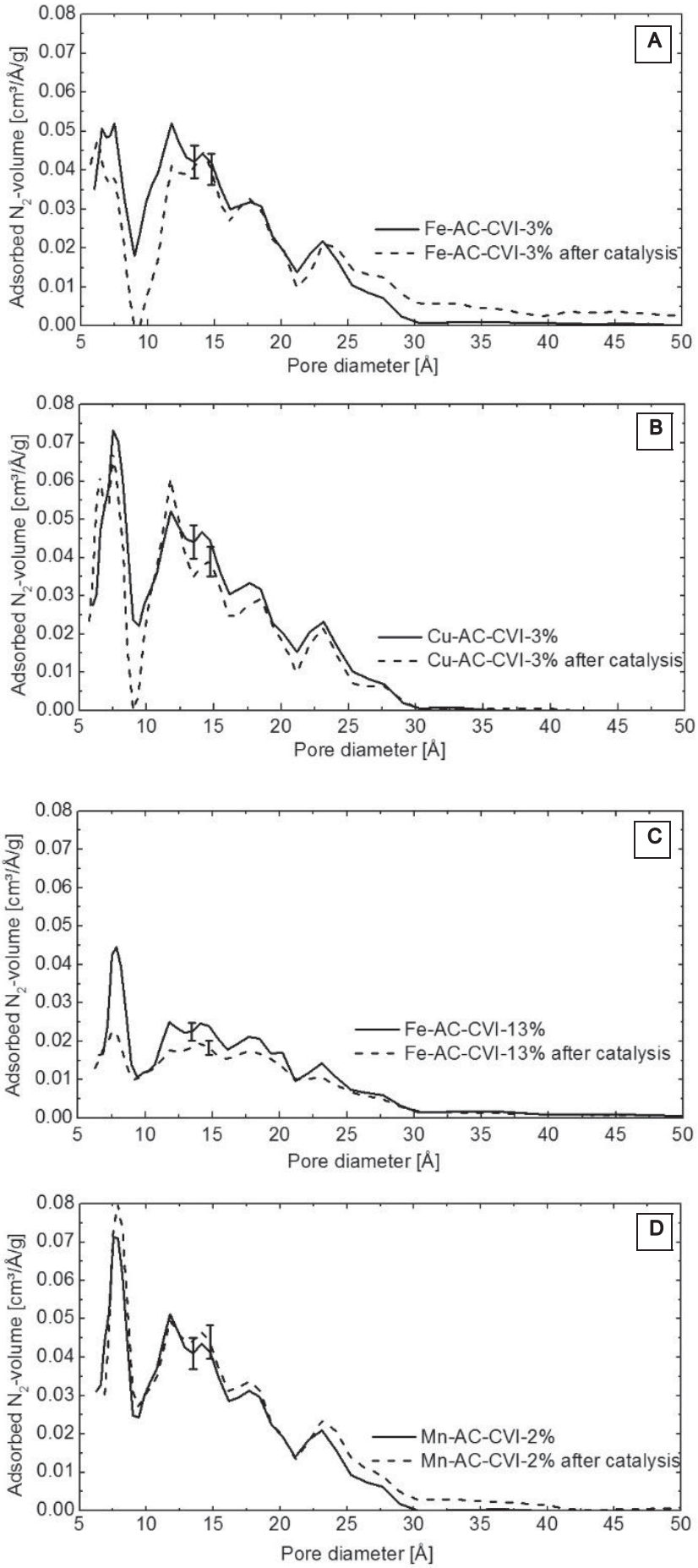

Fig. 68. Change of pore size distribution of CVI-infiltrated activated carbon samples during catalysis

However, the porosity of the samples is influenced by the catalysis experiment. Fig. 68 A-D, shows the change of the pore size distribution of iron-, copper- or manganese-CVI-infiltrated activated carbons before and after the catalysis experiments. The sample, which is moderately infiltrated with iron (A), exhibits a reduced micropore volume, but the very small micropores are not substantially affected. The mesopore volume is slightly increased.

The highly infiltrated Fe-AC-CVI-13% (C) exhibits a reduced pore volume at very small pore width and no significant loss in the mesopore region. The micropore volume of the as-synthesized sample is already substantially reduced, compared with its original state, especially in the large micropore region (see section 4.4, Fig. 50).

For Cu-AC-CVI (B) a pore volume loss in the medium micropore region is observed, whereas small micropores are not affected. The pore size distribution of Mn-AC-CVI (D) is not affected at all by the catalysis experiments.

In Fig. 69 the catalysis-induced change in the pore size distribution for silica-doped Fe-SiO_2-AC-IWM (B) is compared with the non-doped sample (A). A slight loss of pore volume in the medium micropore region is observed for Fe-AC-IWM. The silica-doping does not significantly affect the pore size distribution. Some very small pores seem to become better accessible during the catalysis experiments.

The moderate loss of pore volume during the catalysis experiments of Fe-AC-CVI, Cu-AC-CVI and Fe-AC-IWM is possibly attributed to the selective chemisorption of NO (Kaneko 1987; Rubel et al. 1995a; 1995b). Indeed, NO_x species are completely released only at a temperature above 500 K, as previously derived from Fig. 56 in section 4.5, whereas the applied outgassing temperature for the conducted nitrogen adsorption measurements is considerably lower (423 K).

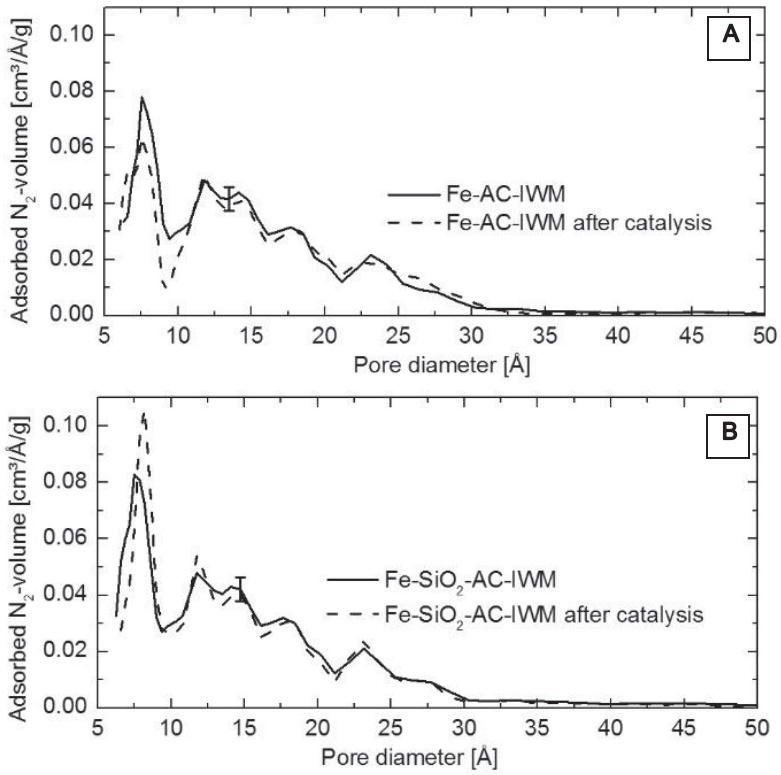

Fig. 69. Change of pore size distribution of IWM-infiltrated activated carbon samples during catalysis

The chemisorption of NO is stronger on activated carbon than it is on silica (Marsh & Rodríguez-Reinoso 2006, p. 265f). Hence, the addition of SiO_2 may prevent a selective pore clogging by NO_x species. The heat of adsorption of NO_x in these silica-enforced micropores is possibly lowered. The deposition of manganese oxide in Mn-AC-CVI seems to confer the catalyst with a similar effect, which may explain its lower catalytic conversion of NO into N_2O and CO as discussed in section 4.7.

In summary, the oxidizing conditions of the catalysis experiment do not change the crystal species and crystallite size of the iron-infiltrated activated carbon. Surface structure changes during the catalysis experiments are very small and mainly limited to the clogging of small micropores, probably due to the pore size selective NO_x adsorption. The co-deposition of silica and also manganese can possibly prevent the strong NO_x adsorption and keep the micropores well accessible.

4.9. Summary and conclusions

The chemical vapor infiltration of iron into activated carbon provides a deep and homogeneous iron dispersion inside the substrate matrix, although some larger particles are formed all over the sample cross section. Some of the metallic iron particles probably exhibit a crystalline metallic core and an oxide shell. The pore system of the samples remains well preserved during the infiltration. Only the introduction of a large metal load severely blocks the micropores of the carbon matrix.

The adsorption of NO_2 in the iron-infiltrated activated carbon probably occurs in pore-size-selective micropore filling and subsequent involvement of iron or iron oxide sites. The catalyst sample with moderate iron load exhibits a very large NO_x adsorption capacity and also the largest NO_x adsorption and desorption rate.

All investigated catalysts remove NO_2 from the test gas almost completely. The major conversion products are NO and N_2O. A substantial amount of CO is released and a minor fraction of catalysts release a notable quantity of CO_2. The conversion of NO into CO and N_2O is largely promoted by the infiltration of activated carbon with transition metals or metal oxides. The copper- and manganese-infiltrated activated carbon catalysts exhibit the best performance in the conversion of NO. The iron-infiltrated samples release the largest amounts of CO and N_2O.

The micropores have a significant effect on the activity of the catalysts, possibly due to the surface area and the overlapping potentials of the micropores. However, a pore size selective chemisorption of NO_x may result in the clogging of some of the micropores. The co-deposition of silica inside the catalysts seems to prevent this effect. Interestingly enough, the preparation method has no independent influence on the catalytic activity.

In conclusion, the most recommendable activated carbon catalyst is the iron-infiltrated and silica-co-doped activated carbon (Fe-SiO_2-AC-IWM), which is prepared by the incipient wetness method. This sample combines an efficient conversion of nitrogen oxides into less harmful gases with a high stability of its framework during the conditions of the catalysis.

5. Results and discussion of zeolite-based catalysts

The application of activated carbon catalysts seems to be inevitably accompanied with the consumption of some of the substrate material, which might be a major drawback in commercial application as a catalyst. Zeolite-based catalysts could be a thermally and chemically more stable and still inexpensive alternative. Since the first reports of Iwamoto (Iwamoto et al. 1986) about copper-infiltrated zeolites they are considered to be a very promising catalyst for the direct conversion of nitrogen oxides.

Especially the introduction of transition metals into the porous zeolite matrix by chemical vapor infiltration is believed to reveal materials with superior catalytic activity (Brandenberger et al. 2011). Hence, iron-, copper- and manganese-infiltrated zeolite MFI, Beta and mordenite are synthesized in this work and the detailed investigations are presented and discussed in the following.

5.1. Sample overview

The prepared zeolite catalysts exhibit several interesting differences in their structure and elemental composition. Table 11 provides an overview of the main properties of the investigated samples. Those samples marked with a black circle are used in the discussion as typical examples for the iron-, copper- and manganese-infiltrated samples. The elemental quantification is performed by averaging consecutive EDX measurements at two different spots of each sample.

The ratio of metal atoms and aluminum atoms provides a very rough estimate on the exchange level of the zeolite, i.e. the accommodation of metal ions inside of the pore channels. Zeolite catalysts which exhibit a metall-cation/Al-ratio larger than 0.5 are usually considered to be highly or excessively exchanged (Sarkany et al. 1992). Such catalysts are generally believed to be more active in the catalytic conversion of nitrogen oxides (Centi & Perathoner 1995; Yahiro & Iwamoto 2001; Brandenberger et al. 2011). Campa et al. report the highest contribution to the catalytic activity in direct NO conversion for the last exchanged 20% of copper ions at 100% exchange level (Campa et al. 1994). These authors also state that over-exchanged copper ions (exceeding the 100% exchange level) are almost ineffective for the reaction. For exchange levels above 200% the copper ions are certainly forming oxides in the zeolite (Shelef 1995).

The metal species in the herein synthesized catalysts are probably quite heterogeneous, i.e. isolated metal cations with different oxidation state and metal oxides are very likely to coexist (Heinrich et al. 2002; Nasibulin et al. 2002; Kumar et al. 2004). Furthermore, not all of the infiltrated metal species are expected to be accommodated inside of the zeolite pore channels, but reside also on the external particle surface.

First indications on this matter can be derived from the sample color. The as-synthesized iron-infiltrated zeolites exhibit a dark grey tone, whereas the copper-infiltrated samples are completely black and the manganese-samples are dark brown. As described in the catalytic decomposition of nitrogen dioxide at 425 K (see section 5.7), these dark tones are brightening up. Only the manganese-infiltrated samples keep their dark brown color. The as-synthesized liquid ion exchanged reference catalysts exhibit a slightly yellowish color.

Table 11. Overview of CVI-infiltrated zeolites

Sample name	Precursor	Infiltrated ion	Ion load (wt.-%)[1)]	Si/Al-ratio[1)]	M/Al-ratio[1),2)]	Specific surface area (m^2/g)	Micropore volume (cm^3/g)	Total pore volume (cm^3/g)
ZSM-5 (MFI) matrix								
• Fe-MFI-CVI-a (MB315)	Ferrocene	Fe	1.9	10	0.3	351	0.075	0.19
Fe-MFI-CVI-a (MB315) after catalysis	Ferrocene	Fe	1.9	n.m.	n.m.	393	0.086	0.23
Fe-MFI-CVI-b (MB172)	Ferrocene	Fe	2.0	n.m.	n.m.	198	0.085	0.13
Fe-MFI-CVI-c (MB182)	$Fe(acac)_3$	Fe	0.5	n.m.	n.m.	245	0.047	0.15
• Cu-MFI-CVI-a (MB300)	$Cu(acac)_2$	Cu	4.2	11	0.5[3)]	226	0.042	0.16
Cu-MFI-CVI-a (MB300) after catalysis	$Cu(acac)_2$	Cu	4.2	n.m.	n.m.	410	0.049	0.63
Cu-MFI-CVI-b (MB295)	$Cu(acac)_2$	Cu	1.0	n.m.	n.m.	n.m.	n.m.	n.m.
Mn-MFI-CVI-a (MB179)	$Mn(acac)_3$	Mn	0.2	n.m.	n.m.	298	0.060	0.18
• Mn-MFI-CVI-b (MB326)	$Mn(acac)_3$	Mn	0.2	10	0.0.	348	0.081	0.19
Zeolite Beta matrix								
• Fe-BEA-CVI (MB319)	Ferrocene	Fe	3.3	16	0.8	490	0.079	0.30
• Cu-BEA-CVI (MB307)	$Cu(acac)_2$	Cu	2.5	14	0.4[3)]	409	0.065	0.26
• Mn-BEA-CVI (MB332)	$Mn(acac)_3$	Mn	1.2	16	0.3	485	0.073	0.32
Mordenite matrix								
• Fe-MOR-CVI (MB322)	Ferrocene	Fe	1.5	5	0.1	453	0.094	0.28
• Cu-MOR-CVI (MB303)	$Cu(acac)_2$	Cu	1.8	5	0.1[3)]	284	0.013	0.34
• Mn-MOR-CVI (MB329)	$Mn(acac)_3$	Mn	0.03	5	0.0	239	0.028	0.17

Black circles mark applied typical examples for iron-, copper- and manganese-infiltrated zeolites, [1)]quantified by EDX, standard error: +/-30%; [2)]M/Al-ratio = ratio of foreign metal atoms and Al-atoms; [3)]corrected by contribution of brass sample holder; n.m. = not measured

The reason for the dark color of the iron-infiltrated samples can be most probably attributed to some deposition of carbon during the thermal decomposition of the metal organic precursors. These carbon traces seem to be gasified in the oxidizing conditions of the catalysis experiment. However, no measurable amount of carbon oxides is detected by the mass spectrometric surveillance of the test gas mixture. Hence, they are unlikely to participate notably in the nitrogen oxide decomposition. The brown color of the manganese-infiltrated samples probably stems from deposited manganese dioxide (Han et al. 2006), since it is not changing during the catalysis experiments.

5.2. Preparation parameter studies

The applied CVI preparation procedure of zeolite catalysts is similar to the preparation of the activated carbon catalysts. Details on this preparation procedure, especially of the time-resolved pressure and temperature regime, are provided in section 3.1.3.

The introduction of metal cations into zeolites is typically performed by a deposition and decomposition of metal precursor molecules at the accessible basic sites inside of the pore channels. The eventually achieved metal load of the sample depends on the nature of the precursor, on the infiltration process and on the number of accessible charged sites in the framework (Capek et al. 2005; Pérez-Ramírez & Gallardo-Llamas 2005).

Fig. 70 shows the relation between the ratio of the applied precursor per sample mass to the respective EDX-measured ion load. Disregarding Fe-BEA-CVI, there is a clear linear correlation between the evaporated relative amount of precursor and the ion load. The measured mass gain of BEA samples is generally larger, probably due to the largest pore channels (7.1 Å diameter (Baerlocher et al. 2007)) of all investigated zeolites and an accommodation for example

of the Ferrocene molecule (6.6 Å molecular diameter (Tajimi et al. 2007)) with less steric hindrance during the pore diffusion.

The diffusion into the framework may become more difficult, if the precursor molecules have almost the same diameter as the pore channel width or even slightly exceed the channel size (Krishna et al. 2003). Especially in this case, some fraction of the precursor may be deposited on the external of the framework.

In summary, the amount of evaporated precursor is obviously a good control parameter for the intended metal load of the zeolite catalyst. However, the actual location of the deposited metal (inside or outside of the framework) requires further refined investigation.

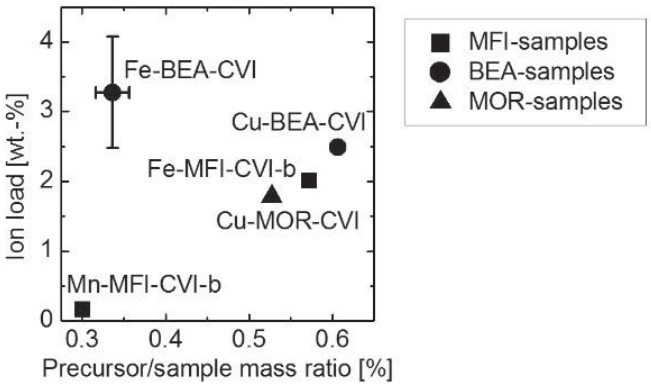

Fig. 70. Relation of precursor/sample-mass ratio and deposited metal ion load (B), derived from EDX elemental quantification of infiltrated zeolite samples; MFI: squares, BEA: circles, MOR: triangles

5.3. Microscopic investigation of selected samples

Detailed differences in the infiltration results from chemical vapor infiltration and liquid ion exchange are apparent from a microscopic inspection of the as-prepared samples. The CVI-samples exhibit some formation of particles outside or inside the zeolite particle, whereas no foreign agglomerations are visible in the smooth zeolite particles of the LIE-samples (see section 3.1.4).

Fig. 71 shows a TEM micrograph of the macrostructure of as-synthesized Cu-MFI-CVI. The zeolite particles show the original agglomerated pile-shape (Fig. 71) with a partially irregular structure (Fig. 72). FFT analysis of a zeolite particle (Fig. 73) reveals the lattice structure of the zeolite with pore channels of 5.4 Å derived from the measured lattice spacing. Cu-MFI-CVI exhibits large smooth areas without visibly formed particles (Fig. 72) and areas with a dense generation of probably nanodisperse copper species (Fig. 74). The diameter of these particles is mostly smaller than 10 nm.

Fe-MFI-CVI exhibits very a similar particle formation, but to a smaller extent (Fig. 75). Comparing the EDX spectra (Fig. 76 and Fig. 77) from one of the particles in Fig. 75 and from a spot with no visual particle as reference, the deposits are identified to be iron or iron oxide.

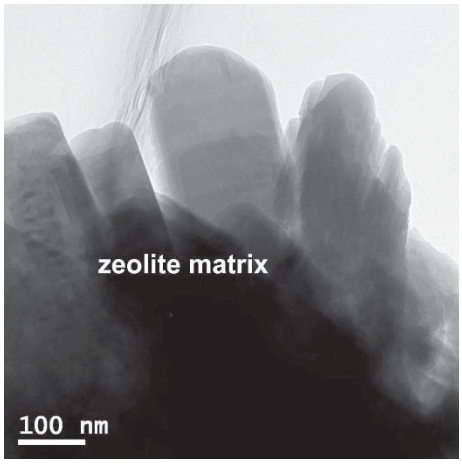

Fig. 71. TEM micrograph of Cu-MFI-CVI showing large particles of zeolite matrix

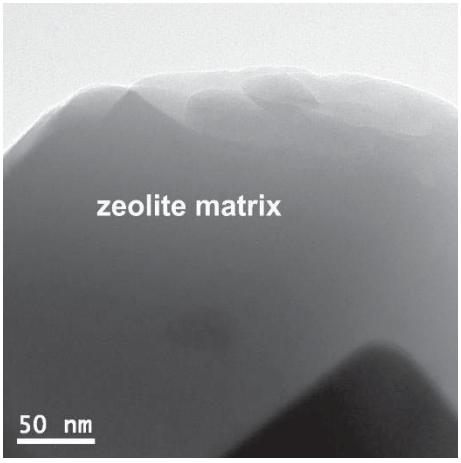

Fig. 72. TEM micrograph of Cu-MFI-CVI showing zeolite matrix without large copper particles

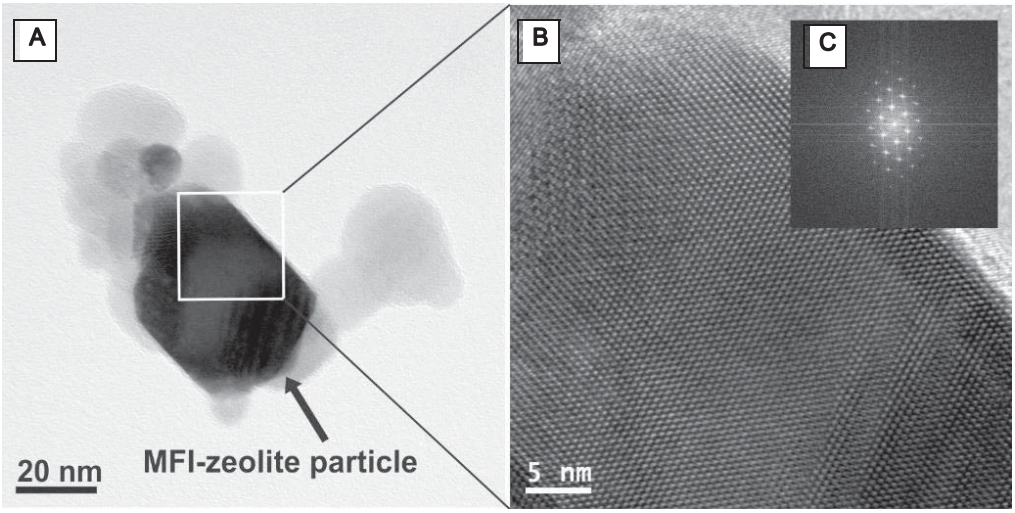

Fig. 73. TEM micrograph (A) of Fe-MFI-CVI, HRTEM micrograph (B) of a section of the particle and FFT (C) of the HRTEM micrograph, confirming the MFI structure

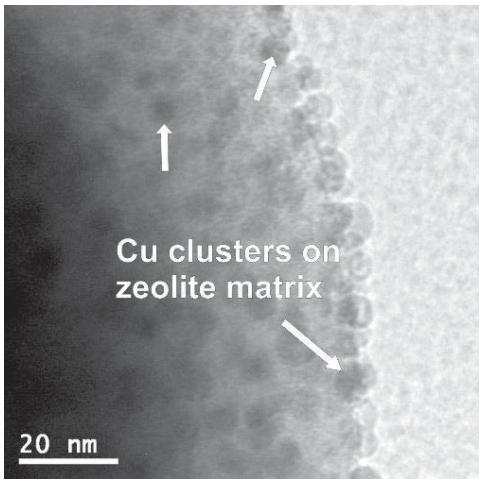

Fig. 74. TEM micrograph of Cu-MFI-CVI showing nanodisperse copper species (white arrows) on the external zeolite matrix

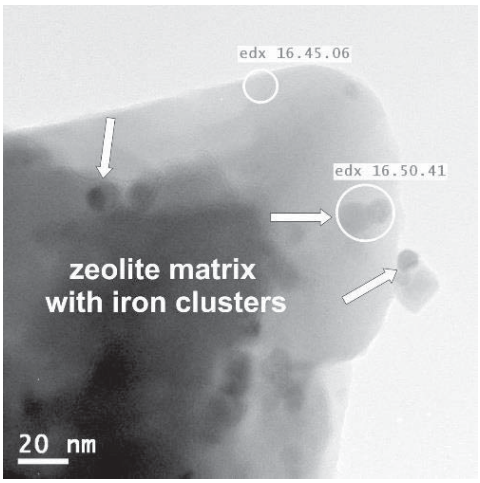

Fig. 75. TEM micrograph of Fe-MFI-CVI showing iron species (white arrows) on the external zeolite matrix, EDX signal is analyzed from the spots marked by white circles

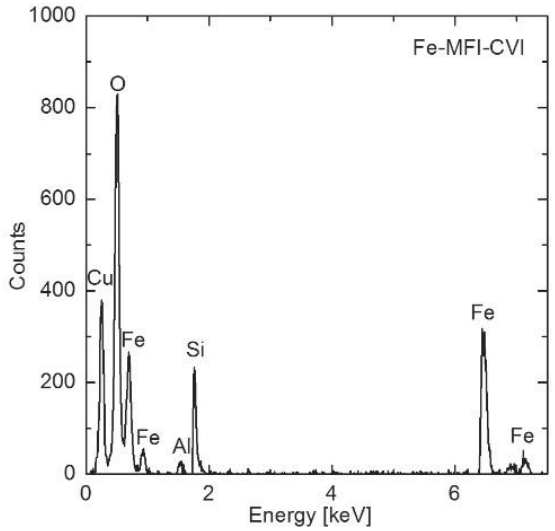

Fig. 76. EDX spectrum of spot "16.50.41" marking the iron oxide particle in Fig. 75, copper signal caused by TEM grid

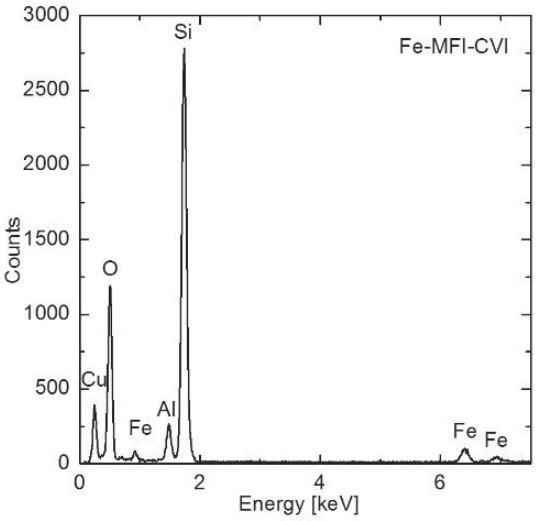

Fig. 77. EDX spectrum of spot "16.45.06" marking a reference spot in Fig. 75, copper signal caused by TEM grid

The formation of particles during CVI-infiltration is interesting, since liquid ion exchanged copper-MFI can be highly exchanged up to 640% (about 4 wt.-% copper load) without any copper oxide agglomerations (Pirone et al. 1996). Although they are rather unlikely to affect the nitrogen oxide decomposition (Heinrich et al. 2002), the particles may provide some information on the deposition process.

Two different phenomena may occur during the infiltration: (1) The sublimation temperature may be chosen too low and hence the precursor vapor is deposited on the outside of the zeolite framework without any deep penetration into the pore channel system, or (2) some of the precursor, which is deposited in pore channels, diffuses during the calcination process to form particles and crystallites inside and/or outside of the pores.

In the first case the observed particles would be found preferentially on the zeolite particle surface. The micropore volume of the samples could be reduced, because the pore entries may become at least partially blocked. In the second case, a large fraction of particles would form inside of the channel system (as mentioned in section 5.2). Clusters that grow excessively could damage the pore channels and reduce the micropore volume (Felthouse & Murphy 1986). Additionally, a migration of deposited metal ions inside the zeolite framework is possible (Itho et al. 1994; Benco et al. 2006; Vennestrom et al. 2014).

The observations in Fig. 74 suggest that at least some of the copper particles are sitting on the outside of the zeolite particle. However, it can be estimated from the reaction kinetics in the similar preparation process with activated carbon-based catalysts (see section 4.2), that some of the precursor is probably decomposing inside the pore channels. In fact, the micropore volume of most zeolite samples presented in Table 11 is considerably reduced in comparison with the original non-infiltrated zeolites. This suggests that the precursor may penetrate the pore channel system, is deposited there and probably also blocks some of the pores.

Concluding, the infiltration with an excessive amount of precursor and its diffusion during the calcination process is probably responsible for the formation of particles. In fact, even liquid ion exchanged samples can exhibit a loss of 18-25% of the micropore volume if they are highly over-exchanged (> 400%) (Kharas et al. 1993). Such a loss of micropore volume may reduce

the activity of the catalyst and hence, changes in the pore volume need to be investigated in the following.

5.4. Structural characterization

5.4.1. Infiltration of the pore channels

The infiltration with a precursor can only account for a slight reduction of the micropore volume of the multiple accessible pore channels of the applied zeolites. Some authors report a blocking of pores due to the CVI-infiltration in the range of 20-30% (Bitter et al. 2003; Kumar et al. 2004). However, excessively growing clusters could damage the pore channels as discussed above in section 5.3 and more strongly reduce the micropore volume.

Typically, the measured loss of micropore volume would be closely related to the amount of deposited metal or to blocking of the pore mouths. But in contrast, as shown in Fig. 78 A, the ion load does not exhibit any notable regular effect on the micropore volume. If the pores were systematically blocked and/or damaged, the relation would be expected to be inverse.

While the thermal and pressure regime during the sample preconditioning and precursor decomposition is equal for all samples, no relation is found between the loss of micropore volume and factors like the amount of matrix material, the precursor quantity or their ratio. But it is noteworthy, that all Ferrocene-infiltrated samples keep their original micropore volume considerably well, whereas the samples which are infiltrated with acetylacetonates suffer from a larger loss in the micropore volume. The correlation among only the latter samples with the micropore volume (Fig. 78 B) seems – ignoring the outlier Mn-MOR-CVI – inversely proportional, indeed.

These observations suggest that the introduction of the large Ferrocene molecule into the narrow pore channels may be intricate, for example due to steric hindrance (Krishna et al. 2003). Those samples which are infiltrated with acetylacetonates are probably better infiltrated in micropores, as derived from the reduced micropore volume. Hence, they are more likely to stabilize a large amount of catalytically active species in the pore channels, but their metal species can also contribute to the framework damage from excessively growing clusters.

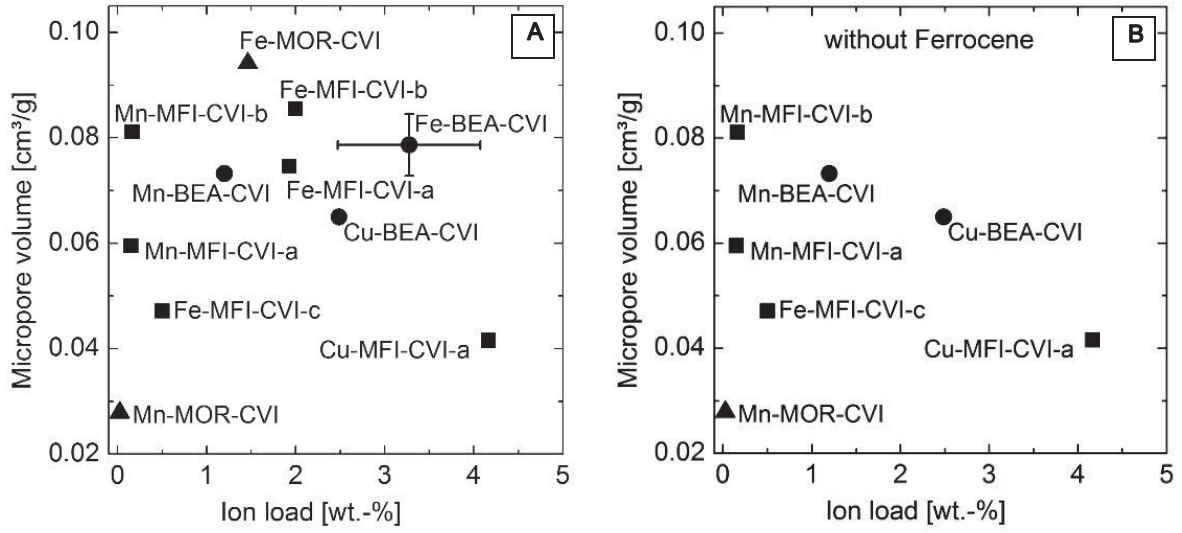

Fig. 78. Specific micropore volume in relation to the ion load of all CVI-infiltrated zeolites (A) and to samples which are only infiltrated with acetylacetonates (B); MFI: squares, BEA: circles, MOR: triangles

5.4.2. Deposition in inter-crystallite pores

The samples, which are infiltrated with Ferrocene, exhibit an ion load of 1.5-3.3 wt.-% (see Table 11), although only a fraction of this amount seems to be accommodated inside the pore channels. This raises the interesting question, where the large residual amount is actually deposited.

Some indications on this matter have been discussed in the previous section for the external copper species of the copper-infiltrated MFI. Further information can be derived from the measured pore volumes. Since the zeolite crystallite framework typically contains neither mesopores, nor macropores, the fraction of the measured total pore volume, which is not attributed to micropores, must originate from pores between the crystallites of the zeolite or damage in the zeolite. Hence, any decrease of the total pore volume can be attributed to the filling of inter-crystallite pores with deposited material.

Fig. 79 shows the change of the micropore volumes and the change of the total pore volumes of the zeolites during the chemical vapor infiltration. Samples, which are infiltrated with Ferrocene, are marked with hollow symbols and their change of the micropore volume are all considerably small. In contrast, the changes of their measured total pore volume are very heterogeneous.

Fe-MOR-CVI and Fe-BEA-CVI exhibit 20-30% change of the micropore volume, while the Ferrocene-infiltrated MFI-samples (Fe-MFI-CVI-a and Fe-CVI-MFI-b) exhibit a lower change. As discussed before, Ferrocene with 6.6 Å molecular diameter (Tajimi et al. 2007) may diffuse easier into the large pore channels of MOR (6.5-7.0 Å) and BEA (7.1-7.6 Å) than into the narrow pores of MFI (5.5 Å). The ion load of the BEA sample is, however, more than twice as large as the ion load of the MOR sample, despite of an identical infiltration procedure. Hence, some of the excessively deposited iron species are probably filling the inter-crystallite pores of the BEA sample, while the inter-crystallite pores of the MOR sample remain free. This is reflected in the large reduction of the total pore volume of Fe-BEA-CVI in Fig. 79.

The lower Si/Al-ratio of the mordenite and its associated high availability of charged sites for the accommodation of foreign cations (see M/Al-ratio in Table 11, section 5.1) (Brandin et al. 1989; Parrillo & Gorte 1993) may be one reason for the lower external deposition on the mordenite. Zeolite Beta with a larger Si/Al-ratio can accommodate less metal ions and hence, an excessive infiltration may lead to the formation of particles on the external of the framework (Shelef 1995).

Many other samples like Cu-MFI-CVI-a show both a decrease in the micropore volume and a decrease of the total pore volume. In these cases the generation of metal species inside the framework channels and in inter-crystallite pores, or a blocking of the pore mouths is possible and may be monitored in the pore size distribution of the samples.

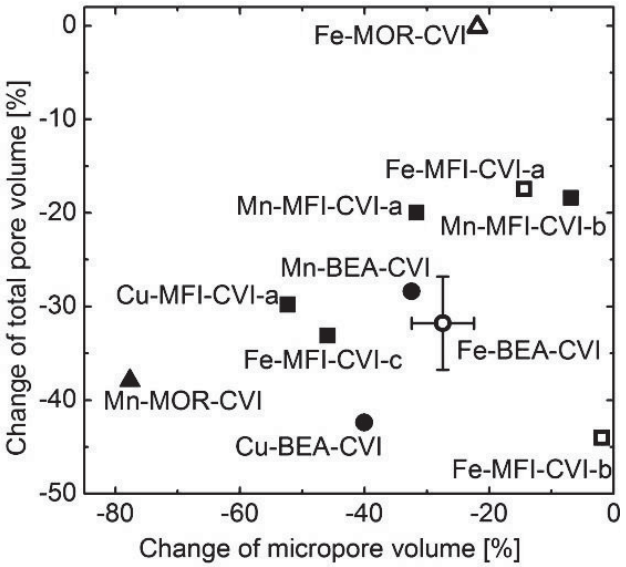

Fig. 79. Change of the micropore volume vs. change of the total pore volume of zeolites during the CVI-preparation; MFI: squares, BEA: circles, MOR: triangles, Ferrocene-infiltrated: hollow symbol

5.4.3. Pore size distribution

Fig. 80 shows the pore size distribution of infiltrated MFI zeolites in comparison to the preconditioned (protonated) MFI. The maximum in the micropore region (Fig. 80 A, below 1 nm) is caused by the pore channels. The maxima in the small mesopore region (Fig. 80 B) characterize the inter-crystallite pores.

In the small mesopore region (Fig. 80 B), there are two maximum peaks, suggesting a binary pore size distribution with pore width modes of about 4 and 6 nm. Both maxima are considerably diminished for all infiltrated samples and the width of the peaks becomes narrower after the infiltration. The decrease probably shows the filling of inter-crystallite pores by deposited metal species. The observation of the binary distribution may be a related with the geometry and/or a binary size distribution of particles of the as-delivered material, which is not further analyzed for the present samples.

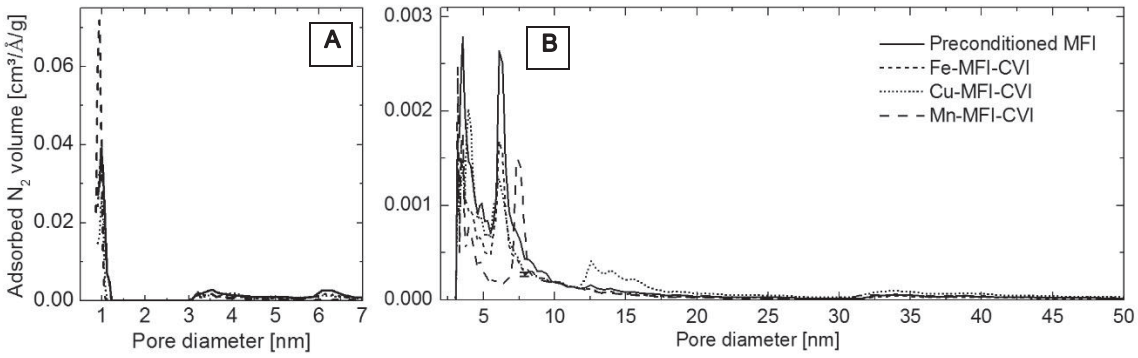

Fig. 80. Pore size distribution of CVI-infiltrated MFI samples before and after infiltration in the micropore/small mesopore region (A) and in the mesopore region (B, enlarged y-axis)

5.4.4. Crystallinity of the formed particles

The crystallinity of the deposited material, especially of larger particles, can be investigated by X-ray diffraction. Fig. 81 and Fig. 82 compare the diffractograms of iron-, copper- and manganese-infiltrated MFI and BEA zeolites, respectively. Surprisingly, crystalline species are only found in the copper-infiltrated samples. Their reflections suggest the formation of larger copper

crystallites with an average size of about 25 nm in Cu-MFI-CVI and even about 48 nm in Cu-BEA-CVI, estimated by means of the Scherrer equation. The growth of such crystallites occurs probably outside of the zeolite crystals, rather than growing to this size inside the pore system.

Other crystalline species are neither found in the iron-infiltrated, nor in the manganese-infiltrated samples. Apparently, most of the excessively deposited material is either amorphous, or the crystallites are very small and cause broad reflections, which cannot be identified.

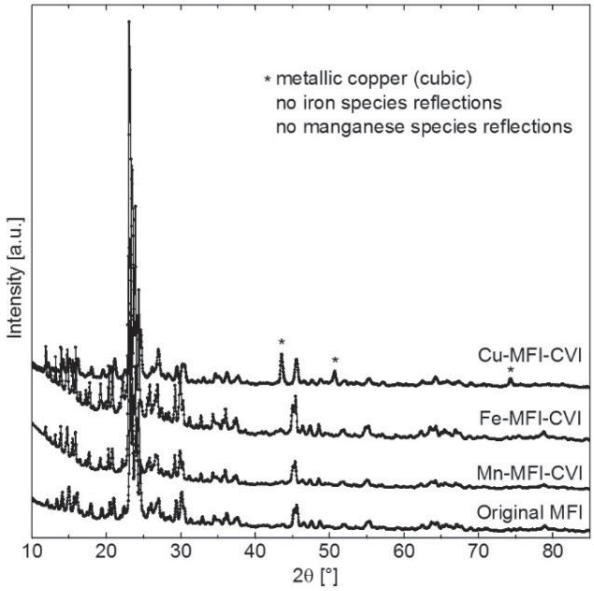

Fig. 81. X-ray diffractograms of infiltrated MFI samples; marked iron and iron oxide reflections are not significant

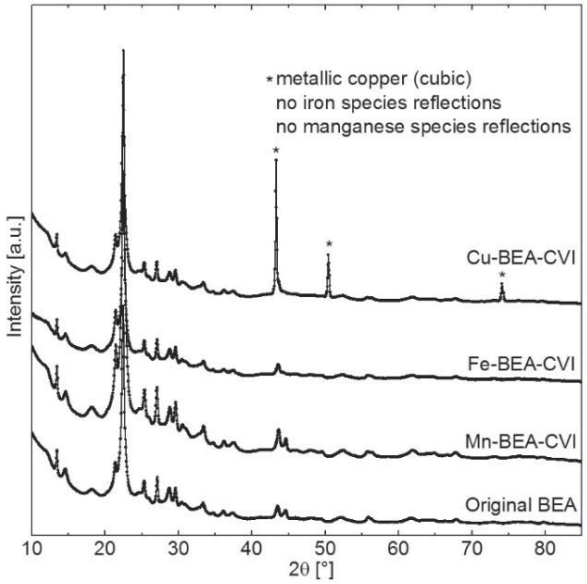

Fig. 82. X-ray diffractograms of infiltrated BEA samples

In summary, the chemical vapor infiltration of zeolite samples reveals catalysts with different structures. Acetylacetonate-based precursors seem to infiltrate the zeolite pore channels deeper than Ferrocene. Some of the deposited material is filling inter-crystallite pores, but crystallites are only forming for the deposition of copper, while no foreign crystalline phases are observed for iron- or manganese-infiltrated samples.

5.5. NO_x adsorption properties

The heterogeneous nature of the catalysts prepared by either infiltration method is likely to affect the adsorption and decomposition properties of nitrogen oxides on these samples (Capek et al. 2005). Fig. 83 shows the differences of the mass specific NO_2 uptake of non-infiltrated and copper-infiltrated MFI samples at 303 K. The samples are all saturated in the course of nine hours in 10 sccm gas flow of 0.3% NO_2 in helium and exhibit approximately similar and uniform adsorption rates. Prior to the experiment all samples are pretreated at 473 K in helium in order to dry the samples.

The uptake capacity of the LIE-prepared sample (4 wt.-%) is significantly larger than the capacity of the non-infiltrated MFI and of Cu-MFI-CVI. The latter two are saturated at 2-2.5 wt.-% mass increase. It is interesting that the LIE-sample exhibits such an increased uptake capacity. Probably, this difference originates from its large specific surface area of 411 m²/g in combination with the probably well dispersed copper species (see section 3.1.4) compared with 226 m²/g of Cu-MFI-CVI.

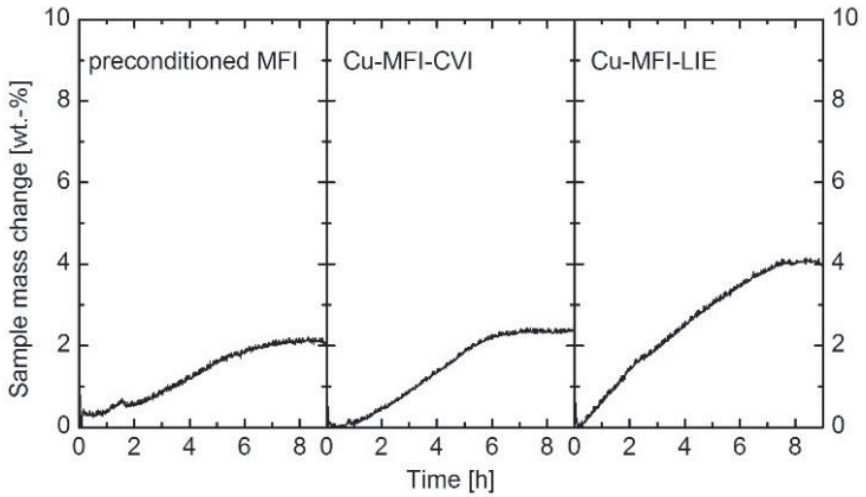

Fig. 83. Mass increase of MFI samples due to NO_2 adsorption at 303 K for 9 hours; gas mixture: 0.3% NO_2 in helium

5.6. Effect of the temperature on NO_x conversion

The actual investigation of the as-prepared catalysts in the decomposition of nitrogen oxides is preferably performed at a low temperature, which is close to the conditions of the intended application. However, the kinetics of the decomposition reactions are expected to be very slow at low temperatures. Hence, the lowest possible temperature is determined in preliminary experiments, similar to the experiments with activated carbon in section 4.7, applying the well characterized Cu-MFI-LIE (Cu-ZSM-5) catalyst.

In Fig. 84 the influence of the temperature in a range of 323 – 673 K on the NO_x conversion properties is analyzed. Fig. 85 shows the corresponding mass balances of the elemental composition of the gas phase. The applied gas mixture is 0.9% NO_2, 10% argon and helium as balance and the displayed gas species concentrations are measured after 120 minutes experimental time. The temperature is kept constant for each experiment.

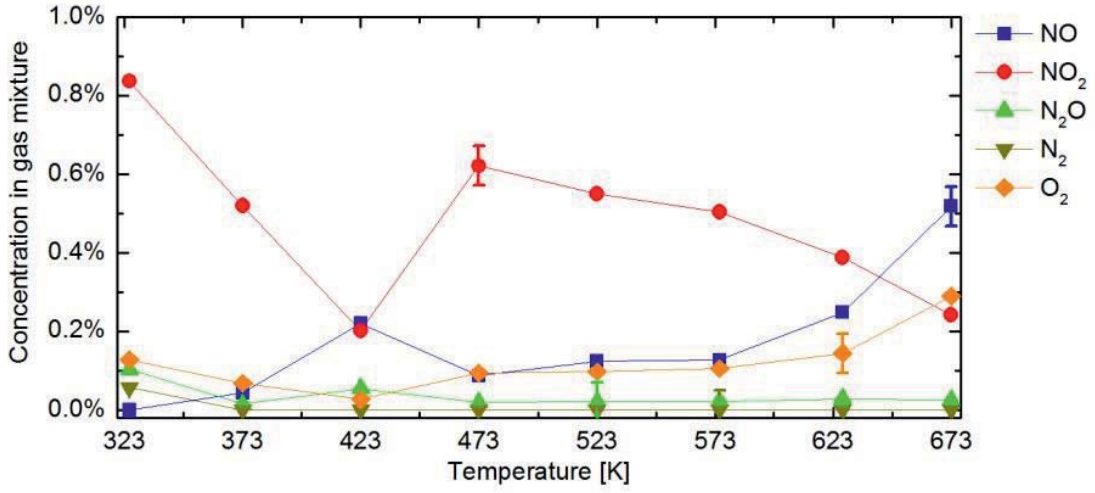

Fig. 84. Gas mixture composition of Cu-MFI-LIE after 120 minutes NO_2 conversion in recycle flow at different temperatures (initially: 0.9% NO_2)

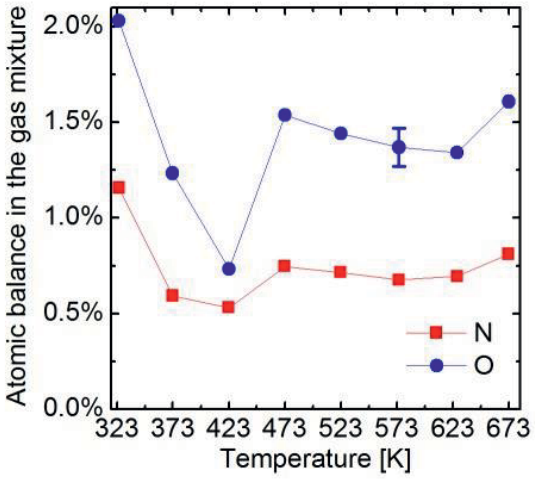

Fig. 85. Elemental composition in gas mixture of the experiments in Fig. 84

At 323 K NO_2 is neither adsorbed, nor converted. With rising temperature the NO_2 concentration is decreasing to a minimum of 0.2% at 423 K. At 473 K the concentration of NO_2 is about 0.6% and decreases constantly with further augmented temperature to 0.25% at 673 K.

The NO concentration is very low at low temperature and passes a local maximum of 0.2% at 423 K. In excess of 473 K the concentration of NO continuously increases up to 0.5% at 673 K. The N_2O concentration remains below 0.1% over the entire temperature range. The O_2 concentration increases very slightly with rising temperature up to a concentration of 0.3% at 673 K. A notable release of N_2 is not detected.

The NO_2 and NO concentrations are anti-correlating. At 373 K and at 673 K the molar sum of NO_x-species in the gas phase is close to the initial amount in the feed gas and no NO_x species remain adsorbed on the catalyst. Between these temperatures a considerable amount of NO_x is adsorbed on the sample. The smallest NO_x concentrations – 0.2% NO_2, 0.2% NO and 0.1% N_2O at 423 K – are about half of the supplied NO_x being also reflected by the balances of the elemental composition in the gas phase (Fig. 85).

The results suggest that the NO_2 adsorption requires a temperature-activated adsorption, for example by dissociation of NO_2. At low temperature adsorbed NO_x species remain adsorbed on the zeolite surface. Only a small fraction is released to the gas phase in form of NO at 423 K. At slightly higher temperature (473 K) the adsorption of NO_2 could already be thermally hindered or a part of the released NO is re-oxidized into NO_2. With further increasing temperature, only a small fraction of NO_2 adsorbs on the surface and a large part of NO_2 is converted into NO and O_2.

As conclusion, the largest NO_x removal at low temperature is observed at a temperature of 423 K, which is eventually chosen for the subsequent experiments.

5.7. NO_x conversion properties

The catalytic activity of the zeolite-based catalysts is investigated in analogy to the investigation of activated carbon catalysts in section 4.7. A sample mass of 0.2 g of each catalyst is fixed between glass wool plugs in a glass tube and the standard test gas mixture (0.9% NO_2, 10% argon and helium balance) circulates through the samples for 120 minutes experimental time at 425 K and 1000 mbar. These are conditions identical to those for the investigation of activated carbon samples (section 4). Fig. 86 provides an overview of the final gas mixture composition for the synthesized samples and the reference catalysts.

All of the investigated samples adsorb and convert NO_2. Differences arise in the actual amount of converted NO_2 and in the release of the product gas species NO, N_2O, N_2 and O_2. In accordance with other authors, the amount of released molecular nitrogen can serve as a measure for the complete decomposition of nitrogen oxides (Teraoka et al. 1998; Tang et al. 2002).

Gas phase iron-infiltrated mordenite (Fe-MOR-CVI) and copper-infiltrated MFI-zeolite (Cu-MFI-CVI) are the most promising catalysts for the complete NO_x conversion. Both samples release the largest quantity of nitrogen and oxygen. However, the latter sample leaves a large portion of NO_2 unconverted. The platinum reference catalyst adsorbs all of the supplied NO_2, but it releases only a small portion of NO, instead of decomposing the pollutant gas completely. Most of the NO_x and possible reaction products remain adsorbed on the sample. The magnetite reference catalyst converts only a small fraction of the supplied NO_2. Even the preconditioned non-infiltrated MFI and MOR are catalytically more active.

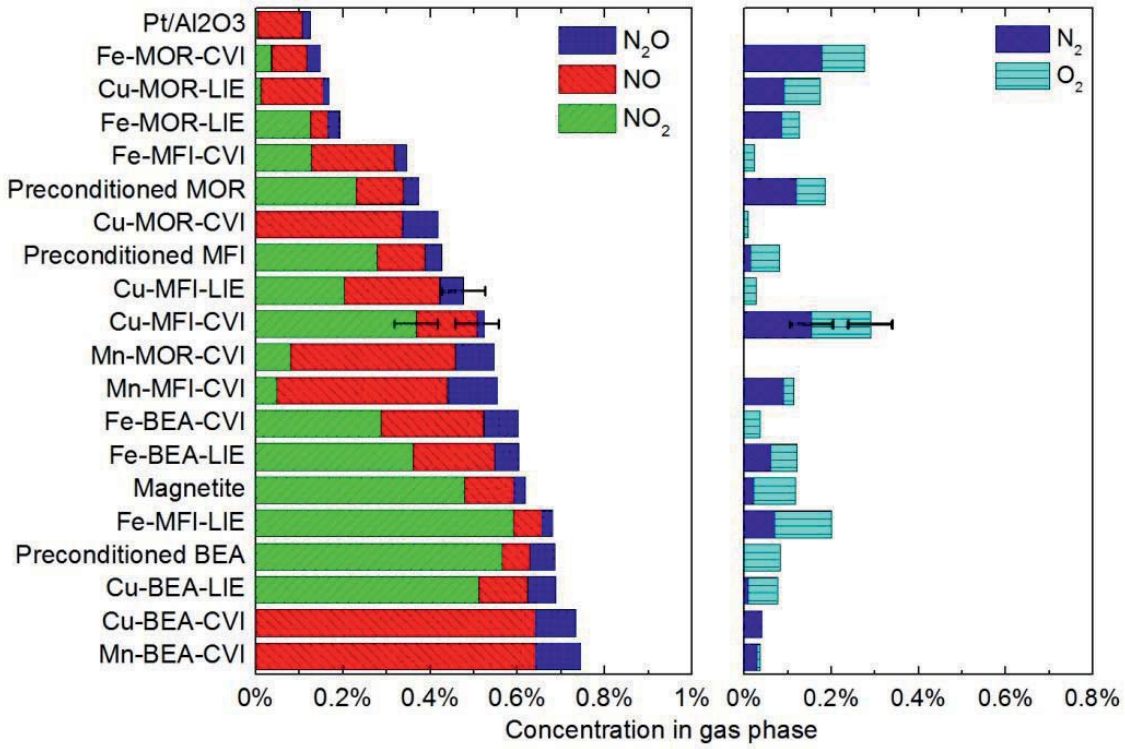

Fig. 86. Gas species concentrations using investigated zeolite samples after 120 minutes NO_2 conversion in recycle flow at 425 K; initial gas mixture: 0.9% NO_2, 10% Ar, 89.1% He

5.7.1. Nitrogen dioxide and nitric oxide conversion

For a more detailed analysis of the above described experiments, the change of the NO_2 concentration and the further decomposition of product NO are investigated separately. Fig. 87 shows the relative decrease of the initially supplied concentration of 0.9% nitrogen dioxide for each catalyst during the 120 minutes experimental time. Five of the six synthesized samples, which remove more than 90% of the initial NO_2 concentration, are chemical vapor infiltrated: Cu-MOR-CVI, Cu-BEA-CVI, Mn-BEA-CVI, Mn-MFI-CVI and Fe-MOR-CVI. Cu-MOR-LIE is the only liquid ion exchanged sample exhibiting a complete NO_2 removal.

Most of the catalysts convert the supplied NO_2 into NO, but the kinetics of this reaction largely varies. Some samples release NO quickly during the first minutes of the experiment and others slowly release NO over the entire experimental time. Among the former catalysts the maximum NO concentration is typically achieved after 10 minutes experimental time and the released NO is usually further decomposed thereafter.

Fig. 88 shows the change of the NO concentration for each sample between the 10^{th} minute and the 120^{th} minute of the catalysis experiment. The formation and decomposition of NO are opposing effects that may occur simultaneously. Hence, the figures show the net change of the NO concentration.

Some samples, like Fe-BEA-CVI convert the supplied NO_2 slowly into NO and hence, the net NO concentration is increasing. However, two copper-infiltrated CVI-catalysts (Cu-MFI-CVI and Cu-MOR-CVI) efficiently decompose the intermediately formed NO and outperform the magnetite reference catalyst. These are the most interesting catalysts regarding the decomposition of nitric oxide.

Overall, the results of the investigated catalysts are very heterogeneous. The decomposition process seems not to be straightforward. Hence, at first the main parameters (type of infiltrated metal, zeolite framework type, infiltration method) are investigated in order to possibly elucidate their effects independently. Subsequently, the catalytic conversion by the most promising catalysts is investigated time resolved and possible mechanisms are discussed in detail.

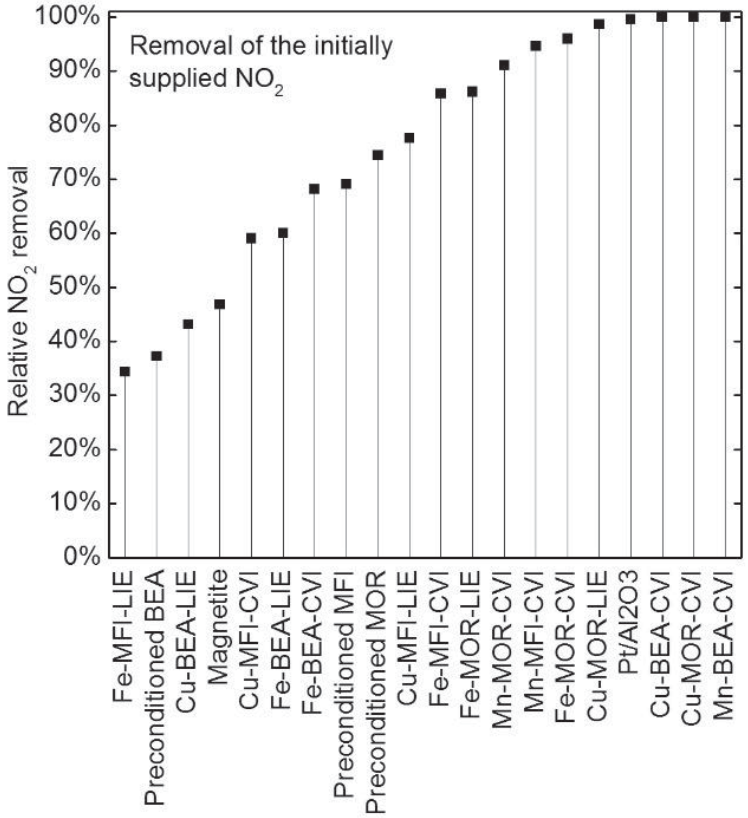

Fig. 87. Relative decrease of the initially supplied NO_2 concentration (0.9%) in the standard test gas mixture after 120 minutes experimental time at 425 K

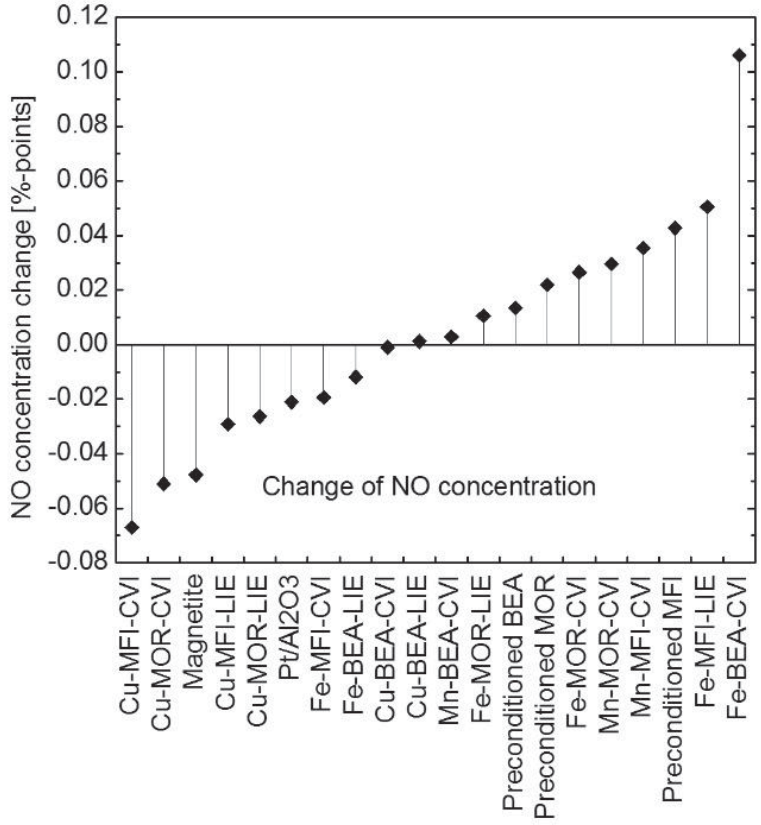

Fig. 88. Absolute change of the NO concentration between the 10th and the 120th minute of the standard catalysis experiment

5.7.2. Effect of the infiltrated metal type

Table 12 summarizes the effects of the synthesized catalysts on the nitrogen oxide conversion, sorted by the introduced metal. The table contains three double-columns, one for each metal (iron, copper, manganese), and it provides qualitative measures for the removal of NO_2 (derived from Fig. 87) and for the decomposition of NO (derived from Fig. 88). Details on the rating and the underlying data are provided in appendix 9.5.

Copper and manganese are the catalysts with superior performance in removal of NO_2. The effect of iron is well pronounced only for one catalyst: Fe-MOR-CVI. In the conversion of the intermediately formed NO copper-infiltrated catalysts exhibit again a very good performance, while the effects of manganese are small. Several iron-infiltrated catalysts do not form notable quantities of NO. Hence, their effect on the decomposition of NO cannot be derived.

Table 12. Overview of the qualitative effects of the infiltrated metal of investigated catalysts on the NO_2 removal and on the decomposition of NO
(NO_2 removal stated in left half-columns and derived from Fig. 87; decomposition of NO stated in right half-columns and derived from Fig. 88)

Catalyst	NO_2 removal / NO decomposition					
	iron		copper		manganese	
MFI-CVI	+	+	o	++	+	o
MFI-LIE	o	n.r.	+	+		
BEA-CVI	o	o	++	+	++	+
BEA-LIE	o	+	o	n.r.		
MOR-CVI	++	n.r.	++	++	+	o
MOR-LIE	+	n.r.	++	+		

Legend: “o” denotes that the catalyst is hardly efficient, ”+” denotes that the catalyst is medium efficient, “++“ denotes that the catalyst is very efficient; n.r. = NO is not notably released to the test gas atmosphere; for details see Table 22 in appendix 9.5

5.7.3. Effect of the zeolite framework type

The effect of the iron-infiltrated catalysts seems to depend on the actual iron-zeolite system. Indeed, factors such as the pore channel width, the micropore volume and the availability of charged aluminum sites in the framework are likely to affect the decomposition of nitrogen oxides and are different for the different zeolite types (Brosius et al. 2004; Pieterse et al. 2004). Table 13 provides an overview of the effects of each of the investigated catalysts on the removal of NO_2 and on the decomposition of NO, sorted by the framework type. In analogy to Table 12, the qualitative measures are derived from Fig. 87 and from Fig. 88.

The mordenite catalysts are most active in the removal of NO_2. Especially the copper-infiltrated mordenite (Cu-MOR-CVI) seems to exhibit outstanding properties, even in the removal of NO. The other effects differ among each type of zeolite and cannot be generalized.

Table 13. Overview of the qualitative effects of the framework type of investigated catalysts on the NO_2 removal and on the decomposition of NO
(NO_2 removal stated in left half-columns, derived from Fig. 87; decomposition of NO stated in right half-columns and derived from Fig. 88)

Catalyst preparation	NO_2 removal / NO decomposition					
	MFI		BEA		MOR	
Non-infiltrated	+	o	o	n.r.	+	o
Fe-CVI	+	+	o	o	++	n.r.
Fe-LIE	o	n.r.	o	+	+	n.r.
Cu-CVI	o	++	++	+	++	++
Cu-LIE	+	+	o	n.r.	++	+
Mn-CVI	+	o	++	+	+	o

Legend: "o" denotes that the catalyst is hardly efficient, "+" denotes that the catalyst is medium efficient, "++"denotes that the catalyst is very efficient; n.r. = NO is not notably released to the test gas atmosphere; for details see Table 21 in appendix 9.5

5.7.4. Effect of the preparation method

As observed in section 5.3, the dispersion of the metal species differs, depending on the infiltration method. Apparently some of the chemical vapor infiltrated zeolites exhibit larger species inside of the pores or outside of the zeolite crystal, whereas no agglomerates are found in the liquid ion exchanged samples. As mentioned before, such differences are likely to affect the catalytic activity of the sample. Table 14 compares the effects of chemical vapor infiltrated catalysts with the effects of the respective liquid ion exchanged zeolites. Here, the qualitative measures assess the difference between the gas concentrations of the two samples, derived from Fig. 87 and Fig. 88, and not the absolute gas concentration change.

The removal of nitrogen dioxide is favored by some of the chemical vapor infiltrated samples, but the effect is not consistent for all samples. For example, the liquid ion exchanged copper-MFI zeolite adsorbs NO_2 better than the CVI-infiltrated counterpart, as also confirmed in the NO_2 adsorption investigations at room temperature in section 5.5. All other effects, like the decomposition of NO and the formation of other product gases, are not notably affected by the infiltration method. Hence, the presence of external metal particles in some CVI-prepared samples seems not notably to affect the catalytic activity.

In summary, the infiltration of copper is most promising for both the removal of NO_2 and the decomposition of NO. Iron is also well suitable, but its performance largely depends on the applied zeolite framework type. Of all zeolites, mordenite samples are most active in the removal of NO_2. The copper-infiltrated mordenites perform well in the complete decomposition of NO_x. If they are infiltrated with iron, they do not even release much NO. The infiltration method seems not to influence the catalytic activity, which is also in good accordance with other authors (Brandenberger et al. 2008; 2011).

Table 14. Effect of catalytic activity of CVI-catalysts in direct comparison to LIE-catalysts

Catalyst system	Ratio of ion load[1)]	NO_x removal	NO_2 removal	NO decomposition	Concentration of … in the final gas mixture			
					NO	N_2O	N_2	O_2
Fe-MOR	0.7	o	+	-	o	o	+	+
Cu-MOR	0.7	--	o	o	++	+	-	-
Fe-BEA	4.1	o	+	---	o	o	-	o
Cu-BEA	1.9	o	+++	o	+++	o	o	-
Fe-MFI	3.2	+++	+++	++	+	o	-	-
Cu-MFI	4.7	o	--	+	-	o	+	+

[1)] Ratio of ion load of CVI-catalyst to ion load of respective LIE-catalyst; quantified by EDX, standard error: +/-30%;
Legend: "+++" denotes that the CVI-catalyst performs much better than the LIE-catalyst, "o" denotes that there is no difference between the catalysts of both preparation methods, "--" denotes that the CVI-catalyst performs worse than the LIE-catalyst, for details see Table 17 in appendix 9.5.

5.8. Discussion of promising zeolite catalysts

In the beginning of the previous section three catalysts have been identified to be the most promising ones: Cu-MFI-CVI, Cu-MOR-CVI and Fe-MOR-CVI. These catalysts need to be discussed in detail, since they exhibit interesting differences. The inspection of Cu-MFI-CVI reveals that this sample is less attractive for the further application. The mordenite catalysts will be discussed and compared separately.

Fig. 89 shows the time-dependent test gas composition of Cu-MFI-CVI during the 120 minutes of the standard catalysis experiment. The left graphs show the first 90 seconds of the experiment in larger resolution of the time, the right side shows the entire time of 120 minutes.

Cu-MFI-CVI initially adsorbs a large fraction of the supplied NO_2 and converts it immediately into NO, N_2 and O_2. The initially formed NO is slowly further converted into N_2 and O_2, but some oxygen seems to accumulate on the surface, since the concentration of oxygen-containing product species is not rising proportionally. At the end of the experiment a large fraction of the toxic NO_2 is left unconverted and its concentration remains constant. Hence, this catalyst is considered to be less interesting for the intended application.

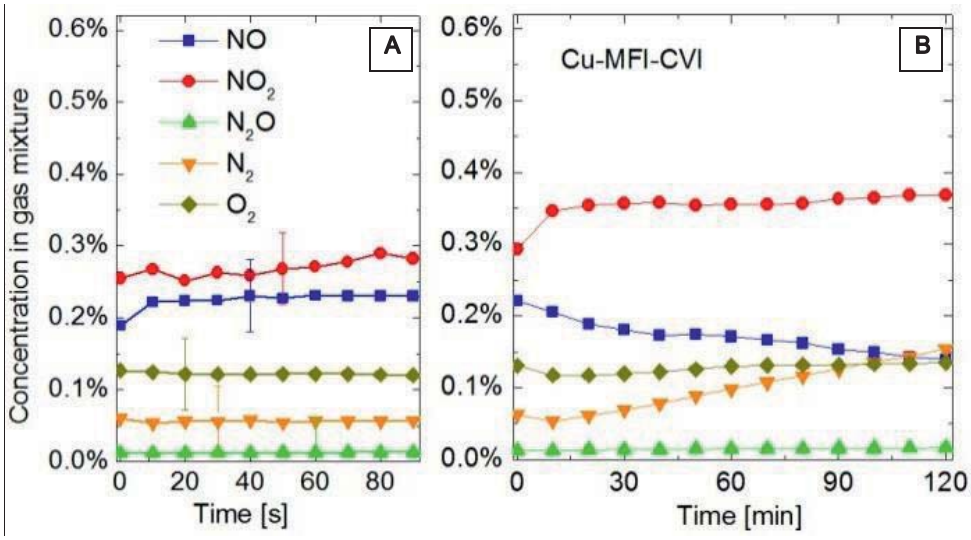

Fig. 89. Composition of the test gas mixture for Cu-MFI-CVI at 425 K during the first 90 seconds (A) and during the entire experimental time (B)

5.8.1. Performance of the mordenite catalysts

The infiltrated mordenite zeolites are especially active in the NOx removal, although they are acting inconsistently. Hence, they provide a good example for the discussion of possible reaction mechanisms in detail. In Fig. 90 the time-resolved gas mixture composition during the 120 minutes catalysis experiment is shown for the non-infiltrated preconditioned MOR, for iron-, copper- and for manganese-infiltrated mordenite.

All catalysts adsorb NO_2 during the first seconds of the experiment and its concentration significantly decreases. The original concentration of NO_2 of 0.9% is not measured, since the test gas mixture has already passed the catalyst sample at the time of the first measurement.

The preconditioned MOR (Fig. 90 A) adsorbs the largest quantity of NO_2, leveling at about 0.2% after one minute. Smaller amounts of NO and O_2 are released and level after 30 seconds. The desorption of N_2O is negligible. The relatively large N_2 release is remarkable for this non-infiltrated sample.

In Fig. 86 Fe-MOR-CVI is identified to be the most promising catalyst regarding the complete decomposition of nitrogen oxides. This catalyst exhibits the largest concentration of molecular nitrogen and the smallest residual sum of all nitrogen oxides. Fe-MOR-CVI (Fig. 90 C) adsorbs NO_2 almost completely. Initially a larger amount of NO is detected (0.2%), but the concentration quickly decreases in the following 60 seconds. Right from the beginning the nitrogen oxides are completely decomposed into nitrogen and oxygen. The initially produced large concentrations of O_2 and N_2 remain constant during the later experiment. However, the oxygen release is lower than expected for the stoichiometric decomposition of NO_2. The residual oxygen is apparently accumulating somewhere on the catalyst.

Cu-MOR-CVI (Fig. 90 B) shows the second best performance in NO decomposition and it completely removes the supplied NO_2 in the first seconds of the experiment. A substantial amount of NO is released with a concentration maximum after 10 minutes and it seems to be slowly converted into the less toxic N_2O. In the following time this NO concentration is decreasing. A substantial amount of O_2 (almost 0.2%) is released right at the beginning, but the concentration is continuously decreasing over the measurement time to almost zero at the end

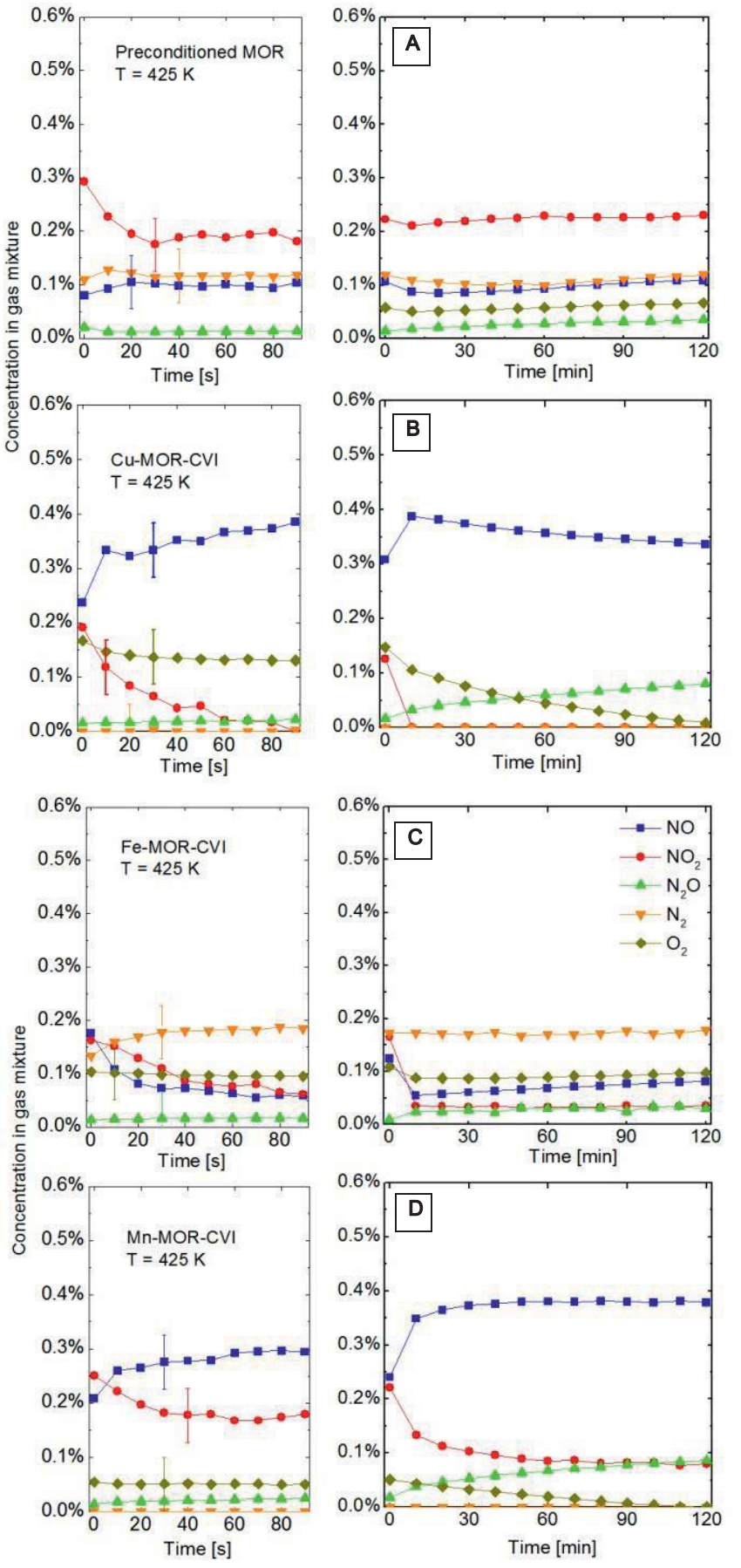

Fig. 90. Gas mixture composition of preconditioned MOR (A), Cu-MOR-CVI (B), Fe-MOR-CVI (C), and Mn-MOR-CVI (D) during 120 minutes NO_2 conversion in recycle flow at 425 K

of the experiment. However, no N_2 is released. The release of N_2O is initially negligible, but increases notably over the measurement time. A large amount of NO remains still unconverted at the end of the experimental time.

Mn-MOR-CVI (Fig. 90 D) removes NO_2 slowly and continuously over the entire experimental time. Inversely to the NO_2 adsorption NO is desorbed. The N_2O concentration is negligible at the beginning, but it increases over the measurement time. N_2 is not released and the O_2 concentration is about 0.05% at the beginning and decreases to zero over the measurement time.

5.8.2. Mass balances

Fig. 91 shows the balances of elements (nitrogen and oxygen) present in the gas phase during the catalysis experiments in Fig. 90. For all samples the nitrogen element fractions are increasing while reaction products of the initially adsorbed NO_2 are released. The element fractions of oxygen-containing reaction products rise for the preconditioned MOR as well as for Fe-MOR-CVI, whereas for Cu-MOR-CVI and Mn-MOR-CVI the oxygen element fractions decrease.

In all cases the oxygen elemental balance is much less than expected from the stoichiometry and concentration of NO_2 in the feed gas. Substantial amounts (60-85% of the oxygen atoms and 30-50% of the nitrogen atoms) remain adsorbed on the catalyst. Preconditioned MOR is the only catalyst exhibiting a larger net element fraction of oxygen than of nitrogen in the gas phase over the entire measurement time.

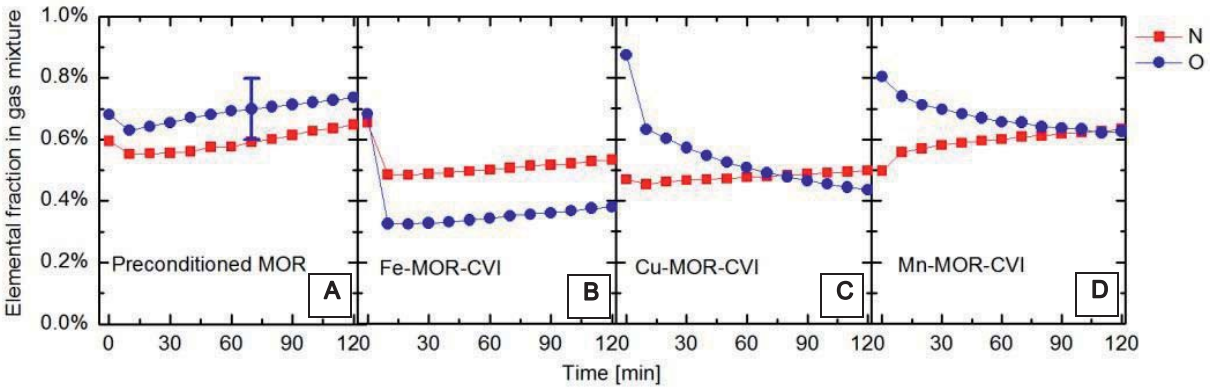

Fig. 91. Elemental fractions in the test gas mixture derived from experiments shown in Fig. 90 of preconditioned MOR (A), Fe-MOR-CVI (B), Cu-MOR-CVI (C) and Mn-MOR-CVI (D); argon and helium are not displayed

5.8.3. Discussion

Although several authors investigate the decomposition of nitrous oxide with a broad set of zeolite catalysts, (Li & Armor 1992; Pieterse et al. 2004), most of the work on the decomposition of nitrogen oxides is focused on the thermally stable ion exchanged ZSM-5 (Iwamoto et al. 1986; Shelef 1992; Kharas 1993; Centi & Perathoner 1995; Heinrich et al. 2002). However, in the present work about the NO_x decomposition at lower temperature the investigated mordenites prove to be the most active candidates.

In contrast to other investigated zeolites (MFI, BEA), molecules diffuse in the mordenite framework only in one dimension along the larger pore channels (Lobo 2003). This process is expected to be slow and in single-file. Hence, the diffusion kinetics may be slower and thus the efficiency of the catalyst may suffer, while on the other hand the residence time of reactant

molecules at active centers is probably increased and decomposition reactions may become more likely.

The adsorption kinetics of NO_2 on the chemical vapor infiltrated mordenite samples is in the order Cu-MOR-CVI > Fe-MOR-CVI > Mn-MOR-CVI > preconditioned MOR. NO_2 adsorbs and dissociates, possibly forming nitrate species with copper ions (Despres et al. 2003):

$$3\,NO_2 + [CuO] \rightarrow NO + Cu^{2+}(NO_3^-)_2 \qquad \textbf{(23)}$$

whereas [CuO] denotes half of the Cu^{2+}-O-Cu^{2+} complex describing copper ions in over-exchanged zeolite bound to lattice or extra-lattice oxygen (Centi & Perathoner 1995). In this case, the residual NO on the right side of the reaction equation quickly desorbs to the feed gas mixture.

The decomposition of the released nitric oxide in the gas phase is still under vivid and controversial discussion (Centi & Perathoner 1995). One mechanism, which was early proposed and broadly accepted, includes the adsorption of nitric oxide on thermally reduced adjacent copper ions inside the zeolite pore channels (Iwamoto et al. 1991; Iwamoto et al. 1992):

$$2\,Cu^{2+} \xrightarrow{thermal\ reduction,e.g.\ -O^{2-}} 2\,Cu^{+} \xrightarrow{+2\,NO} 2\,Cu^{2+} - NO^{-} \xrightarrow{-N_2,-O_2} 2\,Cu^{+} \qquad \textbf{(24)}$$

Further FTIR spectroscopic investigations revealed also the formation and rearrangement of dinitrosylic complexes $Cu^{+}(NO)_2$ to account for the desorption of nitrogen and oxygen (Spoto et al. 1992) and of nitrous oxide, which is typically formed at low temperature (Modén et al. 2002).

However, without a reducing agent in the gas atmosphere the auto-reduction of copper species seems improbable and especially for high-silica zeolites with large spacing of the accommodated copper ions, adjacent copper ions may be scarce (Shelef 1992). Hence, an alternative mechanism has been proposed by Shelef, which avoids the necessity of any redox activity of the cupric ions: Nitric oxide may directly adsorb on Cu^{2+} ions, thus forming 'gem-dinitrosyl' complexes: Cu^{2+}-NO + $NO^{(gas)}$ → $Cu^{2+}(NO)_2$. The interaction of the two adsorbed nitric oxide molecules results in the decomposition of the nitric oxide.

So far, the 'truly' effective mechanism remains unclear and is probably more complicated, since for example isotope labeling experiments revealed at least a partial involvement of lattice oxygen in the decomposition reaction of NO and in the recombination and desorption of oxygen (Valyon et al. 1994).

Independent of the actual mechanism, the ion exchange level has reportedly a large effect on the catalytic activity and the higher the level the better is the NO decomposition (Teraoka et al. 2000). The accommodation of reactive metal species is favored in the zeolites with a moderate Si/Al-ratio. While high-silica zeolites offer few charged sites for the accommodation of reactive foreign ions, these may be well stabilized, but less reactive in zeolites with a high density of charged sites (Voskoboinikov et al. 1998; Benco et al. 2006). Hence, catalysts such as the applied mordenites, may bear an optimal density of catalytically active species.

The structure of the mordenite shows that not all of the possibly active sites are well accessible for gaseous reactants. Fig. 92 provides a schematic drawing of the mordenite structure exhibiting large and small pore channels, which can both accommodate foreign ions. Only the large

pore channels are well accessible for the reactant gases, whereas the ions in the small pore channels do practically not participate in the catalytical reactions (Schoonheydt 1993).

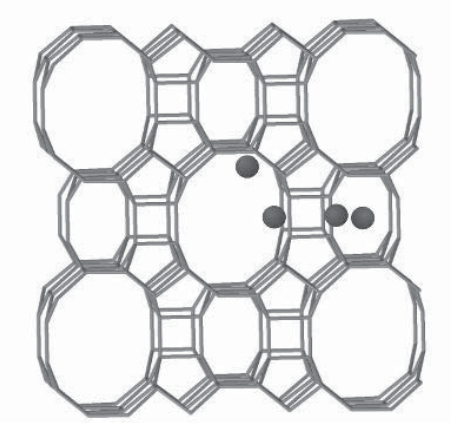

Fig. 92. Schematic structure of mordenite showing accommodated ions (black spheres) on well accessible sites in a large pore channel (center) and on 'hidden' sites in a small pore channel (left side), modified from (Baerlocher & McCusker 2012)

In MFI zeolites and in zeolite Beta the accommodated ions are more facily accessible for gaseous reactants (Kaucký et al. 2000). In addition to the accommodation of reactive metal species, a large Si/Al-ratio also implies a larger availability of Brønsted acid sites. These are likely to take part in the catalysis (Parrillo & Gorte 1993), which explains the good activity even of non-infiltrated zeolites.

The excessive ion load of the copper-infiltrated MFI would be expected to confer this catalyst with a larger number of active sites and superior catalytic activity. However, this sample is weakly performing in the decomposition of nitrogen dioxide. In fact, many of the metal species are probably inaccessibly buried in the metal species particles and cannot participate in the catalytic activity, although some authors report that the degree of metal species agglomeration alone would not affect the nitric oxide decomposition (Heinrich et al. 2002).

Following a similar argument, the catalytic activity in the decomposition of nitric oxide of the copper-infiltrated mordenite is much smaller than the activity of the iron-infiltrated mordenite, despite their identical Si/Al-ratio and ion load. However, the micropore volume of the former is vigorously reduced. Hence, the pore structure of this sample seems to be heavily damaged or blocked during the infiltration procedure and the introduced, but destabilized copper species are likely to aggregate and at least partially deactivate. Furthermore, the copper aggregations in the damaged framework of copper-mordenite may possess a large affinity to oxidize, which can explain the decrease of the oxygen concentration over the experimental time.

It has to be noted, that a part of the framework aluminum atoms can also be thermally extracted into extra-lattice species (Müller et al. 2000). This may occur during the preconditioning procedure at 973 K (see section 3.1.3) or by framework damage during the infiltration procedure as discussed for the copper-CVI-infiltrated MFI (Cu-MFI-CVI, section 5.3). Such framework destruction would be associated with a loss of Brønsted acidic sites as possibly active centers (Walker 1995) and is expected to diminish the activity of the catalyst. Zeolites with a lower Si/Al-ratio are known to be less stable in high temperature conditions (Cruciani 2006). Hence, the mordenite samples (Cu-MOR-CVI, Mn-MOR-CVI, see Table 11) are more sensitive to a harsh thermal treatment than the other zeolite catalysts.

Although most samples quickly reduce the initially supplied nitrogen dioxide into nitric oxide, some catalysts like copper-CVI-infiltrated MFI and non-infiltrated mordenite seem to fail in this reaction very soon. In case of the non-infiltrated mordenite adsorbed nitrogen oxide species and dissociated oxygen atoms may saturate the adsorption sites in the zeolite and soon inhibit further decomposition reactions (Garin 2001).

However, the nitrogen dioxide concentration of the copper-MFI-catalyst remains very large, while the nitric oxide concentration decreases and molecular nitrogen is slowly released to the test gas atmosphere. The external copper species in this sample may participate in the overall reaction, being eventually loaded with loosely adsorbed oxygen during the initial NO_x reduction (Olsson et al. 2009), which is at lower temperature also accumulating in form of Cu-NO_2 and -NO_3 species at the catalyst surface (Centi & Perathoner 1995; Despres et al. 2003). At longer time the catalyst is likely to release NO_2 or re-oxidize NO to NO_2 (Olsson et al. 2009), thus compensating any further reduction of the amount of NO_2.

Reactions of the metal species deposited on the outside of the zeolite crystal – as observed exclusively in the CVI-prepared samples (Fig. 25 and Fig. 75) – may contribute to the overall activity. A fraction of Cu^{2+} may be auto-reducing into Cu^{+} during the catalyst preconditioning (Jacobs et al. 1976). Upon exposure to NO_x the Cu^{+} is re-oxidized to Cu^{2+} (Liu & Robota 1993), thus catalyzing the reduction of nitric oxide for example into nitrous oxide (London & Bell 1973). A similar reaction can be assumed for the iron oxide species (Otto & Shelef 1970).

Any decomposition of the released nitrous oxide is not observed in the current experiments. The direct decomposition is expected to require elevated temperatures or a gaseous reactant with the applied set of catalysts (Pieterse et al. 2004).

In summary, the complete NO_2 decomposition is highly preferred in mordenite zeolites, probably due to its moderate Si/Al-ratio and an ideal stabilization of active species in the pore channels. Fe-MOR-CVI is identified to be the most efficient catalyst since it quickly adsorbs NO_2 and releases more N_2 and O_2 than any other investigated catalyst. Cu-MOR-CVI and Mn-MOR-CVI adsorb NO_2 as well, but they convert it mainly into NO. No nitrogen is released by these samples and the substantial amount of released oxygen is further consumed, possibly by the slow oxidation of metallic phases.

5.9. Structural changes during the catalysis process

During the thermal and chemical treatment of the catalytical process the catalyst surface and structure undergo interesting changes, which are usually known as catalyst ‘aging’. The observed phenomena are presented in the following and are discussed at the end of this section.

5.9.1. Changes of the pore volume

The pore volume of the synthesized catalysts considerably changes during the infiltration process (see section 5.4), as well as during the standard catalysis experiment. In Fig. 93 the change of the micropore volume and of the total pore volume is analyzed for the chemical vapor infiltrated and for the liquid ion exchanged Cu-MFI catalyst in relation to the preconditioning, infiltration and catalysis process steps.

During the preconditioning step the micropore volume is slightly increased, but it is largely decreasing during the subsequent chemical vapor infiltration. The total pore volume remains

unaffected during these first process steps, but it is largely increasing during the catalysis experiment. The liquid ion exchanged sample exhibits a reduced micropore volume and relatively large total pore volume after the preparation and they are not changing during the catalysis experiment.

Fig. 94 shows the development of the total pore volume and micropore volume for Fe-MFI-CVI. The chemical vapor infiltration and also the catalysis experiment do not cause any pore volume change. The pore volumes of the liquid ion exchanged sample are comparable to those of the liquid ion exchanged copper-MFI and only the measured micropore volume is slightly decreasing during the catalysis.

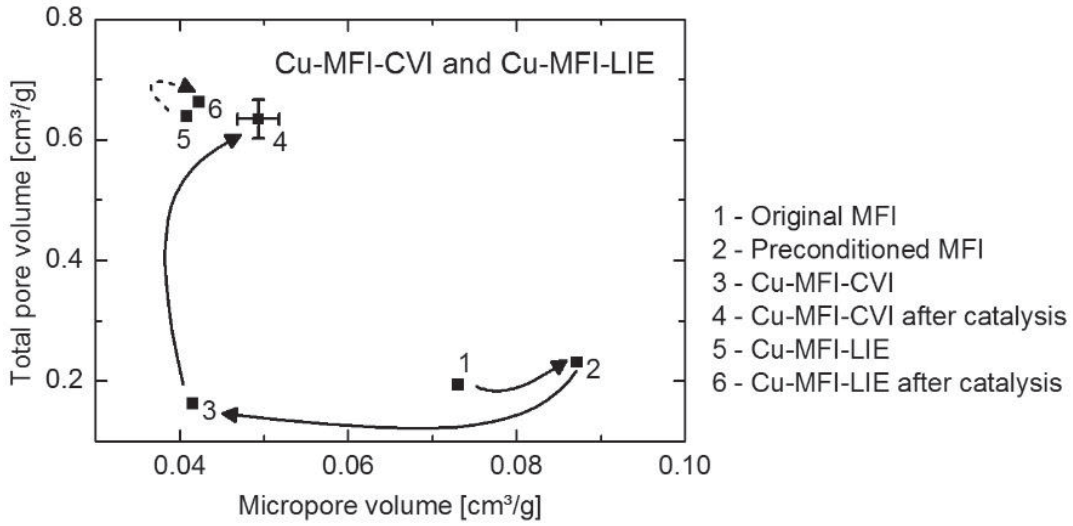

Fig. 93. Evolution of the total pore volume and the micropore volume during infiltration and catalysis process for Cu-MFI; Solid line: Cu-MFI-CVI, dashed line: Cu-MFI-LIE

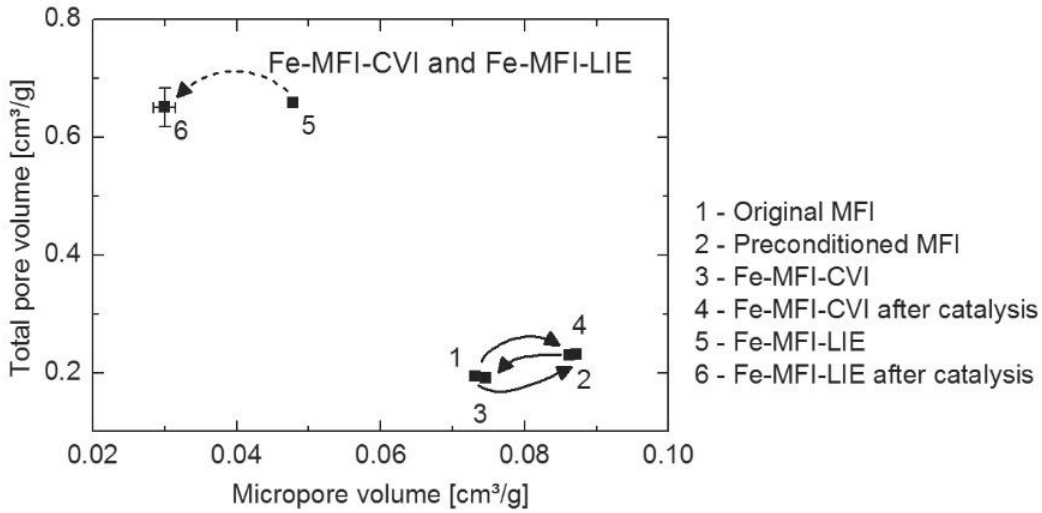

Fig. 94. Evolution of the total pore volume and the micropore volume during infiltration and catalysis process for Fe-MFI; Solid line: Fe-MFI-CVI, dashed line: Fe-MFI-LIE

5.9.2. Changes in the pore size distribution

Further insight into the structural changes during the catalysis experiment can be derived from the pore size distribution of the samples. Fig. 95 shows the pore size distribution of the investigated iron- and copper-infiltrated MFI substrates before and after the catalysis experiment. The pore volume peaks are by one order of magnitude larger in the small micropore region

compared to the large micropore and mesopore regions. For this reason the two regions are displayed separately.

No substantial change during catalysis is observed in the small micropore region (left graphs in Fig. 95). The as-synthesized Fe-MFI-CVI and Cu-MFI-CVI exhibit two similar maxima at 3-4 and at 6 nm pore width. For Fe-MFI-CVI these maxima are conserved after the catalysis experiment. The second maximum is slightly shifted from 6 nm to 5 nm, which could be an inaccuracy of the underlying NLDFT module. In the mesopore region no pores are observed for Fe-MFI-CVI.

For Cu-MFI-CVI the second maximum (at 6 nm) seems to merge during the catalysis with the first maximum at 3 nm. The sample emerges a mesopore system after the catalysis which is not present before. Due to the very defined micropore channel system of the zeolite crystallites, pores, which are larger than 1 nm, have to be assigned to the inter-crystallite pores of adjacent zeolite particles (see section 5.4).

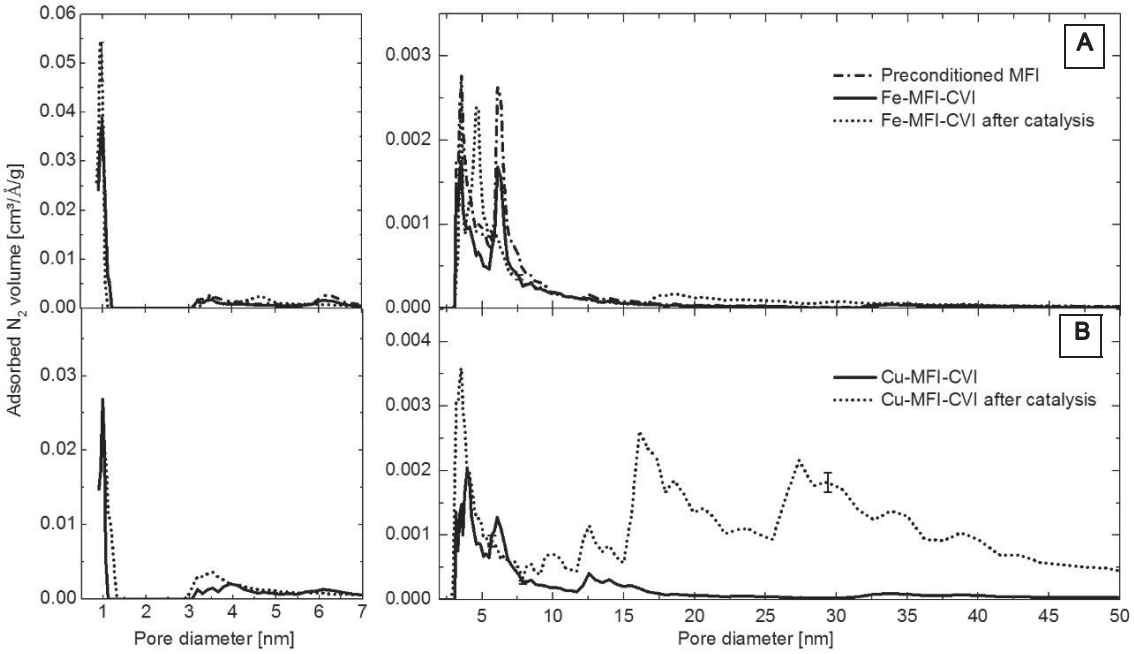

Fig. 95. Pore size distribution of Fe-MFI-CVI (A) and Cu-MFI-CVI (B) before and after catalysis in the micropore/small mesopore region (left graphs) and in the mesopore region (right graphs, note the enlarged y-axis)

5.9.3. Changes of the crystalline species

In section 5.3 at least some of the deposited copper species in Cu-MFI-CVI are identified to be metallic crystallites. An investigation of these crystallites by X-ray diffraction (Fig. 96) before and after the catalysis experiment reveals no changes of these species. The average copper crystallite size of about 25 nm, estimated by the Scherrer equation, is well preserved. No crystalline copper oxide species are detected, neither before, nor after the catalysis.

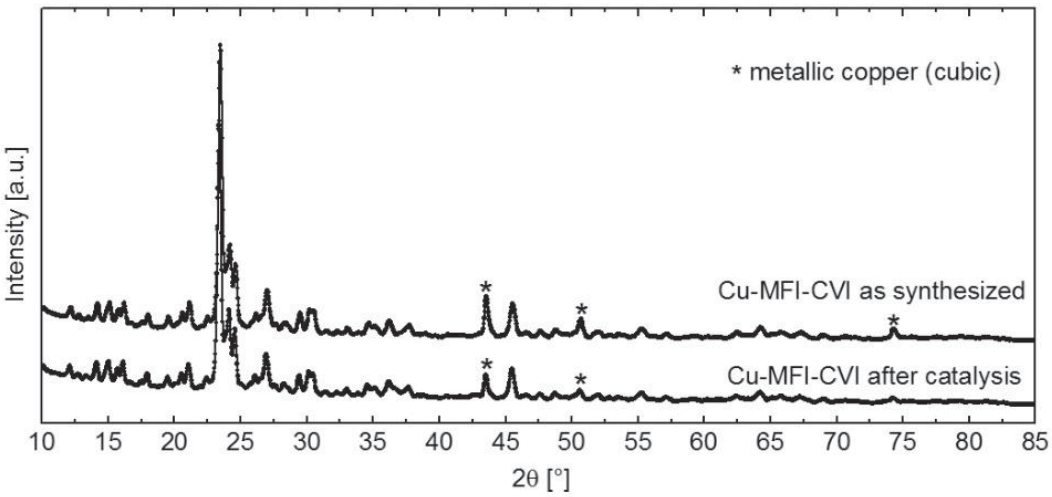

Fig. 96. X-ray diffractograms of Cu-MFI-CVI before and after catalysis

5.9.4. Discussion

In the preconditioning step the ammonia ions and any other adsorbed species are removed from the as-delivered samples and the micropore volume of the eventually protonated MFI zeolite is slightly increased. The introduction of copper species into the pore channels decreases the micropore volume notably, either by accommodated copper species, or by blocking of the pore entries, or by framework damage, e.g. due to the thermal treatment. The latter seems, however, unlikely, since the preconditioning step applies a similar thermal treatment. The chemical vapor infiltration reduces the total pore volume by more than 50%, indicating that the inter-crystallite pores are probably filled or blocked by the generation of copper species.

The total pore volume of the liquid ion exchanged sample is quite large right from the beginning. This phenomenon is probably caused by inter-crystallite pores of the smaller particles in the as-delivered zeolite. The liquid ion exchanged samples are synthesized from a slightly different material. As described in section 2.5.4, their as-delivered MFI zeolite exhibits smaller particles in comparison to the material applied for the chemical vapor infiltrated samples. An increase of the total pore volume of the CVI-samples to the volume of the LIE-samples is observed during the catalysis step. It may be speculated that smaller particles disintegrate from the originally larger agglomerations in the oxidative environment of the catalysis.

For Fe-MFI-CVI (Fig. 94) no substantial changes of the micropore or of the total pore volume are observed during the CVI-infiltration process and the subsequent catalytic testing. In this case, the total pore volume is not increasing during the catalysis and the micropore volume is also unaffected by the infiltration procedure with Ferrocene. As already discussed in section 5.4, this is possibly an indication for a weak penetration of the pore channels by the precursor due to steric hindrance.

As discussed in sections 5.3 and 5.4, the deep infiltration of large amounts of copper into the zeolite pore channels may block some pores, reduce the micropore volume and also damage the framework. While Cu-MFI-CVI is observed to bear copper particles, which are not observed on Cu-MFI-LIE, the differences in the loss of micropore volume between these two samples are small. Hence, framework damage due to cluster growth appears to be less likely. Furthermore, the similarities in the pore size distribution of Cu-MFI-CVI after catalysis and of the as-delivered Cu-MFI-LIE (see section 3.1.4.) suggest an almost identical macrostructure.

However, neither the deposition of copper, nor the calcination procedures alone cause any large increase of the total pore volume. Only in the oxidizing conditions of the catalysis experiment the sample macrostructure seems to change. The responsible mechanism could possibly involve the migration of copper ions inside the zeolite framework (Itho et al. 1994; Benco et al. 2006; Vennestrom et al. 2014). Copper ions could migrate out of the framework and form larger oxides, which could change the surface chemistry of the zeolite crystallites and eventually result in the deactivation of the catalyst (Shwan et al. 2013). However, the actual origin of the increase of the total pore volume would require a deeper investigation, which cannot be provided in the present work.

The implications of the particle disintegration may be important, since the crystal size of zeolites can reportedly have an effect on the catalytic activity, e.g. due to the ratio of external and internal surface (Sugimoto et al. 1987). However, any direct relation between the pore volume and the catalytic activity is not found in the present work, as derived from respective measurements shown in appendix 9.4.

Summarizing, some of the infiltrated zeolite catalysts undergo a substantial change of their micropore and total pore volume during the infiltration and catalysis process. Independent of the infiltration method, the introduction or deposition of metal species significantly reduces the micropore volume. The chemical vapor infiltration of large amounts of copper additionally may block the inter-crystallite pores between the zeolite crystallites. During catalysis the total pore volume of zeolite crystallites can increase, but the actual reason remains unclear. The crystalline metallic copper particles of Cu-MFI-CVI are well preserved during the catalysis. The micropore volume has no observable independent effect on the catalytic conversion of NO_x or on the release of reaction products.

5.10.Summary and conclusions

MFI, Beta and mordenite zeolites are modified by chemical vapor infiltration with iron, copper and manganese. The prepared catalysts are compared with analogous samples prepared by liquid ion exchange. The catalytic activity in the conversion of NO_2 is monitored at 425 K in a recycle flow for 120 minutes and the structure of the samples and changes during the infiltration and catalysis are investigated.

Some metal oxide species are deposited on the external framework of the CVI-infiltrated zeolites. Especially the infiltration of Ferrocene into the narrow pore channels of MFI zeolite causes difficulties, probably due to steric hindrance. Most zeolites, which are infiltrated with acetylacetonate-based precursors show a reduced micropore volume, indication deep infiltration or blocking of pore entries. However, the zeolite framework may be damaged during the infiltration by the growth of intra-framework particles exceeding the diameter of the zeolite supercage.

The pore size distribution of the infiltrated zeolites is not substantially affected by the infiltration procedure, but the inter-crystallite pores of chemical vapor infiltrated samples are partially filled with deposited species. Only the copper-infiltrated samples exhibit metallic crystallites, probably on the surface of the zeolite crystallites.

The NO_2 conversion in Cu-MFI-LIE starts at low temperature (323 K) with the adsorption of NO_2 and conversion of a small fraction. With rising temperature (up to 673 K) the adsorption

is increasingly limited and NO_2 is reduced to NO. The lowest possible temperature for the efficient NO_x removal is 423 K.

Among the investigated framework types, the NO_2 conversion is at an optimum with mordenite zeolites, probably due to an ideal combination of the pore channel architecture and the moderate Si/Al-ratio. The introduction of copper leads for most zeolite catalysts to a superior performance in the complete decomposition of nitrogen oxides and the average metallic copper crystallite size is well preserved during the catalysis. However, the chosen infiltration method (liquid ion exchange or chemical vapor infiltration) seems not to exhibit any independent effect on the catalytic activity.

Of all samples, Fe-MOR-CVI shows the largest complete decomposition of nitrogen oxides in measures of molecular nitrogen release. This sample is identified to be the most efficient catalyst for complete NO_x conversion at 425 K.

In direct comparison with the best performing activated carbon catalyst (IWM-prepared iron- and silica-co-deposited activated carbon, see section 4.9), Fe-MOR-CVI shows a conversion of nitrogen oxides into nitrogen, without formation of any still toxic carbon oxides (Fig. 97). Hence, the zeolite catalyst is suggested for further application in the targeted human workspace environments.

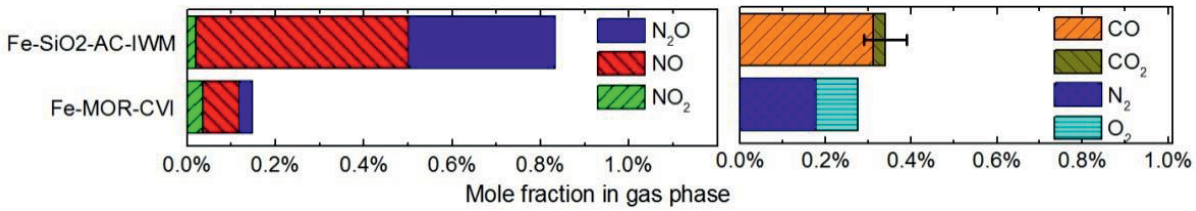

Fig. 97. Gas species concentrations of best performing zeolite and activated carbon catalyst after 120 minutes NO_2 conversion in recycle flow at 425 K; initial gas mixture: 0.9% NO_2, 10% Ar, 89.1% He

6. Summary and conclusions

NO_x emissions are among the most harmful pollutants in ambient air. The present work investigates catalyst systems for the direct NO_x removal at normal pressure and low temperature (425 K). Commercially available activated carbon and three different zeolite types are used as catalyst support and are infiltrated via chemical vapor infiltration with iron, copper and manganese precursors. The resulting catalysts are characterized regarding their structure and catalytical properties.

The activated carbon-based catalysts are deeply and homogeneously infiltrated, although a particle formation in larger cavities and cracks is observed. Some of the particles probably exhibit a metallic core with an oxide shell. During infiltration at moderate metal loads the pore system remains well accessible. The infiltration at high metal loads slightly blocks some of the micro- and mesopores.

At room temperature NO_2 is probably adsorbed in micropores and subsequently iron or iron oxide species may be involved in the formation of surface nitrites and nitrates. All activated carbon catalysts convert NO_2 almost completely, even at 425 K. The major conversion products are NO, N_2O and CO. The introduction of metals or metal oxides into the activated carbons increases the conversion of NO into CO and N_2O. Copper- and manganese-infiltrated activated carbon catalysts exhibit the largest conversion of NO, whereas the iron-infiltrated catalysts are most active in the formation of CO and N_2O. The latter two reaction products are by far less toxic than the original nitrogen oxides (BAuA 2006; WHO 2010).

The micropores in the activated carbon samples have a positive effect on the catalytic activity in general, possibly due their contribution to the active surface area and the overlapping potentials inside the pores. The co-deposition of silica in the catalysts enhances the desorption of CO and N_2O, probably by facilitating the oxygen transport to reactive carbon sites. Additionally, the introduced silica seems to stabilize the pore system and probably prevents the strong chemisorption of reaction products during the catalysis process. Hence, the best applicable activated carbon catalyst is an iron-infiltrated and silica-co-doped activated carbon, which is prepared by the incipient wetness method.

The chemical vapor infiltration process proves to be a viable route for the infiltration of catalyst supports (activated carbons and zeolites) with transition metal species. Some metal species are deposited on the external of the zeolites crystallites, but only the copper-infiltrated samples exhibit metallic crystallites. Some pore channels of most catalysts seem to be deeply infiltrated, although pore entries might become blocked. The zeolite framework can be damaged during the infiltration procedure, probably due to excessively growing intra-framework clusters exceeding the width of the zeolite supercage.

Some of the pores between the zeolite crystallites are filled during the chemical vapor infiltration process. The total pore volume of the copper-infiltrated zeolite crystallites is increasing during the catalysis process, but the actual mechanism remains unclear and requires further investigation. The micropore volume of the zeolites does not exhibit an observable independent effect on the catalytic conversion of NO_x or the release of reaction products.

As for the activated carbon catalysts, the infiltration method of the zeolites shows no independent effect on the catalytic activity. The average size of the metallic copper crystallites, which

are formed during the chemical vapor infiltration of activated carbons and zeolites, is well preserved during the conditions of the catalysis experiments.

Among the investigated zeolite framework types, the decomposition of NO_2 is best promoted by mordenite zeolites, probably due to an ideal combination of several factors like the availability of stabilized active species inside the pore channels and a high intrinsic acidity, caused by the low Si/Al-ratio. Fe-MOR-CVI is identified to be the most promising zeolite catalyst. This sample exhibits the lowest NO_x concentration after the experiment and the greatest release of oxygen and nitrogen, hence it is most efficient in completely decomposing the supplied NO_x. At the investigated low temperature of 425 K, this catalyst is even outperforming the iron-infiltrated, silica-co-doped activated carbon and the well-characterized and often quoted Cu-ZSM-5 catalyst.

7. Limitations of the study and further research outlook

Further research is required to proceed with promising catalyst candidates at lower NO_x concentrations. A typical NO concentration in exhaust gas would be in the range of 600 to 1200 ppm (Garin 2001) and substantially lower in typical human workspace situations. The applied experimental setup at given cost budget revealed a lower limit of 0.9% NO_2 in the feed gas for reliable and reproducible results as tested in the preliminary experiments. Indeed, most other studies use a larger NO_x concentration than realistic in ambient air (Walker 1995).

The elucidation of the effective reaction mechanisms and respective reaction kinetics is difficult using a recycle reactor setup. Adsorption and reactions of the primary educts can be superposed by adsorption and reaction of the reaction products. The importance of this effect is increasing with every gas recirculation (Thomas et al. 1997, p. 481). However, the advantages of a recycle reactor include the investigation of the net effects in a more realistic scenario than investigated using plug flow and a higher sensitivity for kinetically slow reactions, as investigated in this work.

The investigation of the actual nature of the catalytically active sites is out of scope of the present work. Elaborate research has been performed in this field on some of the investigated catalyst systems (Centi & Perathoner 1995; Ertl 2010). The results are ambiguous and will probably remain under vivid discussion for a considerable time.

In order to develop the investigated catalysts into a broadly applicable filter-integrated catalyst system, further research may be conducted in a number of interesting fields:

1) Further studies should be directed on the catalytic activity of promising catalyst systems like copper- or iron-infiltrated mordenite, or on catalysts prepared by the combined infiltration of copper and iron into mordenite.

2) The nature of active sites may be studied in greater detail, including for example characterization by XPS, XANES or EXAFS, in order to synthesize more efficient catalysts. Studies in this field concentrate mainly on Cu-ZSM-5, but investigations on the effects in other zeolite systems remain scarce. Several reaction mechanisms of direct NO_x decomposition in activated carbons and zeolites are proposed in the literature, but few studies concentrate on the kinetics and exact conditions of each mechanism.

3) Further research may be directed on the conversion of very low concentrations of NO_x in ambient air as well as on the effects of co-adsorption and interactions of oxygen, of other pollutants like SO_x or CO_x and water vapor. The results will be of great interest for the commercial application of the catalysts.

4) The emission of unwanted intermediate products like CO and N_2O may be minimized and further studies should diminish the gasification of carbon catalyst during the NO_x decomposition reaction.

5) The aging of catalysts requires further investigations in a realistic environment. Possibly, catalysts can be regenerated and the technology and associated costs need to be analyzed.

8. References

Aarna I., Suuberg E. M. 1997. A review of the kinetics of the nitric oxide-carbon reaction. *Fuel* **76**. 475-491

Aarna I., Suuberg E. M. 1999. The Role of Carbon Monoxide in the NO-Carbon Reaction. *Energy & Fuels* **13**. 1145-1153

Adelman B. J., Lei G. D., Sachtler W. M. H. 1994. Co-adsorption of nitrogen monoxide and nitrogen dioxide in zeolitic De-NO_x catalysts. *Catalysis Letters* **28**. 119-130

Aksoylu A. E., Faria J. L., Pereira M. F. R., Figueiredo J. L., Serp P., Hierso J. C., Feurer R., Kihn Y., Kalck P. 2003. Highly dispersed activated carbon supported platinum catalysts prepared by OMCVD: A comparison with wet impregnated catalysts. *Applied Catalysis A: General* **243**. 357-365

Al-Abadleh H. A., Grassian V. H. 2003. Oxide surfaces as environmental interfaces. *Surface Science Reports* **52**. 63

Azambre B., Collura S., Trichard J. M., Weber J. V. 2006. Nature and thermal stability of adsorbed intermediates formed during the reaction of diesel soot with nitrogen dioxide. *Applied Surface Science* **253**. 2296-2303

Baerlocher C., McCusker L. B. **2012**. *Database of Zeolite Structures*. http://www.iza-structure.org/databases/

Baerlocher C., McCusker L. B., Olson D. H. **2007**. *Atlas of zeolite framework types*: Elsevier Science

Ballester J. M., Dopazo C., Fueyo N., Hernández M., Vidal P. J. 1997. Investigation of low-NO_x strategies for natural gas combustion. *Fuel* **76**. 435-446

Barrett E. P., Joyner L. G., Halenda P. P. 1951. The Determination of Pore Volume and Area Distributions in Porous Substances. I. Computations from Nitrogen Isotherms. *Journal of the American Chemical Society* **73**. 373-380

Bartholomew C. H. 2001. Mechanisms of catalyst deactivation. *Applied Catalysis A: General* **212**. 17-60

Bashkova S., Bandosz T. J. 2009a. Adsorption/Reduction of NO_2 on Graphite Oxide/Iron Composites. *Industrial & Engineering Chemistry Research* **48**. 10884

Bashkova S., Bandosz T. J. 2009b. The effects of urea modification and heat treatment on the process of NO_2 removal by wood-based activated carbon. *Journal of Colloid and Interface Science* **333**. 97-103

Bashkova S., Bandosz T. J. 2011. Reactive Adsorption of NO_2 at Ambient Conditions on Iron-Containing Polymer-Based Porous Carbons. *ChemSusChem* **4**. 404-412

BAuA. **2006**. Technische Regeln für Gefahrstoffe, TRGS 900

Bell A. T. 2003. The Impact of Nanoscience on Heterogeneous Catalysis. *Science* **299**. 1688-1691

Benco L., Bucko T., Grybos R., Hafner J., Sobalik Z., Dedecek J., Hrusak J. 2006. Adsorption of NO in Fe^{2+}-Exchanged Ferrierite. A Density Functional Theory Study. *The Journal of Physical Chemistry C* **111**. 586-595

Bertrand G. L., Caboche G., Dufour L. C. 2000. Low-pressure-MOCVD $LaMnO_{3\pm d}$ very thin films on YSZ (100) optimized for studies of the triple phase boundary. *Solid State Ionics* **129**. 219

Bhambhani M. R., Cutting P. A., Sing K. S. W., Turk D. H. 1972. Analysis of nitrogen adsorption isotherms on porous and nonporous silicas by the BET and alpha-s methods. *Journal of Colloid and Interface Science* **38**. 109-117

Bitter J. H., Battiston A. A., van Donk S., de Jong K. P., Koningsberger D. C. 2003. Accessibility of the Fe-species in Fe/ZSM-5 prepared via $FeCl_3$ sublimation. *Microporous and Mesoporous Materials* **64**. 175-184

Boehm H. P. 1994. Some aspects of the surface chemistry of carbon blacks and other carbons. *Carbon* **32**. 759-769

Boreskov G. K. **2003**. *Heterogeneous catalysis*: Nova Science Pub Incorporated

Bosch H., Janssen F. **1988**. *Catalytic reduction of nitrogen oxides. A review on the fundamentals and technology*: Elsevier VII p

Bradley M. J., Jones B. M. 2002. Reducing Global NO_x Emissions: Developing Advanced Energy and Transportation Technologies. *AMBIO: A Journal of the Human Environment* **31**. 141-149

Brandenberger S., Kröcher O., Tissler A., Althoff R. 2008. The State of the Art in Selective Catalytic Reduction of NO_x by Ammonia Using Metal-Exchanged Zeolite Catalysts. *Catalysis Reviews* **50**. 492-531

Brandenberger S., Kröcher O., Tissler A., Althoff R. 2011. Effect of Structural and Preparation Parameters on the Activity and Hydrothermal Stability of Metal-Exchanged ZSM-5 in the Selective Catalytic Reduction of NO by NH_3. *Industrial & Engineering Chemistry Research* **50**. 4308-4319

Brandin J. G. M., Andersson L. A. H., Odenbrand C. U. I. 1989. Catalytic reduction of nitrogen oxides on mordenite some aspect on the mechanism. *Catalysis Today* **4**. 187-203

Brosius R., Habermacher D., Martens J. A., Vradman L., Herskowitz M., Capek L., Sobalik Z., Dedecek J., Wichterlova B., Tokarova V., Gonsiorova O. 2004. NO oxidation kinetics on iron zeolites: Influence of framework type and iron speciation. *Topics in Catalysis* **30-31**. 333-339

Brunauer S., Emmett P. H., Teller E. 1938. Adsorption of Gases in Multimolecular Layers. *Journal of the American Chemical Society* **60**. 309-319

Bulushev D. A., Renken A., Kiwi-Minsker L. 2005. Formation of the Surface NO during N_2O Interaction at Low Temperature with Iron-Containing ZSM-5. *The Journal of Physical Chemistry B* **110**. 305-312

Burch R., Breen J. P., Meunier F. C. 2002. A review of the selective reduction of NO_x with hydrocarbons under lean-burn conditions with non-zeolitic oxide and platinum group metal catalysts. *Applied Catalysis B: Environmental* **39**. 283

Burch R., Millington P. J. 1993. Role of propene in the selective reduction of nitrogen monoxide in copper-exchanged zeolites. *Applied Catalysis B: Environmental* **2**. 101-116

Burch R., Millington P. J. 1995. Selective reduction of nitrogen oxides by hydrocarbons under lean-burn conditions using supported platinum group metal catalysts. *Catalysis Today* **26**. 185

Busca G., Lietti L., Ramis G., Berti F. 1998. Chemical and mechanistic aspects of the selective catalytic reduction of NO_x by ammonia over oxide catalysts: A review. *Applied Catalysis B: Environmental* **18**. 1-36

Busca G., Lorenzelli V. 1981. Infrared study of the adsorption of nitrogen dioxide, nitric oxide and nitrous oxide on hematite. *Journal of Catalysis* **72**. 303-313

Busch M., Bergmann U., Sager U., Schmidt W., Schmidt F., Notthoff C., Atakan B., Winterer M. 2011. Synthesis of Active Carbon-Based Catalysts by Chemical Vapor Infiltration for Nitrogen Oxide Conversion. *Journal of Nanoscience and Nanotechnology* **11**. 7956-7961

Calvino-Casilda V., López-Peinado A. J., Durán-Valle C. J., Martín-Aranda R. M. 2010. Last Decade of Research on Activated Carbons as Catalytic Support in Chemical Processes. *Catalysis Reviews* **52**. 325-380

Campa M. C., Indovina V., Minelli G., Moretti G., Pettiti I., Porta P., Riccio A. 1994. The catalytic activity of Cu-ZSM-5 and Cu-Y zeolites in NO decomposition: Dependence on copper concentration. *Catalysis Letters* **23**. 141-149

Capek L., Kreibich V., Dedecek J., Grygar T., Wichterlova B., Sobalik Z., Martens J. A., Brosius R., Tokarova V. 2005. Analysis of Fe species in zeolites by UV-VIS-NIR, IR spectra and voltammetry. Effect of preparation, Fe loading and zeolite type. *Microporous and Mesoporous Materials* **80**. 279-289

Carabineiro S. A., Fernandes F. B., Silva R. J. C., Vital J. S., Ramos A. M., Fonseca I. M. 2008. N_2O reduction by activated carbon over iron bimetallic catalysts. *Catalysis Today* **133-135**. 441-447

Casanova F., Chiang C. E., Li C. P., Roshchin I. V., Ruminski A. M., Sailor M. J., Schuller I. K. 2008. Effect of surface interactions on the hysteresis of capillary condensation in nanopores. *EPL (Europhysics Letters)* **81**. 26003

Cejka J., Centi G., Perez-Pariente J., Roth W. J. 2012. Zeolite-based materials for novel catalytic applications: Opportunities, perspectives and open problems. *Catalysis Today* **179**. 2-15

Centi G., Perathoner S. 1995. Nature of active species in copper-based catalysts and their chemistry of transformation of nitrogen oxides. *Applied Catalysis A: General* **132**. 179-259

Chan L. K., Sarofim A. F., Beér J. M. 1983. Kinetics of the NO-carbon reaction at fluidized bed combustor conditions. *Combustion and Flame* **52**. 37-45

Chang Y.-F., McCarty J. G. 1997. Isotopic Study of NO_x-Decomposition over Cu- or Co-exchanged ZSM-5 Zeolite Catalysts. *Journal of Catalysis* **165**. 1-11

Chen H.-Y., Sachtler W. M. H. 1998. Activity and durability of Fe/ZSM-5 catalysts for lean burn NO_x reduction in the presence of water vapor. *Catalysis Today* **42**. 73-83

Chen H.-Y., Wang X., Sachtler W. M. H. 2000. Reduction of NO_x over various Fe/zeolite catalysts. *Applied Catalysis A: General* **194-195**. 159-168

Choi M. J., Kim J. S., Lee S. B., Lee W. Y., Lee K. W. **2003**. Promotion of CO_2 hydrogenation in fixed bed recycle reactors. In *Greenhouse Gas Control Technologies-6th International Conference*, ed. J. Gale, Y. Kaya, pp. 1441-: Pergamon

Chorkendorff I., Niemantsverdriet J. W. **2007**. *Concepts of modern catalysis and kinetics*: Wiley-VCH

Cotton F. A., Wilkinson G. 1952. The Heat of Formation of Ferrocene. *Journal of the American Chemical Society* **74**. 5764-5766

Cruciani G. 2006. Zeolites upon heating: Factors governing their thermal stability and structural changes. *Journal of Physics and Chemistry of Solids* **67**. 1973-1994

Curdts B., Helmich M., Pasel C., Bathen D., Atakan B., Pflitsch C. 2013. Upscaling the Chemical Vapor Infiltration Process of Activated Carbon with TMS. *Physics Procedia* **46**. 248-254

Cybulski A., Moulijn J. A. 1994. Monoliths in heterogeneous catalysis. *Catalysis Reviews - Science and Engineering* **36**. 179-270

Delhaès P. **2003**. Chemical vapor infiltration processes of carbon materials. In *Fibers and composites*, ed. P. Delhaès: CRC Press

Delmas R., Serca D., Jambert C. 1997. Global inventory of NO_x sources. *Nutrient Cycling in Agroecosystems* **48**. 51-60

Despres J., Koebel M., Kröcher O., Elsener M., Wokaun A. 2003. Adsorption and desorption of NO and NO_2 on Cu-ZSM-5. *Microporous and Mesoporous Materials* **58**. 175

Deutschmann O., Knözinger H., Kochloefl K., Turek T. **2009**. Heterogeneous Catalysis and Solid Catalysts. In *Ullmann's Encyclopedia of Industrial Chemistry*: Wiley-VCH Verlag GmbH & Co. KGaA

Dupel P., Pailler R., Bourrat X., Naslain R. 1994. Pulse chemical vapour deposition and infiltration of pyrocarbon in model pores with rectangular cross-sections. *Journal of Materials Science* **29**. 1056-1066

Dyagileva L. M., Mar'in V. P., Tsyganova E. I., Razuvaev G. A. 1979. Reactivity of the first transition row metallocenes in thermal decomposition reaction. *Journal of Organometallic Chemistry* **175**. 63-72

Eley D. D., Rideal E. K. 1940. Parahydrogen conversion on tungsten. *Nature* **146**. 401-402

Elving P., McElroy W. 1941. Removal of Nitrogen Oxides in Semimicrodetermination of Carbon and Hydrogen. *Industrial & Engineering Chemistry Analytical Edition* **13**. 660-663

Ertl G. **2010**. *Reactions at solid surfaces*: Wiley

European Environment Agency. **2011**. Sector share of nitrogen oxides emissions (EEA member countries). European Environment Agency

Falsig H., Bligaard T., Rass-Hansen J., Kustov A. L., Christensen C. H., Narskov J. K. 2007. Trends in catalytic NO decomposition over transition metal surfaces. *Topics in Catalysis* **45**. 117-120

Farrar D. T., Jones M. M. 1964. Heats of Combustion and Bond Energies in Some Octahedral Iron(III) Complexes with Beta-Diketones. *The Journal of Physical Chemistry* **68**. 1717-1721

Farrauto R. J., Heck R. M. 1999. Catalytic converters: State of the art and perspectives. *Catalysis Today* **51**. 351-360

Felthouse T. R., Murphy J. A. 1986. Zeolite-encapsulated platinum catalysts: Preparation, characterization by transmission electron microscopy and their shape selective behavior toward various nitrogen base poisons during the catalytic oxidation of aqueous formaldehyde. *Journal of Catalysis* **98**. 411-433

Flanigen E. M., H. van Bekkum E. M. F. P. A. J., Jansen J. C. **2001**. Chapter 2. Zeolites and molecular sieves: An historical perspective. In *Studies in Surface Science and Catalysis*, pp. 11-35: Elsevier

Forzatti P., Lietti L. 1999. Catalyst deactivation. *Catalysis Today* **52**. 165-181

Furusawa T., Tsunoda M., Tsujimura M., Adschiri T. 1985. Nitric oxide reduction by char and carbon monoxide: Fundamental kinetics of nitric oxide reduction in fluidizedbed combustion of coal. *Fuel* **64**. 1306-1309

Fylstra D., Lasdon L., Watson J., Waren A. 1998. Design and use of the Microsoft Excel Solver. *Interfaces* **28**. 29-55

Gao X., Liu S., Zhang Y., Luo Z., Ni M., Cen K. 2011. Adsorption and reduction of NO_2 over activated carbon at low temperature. *Fuel Processing Technology* **92**. 139-146

Garin F. 2001. Mechanism of NO_x decomposition. *Applied Catalysis A: General* **222**. 183

Giamello E., Murphy D., Magnacca G., Morterra C., Shioya Y., Nomura T., Anpo M. 1992. The interaction of NO with copper ions in ZSM5: An EPR and IR investigation. *Journal of Catalysis* **136**. 510-520

Gohlke O., Weber T., Seguin P., Laborel Y. 2010. A new process for NO_x reduction in combustion systems for the generation of energy from waste. *Waste Management* **30**. 1348-1354

Golecki I. **2003**. Industrial carbon chemical vapor infiltration (CVI) processes. In *Fibers and composites*, ed. P. Delhaès, pp. 112-138

Gómez-García M. A., Pitchon V., Kiennemann A. 2005. Pollution by nitrogen oxides: An approach to NO_x abatement by using sorbing catalytic materials. *Environment International* **31**. 445

Gray P. G. 1993. A fundamental study on the removal of air pollutants (sulfur dioxide, nitrogen dioxide and carbon dioxide) by adsorption on activated carbon. *Gas Separation & Purification* **7**. 213

Green T. E., Hinshelwood C. N. 1926. CCXXIV.-The catalytic decomposition of nitric oxide at the surface of platinum. *Journal of the Chemical Society (Resumed)* **129**. 1709-1713

Gregg S. J., Sing K. S. W. **1967**. *Adsorption, surface area and porosity*: Academic Press Inc

Grinsted R. A., Jen H. W., Montreuil C. N., Rokosz M. J., Shelef M. 1993. The relation between deactivation of Cu-ZSM-5 in the selective reduction of NO and dealumination of the zeolite. *Zeolites* **13**. 602-606

Groen J. C., Peffer L. A. A., Pérez-Ramírez J. 2003. Pore size determination in modified micro- and mesoporous materials. Pitfalls and limitations in gas adsorption data analysis. *Microporous and Mesoporous Materials* **60**. 1-17

Gruenert W., Hayes N. W., Joyner R. W., Shpiro E. S., Siddiqui M. R. H., Baeva G. N. 1994. Structure, Chemistry and Activity of Cu-ZSM-5 Catalysts for the Selective Reduction of NO_x in the Presence of Oxygen. *The Journal of Physical Chemistry* **98**. 10832-10846

Gurrath M., Kuretzky T., Boehm H. P., Okhlopkova L. B., Lisitsyn A. S., Likholobov V. A. 2000. Palladium catalysts on activated carbon supports: Influence of reduction temperature, origin of the support and pretreatments of the carbon surface. *Carbon* **38**. 1241-1255

Hameed S., Dignon J. 1992. Global Emissions of Nitrogen and Sulfur Oxides in Fossil Fuel Combustion 1970-1986. *Journal of the Air & Waste Management Association* **42**. 159-163

Han Y.-F., Chen F., Zhong Z., Ramesh K., Chen L., Widjaja E. 2006. Controlled Synthesis, Characterization and Catalytic Properties of Mn_2O_3 and Mn_3O_4 Nanoparticles Supported on Mesoporous Silica SBA-15. *The Journal of Physical Chemistry B* **110**. 24450

Heck R. M. 1999. Catalytic abatement of nitrogen oxide stationary applications. *Catalysis Today* **53**. 519-523

Heinrich F., Schmidt C., Löffler E., Menzel M., Grünert W. 2002. Fe-ZSM-5 Catalysts for the Selective Reduction of NO by Isobutane: The Problem of the Active Sites. *Journal of Catalysis* **212**. 157

Hensen E. J. M., Zhu Q., Hendrix M. M. R. M., Overweg A. R., Kooyman P. J., Sychev M. V., van Santen R. A. 2004. Effect of high-temperature treatment on Fe/ZSM-5 prepared by chemical vapor deposition of $FeCl_3$: I. Physicochemical characterization. *Journal of Catalysis* **221**. 560-574

Hinshelwood C. N. **1940**. *The kinetics of chemical change*: Clarendon Press Oxford

Hirasawa T., Sung C.-J., Yang Z., Joshi A., Wang H. 2004. Effect of ferrocene addition on sooting limits in laminar premixed ethylene-oxygen-argon flames. *Combustion and Flame* **139**. 288-299

Hoene J. V., Charles R. G., Hickam W. M. 1958. Thermal Decomposition of Metal Acetylacetonates: Mass Spectrometer Studies. *The Journal of Physical Chemistry* **62**. 1098-1101

Holleman A. F., Wiberg N. **2007**. *Lehrbuch der anorganischen Chemie*: de Gruyter

Holstein W. L., Boudart M. 1983. Transition metal and metal oxide catalysed gasification of carbon by oxygen, water and carbon dioxide. *Fuel* **62**. 162-165

Hu Z., Hüttinger K. J. 2001. Chemical vapor infiltration of carbon - revised: Part II: Experimental results. *Carbon* **39**. 1023-1032

Huheey J. E., Keiter E. A., Keiter R. L. **2003**. *Anorganische Chemie: Prinzipien von Struktur und Reaktivität*: Walter de Gruyter

Hüttinger K. J. **2003**. Fundamentals of Chemical Vapor Deposition in Hot Wall Reactors. In *Fibers and composites*, ed. P. Delhaès: CRC Press

Illán-Gómez M. J., Linares-Solano A., Radovic L. R., Salinas-Martínez de Lecea C. 1996. NO Reduction by Activated Carbons. 7. Some Mechanistic Aspects of Uncatalyzed and Catalyzed Reaction. *Energy & Fuels* **10**. 158-168

Illán-Gómez M. J., Linares-Solano A., Salinas-Martinez de Lecea C. 1995. NO Reduction by Activated Carbon. 6. Catalysis by Transition Metals. *Energy & Fuels* **9**. 976-983

Illán-Gómez M. J., Linares-Solano A., Salinas-Martinez de Lecea C., Calo J. M. 1993. Nitrogen oxide (NO) reduction by activated carbons. 1. The role of carbon porosity and surface area. *Energy & Fuels* **7**. 146-154

Illán-Gómez M. J., Raymundo-Pinero E., García-García A., Linares-Solano A., Salinas-Martínez de Lecea C. 1999. Catalytic NO_x reduction by carbon supporting metals. *Applied Catalysis B: Environmental* **20**. 267-275

Illán-Gómez M. J., Salinas-Martínez de Lecea C., Linares-Solano A., Radovic L. R. 1998. Potassium-Containing Coal Chars as Catalysts for NO_x Reduction in the Presence of Oxygen. *Energy & Fuels* **12**. 1256-1264

Imanaka N., Masui T. 2012. Advances in direct NO_x decomposition catalysts. *Applied Catalysis A: General* **431-432**. 1-8

Irving R. J., da Silva M. A. V. R. 1981. Standard enthalpies of formation of bis(pentane-2,4-dionato)copper(II) and tetrakis[bis(pentane-2,4-dionato)cobalt(II)] and an estimation of the metal-oxygen bond energies. *Journal of the Chemical Society, Dalton Transactions*. 99-102

Itho Y., Nishiyama S., Tsuruya S., Masai M. 1994. Redox behavior and mobility of copper ions in NaZSM-5 zeolite during oxidation. *The Journal of Physical Chemistry* **98**. 960-967

Iwamoto M. 1990. Catalytic decomposition of nitrogen monoxide. *Stud. Surf. Sci. Catal* **54**. 121

Iwamoto M., Furukawa H., Mine Y., Uemura F., Mikuriya S., Kagawa S. 1986. Copper (II) ion-exchanged ZSM-5 zeolites as highly active catalysts for direct and continuous decomposition of nitrogen monoxide. *Journal of the Chemical Society, Chemical Communications*. 1272-1273

Iwamoto M., Yahiro H., Mizuno N., Zhang W. X., Mine Y., Furukawa H., Kagawa S. 1992. Removal of nitrogen monoxide through a novel catalytic process. 2. Infrared study on surface reaction of nitrogen monoxide adsorbed on copper ion-exchanged ZSM-5 zeolites. *The Journal of Physical Chemistry* **96**. 9360-9366

Iwamoto M., Yahiro H., Tanda K., Mizuno N., Mine Y., Kagawa S. 1991. Removal of nitrogen monoxide through a novel catalytic process. 1. Decomposition on excessively copper-ion-exchanged ZSM-5 zeolites. *The Journal of Physical Chemistry* **95**. 3727-3730

Iwamoto M., Yokoo S., Sakai K., Kagawa S. 1981. Catalytic decomposition of nitric oxide over copper(II)-exchanged, Y-type zeolites. *Journal of the Chemical Society, Faraday Transactions 1: Physical Chemistry in Condensed Phases* **77**. 1629-1638

Jacobs P. A., de Wilde W., Schoonheydt R. A., Uytterhoeven J. B., Beyer H. 1976. Redox behaviour of transition metal ions in zeolites. Part 3. Auto-reduction of cupric ions in Y zeolites. *Journal of the Chemical Society, Faraday Transactions 1: Physical Chemistry in Condensed Phases* **72**. 1221-1230

Jagiello J., Thommes M. 2004. Comparison of DFT characterization methods based on N_2, Ar, CO_2 and H_2 adsorption applied to carbons with various pore size distributions. *Carbon* **42**. 1227-1232

Jeguirim M., Tschamber V., Brilhac J. F., Ehrburger P. 2004. Interaction mechanism of NO_2 with carbon black: Effect of surface oxygen complexes. *Journal of Analytical and Applied Pyrolysis* **72**. 171-181

Jellinek K. 1906. Über Zersetzungsgeschwindigkeit von Stickoxyd und Abhängigkeit derselben von der Temperatur. *Zeitschrift für anorganische Chemie* **49**. 229-276

Jobson E. 2004. Future Challenges in Automotive Emission Control. *Topics in Catalysis* **28**. 191

Kakei K., Ozeki S., Suzuki T., Kaneko K. 1990. Multi-stage micropore filling mechanism of nitrogen on microporous and micrographitic carbons. *Journal of the Chemical Society, Faraday Transactions* **86**. 371-376

Kaneko K. 1987. Anomalous micropore filling of NO on alpha-FeOOH-dispersed activated carbon fibers. *Langmuir* **3**. 357-363

Kaneko K., Ishii C. 1992. Superhigh surface area determination of microporous solids. *Colloids and Surfaces* **67**. 203-212

Kaucký D., Vondrová A., Dedecek J., Wichterlová B. 2000. Activity of Co-ion sites in ZSM-5, Ferrierite and Mordenite in Selective Catalytic Reduction of NO with Methane. *Journal of Catalysis* **194**. 318-329

Kharas K. C. C. 1993. Performance, selectivity and mechanism in Cu-ZSM-5 lean-burn catalysts. *Applied Catalysis B: Environmental* **2**. 207-224

Kharas K. C. C., Liu D.-J., Robota H. J. 1995. Structure-function properties in Cu-ZSM-5 NO decomposition and NO SCR catalysts. *Catalysis Today* **26**. 129-145

Kharas K. C. C., Robota H. J., Liu D. J. 1993. Deactivation in Cu-ZSM-5 lean-burn catalysts. *Applied Catalysis B: Environmental* **2**. 225-237

Klank D., Lohmeier S. J. 2012. Untersuchungen zur Porenbildung von Feststoffen. *Chemie Ingenieur Technik* **84**. 373-381

Konduru M. V., Chuang S. S. C. 1999. Active and Spectator Adsorbates during NO Decomposition over Cu-ZSM-5: Transient IR, Site-Poisoning and Site-Promotion Studies. *Journal of Catalysis* **187**. 436-452

Kong Y., Cha C. Y. 1996. NO_x adsorption on char in presence of oxygen and moisture. *Carbon* **34**. 1027-1033

Krishna K., Seijger G. B. F., van den Bleek C. M., Makkee M., Mul G., Calis H. P. A. 2003. Selective Catalytic Reduction of NO with NH_3 over Fe-ZSM-5 Catalysts Prepared by Sublimation of $FeCl_3$ at Different Temperatures. *Catalysis Letters* **86**. 121-132

Kumar M. S., Schwidder M., Grünert W., Brückner A. 2004. On the nature of different iron sites and their catalytic role in Fe-ZSM-5 $DeNO_x$ catalysts: New insights by a combined EPR and UV/VIS spectroscopic approach. *Journal of Catalysis* **227**. 384

Kuwana K., Saito K. 2005. Modeling CVD synthesis of carbon nanotubes: Nanoparticle formation from ferrocene. *Carbon* **43**. 2088

Kuwana K., Saito K. 2007. Modeling ferrocene reactions and iron nanoparticle formation: Application to CVD synthesis of carbon nanotubes. *Proceedings of the Combustion Institute* **31**. 1857-1864

Langford R. M., Petford-Long A. K. 2001. Preparation of transmission electron microscopy cross-section specimens using focused ion beam milling. *Journal of Vacuum Science & Technology A* **19**. 2186-2193

Langmuir I. 1918. The Adsorption Of Gases On Plane Surfaces Of Glass, Mica And Platinum. *Journal of the American Chemical Society* **40**. 1361-1403

Lasdon L. S., Waren A. D., Jain A., Ratner M. 1978. Design and testing of a generalized reduced gradient code for nonlinear programming. *ACM Transactions on Mathematical Software (TOMS)* **4**. 34-50

Lewis K. E., Smith G. P. 1984. Bond dissociation energies in ferrocene. *Journal of the American Chemical Society* **106**. 4650-4651

Li Y., Armor J. N. 1991. Temperature-programmed desorption of nitric oxide over Cu-ZSM-5. *Applied Catalysis* **76**. L1-L8

Li Y., Armor J. N. 1992. Catalytic decomposition of nitrous oxide on metal exchanged zeolites. *Applied Catalysis B: Environmental* **1**. L21-L29

Li Y., Hall W. K. 1991. Catalytic decomposition of nitric oxide over Cu-zeolites. *Journal of Catalysis* **129**. 202-215

Linteris G. T., Rumminger M. D., Babushok V., Tsang W. 2000. Flame inhibition by ferrocene and blends of inert and catalytic agents. *Proceedings of the Combustion Institute* **28**. 2965-2972

Liu D.-J., Robota H. 1993. In situ XANES characterization of the Cu oxidation state in Cu-ZSM-5 during NO decomposition catalysis. *Catalysis Letters* **21**. 291-301

Liu G., Gao P.-X. 2011. A review of NO_x storage/reduction catalysts: Mechanism, materials and degradation studies. *Catalysis Science & Technology* **1**. 552-568

Lobo R. F. 2003. Introduction to the structural chemistry of zeolites.

London J. W., Bell A. T. 1973. A simultaneous infrared and kinetic study of the reduction of nitric oxide by carbon monoxide over copper oxide. *Journal of Catalysis* **31**. 96-109

Lowell S., Shields J. E., Thomas M. A., Thommes M. **2006**. *Characterization of porous solids and powders: Surface area, pore size and density*: Springer

Maeda Y., Ogawa N., Takashima Y. 1987. Mossbauer spectroscopic studies on molecular rotation and lattice dynamics of cyclodextrin clathrates of bis([small eta]-cyclopentadienyl)iron(II) and some of its ring-substituted derivatives. *Journal of the Chemical Society, Dalton Transactions* **0**. 627-632

Maesen T., Marcus B., H. van Bekkum E. M. F. P. A. J., Jansen J. C. **2001**. Chapter 1 The zeolite scene - An overview. In *Studies in Surface Science and Catalysis*, pp. 1-9: Elsevier

Marsh H., Rodríguez-Reinoso F. **2006**. *Activated carbon*: Elsevier Science

Mayfield P. L. J., Do D. D. 1991. Measurement of the single-component adsorption kinetics of ethane, butane and pentane onto activated carbon using a differential adsorption bed. *Industrial & Engineering Chemistry Research* **30**. 1262-1270

McCusker L. B., Baerlocher C., H. van Bekkum E. M. F. P. A. J., Jansen J. C. **2001**. Chapter 3 Zeolite structures. In *Studies in Surface Science and Catalysis*, pp. 37-67: Elsevier

McDonald B. C., Dallmann T. R., Martin E. W., Harley R. A. 2012. Long-term trends in nitrogen oxide emissions from motor vehicles at national, state and air basin scales. *Journal of Geophysical Research: Atmospheres* **117**. D00V18

Menendez I., Fuertes A. B. 2001. Aging of carbon membranes under different environments. *Carbon* **39**. 733-740

Microsoft Corporation. **2011**. *Solver Uses Generalized Reduced Gradient Algorithm*. http://support.microsoft.com/kb/82890/en-us

Mikhail R. S., Brunauer S., Bodor E. E. 1968. Investigations of a complete pore structure analysis: I. Analysis of micropores. *Journal of Colloid and Interface Science* **26**. 45-53

Mochida I., Ogaki M., Fujitsu H., Komatsubara Y., Ida S. 1985. Reduction of nitric oxide with activated PAN fibres. *Fuel* **64**. 1054-1057

Modén B., Da Costa P., Lee D. K., Iglesia E. 2002. Transient Studies of Oxygen Removal Pathways and Catalytic Redox Cycles during NO Decomposition on Cu-ZSM-5. *The Journal of Physical Chemistry B* **106**. 9633-9641

Moulijn J. A., Kapteijn F. 1995. Towards a unified theory of reactions of carbon with oxygen-containing molecules. *Carbon* **33**. 1155-1165

Müller M., Harvey G., Prins R. 2000. Comparison of the dealumination of zeolites beta, mordenite, ZSM-5 and ferrierite by thermal treatment, leaching with oxalic acid and treatment with $SiCl_4$ by ^{1}H, ^{29}Si and ^{27}Al MAS NMR. *Microporous and Mesoporous Materials* **34**. 135-147

Nakajima F., Hamada I. 1996. The state-of-the-art technology of NO_x control. *Catalysis Today* **29**. 109-115

Nasibulin A. G., Richard O., Kauppinen E. I., Brown D. P., Jokiniemi J. K., Altman I. S. 2002. Nanoparticle Synthesis by Copper (II) Acetylacetonate Vapor Decomposition in the Presence of Oxygen. *Aerosol Science and Technology* **36**. 899-911

Naslain R., Langlais F., Vignoles G., Pailler R. **2007**. The CVI-Process: State of the Art and Perspective. In *Mechanical Properties and Performance of Engineering Ceramics II: Ceramic Engineering and Science Proceedings*, pp. 373-386

Neathery J. K., Rubel A. M., Stencel J. M. 1997. Uptake of NO_x by activated carbons: Bench-scale and pilot-plant testing. *Carbon* **35**. 1321

Neimark A. V., Ravikovitch P. I., Vishnyakov A. 2000. Adsorption hysteresis in nanopores. *Physical Review E* **62**. R1493

Newsam J. M., Treacy M. M. J., Koetsier W. T., Gruyter C. B. D. 1988. Structural Characterization of Zeolite Beta. *Proceedings of the Royal Society of London. A. Mathematical and Physical Sciences* **420**. 375-405

Norskov J. K., Bligaard T., Hvolbaek B., Abild-Pedersen F., Chorkendorff I., Christensen C. H. 2008. The nature of the active site in heterogeneous metal catalysis. *Chemical Society Reviews* **37**. 2163-2171

Ohring M. 1992. The Materials Science of Thin Films Academic. *New York*. 132

Okuhara T., Tanaka K.-I. 1986. Adsorption and reduction of nitrogen monoxide by potassium-doped carbon. *Journal of the Chemical Society, Faraday Transactions 1: Physical Chemistry in Condensed Phases* **82**. 3657-3666

Olsson L., Sjövall H., Blint R. J. 2009. Detailed kinetic modeling of NO_x adsorption and NO oxidation over Cu-ZSM-5. *Applied Catalysis B: Environmental* **87**. 200-210

Otto K., Shelef M. 1970. The adsorption of nitric oxide on iron oxides. *Journal of Catalysis* **18**. 184-192

Parrillo D. J., Gorte R. J. 1993. Characterization of acidity in H-ZSM-5, H-ZSM-12, H-Mordenite and H-Y using microcalorimetry. *The Journal of Physical Chemistry* **97**. 8786-8792

Parvulescu V. I., Grange P., Delmon B. 1998. Catalytic removal of NO. *Catalysis Today* **46**. 233-316

Payra P., Dutta P. K. 2003. Zeolites: A primer. *Handbook of zeolite science and technology*. 1-19

Pérez-Ramírez J., Gallardo-Llamas A. 2005. Impact of the preparation method and iron impurities in Fe-ZSM-5 zeolites for propylene production via oxidative dehydrogenation of propane with N_2O. *Applied Catalysis A: General* **279**. 117-123

Pfeiffer Vacuum GmbH. **2002**. *Massenspektrometer 2002-2004*. Asslar

Pfeiffer Vacuum GmbH. **2007**. *QMA 200 - Analysers*

Pierson H. O. **1999**. *Handbook of chemical vapor deposition: Principles, technology and applications*: William Andrew

Pieterse J. A. Z., Booneveld S., van den Brink R. W. 2004. Evaluation of Fe-zeolite catalysts prepared by different methods for the decomposition of N_2O. *Applied Catalysis B: Environmental* **51**. 215-228

Pieterse J. A. Z., Pirngruber G. D., van Bokhoven J. A., Booneveld S. 2007. Hydrothermal stability of Fe-ZSM-5 and Fe-BEA prepared by wet ion-exchange for N_2O decomposition. *Applied Catalysis B: Environmental* **71**. 16-22

Pietrzak R., Bandosz T. J. 2007. Activated carbons modified with sewage sludge derived phase and their application in the process of NO_2 removal. *Carbon* **45**. 2537-2546

Pirone R., Ciambelli P., Moretti G., Russo G. 1996. Nitric oxide decomposition over Cu-exchanged ZSM-5 with high SiAl ratio. *Applied Catalysis B: Environmental* **8**. 197-207

Ponec V., Bond G. C. **1995**. *Catalysis by metals and alloys*: Elsevier Science

Premkumar P. A., Bahlawane N., Kohse-Höinghaus K. 2007. CVD of Metals Using Alcohols and Metal Acetylacetonates, Part I: Optimization of Process Parameters and Electrical Characterization of Synthesized Films. *Chemical Vapor Deposition* **13**. 219-226

Ravikovitch P. I., Vishnyakov A., Russo R., Neimark A. V. 2000. Unified Approach to Pore Size Characterization of Microporous Carbonaceous Materials from N_2, Ar and CO_2 Adsorption Isotherms *Langmuir* **16**. 2311-2320

Reimerink W. M. T. M. **1999**. The use of activated carbon as catalyst and catalyst carrier in industrial applications. In *Studies in Surface Science and Catalysis*, ed. A. Dabrowski, pp. 751-769: Elsevier

Richter E., Schmidt H.-J., Schecker H.-G. 1990. Adsorption and catalytic reactions of NO and NH_3 on activated carbon. *Chemical Engineering & Technology* **13**. 332-340

Rideal E. K. 1939. A note on a simple molecular mechanism for heterogeneous catalytic reactions. *Mathematical Proceedings of the Cambridge Philosophical Society* **35**. 130-132

Rodríguez-Reinoso F. 1998. The role of carbon materials in heterogeneous catalysis. *Carbon* **36**. 159-175

Rouquerol J., Llewellyn P., Rouquerol F., P.L. Llewellyn F. R.-R. J. R., Seaton N. **2007**. Is the BET equation applicable to microporous adsorbents? In *Studies in Surface Science and Catalysis*, pp. 49-56: Elsevier

Roy S., Hegde M. S., Madras G. 2009. Catalysis for NO_x abatement. *Applied Energy* **86**. 2283

Rubel A. M., Stencel J. M. 1996. Effect of Pressure on NO_x Adsorption by Activated Carbons. *Energy & Fuels* **10**. 704-708

Rubel A. M., Stencel J. M. 1997. The effect of low-concentration SO_2 on the adsorption of NO from gas over activated carbon. *Fuel* **76**. 521-526

Rubel A. M., Stewart M. L., Stencel J. M. 1995a. Activated carbon for control of nitrogen oxide emissions. *Journal of Materials Research* **10**. 562-567

Rubel A. M., Stewart M. L., Stencel J. M. **1995b**. The Influence of Activated Carbon Type on NO_x Adsorptive Capacity. In *Reduction of Nitrogen Oxide Emissions*, pp. 208-216: American Chemical Society

Sager U., Schmidt F. 2009. Adsorption of Nitrogen Oxides, Water Vapour and Ozone onto Activated Carbon. *Adsorption Science & Technology* **27**. 135-145

Sarkany J., D'Itri J. L., Sachtler W. M. H. 1992. Redox chemistry in excessively ion-exchanged Cu/Na-ZSM-5. *Catalysis Letters* **16**. 241-249

Schieferstein E., Schlüter S., Hennig T., Meller K., Lange M., Möller A. 2013. Untersuchung von Kraftstoffdampf-Rückhaltesystemen bei Einsatz von ethanolhaltigen Biokraftstoffen. *Chemie Ingenieur Technik* **85**. 934-943

Schoonheydt R. A. 1993. Transition Metal Ions in Zeolites: Siting and Energetics of Cu^{2+}. *Catalysis Reviews* **35**. 129-168

Schüth F. 2010. Poröse Materialien im Überblick. *Chemie Ingenieur Technik* **82**. 769-777

Schwab G.-M. **1928**. Theoretische und experimentelle Fortschritte auf dem Gebiete der heterogenen Gasreaktionen. In *Ergebnisse der exakten naturwissenschaften*, pp. 276-341: Springer Berlin Heidelberg

Schwidder M., Kumar M. S., Klementiev K., Pohl M. M., Brückner A., Grünert W. 2005. Selective reduction of NO with Fe-ZSM-5 catalysts of low Fe content: I. Relations between active site structure and catalytic performance. *Journal of Catalysis* **231**. 314

Seredych M., Bashkova S., Pietrzak R., Bandosz T. J. 2010. Interactions of NO_2 and NO with Carbonaceous Adsorbents Containing Silver Nanoparticles. *Langmuir* **26**. 9457-9464

Shah M. S. 1929a. CCCLVI.-The combustion of charcoal in oxygen, nitric oxide and nitrous oxide. Part I. The adsorption of oxygen. *Journal of the Chemical Society*. 2661-2676

Shah M. S. 1929b. CCCLVII.-The combustion of charcoal in oxygen, nitric oxide and nitrous oxide. Part II. The effect of temperature. *Journal of the Chemical Society*. 2676-2692

Shchedrin W. M., Kulikov I. S., Vas'kin V. N., Teleguin A. A. 1978. Vaporization of magnetite and wuestite in ultra-high neutral vacuum with mass-spectrometric analysis of gaseous phase. *The Journal of Chemical Thermodynamics* **10**. 9-18

Shelef M. 1992. On the mechanism of nitric oxide decomposition over Cu-ZSM-5. *Catalysis Letters* **15**. 305-310

Shelef M. 1995. Selective Catalytic Reduction of NO_x with N-Free Reductants. *Chemical Reviews* **95**. 209

Shelef M., Otto K., Gandhi H. 1969. The heterogeneous decomposition of nitric oxide on supported catalysts. *Atmospheric Environment (1967)* **3**. 107-122

Shirahama N., Moon S. H., Choi K. H., Enjoji T., Kawano S., Korai Y., Tanoura M., Mochida I. 2002. Mechanistic study on adsorption and reduction of NO_2 over activated carbon fibers. *Carbon* **40**. 2605-2611

Shpiro E. S., Grünert W., Joyner R. W., Baeva G. N. 1994. Nature, distribution and reactivity of copper species in over-exchanged Cu-ZSM-5 catalysts: An XPS/XAES study. *Catalysis Letters* **24**. 159

Shwan S., Adams E., Jansson J., Skoglundh M. 2013. Effect of Thermal Ageing on the Nature of Iron Species in Fe-BEA. *Catalysis Letters* **143**. 43-48

Sigma-Aldrich Co. LLC. **2014a**. Safety Data Sheet, Copper(II) acetylacetonate.

Sigma-Aldrich Co. LLC. **2014b**. Safety Data Sheet, Ferrocene.

Sigma-Aldrich Co. LLC. **2014c**. Safety Data Sheet, Iron(II) acetylacetonate.

Sigma-Aldrich Co. LLC. **2014d**. Safety Data Sheet, Manganese(III) acetylacetonate.

Sing K. S. W., Everett D. H., Haul R. A. W., Moscou L., Pierotti R. A., Rouquerol J., Siemieniewska T. 1985. Reporting physisorption data for gas/solid systems with special reference to the determination of surface area and porosity. *Pure Appl. Chem* **57**. 603–619

Sircar S., Myers A. L. 2003. Gas separation by zeolites. *Handbook of zeolite science and technology*. 1063-1105

Skalska K., Miller J. S., Ledakowicz S. 2010. Trends in NO_x abatement: A review. *Science of the Total Environment* **408**. 3976-3989

Smith D. M., Hua D.-W., Earl W. L. 1994. Characterization of porous solids. *MRS Bulletin* **19**. 44-48

Sohda Y., Diefendorf R. J. **1985**. The chemical vapor deposition of carbon in open-ended capillary tubes. Extended abstracts. *17th biennial conference on carbon. Lexinton (Kentucky, USA): American Carbon Soc*, pp. 31-32

Sotirchos S. V. 1991. Dynamic modeling of chemical vapor infiltration. *AIChE Journal* **37**. 1365-1378

Spoto G., Bordiga S., Scarano D., Zecchina A. 1992. Well defined $Cu^{I}(NO)$, $Cu^{I}(NO)_2$ and $Cu^{II}(NO)_X$ ($X = O^-$ and/or NO_2^-) complexes in Cu^{I}-ZSM-5 prepared by interaction of H-ZSM-5 with gaseous CuC^{l}. *Catalysis Letters* **13**. 39-44

Stegenga S., van Soest R., Kapteijn F., Moulijn J. A. 1993. Nitric oxide reduction and carbon monoxide oxidation over carbon-supported copper-chromium catalysts. *Applied Catalysis B: Environmental* **2**. 257-275

Storck S., Bretinger H., Maier W. F. 1998. Characterization of micro- and mesoporous solids by physisorption methods and pore-size analysis. *Applied Catalysis A: General* **174**. 137-146

Strem Chemicals Inc. **2014**. Safety Data Sheet, Iron(III) acetylacetonate.

Sugimoto M., Katsuno H., Takatsu K., Kawata N. 1987. Correlation between the crystal zize and catalytic properties of ZSM-5 zeolites. *Zeolites* **7**. 503-507

Sundaresan B. B., Harding C. I., May F. P., Hendrickson E. R. 1967. Adsorption of nitrogen oxides from waste gas. *Environmental Science & Technology* **1**. 151-156

Tajimi N., Sano H., Murase K., Lee K.-H., Sugimura H. 2007. Thermal Immobilization of Ferrocene Derivatives on (111) Surface of n-Type Silicon: Parallel between Vinylferrocene and Ferrocenecarboxaldehyde. *Langmuir* **23**. 3193-3198

Takahashi N., Shinjoh H., Iijima T., Suzuki T., Yamazaki K., Yokota K., Suzuki H., Miyoshi N., Matsumoto S.-i., Tanizawa T., Tanaka T., Tateishi S.-s., Kasahara K. 1996. The new concept 3-way catalyst for automotive lean-burn engine: NOx storage and reduction catalyst. *Catalysis Today* **27**. 63

Tang J., Zhang T., Liang D., Yang H., Li N., Lin L. 2002. Direct decomposition of NO by microwave heating over Fe/NaZSM-5. *Applied Catalysis B: Environmental* **36**. 1

Taylor H. S. 1925. A theory of the catalytic surface. *Proceedings of the Royal Society of London. Series A* **108**. 105-111

Teng H., Suuberg E. M. 1993a. Chemisorption of nitric oxide on char. 1. Reversible nitric oxide sorption. *The Journal of Physical Chemistry* **97**. 478-483

Teng H., Suuberg E. M. 1993b. Chemisorption of nitric oxide on char. 2. Irreversible carbon oxide formation. *Industrial & Engineering Chemistry Research* **32**. 416-423

Teng H., Suuberg E. M., Calo J. M. 1992. Studies on the reduction of nitric oxide by carbon: The nitric oxide-carbon gasification reaction. *Energy & Fuels* **6**. 398-406

Teraoka Y., Harada T., Kagawa S. 1998. Reaction mechanism of direct decomposition of nitric oxide over Co- and Mn-based perovskite-type oxides. *Journal of the Chemical Society, Faraday Transactions* **94**. 1887-1891

Teraoka Y., Tai C., Ogawa H., Furukawa H., Kagawa S. 2000. Characterization and NO decomposition activity of Cu-MFI zeolite in relation to redox behavior. *Applied Catalysis A: General* **200**. 167-176

Thiele E. W. 1939. Relation between Catalytic Activity and Size of Particle. *Industrial & Engineering Chemistry* **31**. 916-920

Thomas J. M., Thomas W. J., Anderson J. R., Boudart M. **1997**. *Principles and practice of heterogeneous catalysis*: VCH Weinheim

Thonstad J., Nordmo F., Vee K. 1973. On the anode effect in cryolite-alumina melts. *Electrochimica Acta* **18**. 27-32

Tissue B. M. **2000**. Quadrupole Mass Spectrometry. In *Chemistry Hypermedia Project at Virginia Tech*, ed. Q. M. Spectrometry. Blacksburg, VA 24061-0002: Chemistry Hypermedia Project at Virginia Tech

Tsyganova E. I., Dyagileva L. M. 1996. The reactivity of metal beta-diketonates in the thermal decomposition reaction. *Russian Chemical Reviews* **65**. 315

Underwood G. M., Miller T. M., Grassian V. H. 1999. Transmission FT-IR and Knudsen Cell Study of the Heterogeneous Reactivity of Gaseous Nitrogen Dioxide on Mineral Oxide Particles. *The Journal of Physical Chemistry A* **103**. 6184-6190

UNSD. **2009**. Environmental Indicators: Air Pollution. In *World Population Prospects: The 2008 Revision*: United Nations, Department of Economic and Social Affairs, Population Division

Valyon J., Millman W. S., Hall W. K. 1994. The desorption of O_2 during NO and N_2O decomposition on Cu- and Fe-zeolites. *Catalysis Letters* **24**. 215-225

Vennestrom P. N. R., Janssens T. V. W., Kustov A., Grill M., Puig-Molina A., Lundegaard L. F., Tiruvalam R. R., Concepción P., Corma A. 2014. Influence of lattice stability on hydrothermal deactivation of Cu-ZSM-5 and Cu-IM-5 zeolites for selective catalytic reduction of NO_x by NH_3. *Journal of Catalysis* **309**. 477-490

Voskoboinikov T. V., Chen H.-Y., Sachtler W. M. H. 1998. On the nature of active sites in Fe/ZSM-5 catalysts for NO_x abatement. *Applied Catalysis B: Environmental* **19**. 279-287

Walker A. P. 1995. Mechanistic studies of the selective reduction of NO_x over Cu/ZSM-5 and related systems. *Catalysis Today* **26**. 107-128

Wang Z.-M., Kaneko K. 1998. Effect of Pore Width on Micropore Filling Mechanism of SO_2 in Carbon Micropores. *The Journal of Physical Chemistry B* **102**. 2863-2868

WHO. **2010**. WHO guidelines for indoor air quality: Selected pollutants, World Health Organization, Bonn

Wood J. L., Jones M. M. 1964. Coordinate Bond Energies and Inner Orbital Splitting in Some Tervalent Transition Metal Acetylacetonates. *Inorganic Chemistry* **3**. 1553-1556

Xia B., Phillips J., Chen C.-K., Radovic L. R., Silva I. F., Menendez J. A. 1999. Impact of Pretreatments on the Selectivity of Carbon for NO_x Adsorption/Reduction. *Energy & Fuels* **13**. 903-906

Yahiro H., Iwamoto M. 2001. Copper ion-exchanged zeolite catalysts in De-NO_x reaction. *Applied Catalysis A: General* **222**. 163-181

Yamamoto M. 1984. Aqueous solubility of tris(acetylacetonato)chromium(III). *The Journal of Physical Chemistry* **88**. 3356-3359

Yamashita H., Tomita A., Yamada H., Kyotani T., Radovic L. R. 1993. Influence of char surface chemistry on the reduction of nitric oxide with chars. *Energy & Fuels* **7**. 85-89

Yokoyama C., Misono M. 1994. Catalytic Reduction of Nitrogen Oxides by Propene in the Presence of Oxygen over Cerium Ion-Exchanged Zeolites: II. Mechanistic Study of Roles of Oxygen and Doped Metals. *Journal of Catalysis* **150**. 9-17

Zhang W.-J., Bagreev A., Rasouli F. 2008a. Reaction of NO_2 with Activated Carbon at Ambient Temperature. *Industrial & Engineering Chemistry Research* **47**. 4358-4362

Zhang W., Hüttinger K. J. 2001. Chemical vapor infiltration of carbon - revised: Part I: Model simulations. *Carbon* **39**. 1013-1022

Zhang W. J., Rabiei S., Bagreev A., Zhuang M. S., Rasouli F. 2008b. Study of NO adsorption on activated carbons. *Applied Catalysis B: Environmental* **83**. 63-71

9. Appendix

9.1. NO_x decomposition mechanisms in detail

Several NO_x decomposition mechanisms are proposed for carbon catalysts and the essentials of the most prominent contributions are summarized in the following.

9.1.1. NO_x decomposition mechanisms in activated carbon

Calo and co-workers describe NO reduction by non-infiltrated activated carbon as a process accompanied by simultaneous CO and CO_2 product evolution and continuous formation of new active surface sites C^* (Teng et al. 1992):

$$C + C\text{-}O + NO \rightarrow C\text{-}O_2 + C\text{-}N \quad \textbf{(25)}$$

$$2\,C + 2\,NO \leftrightarrow 2\,C\text{-}NO \text{ (mainly at T} < 473 \text{ K)} \quad \textbf{(26)}$$

$$C^* + C\text{-}O + NO \rightarrow CO_2 + C\text{-}N + xC^* \quad \textbf{(27)}$$

$$C^* + NO \rightarrow CO + C\text{-}N + yC^* \quad \textbf{(28)}$$

$$C\text{-}O \rightarrow CO + aC^* \quad \textbf{(29)}$$

$$C\text{-}O_2 \rightarrow CO_2 + bC^* \quad \textbf{(30)}$$

$$2\,C\text{-}N \rightarrow N_2 + dC^* \quad \textbf{(31)}$$

where *a, b, d, x, y* mark different reactive carbon sites that are generated during the reaction.

For the adsorption and decomposition of NO_2 on activated carbon fibers the group of Mochida proposes the following mechanism scheme, introducing C-NO_3 surface complexes (Shirahama et al. 2002):

1) NO_2 molecules chemisorb rapidly on C-O complexes,
2) Chemisorbed neighboring NO_2 either disproportionate (they produce C-NO_3 surface complexes and release NO), or they can slowly oxidize (with oxygen from the feed gas) to C-NO_3,
3) Upon heating, both NO and NO_2 can be released,
4) Residual C-O or C-O_2 complexes on the surface can produce CO or CO_2 respectively via further heating,
5) Alternatively to 1-4, NO_2 can weakly adsorb on C-O and desorb as NO_2 upon heating.

The NO_2 adsorption and decomposition mechanism on carbon black proposed by the group of Ehrburger comprises three steps (Jeguirim et al. 2004):

1) Formation of oxygen complexes on carbon during NO_2 adsorption:

$$C^* + NO_2 \rightarrow C\text{-}NO_2 \quad \textbf{(32)}$$

where C* denotes an active carbon site, The C-NO_2 complex is unstable and decomposes quickly:

$$C\text{-}NO_2 \rightarrow C\text{-}O + NO \quad \textbf{(33)}$$

$$C\text{-}O + NO_2 \rightarrow C\text{-}(ONO_2) \quad \textbf{(34)}$$

2) Decomposition of C-(ONO_2) complexes and desorption of corresponding products below 523 K:

$$C\text{-}(ONO_2) \rightarrow C\text{-}O + NO_2 \quad \textbf{(35)}$$

$$C\text{-}(ONO_2) \rightarrow CO_2 + NO \quad \textbf{(36)}$$

$$C\text{-}(ONO_2) \rightarrow CO + NO_2 \quad \textbf{(37)}$$

3) Decomposition of C-O complexes starts to become significant at temperatures above 523 K:

$$2\ C\text{-}O \rightarrow CO_2 + C^* \quad \textbf{(38)}$$

$$C\text{-}O \rightarrow CO \quad \textbf{(39)}$$

If oxygen is present in the atmosphere:

$$C\text{-}(ONO_2) \rightarrow C\text{-}O_2 + NO \quad \textbf{(40)}$$

$$C\text{-}O_2 + NO_2 \rightarrow C\text{-}O_2 \cdots NO_2 \quad \textbf{(41)}$$

where NO_2 interacts with the adsorbed O_2 and upon heating NO_2 and CO_2 are released. The proposed mechanism is able to explain the enhanced NO_2 adsorption after pretreatment of carbon black in O_2 as observed by Jeguirim at al. However, the process disregards the release of N_2 and N_2O as observed in this work.

Rasouli and co-workers question the following three aspects of the mechanisms proposed by Mochida and Ehrburger (Zhang et al. 2008a):

1) The proposed mechanisms do not reasonably explain the large effect of pre-oxidized activated carbon on the observed enhanced NO_2 adsorption as they are only based on C-O complexes,
2) they doubt the existence of C-NO_3 or C-(ONO_2) based on own TPD data,
3) they doubt further the existence of C-NO_3 or C-(ONO_2) complexes due to comparison with thermally pretreated activated carbon where the surface oxygen groups are removed.

For NO_2 adsorption and decomposition on activated carbon at room temperature they introduce the formation of $(NO\text{-}O_2)^{ads}$ surface complex which may be partly caused by oxygen impurity of the feed gas (Zhang et al. 2008a):

$$4\ NO_2 + 2\ C^* \rightarrow 2\ NO + 2\ (NO\text{-}O_2)^{ads} + 2\ C\text{-}O \quad \textbf{(42)}$$

i.e. the outlet concentration of NO is 50% of the NO_2 inlet concentration and the activated carbon surface is oxidized.

$$2\ C\text{-}O \rightarrow CO_2 + C^* \text{ and } C\text{-}O \rightarrow CO \quad \textbf{(43)}$$

where CO desorbs above 413 K from activated carbon. If no oxygen is present in the feed gas, the NO concentration in feed gas has no impact on the reduction of NO_2.

9.1.2. NO_x decomposition mechanisms in metal-infiltrated activated carbon

The metal catalyst in activated carbon can contribute to the chemisorption of NO at the catalyst surface and additional evolution of N_2O (Illán-Gómez et al. 1996):

$$NO + 2\,S^* \rightarrow S\text{-}N + S\text{-}O \quad \textbf{(44)}$$

$$2\,S\text{-}N \rightarrow N_2 + 2\,S \quad \textbf{(45)}$$

$$S\text{-}N + NO \rightarrow S + N_2O \quad \textbf{(46)}$$

where S* is a reduced site on the metal catalyst and oxygen is possibly transferred from the metal surface to the activated carbon. During the catalysis reaction the metal species embedded in carbon can undergo redox reactions (Illán-Gómez et al. 1996):

$$Fe/FeO\ or\ Fe_xO_y/FeO\ or\ Fe_xO_y/Fe_xO_{y+1}$$

$$Cu/CuO\ or\ \ Cu/Cu_2O$$

$$Ni/NiO$$

$$Cr_2O_3/CrO_2$$

$$Co/Co_2O_3\ or\ CoO/Co_2O_3\ or\ Co_3O_4/Co_2O_3$$

In presence of NO_2 and oxygen the formation of iron nitrates is observed (Bashkova & Bandosz 2011):

$$Fe_2O_3 + NO_2 \rightarrow Fe_2O_{3+1} + NO \quad \textbf{(47)}$$

$$Fe_2O_{3+1} + C \rightarrow Fe_2O_3 + CO \quad \textbf{(48)}$$

$$Fe_2O_3 + 6\,NO_2 + \tfrac{3}{2}\,O_2 \rightarrow 2\,Fe(NO_3)_3 \quad \textbf{(49)}$$

but the nitrates decompose at 398 K.

9.1.3. Secondary product participation in the NO_x decomposition mechanism of activated carbons

Especially in the recycle flow reactor reaction products from NO_x decomposition can serve as reactants in further reactions. CO can be oxidized by NO decomposition with carbon at 773 - 953 K (Chan et al. 1983; Furusawa et al. 1985):

$$CO + C\text{-}O \rightarrow CO_2 + C^* \quad \textbf{(50)}$$

$$NO + C^* \rightarrow C\text{-}O + \frac{1}{2}N_2 \quad \textbf{(51)}$$

$$C\text{-}O + NO \rightarrow \frac{1}{2}N_2 + CO_2 \quad \textbf{(52)}$$

At elevated temperature (973-1194 K) CO and N_2 are released:

$$C\text{-}O \rightarrow CO \quad \textbf{(53)}$$

$$C^* + NO \rightarrow C\text{-}O + \frac{1}{2}N_2 \quad \textbf{(54)}$$

The group of Moulijn suggested the reaction of NO with CO to be catalyzed for example by copper-infiltrated activated carbon with release of N_2O, N_2 and CO_2 (Stegenga et al. 1993):

$$2\,NO + CO \rightarrow CO_2 + N_2O \text{ at lower temperature and} \quad \textbf{(55)}$$

$$N_2O + CO \rightarrow CO_2 + N_2 \text{ at higher temperature.} \quad \textbf{(56)}$$

And in absence of CO:

$$NO + S^* \leftrightarrow S\text{-}NO \quad \textbf{(57)}$$

$$S\text{-}NO + S^* \rightarrow S\text{-}N + S\text{-}O \text{ (the dissociation is rate limiting at low temperature)} \quad \textbf{(58)}$$

$$S\text{-}NO + S\text{-}N \rightarrow 2\,S^* + N_2O \quad \textbf{(59)}$$

$$S\text{-}N \rightarrow S^* + N_2 \quad \textbf{(60)}$$

9.2. Calibration routine of the mass spectrometer

The initial preparation and calibration procedure of the applied Pfeiffer Vacuum Prisma QMS 200 quadrupole mass spectrometer is performed once before the entire set of experiments in this work and includes the following steps:

1) Evacuation of the vacuum chamber at closed inlet dose valve and degassing at 393 K for at least 48 hours until the residual gas pressure is below $6 \cdot 10^{-8}$ mbar.
2) Starting the Prisma QMS 200 instrument and ion source two hours before the measurement for thermal equilibration.
3) Setting the electron emission current fixed to 1 mA and choosing detector type C-SEM and scan mode SCAN-F.
4) Opening the inlet dose valve and establishing a pressure of $1 \cdot 10^{-6}$ mbar caused by 1% NO_2 in helium.
5) Auto-calibration of the instrument in “mass scale calibration” mode at the m/e = 46 ion current signal. As a result the exact position of the m/e = 46 peak maximum of NO_2 is identified by the mass spectrometer.
6) Coarse tuning of the m/e = 46 peak by gradual adjustment of the ion reference potential, cathode voltage and scan speed. Fine tuning the peak by gradual adjustment of the focus, field axis, extraction voltage and resolution following the tuning procedure described in the instrument manual (Pfeiffer Vacuum GmbH 2007) by means of the “peak shape optimizer” routine. The finally chosen parameters are provided in Table 8.

A modified calibration procedure is performed prior to each experiment:

1) Starting the pre-evacuated Prisma QMS 200 instrument two hours before the measurement for thermal equilibration.
2) Performing "zero gas calibration" reveals auto-subtraction of the background signals caused by the residual gas in the evacuated vacuum chamber. After background subtraction, the actual measurement routine is ready to start. A mass resolved spectrum of the residual gas in the vacuum chamber is presented in Fig. 98.
3) Every two weeks: Establishing a pressure of $1 \cdot 10^{-6}$ mbar in the vacuum chamber of a pre-mixed mixture of all gas species of interest and performing auto-calibration of the instrument in "mass scale calibration" mode at the m/e = 4, 12, 14, 16, 28, 30, 32, 40, 44, 46 ion current signals. As a result the exact position of the m/e-peak maxima is adjusted by the mass spectrometer.

For each gas species of interest (O_2, N_2, NO, NO_2, N_2O, CO and CO_2) the ion current signal of a predefined mixture of 1% of the respective gas species, 10% argon and 89% helium is acquired for all m/e-ratios stated in the left column of Table15. For helium the predefined mixture is 10% argon and 90% helium. An exemplary N_2O-calibration spectrum of 1% N_2O, 10 % argon and 89% helium is shown in Fig. 99 and the time resolved measurements at predefined m/e-ratios are shown in Fig. 100.

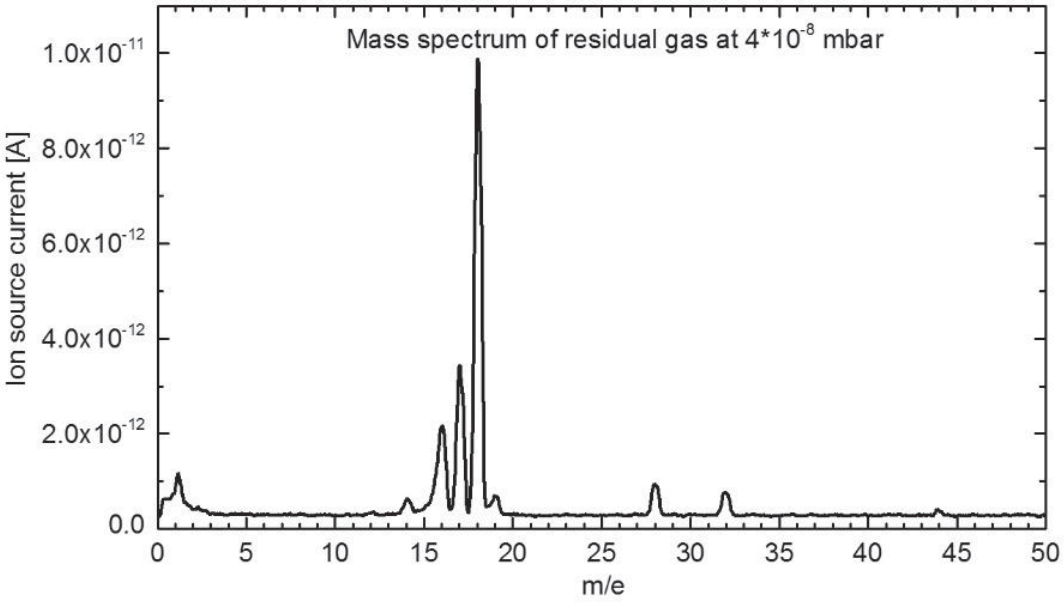

Fig. 98. Mass spectrum of residual gas in the vacuum chamber of the mass spectrometer at closed inlet valve

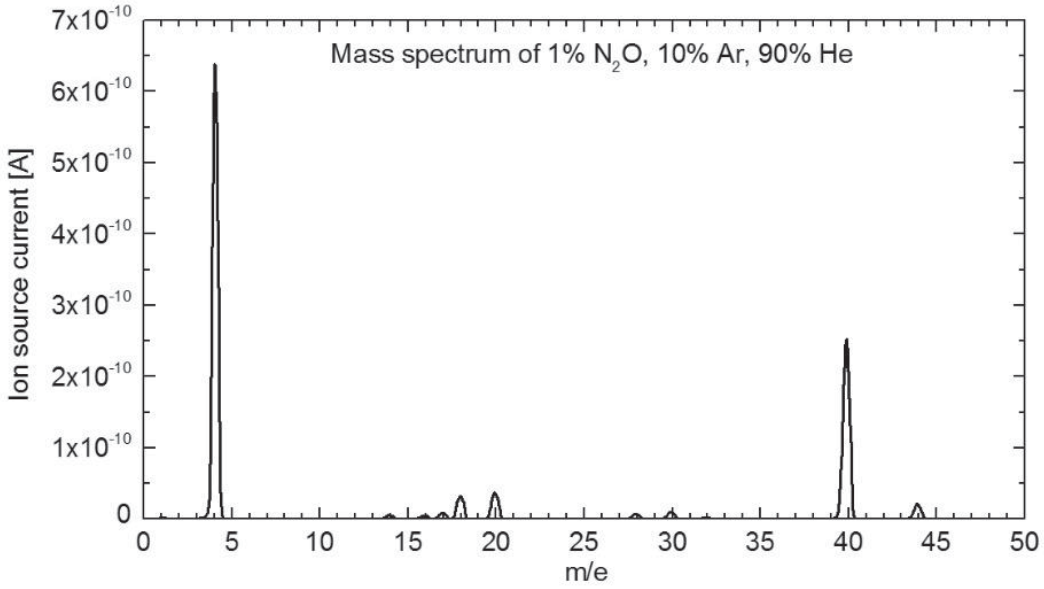

Fig. 99. Mass spectrum of 1% N_2O, 10 % argon and 89% helium

Table 15. m/e-ratios for acquisition of time resolved ion current signals during mass spectrometric investigation

m/e-ratio	Exact calibrated m/e-ratio	Predominantly targeted gas species
4	4.03	He
12	11.99	CO, CO_2
14	13.94	N_2
16	15.94	O_2
28	27.94	N_2, CO
30	29.94	NO, NO_2, N_2O
32	31.94	O_2
40	39.88	Ar
44	43.91	CO_2, N_2O
46	45.91	NO_2

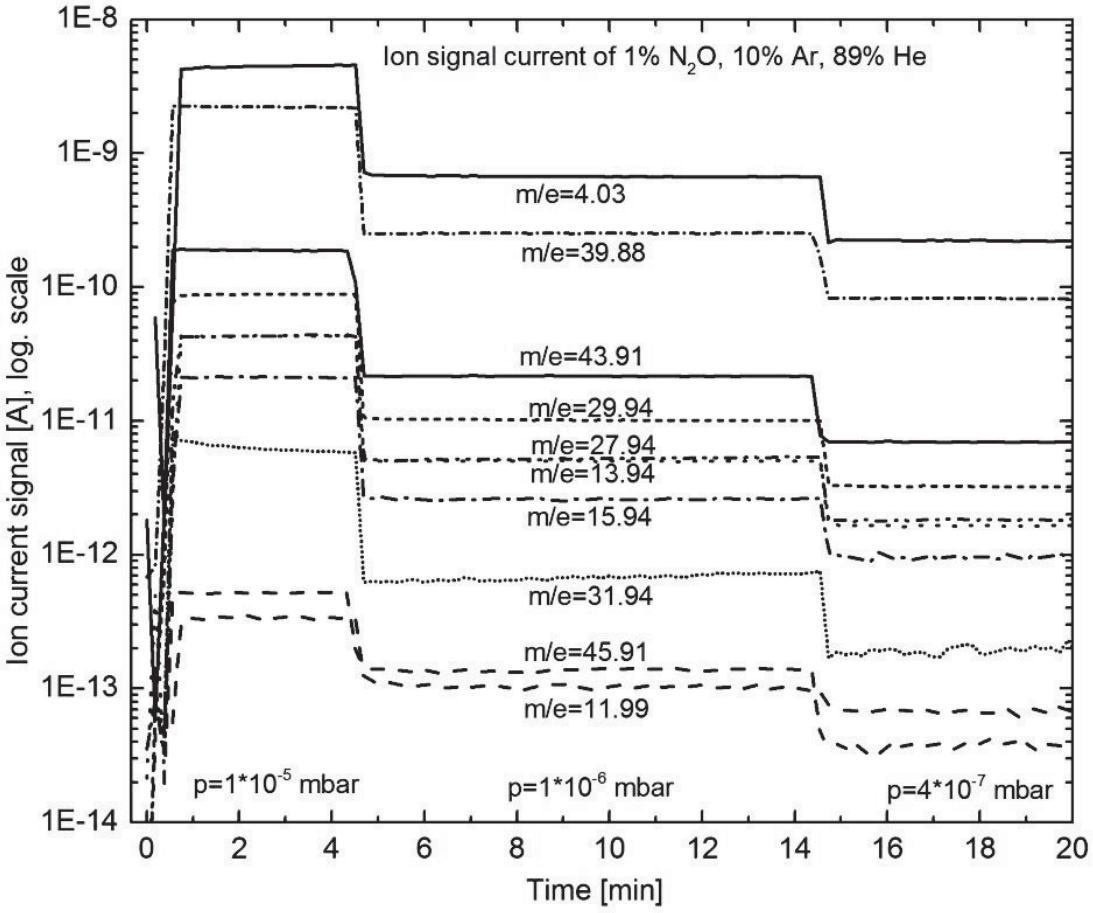

Fig. 100. Ion signal current of 1% N_2O, 10% Ar and 89% He during calibration measurement in three pressure regions

The ion current signals are normalized to the *m/e = 40* signal of argon:

$$\tilde{I}_g^y = \frac{I_g^y}{I_g^{40}} \tag{61}$$

where I_g^y denotes the ion current signal for m/e-ratio y of gas g, i.e. $y \in \{4, 12, 14, 16, 28, 30, 32, 40, 44, 46\}$, $g \in \{O_2, N_2, NO, NO_2, N_2O, CO, CO_2, He\}$.

Hence, for each gas species a calibration vector with the ion signal current at each m/e-ratio is defined and all calibration vectors can be summarized in matrix form:

$$M_{m/e} = \begin{bmatrix} \tilde{I}_{O_2}^4 & \cdots & \tilde{I}_{He}^4 \\ \vdots & \ddots & \vdots \\ \tilde{I}_{O_2}^{46} & \cdots & \tilde{I}_{He}^{46} \end{bmatrix} \tag{62}$$

Non-reasonable ion current signals close to the noise level are set to zero in this matrix, e.g. for all gas species not containing any carbon, the ion current signal at m/e = 12 is set to zero.

9.3. Analysis routine of mass spectral data

The analysis and quantification routine of the mass spectra follows a standardized routine:

1) Time resolved ion current signals of ten preselected m/e-ratios (see Table 15) are acquired.
2) The time resolved ion current signals are normalized to the argon signal:

$$\tilde{I}_t^y = \frac{I_t^y}{I_t^{40}} \quad \textbf{(63)}$$

Where I_t^y denotes the ion current signal *I* for m/e-ratio *y* at time *t*.

3) The ion current signals of six subsequent normalized ion signal data points are averaged. Typically a time interval of about 60 seconds is comprised in order to minimize signal artifacts and noise:

$$\bar{I}_{\bar{t}}^y = \frac{\sum_0^6 \tilde{I}^y}{6} \quad \textbf{(64)}$$

The result is a matrix of all acquired ion current signals over the entire measurement time:

$$M_{ms} = \begin{bmatrix} \bar{I}_{1\,min}^4 & \cdots & \bar{I}_{120\,min}^4 \\ \vdots & \ddots & \vdots \\ \bar{I}_{1\,min}^{46} & \cdots & \bar{I}_{120\,min}^{46} \end{bmatrix} \quad \textbf{(65)}$$

4) Multiplication of $M_{m/e}$ with a vector of suitable coefficients $\vec{v}_t^{\,g}$ for each gas species *g* at time *t*, reveals matrix M_{ms}^* as an approximation of matrix M_{ms}:

$$M_{ms}^* = \left[M_{m/e} \cdot \vec{v}_{1\,min}^{\,g} \ \ldots \ M_{m/e} \cdot \vec{v}_{120\,min}^{\,g}\right] \quad \textbf{(66)}$$

The coefficients are approximated by means of Microsoft Excel 2010 Solver using the generalized reduced gradient method (GRG) for optimization – an algorithm commonly used for finding a local optimum on non-linear problems with continuously differentiable functions (Lasdon et al. 1978; Fylstra et al. 1998; Microsoft Corporation 2011). The algorithm approximates a local optimum of the overall problem (target value) by adjusting each coefficient value (constraint) and trying to bring each partial derivative of the problem close to zero. The stopping of the algorithm at a local optimum requires reasonable estimation of the coefficients at the starting point in order to find the global optimum. In several cases it might be wise to restart the algorithm with a different possible set of coefficients.

In the current problem the target value is defined as the minimum difference between the matrix of all acquired ion current signals and the approximation of this matrix by scaling each gas species calibration vector:

$$M_{ms} - M_{ms}^* \to 0 \quad \textbf{(67)}$$

The defined constraints include non-negativity conditions for the quantity of each gas species. The algorithm stops if the target value is not improving by more than $1 \cdot 10^{-17}$ during five consecutive iteration steps. The common danger of a suboptimal solution by stalling in local and not global minima of the problem is minimized by choosing a reasonable set of

starting values for the coefficients, e.g. reflecting 1% NO_2 and 0% O_2, N_2, NO, N_2O, CO and CO_2.

5) Multiplication of the derived optimal coefficient vector $\vec{v}_t^{\,g}$ for each gas species with the concentration c_{calib}^{g} of the respective gas in the mixture used for the calibration procedure provides the concentration $\vec{c}_t^{\,g}$ of gas species g at time t in the unknown gas mixture:

$$\vec{c}_t^{\,g} = \vec{v}_t^{\,g} \cdot c_{calib}^{g} \; ; \quad \vec{c}_t^{\,g} = \begin{bmatrix} c_{1\,min}^{g} \\ \vdots \\ c_{120\,min}^{g} \end{bmatrix} \tag{68}$$

Hence, the concentration of each gas species can be monitored along the entire experimental time.

The black squares in Fig. 101 show the value of the resulting fit of the optimization algorithm for zeolite samples, which is the difference between the matrix of all acquired ion current signals and the approximation of this matrix, as described above in eq. (67):

$$M_{ms} - M_{ms}^{*} = Fit \tag{69}$$

This fit value can serve as a measure for the quality of the approximation. For gas species NO, N_2O and O_2 a slight correlation between the gas species concentration and the quality of approximation can be derived. The reason for the correlation can stem from a slight imprecision in the calibration for the respective gas species or from difficulties in the approximation of the specific gas composition, especially due to stalling in local, instead of global minima.

In order to limit approximation imprecisions, approximations with a fit value larger than $5.0 \cdot 10^{-6}$ are double checked and in many cases a re-approximation with an adjusted set of starting values improves the final approximation fit. Approximations with a fit value still larger than $5.0 \cdot 10^{-6}$ are usually not admitted for further investigation.

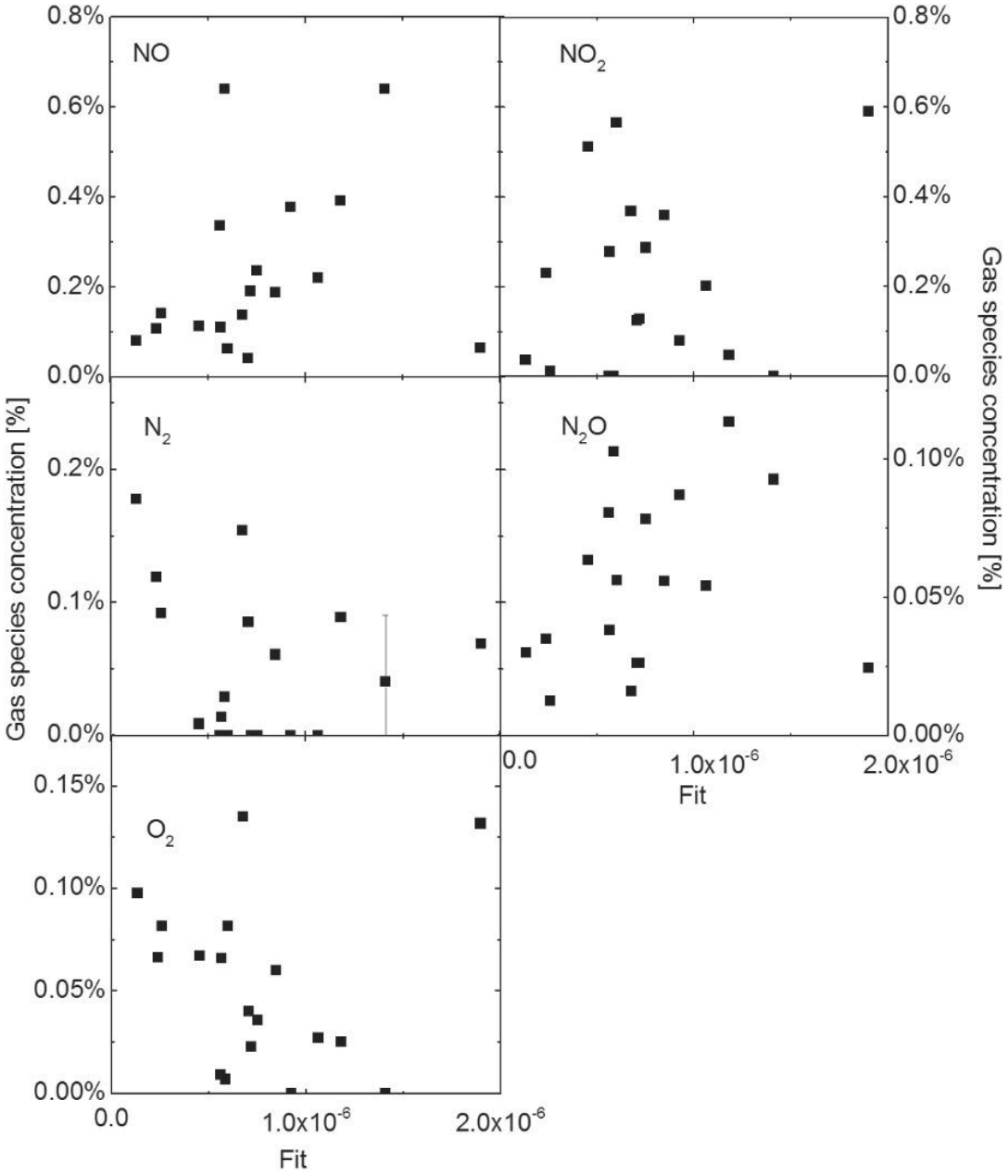

Fig. 101. Relation of the calculated Microsoft Excel 2010 Solver fit value for zeolite samples to concentration of NO, NO_2, N_2, N_2O, and O_2 in gas mixture after 120 minutes NO_2 conversion in recycle flow at 425 K

Table 16 shows a comparison of a predefined reference gas mixture with the approximated results from the acquired mass spectra. Except of the relatively large deviation of the estimation of N_2O and CO the stated differences are typical. The gases are usually estimated in test gas mixtures with an accuracy of 0.1-0.2 %-points.

Table 16. Concentrations of the gas species in a predefined test gas mixture in comparison to the calculated values from acquired mass spectra

Gas species	Gas species concentration in pre-defined reference gas mixture	Calculated gas species concentration in mixture	Concentration difference of mixture	Estimation tendency
NO_2	1.3%	1.3%	0	fairly correct
NO	0.0%	0.0 %	0	fairly correct
N_2O	1.0%	0.6%	-0.4%-points	underestimated
CO	1.0%	0.6%	-0.4%-points	underestimated
CO_2	1.0%	1.0%	0	fairly correct
O_2	0.2%	0.2%	0	fairly correct
N_2	1.6%	1.4%	-0.2%-points	underestimated

9.4. Relation between micropore volume and gas species concentrations

The effect of the micropore pore volume on the release of the gas species NO, NO_2, N_2O, N_2 and O_2 is displayed in Fig. 102 for all zeolite samples (irrespective of their framework structure, ion species, infiltration procedure, etc.) after the standard catalysis experiment with NO_2. The black squares show the concentration of the respective species in the gas phase after 120 minutes experimental time.

From the graphs no clear correlations can be derived between the micropore volume and the release of any gas species. The maximum observed Pearson correlation coefficients are about +/-0.3 for NO, N_2O and N_2. This is too low to assume a significant correlation. Hence, the gas species desorption cannot be related to an independent effect of the pore volume as observed for activated carbon catalysts.

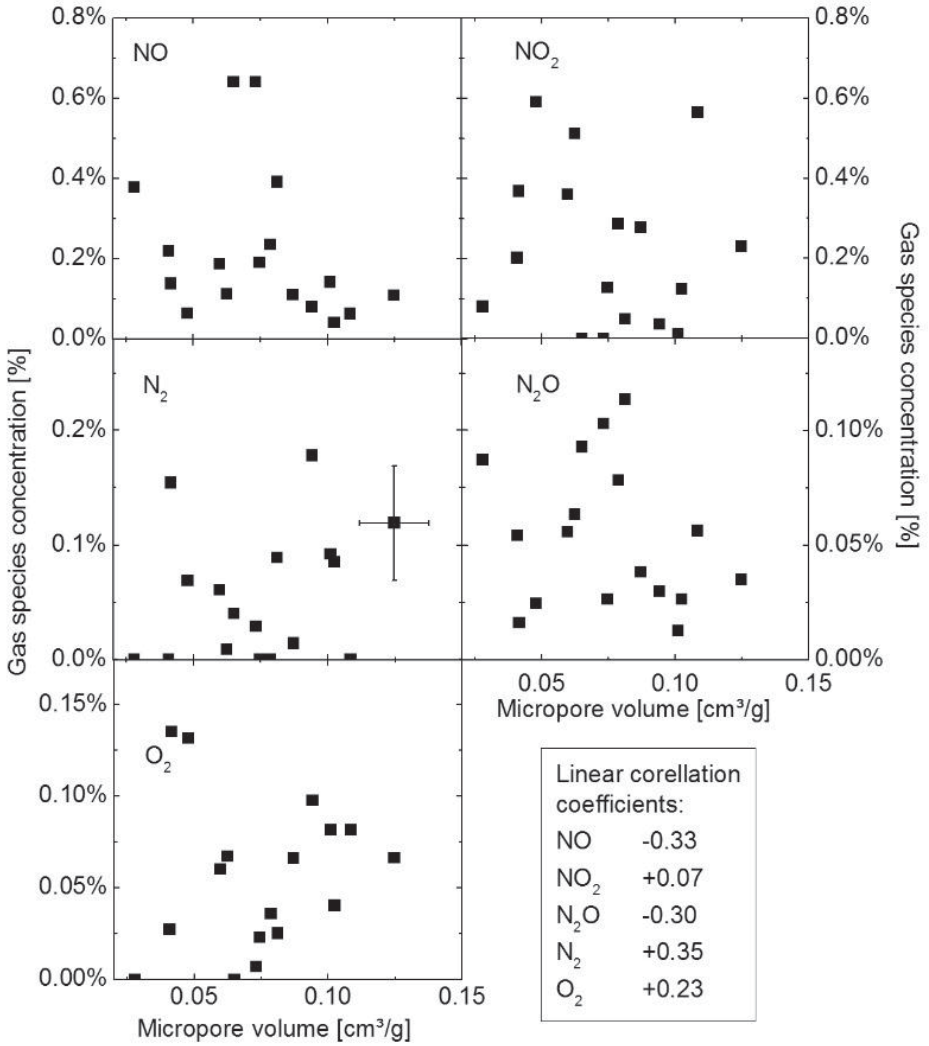

Fig. 102. Concentration of NO, NO_2, N_2, N_2O, and O_2 in gas mixture after 120 minutes NO_2 conversion in recycle flow at 425 K, in relation to the micropore volume of the samples

9.5. Rating of the catalytic activity

The rating of the catalytic activity in section 5.7 is based on the differences in the gas species concentrations, which are compared between the CVI-infiltrated catalyst and the respective catalyst prepared by LIE. The underlying figures are presented in the following tables.

Table 17. Underlying gas concentration differences for Table 14 in section 5.7 for the comparison of CVI- and respective LIE-prepared catalysts in the standard catalysis experiment

Catalyst system	**NO_x-removal**	**NO_2-removal**	**NO-decomposition**	**Concentration of … in the final gas mixture**			
				NO	**N_2O**	**N_2**	**O_2**
	Difference in gas concentration of CVI-sample and respective LIE-sample in %-points						
Fe-MOR	-4	-8	4	4	0	9	6
Cu-MOR	25	-1	-2	20	7	-9	-7
Fe-BEA	0	-7	12	5	2	-6	-2
Cu-BEA	4	-51	0	53	3	3	-7
Fe-MFI	-33	-46	-7	12	1	-7	-11
Cu-MFI	4	17	-4	-8	-3	15	11

For the rating legend see Table 18, Table 19 and Table 20.

Table 18. Rating legend for Table 17 of NO_x/NO_2 removal

Rating	Difference in %-points between the NO_x/NO_2 concentration decrease of CVI-sample and the respective LIE-sample during the 120 minutes standard catalysis experiment
---	> 25
--	25 to >15
-	15 to >5
o	5 to -5
+	<-5 to -15
++	<-15 to -25
+++	< -25

Table 19. Rating legend for Table 17 of NO decomposition

Rating	Difference in %-points between the NO concentration of CVI-sample and the respective LIE-sample between the 10th and 120th minute of the standard catalysis experiment
---	> 10
--	10 to >5
-	5 to > 2
o	2 to -2
+	<-2 to -5
++	<-5 to -10
+++	< -10

Table 20. Rating legend for Table 17 for of the concentration of NO, N_2O, N_2 and O_2 in the final gas mixture of the standard catalysis experiment

Rating	Difference in %-points between the $NO/N_2O/N_2/O_2$ concentration of CVI-sample and the respective LIE-sample after 120 minutes of the standard catalysis experiment
---	< -25
--	-25 to <-15
-	- 15 to <-5
o	-5 to 5
+	5 to <15
++	15 to <25
+++	>25

Table 21. Underlying NO_2/NO concentration changes for Table 13 in section 7.2.7 for the rating of catalysts in the standard catalysis experiment

Catalyst preparation	**NO_2-removal / NO-decomposition**					
	MFI		BEA		MOR	
Non-infiltrated	-72	4	-44	n.r.	-77	2
Fe-CVI	-87	-2	-71	11	-96	n.r.
Fe-LIE	-41	n.r.	-64	-1	-88	n.r.
Cu-CVI	-63	-7	-100	0	-100	-5
Cu-LIE	-80	-3	-49	n.r.	-99	-3
Mn-CVI	-95	4	-100	0	-92	3

Rating legend see Table 23 and Table 24

Table 22. Underlying NO_2/NO concentration changes for Table 12 in section 7.2.7 for the rating of catalysts in the standard catalysis experiment

Catalyst	**NO_2-removal / NO-decomposition**					
	iron		copper		manganese	
MFI-CVI	-87	-2	-63	-7	-95	4
MFI-LIE	-41	n.r.	-80	-3		
BEA-CVI	-71	11	-100	0	-100	0
BEA-LIE	-64	-1	-49	n.r.		
MOR-CVI	-96	n.r.	-100	-5	-92	3
MOR-LIE	-88	n.r.	-99	-3		

Rating legend see Table 23 and Table 24

Table 23. Rating legend for the concentration decrease of NO_2 in Table 21 and Table 22

Rating	NO_2 concentration decrease during the 120 minutes standard catalysis experiment in % of initial NO_2 concentration
o	> -75
+	-76 to -95
++	-95 to -100

Table 24. Rating legend for the concentration decrease of NO in Table 21 and Table 22

Rating	%-points of NO concentration between 10th and 120th minute of the standard catalysis experiment
o	> 0
+	0 to -4
++	< -4

9.6. Error estimation

The stated errors in this work reflect the probable experimental error and instrumental accuracy. They are derived either from the stated accuracy of the applied measurement instruments in the manual or based on own estimations.

In case of many different error sources with accumulating or compensating errors for one stated measure, reference measurements served for better error estimation. For example, the calculation routine for the concentration of gas species from mass spectra data is pre-evaluated by means of reference gas mixtures as stated in appendix 9.3. The error bars for gas concentration data from these calculations are adjusted to the typical errors observed in the reference measurements.

An overview of the main instrumental accuracies and error sources in this work is provided in Table 25:

Table 25. Main error sources and quantification of typical error values in this work

Experimental or measurement procedure	Error source	Stated accuracy/Typical error
Catalyst synthesis		
Sample and precursor mass	Laboratory balance	+/- 1 mg
Sample thermal treatment	Tube furnace	+/- 5 K
Sample extraction from reactor	Sample residue in sample holder	- 50 mg (ca. 2.5 wt.-%)*
Nitrogen adsorption measurements		
Sample mass determination	Laboratory balance	+/- 1 mg (ca. 5 wt.-%)
Instrument accuracy	Autosorb 1C	+/- 3 %
Investigation of catalytic activity		
Sample mass	Laboratory balance	+/- 5 mg (ca. 2.5 wt.-%)
Sample cell temperature	Heating mantle	+/- 5 K
Total pressure in recycle reactor	Heating of gas mixture in sample cell	+/- 20 mbar (2 %)
Gas concentration of NO_2	Dose valve and pressure transducer	+/- 1 % (of 1% NO_2)
Calculation of gas species concentration	Calibration and calculation routine	+/- 0.1 %-points

*) systematic error, has been compensated in this work where applicable

9.7. List of samples and preparation parameters

Table 26. Activated carbon sample preparation parameters and sample properties
n.m. = not measured, *) erroneous measurement by pressure transducer likely

Sample name	Applied mass of matrix (g)	Outgasing temperature (K)	Outgasing time (h)	Pressure at start of precursor infiltration (mbar)	Precursor	Applied mass of precursor (g)	Precursor evaporation temperature (K)	Time of precursor evaporation (h)	Precursor decomposition temperature (K)	Time of precursor decomposition (h)	Infiltrated load (wt.-%)	Specific surface area (m^2/g)	Total pore volume (cm^3/g)	Micropore volume (cm^3/g)
Fe-infiltrated activated carbons														
Fe-AC-CVI (MB46)	6.51	573	1.5	$6.2 \cdot 10^{-1}$	Ferrocene	4.56	413	0.75	653	0.75	8.9	973	0.51	n.m.
Fe-AC-CVI (MB63)	4.49	573	1	$5.9 \cdot 10^{-3}$	Ferrocene	4.02	403	3.25	653	1	0.7	1148	0.53	n.m.
Fe-AC-CVI (MB67)	4.57	573	5	$1.8 \cdot 10^{-3}$	Ferrocene	4.25	403	3.25	653	1	12.5	1098	0.49	0.119
Fe-AC-CVI (MB84)	4.77	573	2	$1.3 \cdot 10^{-3}$	Ferrocene	4.29	403	2	653	0.5	12.1	1200	0.56	0.128
Fe-AC-CVI (MB88)	4.99	573	3	$3.4 \cdot 10^{-3}$	Ferrocene	4.57	403	2	653	0.33	20.6	868	0.40	0.094
Fe-AC-CVI (MB96)	5.59	573	2	$1.3 \cdot 10^{-1}$	Ferrocene	3.97	403	2	653	0.75	13.2	974	0.45	0.103
Fe-AC-CVI (MB100)	4.58	573	1	$1.2 \cdot 10^{-1}$	Ferrocene	0.52	403	2	653	1	0.0	1541	0.66	0.180
Fe-AC-CVI (MB101)	8.92	573	2	$1.1 \cdot 10^{-1}$	Ferrocene	1.05	403	2	653	1	5.7	1449	0.64	0.162
Fe-AC-CVI (MB105)	10.34	573	2	$1.4 \cdot 10^{-1}$	Ferrocene	1.00	403	2	653	1	4.0	2466	1.03	n.m.
Fe-AC-CVI (MB112)	11.00	573	2	$1.2 \cdot 10^{-1}$	Ferrocene	1.02	403	2	653	1	3.2	1737	0.72	0.215
Fe-AC-CVI (MB122)	10.79	573	2	$1.7 \cdot 10^{-1}$	$Fe(acac)_3$	1.00	443	4	653	1	1.0	1363	0.67	n.m.
Fe-AC-CVI (MB131)	10.28	573	4	$1.7 \cdot 10^{-1}$	$Fe(acac)_3$	2.00	443	4	653	1	2.8	1291	0.54	n.m.
Cu-infiltrated activated carbons														
Cu-AC-CVI (MB163)	10.67	573	2	$4.7 \cdot 10^{-3}$	$Cu(acac)_2$	1.09	503	2	653	1	0.7	1636	0.80	0.185
Cu-AC-CVI (MB164)	10.66	573	4	$3.2 \cdot 10^{-8}$ *)	$Cu(acac)_2$	1.00	493	3	653	1	1.1	1834	0.80	0.219
Cu-AC-CVI (MB336)	1.61	573	4	$4.2 \cdot 10^{-3}$	$Cu(acac)_2$	0.38	433	3	673	0.33	3.4	1759	0.72	0.220
Mn-infiltrated activated carbons														
Mn-AC-CVI (MB165)	10.30	573	4	$7.4 \cdot 10^{-3}$	$Mn(acac)_3$	2.06	413	3	653	1	1.9	1651	0.68	0.215
Mn-AC-CVI (MB168)	12.05	573	4	$8.1 \cdot 10^{-3}$	$Mn(acac)_3$	1.50	413	4	653	1	0.8	1736	0.73	n.m.

Table 27. Zeolite sample preparation parameters and sample properties
n.m. = not measured

Sample name	Applied mass of matrix (g)	Outgasing temperature (K)	Outgasing time (h)	Pressure at start of precursor infiltration (mbar)	Precursor	Infiltrated ion	Applied mass of precursor (g)	Precursor evaporation temperature (K)	Time of precursor evaporation (h)	Precursor decomposition temperature (K)	Time of precursor decomposition (h)	Ion load (wt.-%)	Si/Al- ratio	M/Al-ratio	Specific surface area (m^2/g)	Micropore volume (cm^3/g)	Total pore volume (cm^3/g)
ZSM-5 (MFI) matrix																	
Fe-MFI-CVI-a (MB315)	1.51	973	2	$1.3 \cdot 10^{-2}$	Ferrocene	Fe	0.50	403	3	773	1	1.9	10	0.3	351	0.075	0.19
Fe-MFI-CVI-b (MB172)	3.63	773	6	$8.0 \cdot 10^{-3}$	Ferrocene	Fe	2.08	403	4	653	1	2.0	n.m.	n.m.	198	0.085	0.13
Fe-MFI-CVI-c (MB182)	7.14	623	4	$4.4 \cdot 10^{-3}$	$Fe(acac)_3$	Fe	1.01	458	4	673	0.25	0.5	n.m.	n.m.	245	0.047	0.15
Cu-MFI-CVI-a (MB300)	1.63	973	2	$2.5 \cdot 10^{-4}$	$Cu(acac)_2$	Cu	1.13	433	2	773	1	4.2	11	0.5	226	0.042	0.16
Cu-MFI-CVI-b (MB295)	1.43	973	2	$5.4 \cdot 10^{-5}$	$Cu(acac)_2$	Cu	0.98	433	2	773	1	1.0	n.m.	n.m.	n.m.	n.m.	n.m.
Mn-MFI-CVI-a (MB179)	3.49	623	4	$1.2 \cdot 10^{-3}$	$Mn(acac)_3$	Mn	1.00	413	4	673	0.5	0.2	n.m.	n.m.	298	0.060	0.18
Mn-MFI-CVI-b (MB326)	1.52	973	2	$1.0 \cdot 10^{-1}$	$Mn(acac)_3$	Mn	0.61	413	3	773	1	0.2	10	0.0.	348	0.081	0.19
Zeolite Beta matrix																	
Fe-BEA-CVI (MB319)	1.51	973	2	$1.6 \cdot 10^{-3}$	Ferrocene	Fe	0.51	403	3	773	1	3.3	16	0.8	490	0.079	0.30
Cu-BEA-CVI (MB307)	1.50	973	2	$4.1 \cdot 10^{-3}$	$Cu(acac)_2$	Cu	1.00	433	2	773	1	2.5	14	0.4	409	0.065	0.26
Mn-BEA-CVI (MB332)	1.52	923	2	$4.3 \cdot 10^{-3}$	$Mn(acac)_3$	Mn	0.66	413	3	773	1	1.2	16	0.3	485	0.073	0.32
Mordenite matrix																	
Fe-MOR-CVI (MB322)	1.50	973	2	$5.6 \cdot 10^{-3}$	Ferrocene	Fe	0.49	403	3	773	1	1.5	5	0.1	453	0.094	0.28
Cu-MOR-CVI (MB303)	1.46	973	2	$1.4 \cdot 10^{-4}$	$Cu(acac)_2$	Cu	0.96	433	2	773	1	1.8	5	0.1	284	0.013	0.34
Mn-MOR-CVI (MB329)	1.56	973	2	$2.0 \cdot 10^{-4}$	$Mn(acac)_3$	Mn	0.63	413	3	773	1	0.03	5	0.0	239	0.028	0.17

9.8. Photographs of the experimental setup

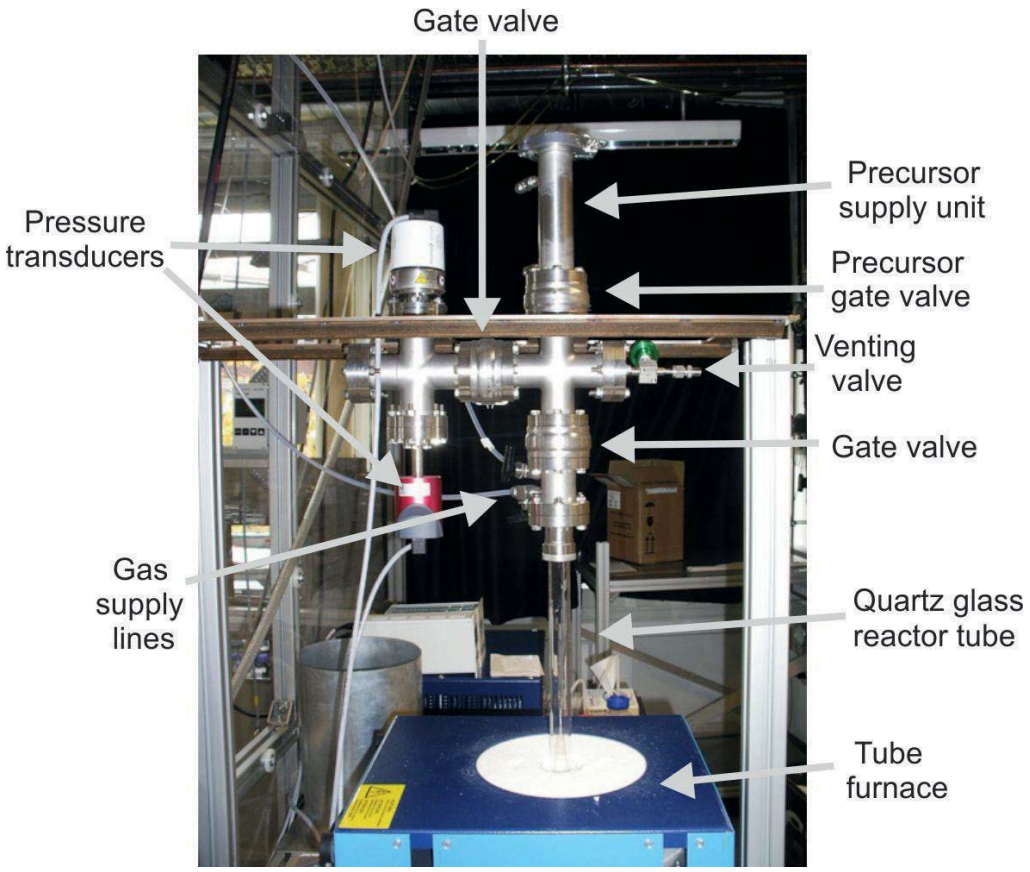

Fig. 103. Upper part of the chemical vapor infiltration setup

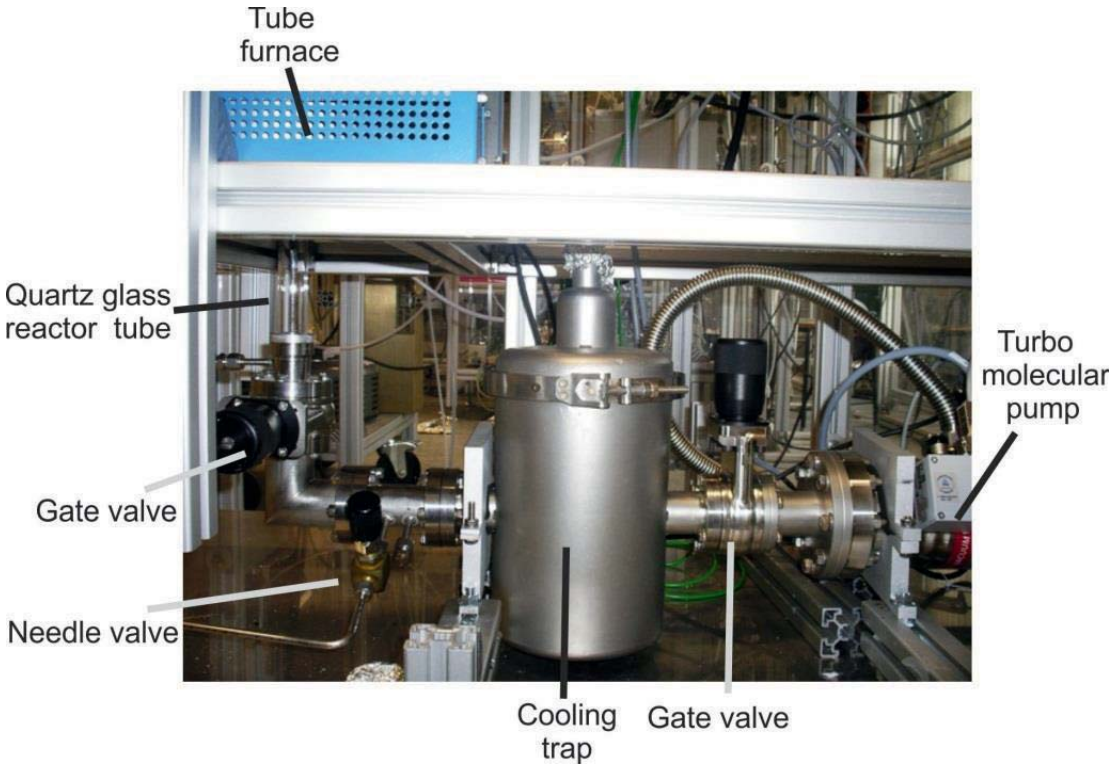

Fig. 104. Lower part of the chemical vapor infiltration setup

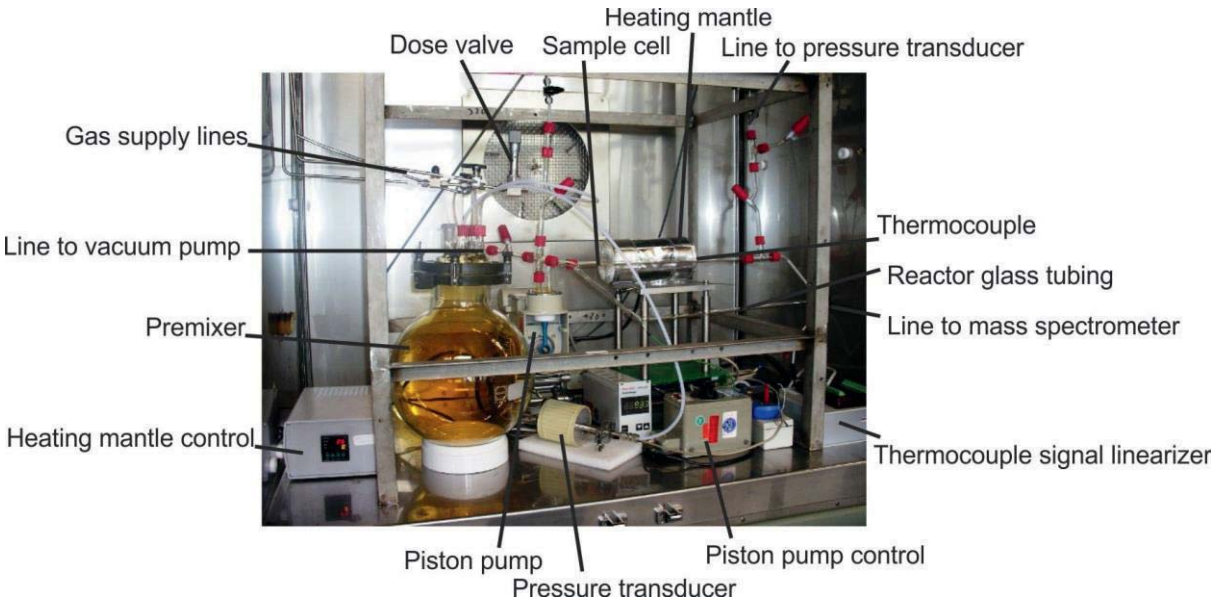

Fig. 105. Recycle reactor setup for investigation of catalytic activity

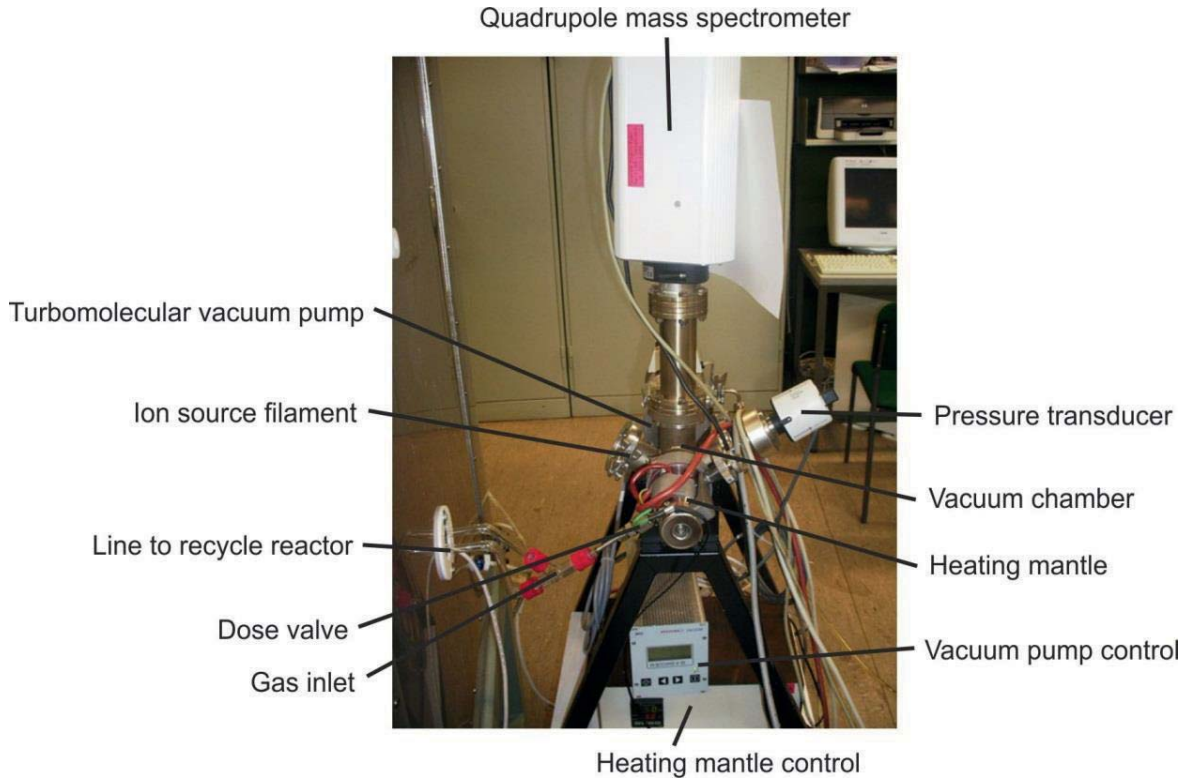

Fig. 106. Quadrupole mass spectrometer for investigation of catalytic activity

10. List of publications

- Busch M, Bergmann U, Sager U, Schmidt W, Schmidt F, Notthoff C, Atakan B, Winterer M. 2011. Synthesis of Active Carbon-Based Catalysts by Chemical Vapor Infiltration for Nitrogen Oxide Conversion. *Journal of Nanoscience and Nanotechnology* 11:7956-7961.

- Darbandi M, Laurent S, Busch M, Li Z-A, Yuan Y, Krüger M, Farle M, Winterer M, Van der Elst L, Muller R, Wende H. 2013. Blocked-micropores, surface functionalized, biocompatible and silica-coated iron oxide nanocomposites as advanced MRI contrast agent. *Journal of Nanoparticle Research* 15(5):1-9.

- Busch M, Schmidt W, Migunov V, Beckel A, Notthoff C, Kompch A, Bergmann U, Winterer M, Atakan B. 2014. Effect of preparation of iron-infiltrated activated carbon catalysts on nitrogen oxide conversion at low temperature. *Journal of Environmental Catalysis B* 160 (2014): 641-650.

- Busch M, Kompch A, Notthoff C, Bergmann U, Atakan B, Winterer M. 2014. NO_x conversion properties of a novel material: Iron nanoparticles stabilized in carbon. *Journal of Environmental Catalysis B* 166 (2015): 211-216.